Controller Motifs for Homeostatic Regulation and Their Applications in Biological Systems

by

Kristian Thorsen

Thesis submitted in fulfillment of
the requirements for the degree of

PHILOSOPHIAE DOCTOR
(PhD)

University of
Stavanger

Faculty of Science and Technology
Department of Electrical Engineering and Computer Science
2015

University of Stavanger
N-4036 Stavanger
NORWAY
www.uis.no

ISBN 978-82-7644-628-9
ISSN 1890-1387

PhD Thesis UiS no. 276

Preface

This thesis is submitted as partial fulfillment of the requirements for the degree of *Philosophiae Doctor* at the University of Stavanger, Norway. The research has been carried out at the Department of Electrical Engineering and Computer Science in collaboration with the Centre for Organelle Research (CORE), both at the University of Stavanger. A period of nine months (from August 2014 to May 2015) was spent as a research stay abroad at the Synthetic Biology and Cellular Control Lab of assoc. prof. David McMillen at the University of Toronto, Mississauga, Canada.

The research has resulted in five published articles. I started writing this thesis with the idea of creating a compilation thesis made out of the five articles. However, as writing progressed I felt that the research and the results deserved a clear, reworked, and thorough presentation. Thus, the thesis evolved into a form that is closer to the coherent monograph. The thesis consists of six chapters, where the main part (chapters 2-6) presents the research and results in a linear and logical progression. The chapters are written so that the reader can understand the work and the results without having to carefully read each of the published articles. The full articles are nevertheless, for completeness, included at the end of the thesis.

Kristian Thorsen, November 2015

Abstract

Living organisms have over billions of years evolved into highly specific and complex entities. Although the range of organisms that inhabit our planet is strikingly diverse, they are all in some extent able to protect their inner environment by keeping important variables within relatively narrow limits. This is called homeostasis and is achieved through elaborate regulatory networks with nonlinear interactions between genes, proteins and metabolites. These regulatory networks incorporate a combination of mechanisms, such as negative feedback, feedforward, integral control and proportional control.

It is clear that concepts from control theory, most often applied in systems engineered by humans, can also be applied to further the understanding of regulatory networks in biology. The complexity and nonlinearity of biological network does, however, make this not as straight forward and easy as one might think. Man-made systems are contrary to biological systems most often engineered from a set of separable components or subsystems, and specifically designed to keep interactions between different subsystems as simple as possible.

This thesis aims to explore how chemical species in a biological system can interact to form simple structures with homeostatic properties. A set of building blocks for regulation, consisting of two-component reaction kinetic schemes called controller motifs, is presented and formalized. The controller motifs have a structure that combines negative feedback with integral control, consequently giving the motifs homeostatic properties.

The controller motifs are useful in modeling and understanding of cellular homeostasis. They are herein employed to explore transepithelial glucose transport and ionic homeostasis in enterocytes. A mathematical enterocyte model is developed, and controller motifs are used in this model to explain how enterocytes can maintain a near constant internal concentration of sodium while dealing with sodium coupled nutrient transport.

Furthermore, this thesis demonstrates how controller motifs can be applied in synthetic biology as guidelines on how to design novel regulatory

networks. A copper controller in the form of a copper transporting Cu-ATPase, under control of a copper dependent promoter, is added to yeast (*Saccharomyces cerevisiae*) by genomic integration. This controller extends the yeast's ability to regulate its internal concentration of copper, and moreover the controller is shown to increase the yeast's survivability in environments with high concentrations of copper.

Finally, the controller motifs and the classical concept of homeostasis are extended and applied on oscillatory systems. A wide range of biological processes are, in fact, oscillatory. Examples include signaling by cytosolic calcium and circadian rhythms. This part of the thesis shows how even oscillatory systems can have properties, such as average level and frequency, that are maintained in a homeostatic fashion.

Acknowledgements

First and foremost I thank my supervisor Tormod Drengstig—for your willingness to comment upon all aspects of my work and for always answering my late night emails promptly before I arrive the next day. Thanks also to my co-supervisor Peter Ruoff—for showing me the value and enjoyment in being a true scholar.

Thank you to my colleagues and co-authors Ingunn W. Jolma, Xiao Y. Ni, Xiang M. Xu, Oleg Agafonov, and Christina H. Selstø—for introducing an electrical engineer to biology, for explaining me the obvious in details, and for our collaboration and many discussions.

To all my other colleagues and friends at IDE and CORE; thank you for your help and support. Special thanks to Sven Ole Aase for luring me into the PhD program.

A special thank to David R. McMillen, for allowing me to visit his lab at the University of Toronto, Mississauga, Canada. Thanks to all the members of his lab for welcoming me and teaching me molecular biology in practice. Thanks to Mostafizur Mazumder, for teaching me the tricks for manipulating bacteria and yeast; to Richard Kill, Jenna Friedt, Zhe Tang, Brendan Hussey, and Ed Harris for help with methods and protocols.

To my family and friends—thank you for all your understanding and support. Special thanks to my parents for your wisdom and for teaching me the value of hard work.

> *The scientist does not study nature because it is useful to do so. He studies it because he takes pleasure in it, and he takes pleasure in it because it is beautiful.*
> —*Jules Henri Poincaré.*

List of publications

The main part of this dissertation is made up of the following published scientific papers:

- **Paper 1**

  A Basic Set of Homeostatic Controller Motifs
  T. Drengstig, I. W. Jolma, X. Y. Ni, **K. Thorsen**, X. M. Xu, P. Ruoff
  Biophys. J., vol. 103, no. 9, pp. 2000-2010, Nov. 2012.

- **Paper 2**

  Robust Adaptation and Homeostasis by Autocatalysis
  T. Drengstig, X. Y. Ni, **K. Thorsen**, I. W. Jolma, P. Ruoff
  J. Phys. Chem. B, vol. 116, no. 18, pp. 5355-5363, Apr. 2012.

- **Paper 3**

  Control Theoretic Properties of Physiological Controller Motifs
  K. Thorsen, P. Ruoff, T. Drengstig
  IEEE Int. Conf. Syst. Sci. Eng. (ICSSE2013), pp. 165-170, Jul. 2013.

- **Paper 4**

  Transepithelial glucose transport and Na/K homeostasis in enterocytes: an integrative model
  K. Thorsen, T. Drengstig, P. Ruoff
  Am. J. Physiol. - Cell Physiol., vol. 307, no. 4, pp. C320-337, Aug. 2014

- **Paper 5**

  Robust Concentration and Frequency Control in Oscillatory Homeostats
  K. Thorsen, O. Agafonov, C. H. Selstø, I. W. Jolma, X. Y. Ni, T. Drengstig, P. Ruoff
  PLoS One, vol. 9, no. 9, p. e107766, Sep. 2014.

List of other imparts

Results from the dissertation have in addition to the published papers been communicated to the scientific community at:

(i) **Modeling and simulation of intestinal nutrient uptake.**
K. Thorsen, T. Drengstig and P. Ruoff, *Poster presentation.* ICSB. The 13th international conference on systems biology, Toronto, Canada. 2012.

(ii) **Integrative modeling of glucose transport and homeostasis in enterocytes.**
K. Thorsen, T. Drengstig and P. Ruoff, *Poster presentation.* CSH Computational Cell Biology 2013, Cold Spring Harbor, USA. 2013.

(iii) **Control theoretic properties of physiological controller motifs.**
K. Thorsen, P. Ruoff and T. Drengstig, *Talk.* IEEE International Conference on System Science and Engineering (ICSSE 2013), Budapest, Hungary. 2013

(iv) **Building controller motifs to manipulate copper tolerance and homeostasis in S. cerevisiae.**
K. Thorsen, *Talk.* CORE Research Seminars, Stavanger, Norway 2015.

Results from the dissertation have been communicated to the general public (in a popular scientific manner) at:

(i) **Kybernetikk og fysiologi (Cybernetics and physiology).**
K. Thorsen. *Talk.* NFA Servomøtet (Norwegian Society of Automatic Control meeting), Stavanger Norway, Oct. 2012. Also given at Stavanger Offshore Technical College, Stavanger, Norway, March 2013.

(ii) **Fysiologiske reguleringsmekanismer (Physiological control mechanisms).**
T. Drengstig, I. W. Jolma, **K. Thorsen**, P. Ruoff, *Article.* Naturen, 137, 4, pp. 128-137, 2013.

Contents

Chapter 1

Introduction

The ability to create, at least temporary, a local environment protected against the law of increasing entropy is one, if not the most, important property of all living organisms. Single- and multicellular organisms create their own internal environment, a milieu intérieur, protected against the outside. The chemical composition of the internal environment is regulated and maintained so that the biochemical processes that make out life can occur. As put by Claude Bernard «*La fixité du milieu intérieur est la condition de la vie libre*».

The first requirement to create a local environment is of course the existence of some kind of border. All cells are enclosed by a membrane, the plasma membrane, that enables the cell to create an internal environment different from the environment outside. Some cells also have cell walls, a tougher and more rigid layer. More complex multicellular organisms as plants and animals even have specialized cells that creates protective borders such as bark and skin.

The border cannot be absolute; an organism must be able to import raw materials, such as nutrients, and export unwanted waste products. Cells have specialized membrane bound proteins that transport specific molecules from one side to the other. Some of these proteins are active, that is, they use energy to move chemical species against their electrochemical equilibrium. In the most simple cases the energy can be harvested from the external environment by the proteins themself. One such example is *bacteriorhodopsin*, which is a transport protein used by certain *archaea*[1] that absorbs energy from light and uses it to move protons out of the cell [73].

Thus, the internal environment of a cell is protected by its cell membrane and proteins that can use energy, ultimately derived from external sources,

[1] Archaea is one of the three main domains of life together with bacteria and eucaryotes. Both archaea and bacteria are procaryotes, i.e., they have no distinct nucleus.

to keep the internal environment away from chemical (thermodynamic) equilibrium with the outside.

Another hallmark property of living system is the ability to receive and communicate information. We humans receive information through the basic senses, and communicate information by the use of language and body language. Information can also be received and passed by more subtle means: between animals, between cells within an organism, between single cells, and between cells and their environment. Hormones send messages between the different organs and cells inside the body, and pheromones do the same outside the body. Even the most simple organisms such as bacteria can sense certain chemicals in their environment [1, 45].

However, having a local environment different from the outside, and being able to receive and send information, is not enough. The local environment has to be regulated, and the organism have to react to the information it receives in order to do so. To live is to be able to use information to adjust to changes in the outer environment[2]. An illustrative example is how bacteria senses certain chemicals, and move accordingly either towards nutrients or away from toxins, a property known as chemotaxis [1, 45, 205]. Physical conditions, and chemical substances, in the internal environment have to be kept within certain golden ranges. Our body temperature is tightly regulated within a couple of degrees. Regulation of blood glucose by insulin and glucagon is an example with a somewhat larger range; healthy people have a blood concentration of glucose between 4 and 8 mM. The degree of regulation varies in the kingdom of life, and higher species often have, if not more refined, at least, more complex regulatory mechanisms.

In essence this thesis deals with the questions of how, by which mechanisms and interactions, cells and animals respond to information and regulate their internal environment to compensate for outside disturbances. And to how these mechanisms behave, i.e., what does it do. These questions lie within the field of *cybernetics*.

Cybernetics is the child of Norbert Wiener who coined the term with his book *Cybernetics: or Control and Communication in the Animal and the Machine* [200] first published in 1948. Cybernetics is the study of control and communication in self-regulating entities, and combines the theories of servomechanisms from mechanics and electronics with the theory

[2]Sentence adapted from Norbert Wiener: *The Human Use of Human Beings, Cybernetics and Society* [199] (pp. 17-18).

of homeostasis (see next section) from physiology and biology[3]. Both machines and living organisms are entities that respond to information and create local environments with order, environments that are maintained and regulated.

1.1 Biological regulatory systems: homeostasis and adaptation

Organisms have through evolution developed mechanisms that help them survive and reproduce; networks consisting of genes, proteins, organelles, cells, and whole organs create regulatory systems that interact to keep internal variables protected against variations in the external environment.

Homeostasis is the concept that describes the coordinated physiological processes that regulate and keep internal variables maintained at constant or near constant values. The term homeostasis was introduced by Walter Cannon in the 1920s. Cannon redefined the terminology of constancy (*fixité*) used by Claude Bernard; homeostasis does not mean regulation to a single always constant value, but coordinated regulation that maintain internal variables within narrow limits[4] [24, 25].

The concept of *adaptation* is tightly intertwined with homeostasis. A system shows adaptation if the system's response reverts back towards its original state when exposed to a constant change (a step) in one of its inputs. There is perfect adaptation in a variable if the response of that variable returns to precisely the same value as it had before the input change. Fig. 1.1 shows different modes of adaptation. Perfect adaptation is the ideal for a homeostatic control mechanism that aims to maintain an output at a specific setpoint in spite of environmental disturbances.

In biology adaptation is often encountered in sensory systems. A sensor that gives a response and then returns to its original prestimuli state when faced with sustained stimuli can function over a larger dynamic range in stimuli input. One example of adaptation in sensory response is how our eyes adjust to various levels of darkness and light. The intensity of sunlight

[3]The word cybernetics is borrowed from Greek $\chi\upsilon\beta\epsilon\rho\nu\acute{\eta}\tau\eta\varsigma$ meaning *steersman, governor*. Although the term was not coined until 1948 the field itself dates further back [200].

[4]Cannon derived the term from *homoio*, meaning similar (instead of just *homo*), and *stasis*, in the meaning of a condition [24]. Although Cannon had used the term before, it was his book *The Wisdom of the Body* (1932) [25] that made it famous.

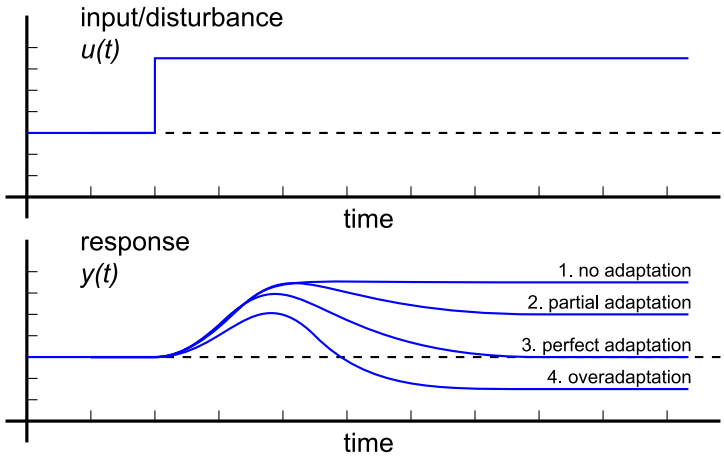

Figure 1.1: Systems respond to stepwise changes in their input with different degrees of adaptation.

is about 10 billion times that of starlight; the eye adapts to dark or light conditions and can change its sensitivity to light with a factor of up to 10^6 [69][5]. Adaptation also occurs in the auditory system. Both inner and outer hair cells function as transducers converting deflections in small hairs to electrical signals [168]. Fig. 1.2 shows experimental data of how the electrical current, emitted from these cells, adapts to sustained deflections.

An indispensable concept in homeostatic and adapting mechanisms is control/regulation by negative feedback[6]. Fig. 1.3 shows a general representation of a control system with negative feedback. The overall system is divided into two part, the *process* (or the controlled system) and the *controller*. The output signal $y(t)$ of the process (controlled variable or response) is fed back to the controller. The controller uses current and/or past information[7] about the value of the output signal to adjust the process with a signal $u(t)$ (also called manipulated variable). Negative feedback

[5]There are several regulatory systems that contribute to the adaptation of the eye. The amount of light that reach the retina is regulated by a change in pupillary size ($\sim$ 30 fold change in sensitivity). The rods and cones on the retina adapt their response in the photochemical system ($\sim$ ten thousandfold change in sensitivity), and adaptation also occurs in the neurons in the visual chain, from the retina to the brain ($\sim$ fewfold change in sensitivity) [69].

[6]Note that homeostasis is not exclusively equal to negative feedback. Other mechanisms such as feedforward and prediction may also have homeostatic properties.

[7]Information about past values requires some sort of memory in the controller.

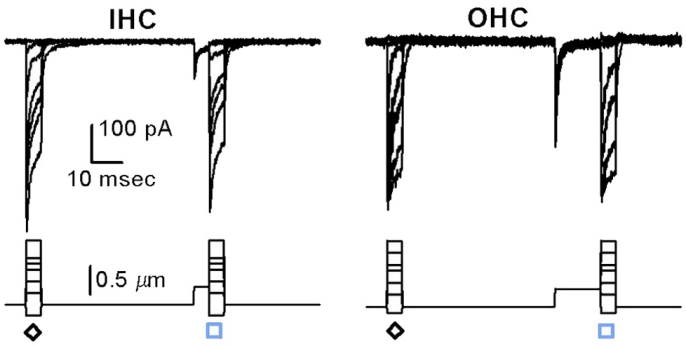

Figure 1.2: Adaptation in inner and outer hair cells of mice, IHC and OHC. Recorded transduction currents [pA] (upper) and stimulus [deflection in µm] (lower). Adaptation is seen in the parts marked by grey squares. The transduction current falls back during the conditioning step even though the displacement is sustained. Reprinted from [168] with permission.

means that the controller opposes changes in $y(t)$; if $y(t)$ increases then the controller will act to decrease it, and vice versa.

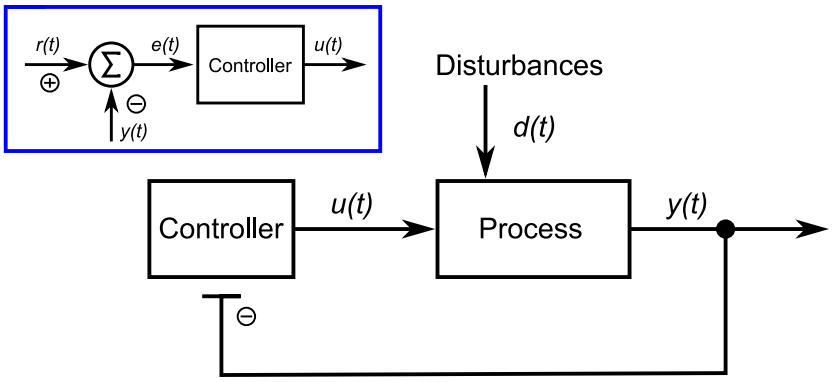

Figure 1.3: Schematic block diagram of a regulatory system with negative feedback. The controller has information about current (and previous) values of the output $y(t)$ through feedback. The overall sign of the closed control loop is negative: the process output $y(t)$ affects the controller output $u(t)$ negatively and $u(t)$ affects $y(t)$ positively (the opposite also gives a negative loop). The inset shows a realization of a controller operating on the error between $y(t)$ and a reference $r(t)$, see main text.

Any inputs to the process other than the input from the controller is called disturbances $d(t)$. Although such (uncontrolled) inputs act against the controller, they are often very important for the overall system; e.g.,

eating and muscle use disturb the glucoregulatory system of the blood. Opposed to ordinary design in control engineering it is often vital that a disturbance in a biological system creates a large transient in the output, since the output of one regulatory system is often used for signal detection in other connected systems. This is certainly true for the many sensory systems, a forever stable output cannot carry information!

In control engineering it is common to have a controller operating on the error $e(t)$ between the current output signal $y(t)$ and the desired output signal $r(t)$ ($e(t) = r(t) - y(t)$), see inset in Fig. 1.3. In cases where the reference signal is constant (or very slowly changing) the term *setpoint* is used instead of reference, $r(t) = y_{set}$. This concept of a reference signal, or a setpoint, can also be applied to biological systems, even though the controller may not have an easily distinguishable, or external, reference signal $r(t)$.

Likewise it is in biological systems often not easy to distinguish the process from the controller. Strictly speaking such a separation is not necessary; the overall system can still be analyzed and shown to have regulatory properties. Nevertheless, there can be significant advantages by, at least conceptually, separating the different parts of a biological system into modules with well defined roles as *processes* and *controllers*; and this thesis will show that it is advantageous to do so.

1.2 Robust perfect adaptation: integral feedback

An important aspect of homeostatic and adaptive systems is their robustness [3, 12, 171, 205]. In general a system is robust if its characteristic behavior is the same under a range of perturbations or uncertainties. The regulatory system in Fig. 1.3 shows robust perfect adaptation if it can reach the same steady-state value in $y(t)$ for a whole class of disturbances; it is then robust to that class of disturbance signals. In this thesis robust perfect adaptation[8] is taken to mean robust against the class of all step-type disturbances, unless stated otherwise.

Some of the mechanisms that account for perfect adaptation have been argued to stem from a balance between various opposing components within a reaction network [12, 153]. However, a balancing based approach like

[8]There is in this thesis no difference in the concepts of robust perfect adaptation and robust perfect homeostasis.

this does not guarantee a fixed steady state of the controlled variable in the presence of perturbations, i.e., it is not robust. Yi et al. [205] elegantly showed this by doing bifurcation analysis of balanced based model for chemotaxis proposed by Spiro et al. [167].

The alternative to a balancing approach is a regulatory system with a structure that inherently provides robustness. It is from control engineering well known that this is provided by *integral control* [116]. With integral control the controller output $u(t)$ is the integrated error $e(t)$ over time, expressed mathematically as,

$$u(t) = G_i \int_0^t e(\tau)\, d\tau = G_i \int_0^t (r(\tau) - y(\tau))\, d\tau \tag{1.1}$$

where G_i is a constant called the (integral) *gain* of the controller. An equation describing the output $u(t)$ in a controller such as Eq. 1.1 is in control engineering called a *control law*. The integral controller uses information about the current and all past errors, i.e., it sums up the difference between the reference and the output over time.

The inherent robust perfect adaptation can be proven by contradiction. Assume that the system is in steady state at time t=0, and that the error e_0 then has a value different from 0, e_0=$\xi \neq 0$ (assuming that the adaptation is not perfect). Integrating Eq. 1.1 to t gives,

$$u(t) = G_i \int_0^t \xi\, d\tau = G_i \xi t \tag{1.2}$$

but $u(t)$ is not constant, because it depends on t. This contradicts the assumption about steady state, and the conclusion is that if we are in steady state then $e(t) = \xi = 0$. Thus, integral control has robust perfect adaptation[9].

The integral controller can equivalently be described by its derivative form:

$$\frac{du(t)}{dt} = G_i e(t) = G_i\,(r(t) - y(t)) \tag{1.3}$$

The property of zero steady-state error is often demonstrated by this equation, as the assumption of steady state implies that all time derivatives are zero.

[9]Robust integral control does not imply stability. The proof assumes steady state, i.e., stability. Integral feedback actually decreases the stability margin of a system and may lead to sustained oscillations or a diverging output.

1.2.1 Sufficiency and necessity of integral feedback for robust adaptation

It can be proven that any system that shows robust perfect adaptation to step disturbances must have integral feedback; it is both a sufficient and necessary structural property. This is a special case of the internal model principle (IMP) [54, 83, 166]; it states that in order for a regulatory system to asymptotically adapt its output $y(t)$, under disturbances by a specified class of signals, the system must necessarily contain a subsystem which itself is capable of creating the same class of signals. And this subsystem must do so while having only the system output $y(t)$ as input. In other words, if a system is to be robust against all constant disturbances, then the system must contain a subsystem that can generate all constant signals. An integral controller operating on the error $e(t)$ is such a system; constant signals are generated by the differential equation $\dot{u} = (r(t) - y(t))$. The controller output $u(t)$ becomes constant when $y(t) = r(t)$, i.e. when the output is perfectly adapted to the reference.

1.3 Homeostasis and oscillatory processes

A wide range of biological processes are oscillatory. We are all familiar with our own periodic breathing and our heartbeats. Oscillations are observed over the whole range from cellular to ecological systems. Examples include metabolic glycolysis [38, 161], the p53 Mdm2 system controlling *apoptosis*[10] (often related to cancer) [85, 119], cellular signaling by Ca^{2+} [17, 26, 56], circadian rhythms [48, 121, 135], and ecological predator prey systems [19, 179]. Fig. 1.4 shows an example of oscillations observed in cytosolic Ca^{2+} and membrane potential for pancreatic islets of insulin producing β-cells. Islets (collections of β-cells) show synchronous oscillations when exposed to high concentrations of glucose (10 mM).

Intracellular oscillations are often related to signaling. Ca^{2+} oscillations in β-cells (Fig. 1.4) are a key signal for the secretion of insulin as a response to high blood glucose [56]. Ca^{2+} oscillations are found in most cell types and Ca^{2+} is one of the most common messenger species found in cells [137].

At first glance oscillations may be considered to contradict active control and regulation, and it has been suggested that oscillations represent a

[10] Programmed cell death, occurs in development, and as a response to cellular injury.

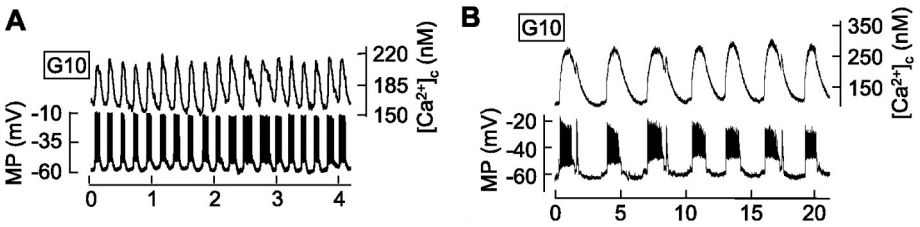

Figure 1.4: Oscillations in membrane potential (MP) and cytosolic Ca^{2+} in β-cells in a pancreatic islet. (The islets of Langerhans are regions in the pancreas with hormone producing cells; β-cells make out 60-70% of the cells in an islet [96].) The cells were perifused with a solution containing 10 mM glucose (stimulus). Both fast (**A**) and slower oscillations (**B**) can be observed. Reprinted from [14] with permission. Copyright © 2006, The American Physiological Society.

breakdown of homeostasis[11] [109]. A chapter in the book Chronobiology Biological Timekeeping [186] describes the circadian oscillations in human body temperature as «cracks in the homeostasis theory». This leads to the question: how can homeostatic mechanisms possibly work when many of the regulatory processes within a cell are based on oscillations.

To answer this it should be realized that oscillations do not necessarily contradict homeostasis as defined by Cannon [121]. Physiological variables are allowed to fluctuate within a homeostatically defended range, which can be quite wide. Cannon's only figure in his 1929 paper on homeostasis [24] illustrates the concept by showing how the normal level of human blood glucose oscillates between 70 mg/dL and 130 mg/dL. This range is what Cannon called «relatively narrow». Furthermore, whether conditions are pathologic or not may in many cases depend on average values over longer periods, and not on maximum values with only a short duration.

In fact, even oscillatory systems can have properties that are defended in a homeostatic fashion, as will be shown in chapter 5 in this thesis. The period of the circadian clock is a prime example. Regulatory mechanisms keep the period of this internal clock more or less constant against temperature changes [48, 72].

A further introduction to the mathematical definition, classification, and description of oscillators is given in chapter 5.

[11] The tendency to think so may be even greater among scientists with a background in engineering. Control systems that oscillates are in general frowned upon in the engineering community.

1.4 A new age for research on homeostasis.

The type of biological systems that have been subject to analysis for homeostatic properties have changed over time. In the years of Bernard and Cannon homeostasis was applied on large scale physiological systems of humans and higher mammals, such as body temperature, blood concentrations, oxygen supply, thirst, hunger, and so on [25, 102]. At their time homeostasis was more of a philosophical concept. Bernard's *la vie constante* was reserved for humans and warm-blooded animals [102], and Cannon's *homeostasis* gave higher animals freedom to be conscious about other things than to alter the rate of bodily processes to maintain constancy [25]. Humans were at that time still regarded to be on the top of the evolutionary pinnacle, and homeostasis gave us freedom from being an animal.

In the years after the second world war (late 1940's and 1950's) the mechanisms behind homeostasis became more apparent [102]. The mathematical formalization with cybernetics introduced new terms such as feedback, loops, servomechanisms, transfer functions, and many other expressions to physiology. This created an explosion of publications dealing with regulation and homeostasis. Homeostasis became mechanistic and the body was treated as any other machine. Fig. 1.5 shows the relative trend of publications dealing with homeostasis, in some way or another, indexed in PubMed [126]. While around 3‰ of papers mentioned homeostasis in 1960, as many as 11‰ did so in 1971. The publication rate then peaked around the same time as Langley edited the book *Homeostasis: Origins of the Concept* [102], a collection of seminal papers on homeostasis. The introduction to the most recent papers in this collection had the comment: «*Any paper published today, at least in physiology, which is worth the paper it is printed on, should further clarify a homeostatic mechanism.*»([102] p. 293)

The research from the 1950's to the 70's mainly dealt with homeostasis of organs and the whole body; the main theme was understanding *human* physiology. The work by Robert Steele and others [170, 183] on elucidating the glucoregulatory system by dividing it up into compartmentalized pools, building mathematical models for the interaction and passing of glucose and insulin between these pools, creating electrical analog circuits for simulation studies, and doing experiments with radioactively labelled sugar molecules is representative for this period.

A new rise in work on homeostasis started around the new millennium. Revolutionary methods in molecular biology have now opened up a whole new world to the study of homeostasis; the internal regulation of cells

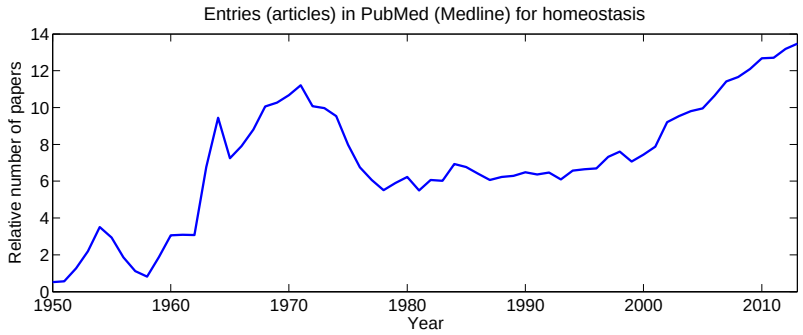

Figure 1.5: Relative number of articles in PubMed (Medline) published every year that have homeostasis in any of the searchable fields in the database entry. The results are relative, to account for the general inflation of publications, and given in ‰. Retrieved by using Medline trend [33].

and single-cellular organisms. The sequencing of the human genome, and other sequencing projects have created incredible amounts of information; and made it possible to research regulation on the gene-protein-cell scale. Moreover, methods for genomic modification have made it possible to add reporter genes, genes that confer characteristics that are easily identified and measurable. For example the gene of a green fluorescent protein[12] (GFP) can be added to the end of the gene of the protein of interest to create a fusion protein. Whenever the cell translates this protein it will glue a fluorescent protein onto it. This technique and others have made it possible to do quantitative time-series measurements of intracellular concentrations, producing data that is suitable to test and refine mathematical models.

Two emerging, or now established, fields related to this new age are *Systems Biology* and *Synthetic Biology*. Systems biology is a top-down approach, enabled by the recent advances in high-throughput assays. It is a system of systems approach, and focuses on investigating the behavior of several elements, or subsystems, in a larger system (the cell) at once [79, 95]. The typical experimental procedure is to perturb one element in the system, and gather data about how all other elements behave. System behavior is integrated by systematically doing this perturbation for all, or the most interesting, elements in the system. The acquired information is then compared to a predicted model and used to establish relationships between elements. Synthetic biology on the other hand takes the bottom-up

[12] First isolated from jellyfish. Today variants in different colors are available, engineered by mutations.

approach [4, 68]. The focus of synthetic biology is to study simple molecular networks and to uncover fundamental principles or mechanisms. The idea is that complex network behavior can be understood by well-characterized submodules. A major part of synthetic biology is the construction of designed submodules with various functions that are built by constructing novel gene networks inside living cells. Examples include: a genetic toggle switch [59], oscillators [8, 52], logic gates [10, 184], and more [91].

Although far from all topics in systems and synthetic biology are directly related to homeostasis, they are all important for understanding the overall regulation of cells and organisms. Both fields rely heavily on mathematical models, control theory and informatics and thus fit nicely under the umbrella of cybernetics. Several books have been published in the last five years aimed at introducing the reborn field of control and regulation in biological systems to biologists, chemists, mathematicians, engineers and physicists [36, 80, 82, 108].

1.5 Aim of this thesis

The main objective of this thesis is to take a bottom-up approach to homeostasis on a cellular level and to:

- Explore the mechanisms of how chemical species can interact to achieve homeostatic properties particular in relation to the internal regulation of cells and single-cellular organisms.
- Present a set of building blocks for homeostatic control termed *controller motifs*, which are reaction kinetic schemes with structure that incorporates integral control.
- Show how these controller motifs can be used as building blocks in mathematical modeling of cells and their regulatory systems.
- Present a mathematical model of sodium driven transport and ionic homeostasis in intestinal enterocytes.
- Show how the controller motifs can be used as blueprints for designing regulatory networks in synthetic biology.
- Extend the controller motif to model oscillatory systems, and highlight the homeostatic properties of such systems.

1.6 Main contribution

Taken together, the parts of this thesis present a guideline for construction of regulatory networks. It presents a way of doing modeling by submodules with known homeostatic properties that can be interconnected and expanded in a multitude of ways. In popular jargon, the thesis presents a controller motif modeling framework for homeostatic molecular and physiological mechanisms. The scientific contribution of the thesis is made up of five published scientific papers, and the, so far, unpublished results of a synthetic implementation of a controller motif in yeast cells. Fig. 1.6 visualizes the connections between the different parts of this thesis.

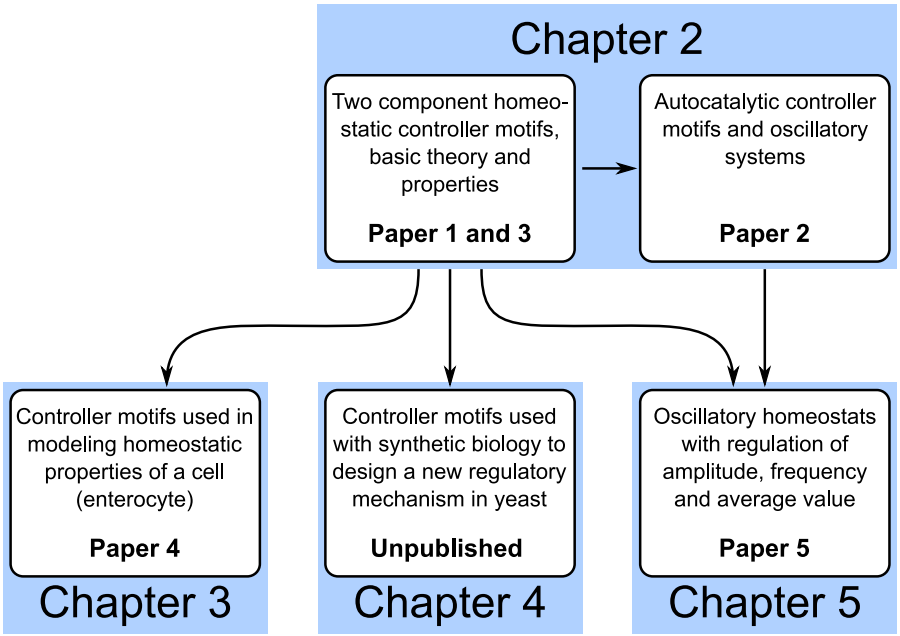

Figure 1.6: Connections between the main parts of this thesis.

Chapter 2 presents the results from Paper 1 and Paper 3 together with some parts from Paper 2. The submodules in this work are made out by a complete set of two-component molecular controller motifs with negative feedback and integral control that show robust homeostasis. The controller motifs consist of a controlled species A that is regulated by a controller species E. The work in these papers formalizes the construction of controller motifs and clarifies their control properties when used individually and

together in pairs[13]. Emphasis is put on how integral control is dependent on zero-order degradation of the controller species E. It is shown how the controller motifs have properties such as setpoints, integral gain and measurement functions, and how diversion from ideal conditions affects the accuracy of the controllers. The operating limits of the controller motifs and the cases where they break down are explored in detail. Furthermore, it is shown how controllers can be combined within a cell to explain mechanisms such as the integrated uptake and metabolization of homeostatic controlled species, and the activation of pathways that leads to formation of alternative products. Chapter 2 also includes the first part of Paper 2, which extends the work in papers 1 and 3 by showing how integral control can be achieved by autocatalytic formation and first-order degradation of the controller species.

In chapter 3, the controller motifs are put to use as a part of a study on transepithelial glucose transport and ionic homeostasis in enterocytes. Whereas chapter 2 is largely theoretical, this chapter presents a practical case of modeling a specific mechanism in a specific cell type. A mathematical model of the enterocyte is developed, and this model is extended with controller motifs. The controller motifs are used to test the hypothesis that sodium homeostasis in enterocytes can be explained by a sodium mediated regulation of the amount of active sodium-pump proteins (Na-K-ATPase) in the enterocyte membrane. Simulation results of the model show that the proposed hypothesis together with a regulation of K-channel permeability provide ionic homeostasis during absorption of glucose. This model is also the first mathematical model of enterocytes that integrates realistic reaction kinetic expression for transport through major transporter proteins.

Chapter 4 presents preliminary, unpublished, results from implementation of a Cu regulation controller motif in the yeast *Saccharomyces Cerevisiae*. This work was done during my stay at the Synthetic Biology and Cellular Control Lab of assoc. prof. David McMillen at the University of Toronto, Mississauga. These results show how the addition of an outflow controller, in the form of a copper transporting Cu-ATPase under control of a copper dependent promoter, can increase the yeast's survivability in environments with high concentrations of copper. The added outflow controller extends

[13]Homeostatic controller motifs had already been an useful idea of our group before I joined in August 2011. Four years earlier, less formalized, motifs were presented in a paper in 2009 [130] and some had been used in a modeling study of the p53 system [85]. Seeing how powerful these motifs where, we wanted to formalize their construction and clarify their control properties when used individually and together in pairs.

the range of external copper wherein the yeast can maintain homeostatic regulation. The outflow controller was synthetically added to the yeast genome by genomic integration.

Chapter 5 is based on Paper 5 and the second part of Paper 2. The chapter introduces oscillatory systems and shows how the two-component controller motifs can show simple conservative oscillations, and how they, by extension of an intermediate species in the formation of the controlled species A or the controller species E, can exhibit stable limit-cycle type oscillations. Also, the well-known Lotka-Volterra oscillator is demonstrated to be equivalent to a controller motif with an autocatalytic loop in both A and E. This chapter demonstrates how oscillations can emerge in regulatory systems with negative feedback, and furthermore, investigates whether biological oscillators can show robust homeostatic and adaptive behaviors. Controller motifs are added to already oscillating systems to create oscillatory homeostats. These homeostats are oscillators that have the ability to keep the average level of a controlled variable at a defined setpoint, and to keep the period/frequency of the that variable tuned within a certain well-defined range. The work presented in chapter 5 is an attempt to extend the classical concept of homeostasis to biological systems that show sustained oscillations, such as circadian rhythms and calcium signaling.

1.7 Modeling methods and presentation

The majority of the work in this thesis is dry in the opposite sense of how the term wet is used to describe experimental benchtop experiments with chemicals and living cells. Mathematical models are used to study how chemical species, such as proteins, interact to form networks that show regulatory and homeostatic properties. The mathematical models are dynamic and formed by sets of, in general, nonlinear differential equations.

Chapters 2 and 5 (Papers 1, 2, 3, and 5) consider general networks of interacting species with the goal of finding structures that have homeostatic and oscillatory properties. Compared to the papers these chapters are more focused on the theoretic concepts and properties. I have relaxed the focus on showing examples of where such motifs are found in biology; relations to well known mathematical models for biological systems are on the other hand well covered.

Standard reaction kinetic expressions for activation and inhibition are used to describe the flow of species caused by production, degradation, transport. For the most part no particular species are considered and variables and states are hence in arbitrary units, unless stated otherwise. Parameters, such as rate constants, used in examples in these chapters are selected to give representative system responses, which visualize the underlying concepts and properties.

The biological significance of this work is thoroughly covered by chapters 3 and 4. Specific species are used in the model in chapter 3, which considers the case of regulation of ionic species in enterocytes during glucose absorption. Results in this chapter are given in proper units, and flow expressions are based on experimental kinetic data and models of the particular molecular mechanisms in question.

The mathematical models are explored by analysis and by numerical simulations. The models are implemented and simulated in Matlab/Simulink from MathWorks. The low level programming language Fortran is also used together with the subroutine LSODE [143].

1.7.1 Partition of inflow and outflow

Consider the regulation of a chemical species A in a compartment such as a cell. The amount of A can change by (Fig. 1.7):

Inflow: A is transported over the border and into the compartment or produced inside.

Outflow: A is transported over the border and out of the compartment, or used/degraded inside.

In agreement with the above definitions, *inflow* and *outflow* are throughout this thesis used to described any positive and negative terms in the differential equations describing the change of a species in a certain compartment, i.e.,

$$\frac{dA}{dt} = \text{Inflow} - \text{Outflow} \tag{1.4}$$

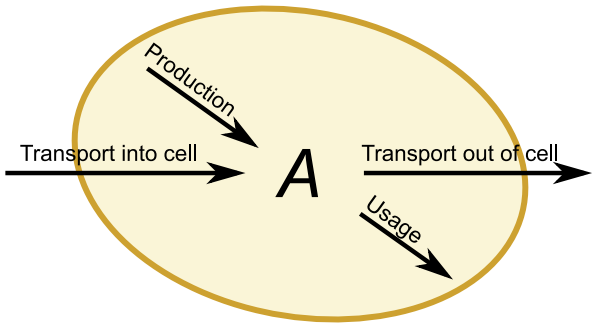

Figure 1.7: Inflows (transport into the cell and internal production) increase the amount of a chemical species A in a cell, and outflows (transport out of the cell and internal usage) decrease it.

1.7.2 Assumption of a fixed volume

The differential equation describing the change of A, Eq. 1.4, is called the *law of mass balance*. It is based on the fact that matter cannot be created nor destroyed, except for radioactive and nuclear reactions.

In most biological systems amounts are measured in units of concentration. Concentration is mass divided by volume, $c = m/v$. Consequently $m = cv$, and the law of mass balance can by the product rule be written as:

$$\frac{dm}{dt} = \frac{dc}{dt}v + \frac{dv}{dt}c \tag{1.5}$$

The change in concentration is then:

$$\frac{dc}{dt} = \frac{1}{v}\left(\frac{dm}{dt} - \frac{dv}{dt}c\right) \tag{1.6}$$

So when A is measured as a concentration, often denoted by using square brackets $[A]$, the differential equation describing its change becomes,

$$\frac{d[A]}{dt} = \frac{1}{V}\left(\frac{dA}{dt} - \frac{dV}{dt}[A]\right) \tag{1.7}$$

where dA/dt is sum of inflows and outflows of A (in mass or molecules per time). The distinction between Eq. 1.4 and Eq. 1.7 may be important in systems with a nonconstant volume, such as growing cells. An increasing cellular volume acts to reduce $[A]$ by diluting the molecular concentration. How important this distinction is depends, however, on how fast the cells are growing compared to the rest of the dynamics in A.

The effects of a changing volume is for the systems studied in this thesis considered to be negligible and is therefore not included. It is assumed that the volume is either constant, or very slowly changing compared to the rest of the system dynamics, that is, $dA/dt \gg [A]dV/dt$. The volume is not explicitly included in the theoretical treatment of the controller motifs in chapters 2 and 5 (implicitly assumed that $V = 1$). Furthermore, to make notation simpler, concentrations are written without square brackets[14].

[14]Square brackets are used in section 3. This is simply because they were used in Paper 4, which section 3 is based on.

Chapter 2

The controller motif framework (papers 1 to 3)

This chapter presents the main components of our framework for modeling and understanding of homeostatic mechanisms: the basic controller motifs. These two-component, reaction kinetic, motifs serve as building blocks, as simple subsystems that exhibit homeostatic properties. To be able to understand and use the controller motifs we give here, a detailed and thorough exploration of their inner workings and their underlying features. This chapter highlights capabilities as well as limits with the controller motifs.

2.1 Analysis of regulation and homeostasis: Controller motifs

The basic set of two-component controller motifs, shown in Fig. 2.1, consists of negative feedback loops with two species: A, the controlled species (or controlled variable CV) and E, the controller species (or manipulated variable MV). The controller motifs are constructed in the following way: from E and A inhibition or activation signals act on the other species' synthesis or degradation processes, but not on both. Uncontrolled disturbances in inflow and outflow of A, marked d_i and d_o, are compensated for by E which adjusts a *compensatory flow* j. There are four configurations by which E can affect A through a compensatory flow j, and these are:

(i) Synthesis of A is:

   (a) Activated by E (motif 1 and 3)
   (b) Inhibited by E (motif 2 and 4)

(ii) Degradation of A is:

(a) Activated by E (motif 5 and 7)

(b) Inhibited by E (motif 6 and 8)

And likewise there are four configurations by which A can affect E. Four by four configurations gives a total of 16 different motifs. Eight of these have an overall negative feedback loop (shown in Fig. 2.1) and eight are positive feedbacks (see Fig. S3 in the Supporting Material for Paper 1).

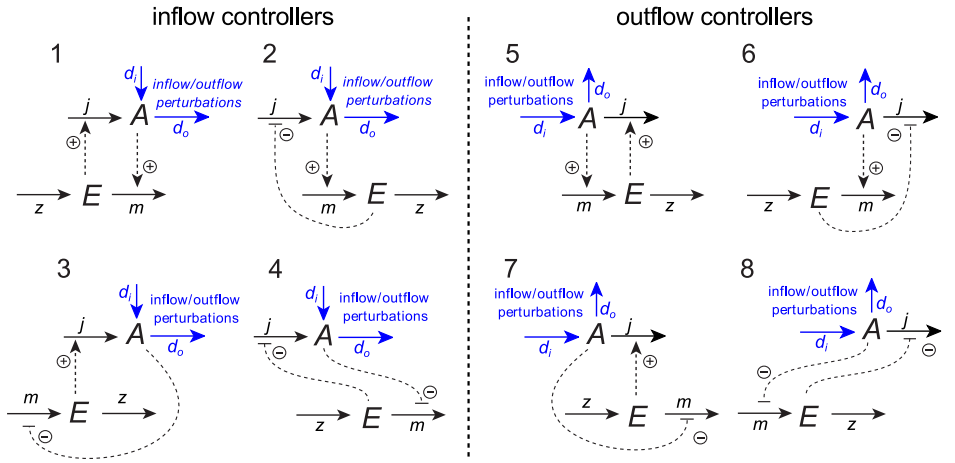

Figure 2.1: Two-component controller motifs. The motifs fall into two operational classes termed inflow and outflow controllers (for definition, see main text). A is called the controlled species, and E is called the controller species. The dashed lines refer to signal transduction that originates from one species and affects the inflow or outflow of the other. The different inflows and outflows (solid arrows) are explained in the main text.

The sign of the overall feedback loop is determined by starting at A and moving along the loop while multiplying the plus/minus signs of the activation/inhibition steps with the plus/minus signs of the synthesis/degradation. This procedure is illustrated in Fig. 2.2.

Inspection of the motifs shows that the set divides equally into two operational classes termed inflow and outflow controllers. Inflow controllers are defined by that they compensate by adding A to the system from an internal or environmental source, whereas outflow controllers compensate by removing A from the system.

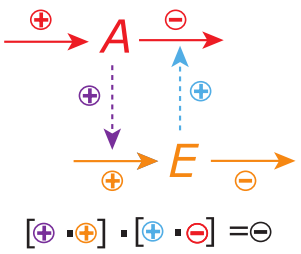

Figure 2.2: The type of feedback is determined by multiplying the signs along the feedback loop.

2.2 The controlled part of the system, A

The dynamics of A can be written as,

$$\dot{A} = d_i(\cdot) - d_o(\cdot) \pm j(\cdot, E) \tag{2.1}$$

where $d_i(\cdot)$ and $d_o(\cdot)$ are disturbances related to uncontrolled inflow/outflow, and $j(\cdot, E)$ is the E-mediated compensatory flow.

The disturbance functions can by principle take any form; we have most often used $d_i(\cdot) = k_p^i$ and $d_o(\cdot) = k_p^o A$, where the two k's are parameters that we perturb to emulate disturbances (e.g., in a stepwise manner)[1].

Throughout this thesis E-mediated compensatory flows are mostly written on the form,

$$j(\cdot, E) = f_c f(\cdot) E, \qquad \text{activation.} \tag{2.2}$$

$$j(\cdot, E) = f_c f(\cdot) \frac{K_I^E}{K_I^E + E}, \qquad \text{inhibition.} \tag{2.3}$$

where f_c is typically a rate constant and the function $f(\cdot)$ describes the flow's dependence on other parameters, e.g., the level of A or external species, temperature, or pH. For the inflow controllers we often use $f_c f(\cdot) = k_1$, $f_c f(\cdot) = k_1 A_{ext}$, or a saturable function of A_{ext}; for the outflow controllers we often use $f_c f(\cdot) = k_2 A$, or a saturable function of A.

The E-activated flow, Eq. 2.2, has first-order kinetics with respect to E, so that the flow increases with increasing E. The E-inhibited flow, Eq. 2.3,

[1] The subscript p denotes perturbation and the superscripts i and o denotes inflow and outflow. The k's were written as k_{pert}^{inflow} and $k_{pert}^{outflow}$ in Paper 1 and Paper 2.

decreases as E increases; its maximum rate is $f_c f(\cdot)$ when E=0. K_I^E is the concentration of E where the flow is half of its maximum rate. No specific inhibition mechanism is assumed at this point, i.e., the inhibition constant K_I^E does not have to be a constant in the sense of a chemical equilibrium (dissociation) constant for a specific enzymatic inhibition type[2].

2.3 The controller, E

Information about the level of A is passed to E by the measurement flow m (Fig. 2.1). As with the compensatory flow, this flow is written on the form,

$$m(\cdot, A) = g_c g(\cdot) A, \qquad \text{activation.} \tag{2.4}$$

$$m(\cdot, A) = g_c g(\cdot) \frac{K_I^A}{K_I^A + A}, \qquad \text{inhibition.} \tag{2.5}$$

where g_c is a constant and the function $g(\cdot)$ describes the flow's dependence on other parameters, e.g., the level of E or external species, temperature, or pH.

Negative feedback is in itself not sufficient to provide homeostasis in the sense of perturbation independent regulation of A to a setpoint. Our controller motifs incorporate integral feedback, which is both necessary and sufficient for robust adaptation, see section 1.2.1 in the introduction. One way to achieve integral feedback is to remove E with zero-order kinetics in relation to its own concentration; this has been shown both by our group [130] and by others [6, 7]. Zero-order degradation can occur in a biochemical environment if E is degraded by a saturated enzyme (e.g., Michaelis–Menten kinetics with a low K_M value).

I will illustrate this here by using motif 5 from Fig. 2.1. The change in E is described by the following differential equation,

$$\dot{E} = k_s^E A - \frac{V_{max}^{E_{set}} E}{K_M^{E_{set}} + E} \tag{2.6}$$

which can be rewritten as:

$$\dot{E} = -k_s^E \left(\frac{V_{max}^{E_{set}}}{k_s^E} \frac{E}{K_M^{E_{set}} + E} - A \right) \tag{2.7}$$

[2] A case where K_I^E is a real equilibrium constant is outlined in the Supporting Material for Paper 1.

With zero-order degradation, i.e. $K_M^{E_{set}} \ll E$, this reduces to,

$$\dot{E} = -k_s^E \left(\frac{V_{max}^{E_{set}}}{k_s^E} - A \right) = -k_s^E \left(A_{set} - A \right) \tag{2.8}$$

where A_{set} is the theoretical setpoint for this controller, found by the steady-state condition in E (setting $\dot{E} = 0$).

$$A_{set} = \frac{V_{max}^{E_{set}}}{k_s^E} \tag{2.9}$$

Equation 2.8 is structurally similar to the standard integral control law, in control engineering commonly written as $\dot{u} = G_i(r - y)$, where r is the reference (setpoint), y is the measurement and G_i is the integral gain (Eq. 1.3).

Controller motif 5, shown in Fig. 2.3A, can with the assumptions above be represented in a block schematic form as shown in Fig. 2.3B. The feedback loop with integral action can be identified by following the line from A via k_s^E, the E integrator, the multiplication block, and k_2, colored red in Fig. 2.3B. The block schematic representation can also be rearranged in such a way that the controller, given by Eq. 2.8, and the setpoint is clearly shown, see Fig. 2.3C. This is the conventional visualization of a feedback system in control engineering; it clearly shows the controller integrating the error between the setpoint and the fed back measurement of A, enabling it to compensate for the disturbances (k_p^i and k_p^o).

The negative integral gain $G_i = -k_s^E$ in Eq. 2.8 is essential as controller motif 5 removes A by a compensatory outflow. If perturbations cause A to increase, then E must increase so that the compensatory outflow can increase to remove more A.

The same approach can be used to show the homeostatic behavior of all the eight two-component motifs in Fig. 2.1. This is done in Paper 1 and its Supporting Material with some added generality that shows how $K_M^{E_{set}}$ and the inhibition constant K_I^A (for controllers 3, 4, 7, and 8) may affect the accuracy of the controller, see also section 2.6

2.4 Setpoint determination

The setpoint A_{set} of outflow controller motif 5, where A is activating the measurement flow (m), was above found by the steady-state condition of

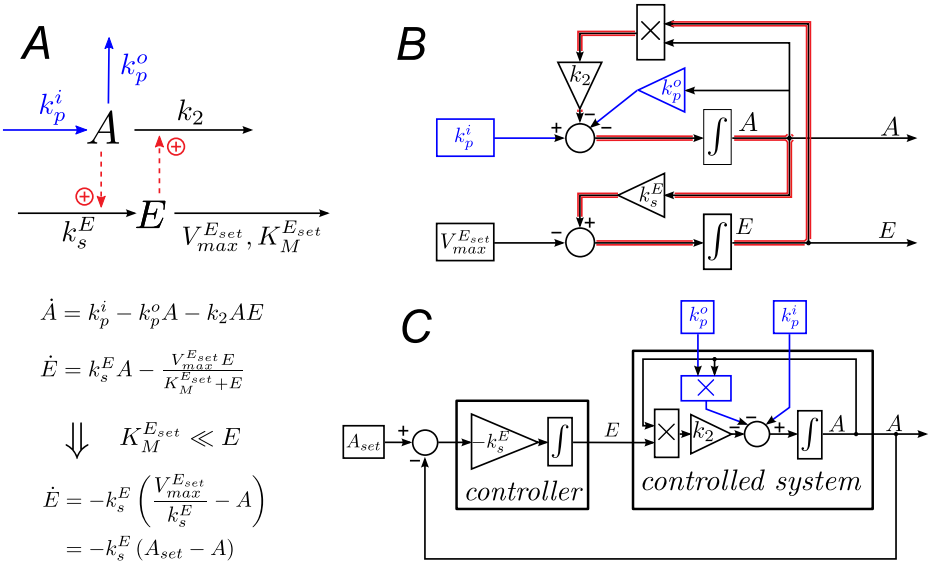

Figure 2.3: Controller motif 5. **A** Reaction kinetic representation and equations for zero-order removal of E. **B** Block schematic representation of the system. The feedback loop is highlighted in red. **C** Control engineering type block schematic representation showing the distinction between the controller and the controlled system.

the manipulated variable E together with the assumption of zero-order degradation, i.e., $K_M^{E_{set}} \ll E$. Inflow controller 3, where A is inhibiting the measurement flow, is used below to show how A_{set} is determined and defined in general. Letting the A-inhibiting measurement flow be given by Eq. 2.5 the change in E is described by,

$$\dot{E} = g_c g(\cdot) \frac{K_I^A}{K_I^A + A} - z_c z(\cdot) \tag{2.10}$$

where a general form $z_c z(\cdot)$ is used for the degradation term. The steady-state condition in E and *ideal conditions*, i.e., $g(\cdot) = z(\cdot) = 1$, are used to determine the theoretical setpoint. For inflow controller 3:

$$A_{set} = \frac{g_c K_I^A}{z_c} - K_I^A \tag{2.11}$$

The basis for setting $g(\cdot)$ and $z(\cdot)$ equal to 1 is to make A the only variable in the differential equation for the manipulated variable (E), thus making it possible to find a constant solution for A using only the steady-state condition in $\dot{E}$.

The procedure above was used in Paper 3; the presentation in Paper 1 is slightly different. Inflow controller 3 is therein given by the following equation (*Eq. 2* in Paper 3):

$$\dot{E} = k_s^E \frac{K_I^A}{K_I^A + A} - \frac{V_{max}^{E_{set}} E}{K_M^{E_{set}} + E} \tag{2.12}$$

This is the same as Eq. 2.10 with $g_c = k_s^E$, $g(\cdot) = 1$, $z_c = V_{max}^{E_{set}}$, and $z(\cdot) = E/(K_M^{E_{set}} + E)$. With $g(\cdot) = 1$, the remaining idealization is to assume $K_M^{E_{set}} \ll E$ so that $z(\cdot) \to 1$. Paper 1 then defines the setpoint as,

$$A_{set} = \frac{k_s^E K_I^A}{V_{max}^{E_{set}}} - K_I^A \tag{2.13}$$

which is exactly the same definition as in Eq. 2.11.

A list of the setpoint expressions for all the eight controller motifs is given in Table 1 in Paper 1. Our definition of the controller setpoint always assumes ideal conditions[3], even when the motifs are used in modeling real systems where for example removal of E is not perfectly zero-order. In such cases controller accuracy is introduced to describe the difference between the theoretical setpoint (A_{set}) and the steady-state value of A (A_{ss}), see section 2.6.

2.5 Controller breakdown

The homeostatic behavior of inflow controllers breaks down when there are large uncontrolled inflows. This happens when the E-mediated compensatory flow (j) becomes close to zero. Simply put, an inflow controller cannot compensate if there is already too much A; it can only add more A, not remove it. Likewise, the outflow controllers lose their homeostatic behavior in the presence of large uncontrolled outflows. We will in the following use the wording dominating inflow/outflow disturbances to describe whether the net disturbance is an inflow or an outflow ($d(\cdot) = d_i(\cdot) - d_o(\cdot)$). An inflow controller breaks down at dominating inflow disturbances, and an outflow controller breaks down at dominating outflow disturbances.

In the event of a controller breakdown the steady-state behavior in A is determined by the disturbances, $d_i(\cdot)$ and $d_o(\cdot)$. Fig. 2.4 shows typical

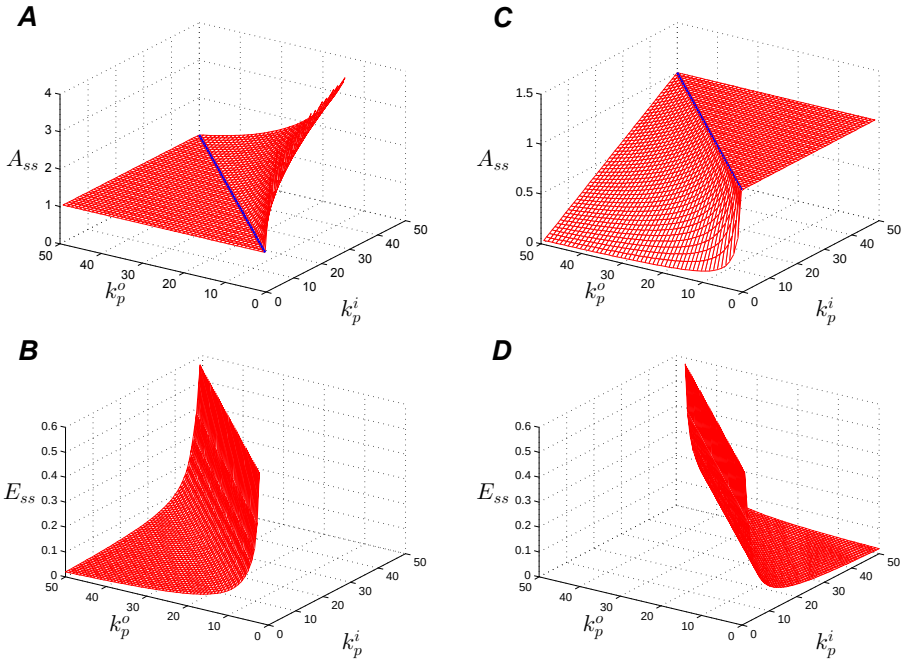

Figure 2.4: Controller breakdown. Steady-state values of A and E as functions of inflow and outflow disturbances, $d_i(\cdot) = k_p^i$ and $d_o(\cdot) = k_p^o A$. Inflow controller motif 4 shown in **A** and **B**, and outflow controller motif 6 shown in **C** and **D**. The setpoint for both controllers is $A_{set} = 1.0$. The behavior of A_{ss} in **A** and **C** is typical for inflow and outflow controllers, respectively. In the breakdown region E_{ss} will either go towards zero or infinity depending on whether the compensatory flow is E-activated or E-inhibited. Both motif 4 and 6 have E-inhibited compensatory flows causing $E \to \infty$ in **B** and **D**. The rate equations for motif 4 are: $\dot{A} = k_1 K_I^E/(K_I^E + E) + k_p^i - k_p^o A$, $\dot{E} = k_s^E - (V_{max}^{E_{set}} E/(K_M^{E_{set}} + E))(K_I^A/(K_I^A + A))$, and the parameters used are: $k_1 = 10^6$, $K_I^E = 10^{-6}$, $k_s^E = 1$, $V_{max}^{E_{set}} = 10^6$, $K_M^{E_{set}} = 10^{-6}$, $K_I^A = 10^{-6}$ The rate equations for motif 6 are $\dot{A} = k_p^i - k_p^o A - k_1 A K_I^E/(K_I^E + E)$, $\dot{E} = k_s^E - V_{max}^{E_{set}} EA/(K_M^{E_{set}} + E)$. The parameters used are: $k_1 = 10^6$, $K_I^E = 10^{-6}$, $k_s^E = 1$, $V_{max}^{E_{set}} = 1$, $K_M^{E_{set}} = 10^{-6}$, $K_I^A = 10^{-6}$.

behavior of controller breakdown using inflow controller 4 and outflow controller 6 (Fig. 2.1) as examples.

The horizontal segments of the surfaces in panels A and B of Fig. 2.4 are where the steady-state level of the controlled variable (A_{ss}) is regulated so that it has the same value as the setpoint (A_{set}). These segments form the *homeostatic region*, where the manipulated variable (E) is able to adjust

[3]It is only under ideal conditions, $z(\cdot) = g(\cdot) = 1$, that the steady-state solution of $\dot{E}$ gives a well defined setpoint for A.

the compensatory flow j to compensate for changes in inflow and outflow. The controller breakdown at $d_i(\cdot) = d_o(\cdot)$ limits the homeostatic region, creating a border.

2.6 Controller accuracy

Even in the homeostatic region the actual steady-state value of A (A_{ss}) may deviate from the theoretical setpoint A_{set}. This happens when the value of $K_M^{E_{set}}$ is comparable to the level of E, i.e., there is no longer perfect zero-order removal of E. The difference between the actual steady-state value and the setpoint is called the controller's *inaccuracy*, defined as:

$$\alpha_i = |A_{set} - A_{ss}| \tag{2.14}$$

A high accuracy means that the inaccuracy α_i is low and vice versa. Fig. 2.5 illustrates how controller accuracy changes with variations in $K_M^{E_{set}}$. It also shows the difference between controller breakdown (region where $j \to 0$) and controller accuracy.

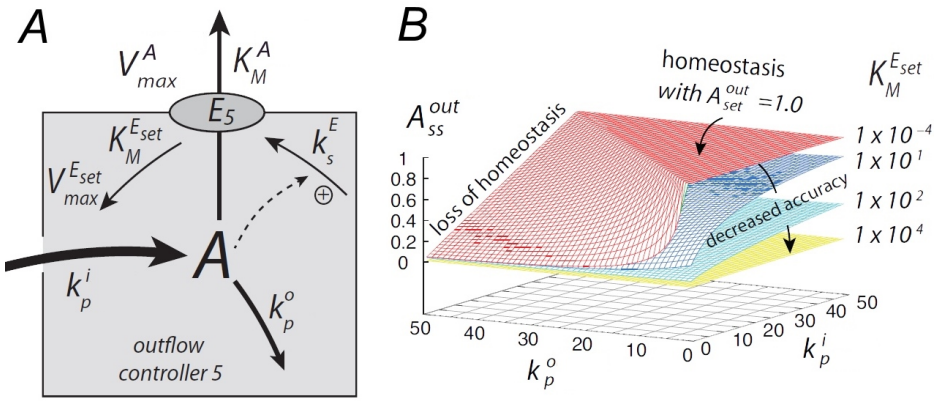

Figure 2.5: Controller accuracy and controller breakdown. **A** System where the outflow of A is controlled by outflow controller 5. **B** Steady state values of A as a function of disturbances in inflow ($d_i(\cdot) = k_p^i$) and outflow ($d_o(\cdot) = k_p^o A$) shown for increasing $K_M^{E_{set}}$. A decreased accuracy (increased inaccuracy) is observed as $K_M^{E_{set}}$ increases. Controller breakdown and loss of homeostasis happens when the uncontrolled outflow becomes larger than the inflow. The rate equations used for motif 5 are: $\dot{A} = k_p^i - k_p^o A - E(V_{max}^A A)/(K_M^A + A)$, $\dot{E} = k_s^E A - (V_{max}^{E_{set}} E)/(K_M^{E_{set}} + E)$, and the parameters used are: $k_s^E = 1, V_{max}^{E_{set}} = 1, V_{max}^A = 1$, and $K_M^A = 10^{-3}$.

The rate equations of the individual controller can be compared with the structure of a standard integral control law to further elucidate what happens at nonideal conditions. For instance Eq. 2.10, which describes controller motif 3 and 8 can be written on the form $\dot{E} = G_i\,(A_{set} - A_{meas})$,

$$\dot{E} = \underbrace{\frac{z_c g(\cdot)}{A + K_I^A}}_{G_i}\Bigg[\underbrace{\left(\frac{g_c K_I^A}{z_c} - K_I^A\right)}_{A_{set}} - \underbrace{\left(\frac{z(\cdot)}{g(\cdot)}\left(A + K_I^A\right) - K_I^A\right)}_{A_{meas}}\Bigg] \tag{2.15}$$

where G_i is the integral gain, and A_{meas} is the measurement signal that is compared to the setpoint A_{set}. Note that the measurement signal, A_{meas}, is not an easily measurable physical signal or flow[4]. It is in regard to the controller motifs an abstraction, which reflects the overall signal-transduction events originating from A and leading to a change in E. Fig. 2.6 shows a schematic block diagram of how a measurement system can be thought to affect the feedback of A.

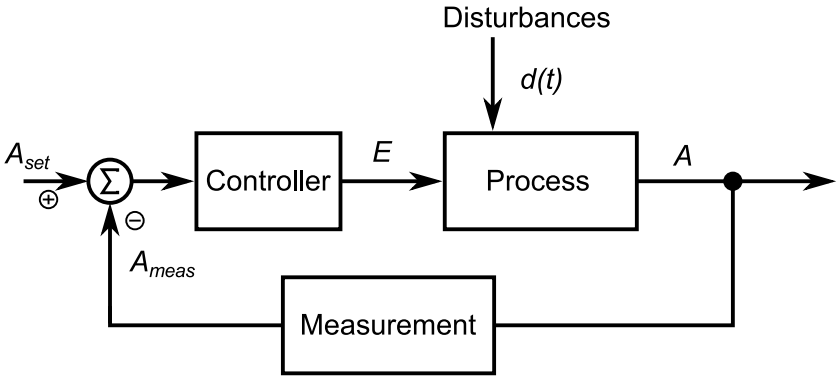

Figure 2.6: Schematic block diagram of a regulatory system with a measurement system included in the feedback path. The output A will only reach the setpoint A_{set} if the output and the measurement is one-to-one.

Expressions for accuracy, α, the measurement signal, A_{meas}, and integral gain, G_i, for each controller motif can be found in Table 1 in Paper 1[5].

[4]The idea of a measurement is adapted from control engineering where a measurement system is used to convert a measured quantity to a signal which can be processed by an electronic controller, e.g. a voltage, or a current signal between 4-20 mA.

[5]Notice that Paper 1 uses the word *accuracy* (defined as $\alpha = A_{set} - A_{ss}$) to denote what really is a measure of inaccuracy. The definition of *inaccuracy* in this thesis is used to avoid that awkwardness. Also note that in Table 1 in Paper 1 $g(\cdot)$ is assumed to be 1 and $z(\cdot) = f(E) = E/(K_M^{E_{set}} + E)$.

2.7 Combining controllers

Many of the homeostatic control mechanisms that occur in higher organisms are mediated by hormones that often act as *antagonistic* pairs when exercising control on a particular compound, such as blood glucose [155]. One mechanism (e.g. glucagon in the glucose system) is responsible for increasing the amount of the controlled compound and another mechanism (e.g. insulin in the glucose system) is responsible for decreasing the amount of the controlled compound. The use of two controllers, each operating in their own direction, in biological systems has been called (integral) rein control [31, 155, 156]. The reason for having two antagonistic controllers is to allow the system to be stable against relatively large perturbations in either direction[6].

The same type of antagonistic pairs is also often seen with membrane bound transporter protein on the cellular level. The invasive yeast *Candida albicans* uses a high affinity copper transporter, Ctr1p, to transport copper ions into the cell [117], and an ATPase pump protein, Crp1p, to transport copper ions out of the cell if the internal concentration gets too high [198]. Copper is an essential cofactor for several enzymes, but very toxic at higher concentrations. The yeast regulatory system for copper is presented in detail in chapter 4.

The controller motifs can be used as building blocks and combined to model this type of pairwise control. Fig. 2.7 shows an archetypical example of combined inflow/outflow controllers using controllers 1 and 5, described by the following differential equations:

$$\dot{A} = k_p^i - k_p^o A + \frac{V_{max}^{A_{ext}} A_{ext}}{K_M^{A_{ext}} + A_{ext}} E_1 - \frac{V_{max}^{A} A}{K_M^{A} + A} E_5 \tag{2.16}$$

$$\dot{E}_1 = k_s^{E_1} - \frac{V_{max}^{E_{set,1}} E_1}{K_M^{E_{set,1}} + E_1} A \tag{2.17}$$

$$\dot{E}_5 = k_s^{E_5} A - \frac{V_{max}^{E_{set,5}} E_5}{K_M^{E_{set,5}} + E_5} A \tag{2.18}$$

The two manipulated variables E_1 (controller 1) and E_5 (controller 5) have the functions of inflow and of outflow transporters[7]. The compensatory

[6] It is in a way similar to a car where you have one mechanism for acceleration and one mechanism for deceleration.

[7] Additional combinations with two controllers of the same type (inflow-inflow or outflow-outflow) are discussed in Paper 1.

flow in A from the external source (A_{ext}) and the compensatory flow of A out of the system are both described by Michaelis–Menten kinetics with respect to A_{ext} and A, respectively. The inflow controller has the setpoint A^{in}_{set} (from Eq. 2.17) and outflow controller has the setpoint A^{out}_{set} (from Eq. 2.18). For combined inflow/outflow controllers there are three possible setpoint combinations, $A^{in}_{set} < A^{out}_{set}$, $A^{in}_{set} = A^{out}_{set}$, and $A^{in}_{set} > A^{out}_{set}$. These combinations are described in detail in the following sections.

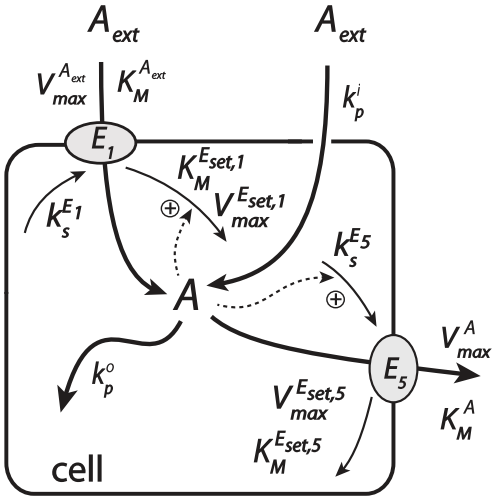

Figure 2.7: Combining inflow controller 1 and outflow controller 5. The inflow controller will add A when the outflow perturbation is larger than the inflow perturbation. In a similar way, the outflow controller will remove A when the inflow perturbation is larger than the outflow perturbation. Both controllers have their own setpoints, see main text.

2.7.1 Combination 1, $A^{in}_{set} < A^{out}_{set}$

Having the setpoint of the inflow controller at a lower level than the setpoint of the outflow controller is unquestionably the most logic and sane combination. The outflow controller can compensates for high inflow disturbances and is active when the level of A is higher than A^{out}_{set}; the inflow controller is in this case inactive because of its lower setpoint. Moreover, the inflow controller can compensate for high outflow disturbances and is active when the level of A is lower than A^{in}_{set}; the outflow controller is in this case inactive because of its higher setpoint. When combined like this the two controllers operate independently, and for the system as a

whole this effectively removes the nonhomeostatic regions of the individual controllers (Fig. 2.4). Thus, the overall region of homeostasis is the union of the homeostatic regions of the inflow/outflow controllers, see Fig. 2.8h.

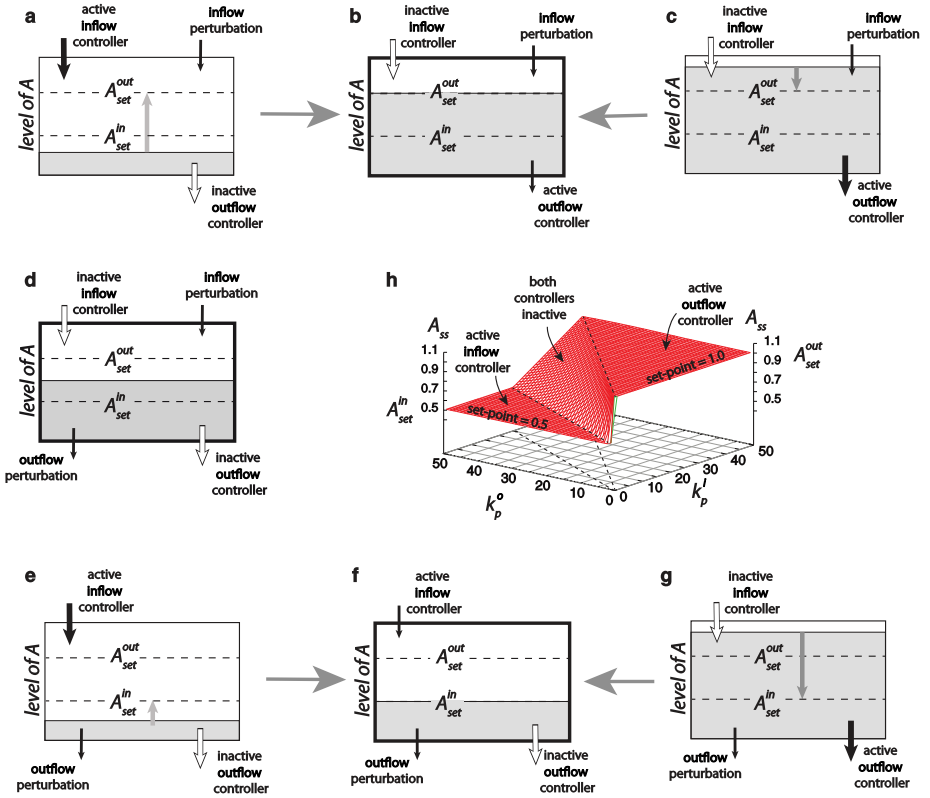

Figure 2.8: System behavior when combining an inflow and an outflow controller such that $A^{in}_{set} < A^{out}_{set}$ described with a simplified tank analogy. Black arrows indicate active controllers and active inflow/outflow perturbations, and white arrows indicate inactive controllers. **a, b, c** The upper row shows how A settles to A^{out}_{set} (**b**) in the presence of a dominating inflow perturbation. **e, f, g** The lower row shows how A settles to A^{in}_{set} (**f**) in the presence of dominating outflor perturbations. **d** Both controllers are inactive when $A^{in}_{set} < A < A^{out}_{set}$. **h** The steady-state value of A as a function of the inflow and outflow disturbances/perturbations (k^i_p and k^o_p); the three segments in A_{ss} corresponds to the steady-state levels shown in **b**, **d** and **f**. Parameters listed in Paper 1 SM.

The homeostatic domains of the two controllers are separated by a transition zone, in which both controllers are inactive. This transition zone may be interpreted as the acceptable range of A; no regulatory action is needed if A is between the two setpoints.

2.7.2 Combination 2, $A^{in}_{set} > A^{out}_{set}$

This setup is far from optimal as the two controllers will be working against each other. The inflow controller adds A to the system to increase the level to A^{in}_{set}, but at the same time the outflow controller removes A to reduce the level to A^{out}_{set}.

During this process the compensatory flows (j_{E_1} and j_{E_5}) and the levels of E^{in} and E^{out} will continually increase if the controllers have an E-activated compensatory flow (1, 3, 5 and 7). The actual level of A will be somewhere between the two setpoints dependent on which of the two controllers is most dominant (depending on the parameters for the individual controllers). If the controllers are of the inhibiting kind (2, 4, 6 and 8), E will become close to zero, leading to the least possible inhibition and the maximum compensatory flow.

2.7.3 Combination 3, $A^{in}_{set} = A^{out}_{set}$

In the trivial case with just one common setpoint the steady-state level of A ends up in the common setpoint (within the limits of the accuracy). Both controllers will in general be active and the level of activity (i.e., the size of the compensatory flows) depends on the levels of disturbances in inflow and outflow. Although this setup might be tempting due to a tight regulation, it is not preferable as small changes in the parameters of the motifs can bring the whole system into the $A^{in}_{set} > A^{out}_{set}$ region.

2.8 Integral windup in combined controllers

Integral windup is the occurrence of an unlimited growth in the manipulated variable E (integrated error). Windup issues can occur in many cases, particularly when controllers are combined in pairs as described in the previous section. The thing to consider is the sign of the derivative of E when the controller is in its region of breakdown, i.e., when its compensatory flow j is close to zero. Take inflow controller 2 and outflow controller 6 as an example, they breakdown with $E \to \infty$, and $\dot{E} > 0$.

A graphical method to determine whether windup issues may occur is shown in Fig. 2.9A, where the signs of the derivatives of the manipulated variables are given for each controller motif. Possible windup issues in a combination of controllers can be found by organizing the pair according

to their setpoints along the axis of steady-state A values. This is done in Fig. 2.9B, for the example of combined inflow 1 and outflow 5 controllers with $A^{in}_{set} > A^{out}_{set}$.

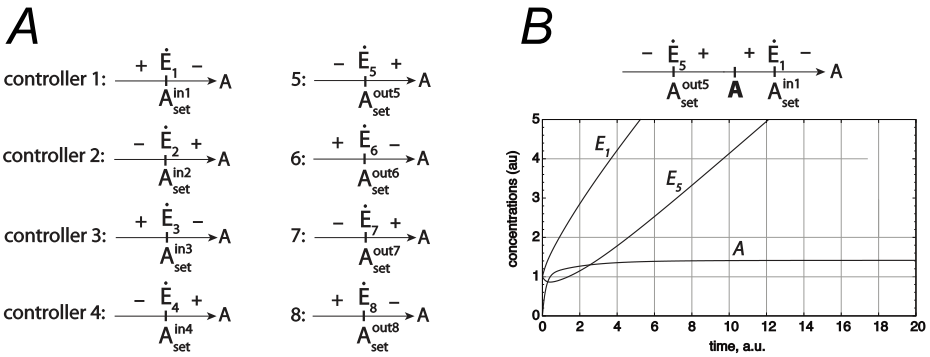

Figure 2.9: Determination of possible windup behavior using combined controllers. **A.** Sign-change of $\dot{E}$ for the eight controllers as a function of steady-state concentration of A. $\dot{E} = 0$ at $A = A_{set}$. **B.** Inflow controller 1 and outflow controller 5 combination with $A^{in}_{set} > A^{out}_{set}$; both controllers are active and the A_{ss} lies between the two setpoints. Integral windup in both E_1 and E_2.

2.8.1 The dangers of combining two inhibiting controllers

Studying Fig. 2.9 it becomes apparent that any combination of controllers that inhibits the compensatory flow (2, 4, 6 or 8) will have windup issues when $A^{in}_{set} < A^{out}_{set}$. An example is shown in Fig. S19 in the Supporting Material for Paper 1. These issues may be tolerable if there are some other mechanisms that limits the maximum amount of E, see section 2.9 about controller limitations.

An inhibiting inflow and an inhibiting outflow controller can be combined without windup issues if the setpoints are arranged as in combination 2 ($A^{in}_{set} > A^{out}_{set}$). Although this leads to maximum compensatory inflow and outflow when A is between the two setpoints, it keeps the manipulated variables near zero. It is counter-intuitive to regulate the level of A by adding and removing as much as possible at the same time. Nevertheless, there are cases where such an arrangement might be advantageous. Imagine that A is a chemical species that is part of a larger pathway. A cell may want to keep A within certain limits, but at the same time also maximize the total flow of A through the pathway; for example to maximize energy

uptake or growth. If A falls below the lower limit (A_{out}^{set}) the outflow is reduced while the inflow is maintained at its maximum. Likewise if A increases above its high limit (A_{set}^{in}) the inflow is reduced while the outflow (consumption) is kept at its maximum.

Of course, the flows could also be maximized in the same way by combining two activating controllers (1, 3, 5 and 7) with the setpoints arranged as in combination 2 ($A_{set}^{in} > A_{set}^{out}$). But, then some other mechanism would be needed to limit the maximum amount of E as these controllers have windup issues in this type of setpoint combination.

2.9 Controller limitations

Breakdown and controller accuracy are two factors that affect the performance of our controller motifs. Controller breakdown occur when individual inflow or outflow controllers experience dominating inflow or outflow disturbances so that the compensatory flow becomes close to zero.

One additional factor for controller performance not considered so far is saturation in the compensatory flow. Any biophysical system will have a limit in how high the compensatory flow can become. At some point the compensatory flow becomes saturated. This can either happen because there is a limit in the amount of E, for example if E is a transporter protein, or because there are other factors limiting the compensatory flow so that it saturates and becomes independent of E. These two situations are different in that the first one limits the amount of E (E itself is saturated), whereas the second one does not (the flow is saturated). The effect of the first situation in illustrated in Fig. 2.10. This is the same system as in Fig. 2.8, but with limits in the amount of E. The combined homeostatic region (Fig. 2.10A) is now reduced and homeostasis breaks down both at high inflow and outflow disturbances when $E^{out,5}$ and $E^{in,1}$ saturates, see Fig. 2.10B.

In the second situation the compensatory flow saturates before the manipulated variable. The homeostatic region of A is similar to the one shown in Fig. 2.10A, but when the flow saturates there will be a steady increase in E towards infinity[8]. This is again a type of integral windup.

[8]Or towards the point where E begins to saturate.

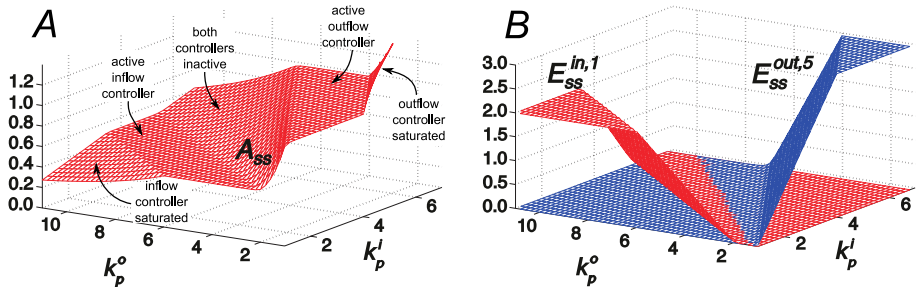

Figure 2.10: Homeostatic region for combined controllers with capacity limits due to saturation in the manipulated variables. **A** Steady-state levels of A. **B** Steady-state levels of $E^{in,1}$ and $E^{out,5}$. A hard saturation is introduced, limiting $E^{in,1}$ to 2 and $E^{out,5}$ to 3. Parameters listed in Paper 1 SM.

2.9.1 A note on the expressions used for inhibition and activation

Strictly speaking the form used for E-inhibited compensatory flow does saturate; the factor $K_I^E/(K_I^E+E)$ has a maximum value of 1 when $E = 0$. In most of our calculations, however, this capacity limit (saturation) is placed so that it lies beyond the operating range of the controller (idealization). The K_I^E value nonetheless affects accuracy of the inhibiting controllers in their operating range. The form used for E-activated compensatory flow is first-order and does not saturate. If it was replaced by saturation kinetics, e.g. $E/(K_a^E + E)$, then the homeostatic performance and accuracy of activating controllers would also be affected by the value of K_a^E.

2.9.2 A note on why zero-order kinetics is modeled by a Michaelis–Menten expression

In this thesis zero-order removal of any of the state variables is almost exclusively modeled as Michaelis–Menten kinetics with a very low K_M. This is done even though ideal zero-order is used as a condition to define the setpoint in sections 2.3 and 2.4. A Michaelis–Menten expression is preferred, especially when the model is simulated, as it protects state variables from attaining negative values. This can be seen easily by inspecting the differential equation, consider for example Eq. 2.12 for the controller species in controller motif 3; the following holds for any $K_M^{E_{set}}$,

$$\lim_{E\to 0} \frac{V_{max}^{E_{set}} E}{K_M^{E_{set}} + E} = 0 \tag{2.19}$$

which makes it impossible for a positive E to ever become negative[9]. A Michaelis–Menten expression is asymptotically zero-order when $E \gg K_M^{E_{set}}$, and asymptotically first-order when $E \ll K_M^{E_{set}}$.

The use of this expression is particularly important when modeling systems with both inflow and outflow controllers. As discussed in section 2.7, one controller is often inactive, with $E \to 0$, in a combined setup.

2.10 Controller motifs with autocatalysis

The requirements of zero-order kinetics in the removal of the manipulated variable can be replaced by *autocatalysis* and first-order removal. Autocatalysis is used to described a reaction where the product is also a reactant and therefore a catalyst of its own production[10]. Consider the equation for E in outflow controller 5 (Fig. 2.3) with autocatalysis in the formation of E and first-order removal of E.

$$\dot{E} = k_s^E AE - k_8 E \tag{2.20}$$

Replacing $\dot{E}/E$ with $\ln(\dot{E})$ (valid for $E > 0$) gives,

$$\ln(\dot{E}) = k_s^E A - k_8 = -k_s^E \left(A_{set} - A\right) \tag{2.21}$$

where the theoretical setpoint A_{set} is k_8/k_s^E. Again we have a similar structure as the standard integral control law; the same structure as in Eq. 2.8, but with the error being proportional to the derivative of the logarithm of the manipulated variable instead of the usual derivative.

Panels A and B in Fig. 2.11 show inflow controller 1 and outflow controller 5 with autocatalytic formation and first-order removal of E; the steady-state value of A is shown for different disturbances in inflow and outflow (k_p^i and k_p^o). Both controllers show the typical behavior of breakdown at high inflow and outflow disturbances, respectively.

[9] In addition to being convenient the Michaelis–Menten expression is also more close to the real behavior of a biochemical reaction.

[10] The reaction X + Y $\xrightarrow{k}$ X is autocatalytic with a positive feedback from X to its own production. The production of X is given by the differential equation $\dot{\mathrm{X}} = k\mathrm{XY}$.

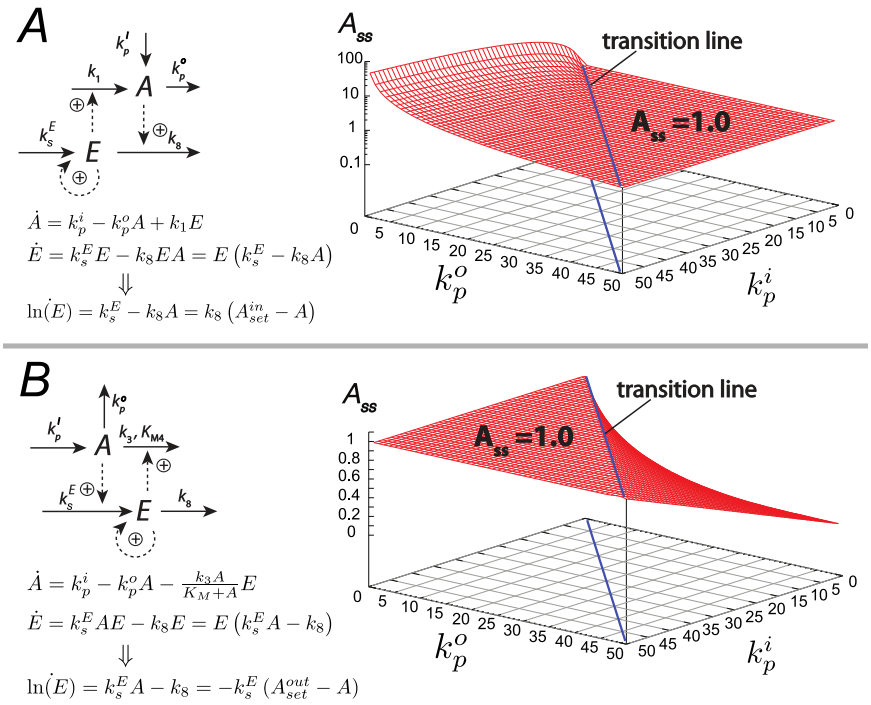

$$\dot{A} = k_p^i - k_p^o A + k_1 E$$
$$\dot{E} = k_s^E E - k_8 E A = E\left(k_s^E - k_8 A\right)$$
$$\Downarrow$$
$$\ln(\dot{E}) = k_s^E - k_8 A = k_8\left(A_{set}^{in} - A\right)$$

$$\dot{A} = k_p^i - k_p^o A - \frac{k_3 A}{K_M + A} E$$
$$\dot{E} = k_s^E A E - k_8 E = E\left(k_s^E A - k_8\right)$$
$$\Downarrow$$
$$\ln(\dot{E}) = k_s^E A - k_8 = -k_s^E\left(A_{set}^{out} - A\right)$$

Figure 2.11: Integral control by autocatalysis. **A** Inflow controller 1 with autocatalysis in E. $d\ln(E)/dt$ is proportional to the error between the setpoint and A. The plot to the right shows steady-state behavior at varying k_p^i and k_p^o; all other rate constants are kept at 1. **B** Outflow controller 5 with autocatalysis in E. $d\ln(E)/dt$ is proportional to the error between the setpoint and A. The plot to the right shows steady-state behavior at varying k_p^i and k_p^o; all other rate constants are kept at 1.

2.11 Stability analysis

The previous sections have focused on showing qualitative and quantitative steady-state properties of the controller motifs. The ability to reach a steady state does however depend on the actual kinetics and the values of rate constants. We will in the following show how the stability[11] of a controller motif can be analyzed by using standard methods from control theory. There is in itself nothing new with this type of analysis, but it is helpful for the understanding of the controller motifs and their behavior.

We will use outflow controller 5 with autocatalytic formation and first

[11] We are here interested in stability in the sense of Lyapunov stability (of equilibrium points), see definition in [92 chap. 4].

order removal of E, shown in Fig. 2.11B, as an example. This controller motif is described by the following differential equations,

$$\dot{A} = k_p^i - \frac{k_3 A}{K_M + A} E \tag{2.22}$$

$$\dot{E} = k_s^E A E - k_8 E \tag{2.23}$$

where the outflow disturbance k_p^o is set to zero (removed) to avoid controller breakdown. The states and parameters are all real and positive[12], i.e., $A, E, k_p^i, k_3, K_M, k_s^E, k_8 > 0$. This system has an equilibrium point in:

$$A_{ss} = \frac{k_8}{k_s^E}, \qquad E_{ss} = \frac{k_p^i k_s^E K_M + k_p^i k_8}{k_3 k_8} \tag{2.24}$$

A common way to analyze the stability of a nonlinear system is to linearize it with respect to the equilibrium point [92], and then use linear methods to analyze the behavior of the linear system. This procedure is straightforward, but does only provide information about local behavior around the equilibrium point. We will here instead show how to analyze the stability of a nonlinear controller motif directly by using Lyapunov's direct method, summarized as a theorem below (from [92 chap. 4]).

Theorem: Lyapunov's direct method. Lyapunov's direct method uses functions with special properties to prove stability in a domain $\mathbb{D}$. (The domain may also be global, i.e., $\mathbb{R}^n$.) Let the origin be an equilibrium point for the system $\dot{x} = f(x)$ and $\mathbb{D} \subset \mathbb{R}^n$ be a domain containing $x = 0$. Let $V : \mathbb{D} \to \mathbb{R}$ be a continuously differentiable function such that:

$$V(0) = 0 \quad \text{and} \quad V(x) > 0 \text{ in } \mathbb{D} - \{0\} \tag{2.25}$$

$$\dot{V}(x) \leq 0 \text{ in } \mathbb{D} \tag{2.26}$$

Then, the origin is stable. Moreover if,

$$\dot{V}(x) < 0 \ \text{ in } \mathbb{D} - \{0\} \tag{2.27}$$

then the origin is asymptotically stable. A function V that fulfills these criteria is called a *Lyapunov function*. For *proof* see [92 chap. 4].

The kinetics of the removal of A plays a key-role in the stability of this system. We will first consider the mathematically simpler case where the removal of A is completely independent of the level of A, i.e., saturated kinetics with $K_M = 0$.

[12]Notice that $E = 0$ should never be an initial condition of this system, because E will then stay identically at 0 forever. E will however never become 0 by itself in final time ($\dot{E} \to 0$ as $E \to 0$).

2.11.1 Conservative oscillations with $K_M = 0$

With $K_M = 0$, Eqs. 2.22 and 2.23 reduces to,

$$\dot{A} = k_p^i - k_3 E \tag{2.28}$$

$$\dot{E} = k_s^E AE - k_8 E \tag{2.29}$$

and the equilibrium point reduces to ($A_{ss} = k_8/k_s^E$, $E_{ss} = k_p^i/k_3$). The analysis is further simplified by introducing the variable change $\xi = \ln(E)$ ($E = e^{\xi}$)[13], so that the system can be expressed as:

$$\dot{A} = k_p^i - k_3 e^{\xi} \tag{2.30}$$

$$\dot{\xi} = k_s^E A - k_8 \tag{2.31}$$

Moreover, we move the equilibrium point to the origin by the variable change:

$$\alpha = A - \frac{k_8}{k_s^E}, \qquad \varepsilon = \xi - \ln(\frac{k_p^i}{k_3}) \tag{2.32}$$

The resulting system is,

$$\dot{\alpha} = k_p^i - k_p^i e^{\varepsilon}, \qquad \alpha > -\frac{k_8}{k_s^E} \tag{2.33}$$

$$\dot{\varepsilon} = k_s^E \alpha, \qquad \varepsilon \in \mathbb{R} \tag{2.34}$$

which has an equilibrium point in $(0, 0)$.

We will now show that the function,

$$V(\alpha, \varepsilon) = k_p^i \left(e^{\varepsilon} - \varepsilon - 1\right) + \frac{1}{2} k_s^E \alpha^2 \tag{2.35}$$

is a *Lyapunov function* that can be used to show the stability properties of the transformed system (Eqs. 2.33–2.34), and hence also the stability properties of the untransformed system (Eqs. 2.28–2.29). To be a Lyapunov function $V(\alpha, \varepsilon)$ must be *positive definite* (Eq. 2.25). It is easy to see that $V(0, 0) = 0$, and that last term $\frac{1}{2} k_s^E \alpha^2 > 0$ when $\alpha \neq 0$. The first term can by a short analysis of the sign of its derivative be shown to also be positive definite: $e^{\varepsilon} - \varepsilon - 1 > 0$ when $\varepsilon \neq 0$. Thus,

$$V(0, 0) = 0 \quad \text{and} \quad V(\alpha, \varepsilon) > 0 \text{ in } \mathbb{D} - \{0\} \tag{2.36}$$

[13]The ln function is an isomorphism from $\mathbb{R}^+ \to \mathbb{R}$.

where the set $\mathbb{D} = \left\{(\alpha, \varepsilon) \in \mathbb{R}^2 \,\middle|\, \alpha > -\frac{k_8}{k_s^E}\right\}$. Furthermore, the derivative of a Lyapunov function along the system trajectories must be *negative semidefinite* (Eq. 2.26).

$$\dot{V}(\alpha, \varepsilon) = \frac{\partial V}{\partial \alpha}\dot{\alpha} + \frac{\partial V}{\partial \varepsilon}\dot{\varepsilon} \tag{2.37}$$

$$\dot{V}(\alpha, \varepsilon) = k_p^i k_s^E \alpha - k_p^i k_s^E \alpha e^{\varepsilon} + k_p^i k_s^E \alpha e^{\varepsilon} - k_p^i k_s^E \alpha = 0 \tag{2.38}$$

Thus, both conditions of Lyapunov's direct method (Eqs. 2.25 and 2.26) are satisfied, and we conclude that the transformed system is stable in $\mathbb{D}$. The origin is not asymptotically stable, since $\dot{V}(\alpha, \varepsilon) = 0$; the origin is in fact marginally stable, and the system shows conservative oscillations. Trajectories starting at a Lyapunov surface $V(\alpha, \varepsilon) = C$ will always remain on the same surface. This holds for all $k_p^i, k_3, k_s^E, k_8 > 0$ when $K_M = 0$. Conservative oscillations are discussed in detail in chapter 5.

Fig. 2.12 shows an example of the behavior when $K_M = 0$. The reduced system in Eqs. 2.28 and 2.29 shows oscillations in both A and E, with different amplitudes for different initial conditions, see Fig. 2.12A. The Lyapunov function (Eq. 2.35) is plotted in Fig. 2.12B, together with the system trajectories of the transformed system in Eqs. 2.33–2.34.

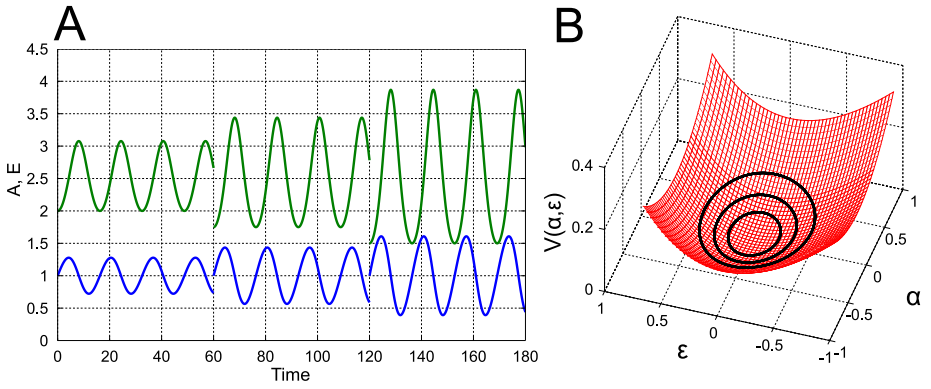

Figure 2.12: A. Oscillations in A (blue) and E (green) shown for controller motif 5 with autocatalytic formation and first-order removal of E, and with zero-order removal of A with respect to A (Eqs. 2.28–2.29). At time $t = 60$ and $t = 120$ A and E are abruptly changed to new values (new initial conditions). **B.** Lyapunov function (Eq. 2.35) of the transformed system in Eqs. 2.33–2.34. The function value is 0 at the origin and the function is positive definite. Trajectories of the transformed system remains at a constant value of $V(\alpha, \varepsilon)$. Parameters used: $k_p^i = 0.5$, $k_3 = 0.2$, $K_M = 0$, $k_s^E = 0.3$, and $k_8 = 0.3$; initial conditions $(A, E) = (1, 2), (1, 1.75), (1, 1.5)$.

What happens if we include a first-order outflow disturbance

To avoid having to deal with the region of controller breakdown, we analyzed the controller motif (Eqs. 2.28–2.29) without including outflow disturbance. Another reason for doing this is that a first-order outflow on the form $k_p^o A$ acts similar to friction in a physical system. We would thus not have observed conservative oscillations with $K_M = 0$, if a first-order outflow disturbance had been included.

It is possible to prove that the controller motif becomes asymptotically stable in the homeostatic region when a first-order outflow disturbance on the form $k_p^o A$ is added to A. The homeostatic region is the region where inflow disturbances are dominating, i.e., $k_p^i > k_p^o k_8/k_s^E$, see section 2.5. We will not include the proof here, as the procedure is almost the same as above[14].

2.11.2 Asymptotic stability with $K_M > 0$

We will now consider the more general case with $K_M > 0$. The controller motif (Eqs. 2.22–2.23) is transformed by the same two step process. First by doing the variable change $\xi = \ln(E)$, and by moving the equilibrium point the origin[15]. The transformed system is:

$$\dot{\alpha} = k_p^i - \frac{(\alpha + \frac{k_8}{k_s^E})(k_p^i k_s^E K_M + k_p^i k_8)e^{\varepsilon}}{k_8(K_M + \alpha + \frac{k_8}{k_s^E})}, \qquad \alpha > -\frac{k_8}{k_s^E} \tag{2.39}$$

$$\dot{\varepsilon} = k_s^E \alpha, \qquad \varepsilon \in \mathbb{R} \tag{2.40}$$

We continue by using the same Lyapunov function as before, which we know is positive definite (Eq. 2.36). The derivative along the system trajectories is now given by:

$$\dot{V}(\alpha, \varepsilon) = \frac{\partial V}{\partial \alpha}\dot{\alpha} + \frac{\partial V}{\partial \varepsilon}\dot{\varepsilon} \tag{2.41}$$

$$\dot{V}(\alpha, \varepsilon) = k_s^E \alpha \left(k_p^i - \frac{(\alpha + \frac{k_8}{k_s^E})(k_p^i k_s^E K_M + k_p^i k_8)e^{\varepsilon}}{k_8(K_M + \alpha + \frac{k_8}{k_s^E})} \right) + \left(k_p^i e^{\varepsilon} - k_p^i \right) k_s^E \alpha \tag{2.42}$$

[14]The proof can be done with the same transformations (note that E_{ss} is changed), but requires a slightly adjusted Lyapunov function ($V(\alpha, \epsilon) = (k_p^i - k_p^o \frac{k_8}{k_s^E})(e^{\varepsilon} - \varepsilon - 1) + \frac{1}{2} k_s^E \alpha^2$), and the theorem of Barbashin and Krasovskii, which is introduced in the following section.

[15]The procedure is the same as in the previous section, and hence not repeated.

$$\dot{V}(\alpha,\varepsilon) = k_p^i k_s^E \alpha e^{\epsilon} \left(1 - \frac{\left(\alpha + \frac{k_8}{k_s^E}\right)\left(k_s^E K_M + k_8\right)}{k_8\left(K_M + \alpha + \frac{k_8}{k_s^E}\right)}\right) \tag{2.43}$$

We will proceed to show that $\dot{V}(\alpha,\varepsilon)$ is negative semidefinite in $\mathbb{D} = \left\{(\alpha,\varepsilon) \in \mathbb{R}^2 \middle| \alpha > -\frac{k_8}{k_s^E}\right\}$ by considering the three cases: $\alpha < 0$, $\alpha > 0$, and $\alpha = 0$.

(i) $\alpha < 0$

$\dot{V}(\alpha,\varepsilon) < 0$ when $\alpha < 0$ if,

$$\frac{\left(\alpha + \frac{k_8}{k_s^E}\right)\left(k_s^E K_M + k_8\right)}{k_8\left(K_M + \alpha + \frac{k_8}{k_s^E}\right)} < 1 \tag{2.44}$$

$$\alpha k_s^E K_M < 0 \tag{2.45}$$

which is true for all $\alpha < 0$.

(ii) $\alpha > 0$

$\dot{V}(\alpha,\varepsilon) < 0$ when $\alpha > 0$ if,

$$\frac{\left(\alpha + \frac{k_8}{k_s^E}\right)\left(k_s^E K_M + k_8\right)}{k_8\left(K_M + \alpha + \frac{k_8}{k_s^E}\right)} > 1 \tag{2.46}$$

$$\alpha k_s^E K_M > 0 \tag{2.47}$$

which is true for all $\alpha > 0$.

(iii) $\alpha = 0$

$\dot{V}(\alpha,\varepsilon) = 0$ when $\alpha = 0$.

Taken together these three cases proves that $\dot{V}(\alpha,\varepsilon) \leq 0$.

$$\dot{V}(\alpha,\varepsilon)|_{\alpha\neq 0} < 0, \quad \text{and} \quad \dot{V}(\alpha,\varepsilon)|_{\alpha=0} = 0 \tag{2.48}$$

We can however only conclude with stability and not with asymptotic stability by Lyaponov's direct method. Asymptotic stability by Lyapunov's direct method requires that $\dot{V}$ is negative definite everywhere except the origin, see Eq. 2.27.

Finding a Lyapunov function that has a strictly negative definite derivative can be very difficult compared to finding a function with only a negative

semidefinite derivative. We can, however, conclude with asymptotic stability if the negative semidefinite derivative can be shown to comply with the so-called theorem of Barbashin and Karsovskii[16] [92 chap. 4].

The theorem of Barbashin and Krasovskii. Let $x = 0$ be an equilibrium point for the system $\dot{x} = f(x)$. Let $V : \mathbb{D} \to \mathbb{R}$ be a continuously differentiable positive definite function on a domain $\mathbb{D}$ containing the origin, such that $\dot{V}(x) \leq 0$ in $\mathbb{D}$. Let $\mathbb{S}$ be the set of all states where $\dot{V}(x) = 0$, that is:

$$\mathbb{S} = \left\{ x \in \mathbb{D} \middle| \dot{V}(x) = 0 \right\} \tag{2.49}$$

Suppose that no solution can stay identically in $\mathbb{S}$, other than the trivial solution $x(t) = 0$. Then, the origin is asymptotically stable. For *proof* see [92 chap. 4].

In our case the set $\mathbb{S} = \{(\alpha, \varepsilon) \in \mathbb{D} \,|\alpha = 0\}$. The derivative of α, Eq. 2.39 in $\mathbb{S}$ is,

$$\dot{\alpha} = k_p^i - k_p^i e^{\varepsilon} \tag{2.50}$$

showing that the only solution that can stay identically in $\mathbb{S}$ is the trivial solution. Thus, we conclude that the transformed system is asymptotically stable in $\mathbb{D}$. This holds for all $k_p^i, k_3, k_s^E, k_8 > 0$ when $K_M > 0$.

Fig. 2.13 illustrates the typical behavior of controller motif 5 with autocatalytic formation and removal of E (Eqs. 2.22–2.23) when $K_M > 0$. A and E ends up at the equilibrium point (Eq. 2.24) for all nonzero initial conditions, see Fig. 2.13A. The value of $V(\alpha, \varepsilon)$ diminishes as the trajectories of the transformed system (Eqs. 2.39–2.40) spiral down towards the origin, see Fig. 2.13B.

[16] The theorem of Barbashin and Karsovskii was published before La Salle published the better known *invariance principle*, which is more general [110].

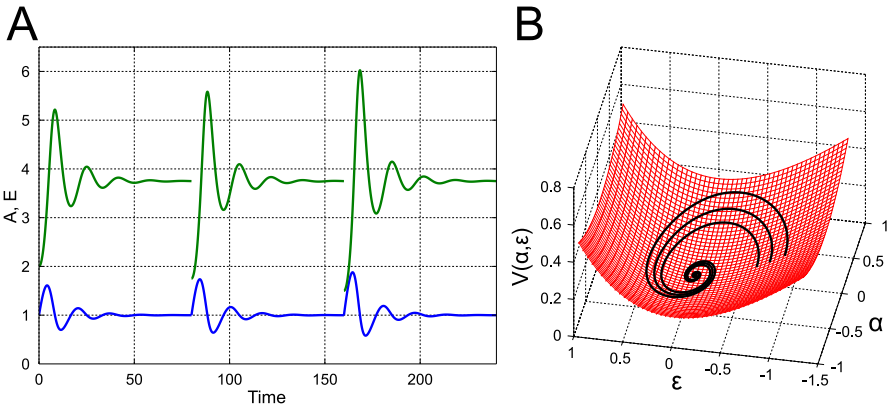

Figure 2.13: Typical behavior of of controller motif 5 with autocatalytic formation and removal of E (Eqs. 2.22–2.23) when $K_M > 0$. **A.** System response in A (blue) and E (green) shown for three different initial conditions (changed at $t = 80$ and $t = 160$). **B.** Lyapunov function (Eq. 2.35) plotted together with trajectories of the transformed system (Eqs. 2.39–2.40). (Note that the Lyapunov function is exactly the same function as plotted in Fig. 2.12B, but this plot has a slightly different axis and camera angle.) Parameters used: $k_p^i = 0.5$, $k_3 = 0.2$, $K_M = 0.5$, $k_s^E = 0.3$, and $k_8 = 0.3$; initial conditions $(A, E) = (1, 2), (1, 1.75), (1, 1.5)$.

Chapter 3

Modeling glucose transport and ionic homeostasis in enterocytes (paper 4)

The study and modeling of ionic homeostasis in enterocytes started off as an idea to build a mathematical model of a cell; the idea was to have a virtual cell, implemented in Matlab/Simulink, that we could use to test out different controller motifs and regulatory structures. The decision to study enterocytes was partly taken because of the important role they have in enabling uptake and transport of nutrients; we thought that an enterocyte model could, in the future, be a piece in studying the regulation of nutrient uptake and in particular the glucoregulatory system of the whole animal.

Enterocytes are also on their own an intricate and fascinating regulatory system. The uptake of nutrients like glucose and amino-acids is coupled to the uptake of sodium [69, 136, 146, 201], and enterocytes therefore must have regulatory mechanisms that respond to the considerable changes in the inflow of sodium during absorption. The Na-K-ATPase membrane protein, a sodium potassium pump, plays a major role in this regulation. When the inflow of Na^+ increases, e.g. due to absorption of glucose, the enterocyte has to adapt the outflow of Na^+. Experiments have shown that there is no sustained higher concentration of intracellular Na^+ during absorption of nutrients [78, 159]. The outflow of Na^+ can be increased through the Na-K-ATPase, but Na-K-ATPase also imports K^+ into the cell; thus an increase in Na-K-ATPase Na^+ outflow must be followed by an increase in K^+ outflow. If not, the enterocyte would be flooded by either Na^+ or K^+.

To elucidate the regulatory mechanisms behind ionic homeostasis during changing nutrient transport we have, in this thesis, developed an integrative model of glucose transport and ionic homeostasis in enterocytes. The

model is built by combining reaction kinetic expressions for transport through major transporter proteins and diffusive flows into a set of nonlinear differential equations. The model also includes calculation of membrane potentials using the iterative Newton-Raphson method.

3.1 Physiological work mode of enterocytes

The active surface area for absorption in the small intestine is greatly increased by circular folds lined with intestinal villi. Along these villi the intestinal epithelium consists of a single columnar layer of nutrient absorbing enterocytes. The active surface area is increased even more by the apical brush border membrane (microvilli) on the enterocytes.

Pancreatic enzymes hydrolyze carbohydrates to disaccharides that are further hydrolyzed into glucose, galactose, and fructose at the brush border membrane of the enterocytes.

Enterocytes are known to be sodium absorbing epithelia [160]. It has been shown that Na^+ and Cl^- enters across the brush border membrane by a mechanism that behaves as an obligatory one-for-one process [127]. Sodium is also absorbed in cotransport with glucose and amino-acids. Glucose is actively transported against its chemical gradient into the enterocyte by cotransport with sodium in SGLT1 [136, 201], a cotransporter protein primarily expressed on the apical, brush border, membrane of intestinal enterocyte. SGLT1 works by undergoing a cycle of conformational changes, translocating its binding site from the outside to the inside of the cell; the stoichiometry is two Na^+ ions for each glucose molecule [81, 138]. Galactose can also bind to SGLT1 in the same way as glucose. Fructose enters by facilitated diffusion through GLUT5. Fig. 3.1 gives an overview of important transporter proteins in the enterocyte.

The sodium concentration inside the enterocyte ($[Na_c]$) is kept low by basolateral Na,K-ATPase, which cleaves ATP in order to transport sodium ions against their concentration gradient out of the cell, and potassium ions against their gradient into the cell [69, 146]. The sodium concentration in the intestinal chyme ($[Na_m]$) is roughly the same as in extracellular fluid and plasma, i.e. around 140 mM. This is much higher than the concentration inside the enterocytes, i.e. around 50 mM [69]. The Na-K-ATPase extrudes three Na^+ ions, takes in two K^+ ions, and consumes one ATP molecule in each pump cycle, under normal in vivo conditions [69, 145].

The imported glucose, galactose and fructose are transported out of the enterocytes and into the serosal extracellular area by GLUT2 [114, 177], except for of the part of it that is metabolized by the enterocyte. Movement of galactose and fructose is always favorable as their concentrations in blood are low (they are swiftly taken up by the liver). The cotransport of glucose through SGLT1 is utilized to up-concentrate glucose in the enterocyte so that it also can exit through GLUT2 into the extracellular area and further into the capillaries.

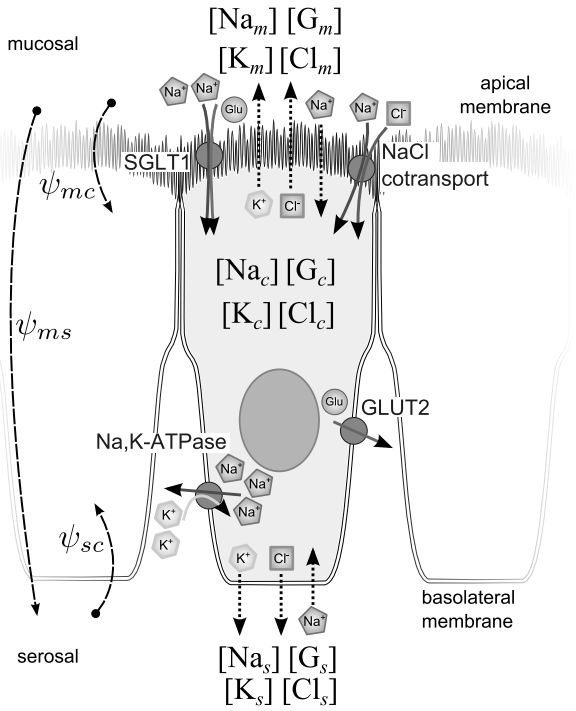

Figure 3.1: Epithelial enterocytes. Subscripts m, c, and s mark mucosal, cell inside, and serosal side. SGLT1 absorbs glucose on the apical (mucosal) side of the enterocyte. GLUT2 transports glucose from the cell into the extracellular space on the basolateral (serosal) side, where the glucose diffuses into capillaries. The absorption of glucose is driven by a sodium gradient maintained by basolateral Na-K-ATPase. Additional sodium enter together with chloride by a coupled flow. Dotted arrows shows ions that diffuse in and out of the enterocyte (paracellular flow is not shown in the figure). The arrows point in the normal direction of each flow, which may not be the same as the positive defined direction in the flow expressions used in our model. ψ_{mc} is the membrane potential between the mucosal side and the cell inside, ψ_{sc} is the membrane potential between the serosal side and the cell inside, and ψ_{ms} is the transepithelial potential from the mucosal to the serosal side.

Ions can diffuse in and out of the enterocyte, either directly through the membrane or through ion channels. The most notable type of ion channels in enterocytes is the basolateral K channel [74, 185]. These channels give the basolateral membrane a high K-permeability, thus providing a return path for the potassium ions that are imported into the cell by Na,K-ATPase. This allows the absorption of nutrients to continue without a buildup of positive ions [74, 146]. Ions also diffuse directly from the mucosal to the serosal space through paracellular tight junctions between the enterocytes.

The SGLT1 and the NA-K-ATPase are both electrogenic transporters, i.e., the transport of ions through these proteins constitute electrical currents flowing in and out of the enterocyte. Diffusive ion flows are also electrical currents, and this, together with the fact that the flows are driven by processes that are dependent on the membrane potential, makes it essential to include the membrane potential of the enterocyte in the modeling. There is a mucosal to cell (apical) membrane potential ψ_{mc}, a serosal to cell (basolateral) membrane potential ψ_{sc}, and a potential over the whole epithelial layer from mucosal to serosal ψ_{ms}, see Fig. 3.1.

3.2 Modeling transport across epithelia

While there are no detailed mathematical models of enterocytes, several models exist for other epithelial cells. A model for transport of Na^+, K^+ and Cl^- in Necturus gallbladder epithelium was developed by Baerentsen and colleagues in 1982 [9]. At that time little was known on the existence and kinetics of different transporter proteins, so their model was based on diffusion and an expression for the flow through Na, K-ATPase. Noteworthy is also the work of Stephenson and Weinstein [172, 197], and later Weinstein alone [190, 191, 192, 193, 194, 195, 196], which mainly have focused on models of kidney epithelium. Weinstein's model of the rat proximal tubule is particularly remarkable; this model has been developed and refined continuously over decades. It started with a cell centric model based on a metabolically active Na, K-ATPase and passive membrane transport based on linear equations from nonlinear thermodynamics [190]; linear glucose and sodium cotransport was added in [191]. The model was extended to represent a segment of tubule epithelium [192], and then further extended with pathways for Cl^- transport [193], and ammonia [194].

Our enterocyte model is not based on any of these models, i.e. it is not an old model with new parameters. It is instead a fresh start where

we have tried to use the available knowledge from studies on individual transporter proteins to employ flow expressions that are based on kinetics rather than linear relations. In our modeling, we have followed the principle that all parameters should be identifiable from experiments reported in the literature. Using rate expressions where the proteins are considered to be in steady state (i.e., we do not consider dynamic distribution of different conformations of the same protein) keeps the mathematical model on a moderate level of complexity.

The kinetic expressions used to model the flows for the different transporter proteins are summarized in the following. A more detailed assessment of important aspects with each expression is given in Paper 4 itself.

3.2.1 SGLT1

The flow of glucose and Na^+ through SGLT1 can be described by a co-transport carrier model with six states and ordered binding, see Fig. 2 in Paper 4. The model, first introduced by Parent et. al in 1992 [139], describes each subreaction by its corresponding forward and reverse rates. Parent et. al derived the equation for the sodium current through SGLT1 by assuming steady state in the distribution of the different carrier states; the distribution is estimated by employing the King-Altman procedure [139]. We use an expression based on these results to describe the flow of Na^+ through SGLT1:

$$J_{\mathrm{Na}}^{\mathrm{SGLT}} = -\frac{2n_{\mathrm{SGLT}}}{1.672 \cdot 10^{14}} \left(\frac{\varepsilon[\mathrm{Na_m}]^2[\mathrm{G_m}] + \phi[\mathrm{Na_m}]^2 + \gamma}{\alpha + \beta[\mathrm{G_m}] + \chi[\mathrm{Na_m}]^2 + [\mathrm{Na_m}]^2[\mathrm{G_m}]} \right) \tag{3.1}$$

The expression in the parenthesis, from *Eq. A21* in [139], is the number of whole cycles per second. α, β, χ, ε, ϕ, and γ are macroconstants, they are functions of the individual rate constants for each step in the six state model, the concentration of intracellular Na^+ ($[\mathrm{Na}_c]$), intracellular glucose ($[\mathrm{G}_c]$), and the membrane potential (ψ_{mc}). The expressions are too long to be given here, but they are all listed in *Eqs. A22–A28* in [139]. The flow of Na^+ ($J_{\mathrm{Na}}^{\mathrm{SGLT}}$) is two times the number of cycles (2 Na^+ ions and 1 glucose molecule is transported per cycle) multiplied with the number of SGLT1 transporter proteins situated in the membrane, n_{SGLT}. The division by $1.674{\cdot}10^{14}$ is used to convert from number of Na^+ ions transported per second to the flow $J_{\mathrm{Na}}^{\mathrm{SGLT}}$, which is expressed in µmol/h. The rate constants and the estimated number of SGLT1 proteins in the membrane are listed in Table A2 in Paper 4.

3.2.2 Na-K-ATPase

The expression for the flow through Na-K-ATPase is based on experimental data from Gadsby and Nakao [57, 125]. The turnover rate (cycles per second) can be described as a voltage-dependent function of the membrane potential ψ_{sc} (between the serosal side and the inside of the enterocyte). In our model we describe this voltage-dependent turnover with the function $V^{\mathrm{NaK}}(\psi_{sc})$, which is a polynomial fitted to the experimental data from Gadsby and Nakao [57] (see Fig. A2 in Paper 4).

Further studies [125] on the change in turnover rate under different internal concentrations of Na^+ and external concentrations of K^+ showed that the turnover rate was scaled by saturable functions of these two variables. The total rate expression used in our model is,

$$J^{\mathrm{NaK}} = V^{\mathrm{NaK}}(\psi_{sc}) \cdot n_{\mathrm{NaK}} \cdot \frac{1.13[\mathrm{Na_c}]^{1.36}}{(K_{0.5}^{\mathrm{Na_c}})^{1.36} + [\mathrm{Na_c}]^{1.36}} \cdot \frac{1.3[\mathrm{K_s}]}{K_{0.5}^{\mathrm{K_s}} + [\mathrm{K_s}]} \tag{3.2}$$

where n_{NaK} (the number of Na-K-ATPase transporter proteins in the cell membrane), $K_{0.5}^{\mathrm{Na_c}}$ and $K_{0.5}^{\mathrm{K_s}}$ are given in Table A2 in Paper 4.

External Na^+ and internal ATP do not affect this expression at the concentrations they have in our modeling (see Paper 4).

3.2.3 Coupled sodium chloride inflow

The coupled inflow of sodium and chloride is in our model described by a simplified expression for the flow through a general cotransporter carrier model with random binding. The simplification, backed up by experimental evidence [127], lies in that the disassociation on the cell inside is so fast that it does not contribute significantly to alter the inflow of ions per time unit. The expression used is,

$$J^{\mathrm{NaCl}} = \frac{2V_{\mathrm{max}}^{\mathrm{NaCl}}([\mathrm{Na_m}][\mathrm{Cl_m}] - [\mathrm{Na_c}][\mathrm{Cl_c}])}{2K_1K_3 + K_3[\mathrm{Na_m}] + K_4[\mathrm{Cl_m}] + 2[\mathrm{Na_m}][\mathrm{Cl_m}]} \tag{3.3}$$

where the parameter values are given in Table A2 in Paper 4.

3.2.4 GLUT2

To model the flow of glucose through GLUT2 we use an expression based on the so-called fixed-site carrier model, suggested by Baker and Widdas [11]. This model treats the transporter protein as a pore with two binding sites, one on the inward facing side (c) and one on the outward facing (s). The net flow from the inside to the outside of the cell is then given as,

$$J^{\mathrm{GLUT}} = \frac{V_{\mathrm{max}}^{\mathrm{G_c}} K_{0.5}^{\mathrm{G_s}} [\mathrm{G_c}] - V_{\mathrm{max}}^{\mathrm{G_s}} K_{0.5}^{\mathrm{G_c}} [\mathrm{G_s}]}{\left(K_{0.5}^{\mathrm{G_c}} + [\mathrm{G_c}]\right)\left(K_{0.5}^{\mathrm{G_s}} + [\mathrm{G_s}]\right)} \cdot n_{\mathrm{GLUT}} \tag{3.4}$$

where $V_{\mathrm{max}}^{\mathrm{G_c}}$ and $V_{\mathrm{max}}^{\mathrm{G_s}}$ are the maximum transport rate out of and into the enterocyte for one single GLUT2 transporter. $K_{0.5}^{\mathrm{G_c}}$ and $K_{0.5}^{\mathrm{G_s}}$ are the half saturation constants for the inside facing and the outside facing binding sites, respectively. $[\mathrm{G_c}]$ and $[\mathrm{G_s}]$ are the concentrations of glucose inside and outside of the enterocyte, respectively, and n_{GLUT} is the number of GLUT2 transporter proteins in the basolateral membrane. The parameter values are given in Table A2 in Paper 4.

3.2.5 Diffusive flows

Diffusive flows of $\mathrm{Na^+}$, $\mathrm{K^+}$ and $\mathrm{Cl^-}$ are also included in our model. We use the Goldman-Hodgkin-Katz (GHK) flux-equation [157] to describe the diffusive flows across the apical and the basolateral membrane. The equation has the form:

$$J_i^{\mathrm{D}} = -\frac{P_i z_i F \psi}{RT} \left(\frac{[i_{out}] - [i_{in}] \exp\left(z_i F \psi / RT\right)}{1 - \exp\left(z_i F \psi / RT\right)} \right) \cdot A \tag{3.5}$$

The subscript i denotes the ion ($\mathrm{Na^+}$, $\mathrm{K^+}$ or $\mathrm{Cl^-}$), P_i is the membrane permeability of ion i, z_i is the valence of the ion, $[i_{out}]$ and $[i_{in}]$ are the outer and inner concentrations of the ion, and ψ is the membrane potential (ψ_{mc} for the apical and ψ_{sc} for the basolateral membrane). F, R, and T are the Faraday constant, the gas constant and the temperature, respectively. The GHK flux-equation gives the diffusive flow as a flux, i.e. flow per membrane area, so we multiply with the membrane area A (see Table A2 in Paper 4) to find the total diffusive flow over the membrane. The diffusive flows given by Eq. 3.5 are positive when directed into the cell.

The permeability coefficients account for the total diffusive flow, including diffusion through ion channels. The most notable type of ion channels in

enterocytes are the basolateral K channels [74, 185]. The K channels give the enterocyte a high permeability for K^+ and provides a return path for the K^+ ions imported into the cell by the Na,K-ATPase.

In addition to diffusive flows into the cell we also include diffusive paracellular flows that allow ions to travel directly from the mucosal to the serosal side through the tight junctions. These paracellular flows are calculated by Eq. 3.5 , using the mucosal concentration of the ion as the outer-, the serosal concentration as the inner concentration, and ψ_{ms} as the membrane potential from the mucosal to the serosal side. The paracellular flows are positive when directed from the mucosal to the serosal side.

3.3 Mathematical model and calculation of membrane potential

The reaction kinetic expressions for SGLT1, Na-K-ATPase, coupled NaCl, GLUT2, and diffusive flows are combined into a set of nonlinear differential equations describing the internal concentrations,

$$[\dot{\mathrm{G}_\mathrm{c}}] = \frac{1}{V_c}\left(\frac{1}{2}J_{\mathrm{Na}}^{\mathrm{SGLT}} - J^{\mathrm{GLUT}}\right) \tag{3.6}$$

$$[\dot{\mathrm{Na}_\mathrm{c}}] = \frac{1}{V_c}\left(J_{\mathrm{Na}}^{\mathrm{SGLT}} - 3J^{\mathrm{NaK}} + J^{\mathrm{NaCl}} + J_{\mathrm{Na}}^{\mathrm{Da}} + J_{\mathrm{Na}}^{\mathrm{Dbl}}\right) \tag{3.7}$$

$$[\dot{\mathrm{K}_\mathrm{c}}] = \frac{1}{V_c}\left(2J^{\mathrm{NaK}} + J_{\mathrm{K}}^{\mathrm{Da}} + J_{\mathrm{K}}^{\mathrm{Dbl}}\right) \tag{3.8}$$

$$[\dot{\mathrm{Cl}_\mathrm{c}}] = \frac{1}{V_c}\left(J^{\mathrm{NaCl}} + J_{\mathrm{Cl}}^{\mathrm{Da}} + J_{\mathrm{Cl}}^{\mathrm{Dbl}}\right) \tag{3.9}$$

where the volume of the enterocyte, V_c, is considered to be constant, see the appendix and Table A2 in Paper 4.

In addition to these concentrations our model also includes the mucosal to cell (apical) membrane potential ψ_{mc}, the serosal to cell (basolateral) membrane potential ψ_{sc}, and the potential over the whole epithelial layer from mucosal to serosal ψ_{ms}, see Fig. 3.1. Only two of these are independent as the potentials are related by the equation:

$$\psi_{ms} = \psi_{mc} - \psi_{sc} \tag{3.10}$$

An important principle for any form of transport of ions into and out of cells is the principle of electroneutrality [98, 157], which states that the bulk or macroscopic concentrations of positive and negative ions has to be equal at all times. The reason behind this principle is that only a very small amount of charge separation is needed to create a large electric field.

Cell electroneutrality holds when there is no net current into the cell, i.e.,

$$\sum_i z_i \left(J_i^{\mathrm{a}} + J_i^{\mathrm{bl}} \right) = 0 \tag{3.11}$$

where J_i^{a} and J_i^{bl} are the inflow of species i, with valence z_i, over the apical and basolateral membrane, respectively. For the same reasons as above, any buildup of charge on either the mucosal or the serosal side would result in unphysical high values for the transepithelial potential (ψ_{ms}). To preserve mucosal and serosal bath electroneutrality the net epithelial current must thus also be zero, i.e.,

$$\sum_i z_i \left(J_i^{\mathrm{p}} - J_i^{\mathrm{bl}} \right) = 0 \tag{3.12}$$

where J_i^{p} is the paracellular inflow into the serosal space of species i, with valence z_i.

The principle of electroneutrality, in the form of Eqs. 3.11 and 3.12, is used as a condition to help calculate the membrane potentials. The idea is to compute a value for the membrane potential that, when used to calculate the individual flows, gives a zero net current.

We use an iterative approach to calculate the membrane potentials. At each time step we start with guess values for the membrane potentials and calculate the flows; the estimate for the membrane potentials is then refined using the Newton-Raphson method and the flows are recalculated until the net cell current (Eq. 3.11) and the net epithelial current (Eq. 3.12) are sufficiently close to zero. Once the flows are in keeping with Eqs. 3.11 and 3.12 we integrate the net flow of each species over the length of the time step to update the concentrations. This iterative calculation of the membrane potentials is well proven for epithelial models [70, 103, 181]. A detailed description of our implementation is given in section 3.5, and a further description and validation of the iterative method is also given in the appendix of Paper 4.

3.4 Controller motifs for ionic homeostasis

As presented above the enterocyte model can be used to study short-term behavior, i.e., behavior over a short timeframe where the amount of the different transporter proteins and the diffusive permeabilities (amount of ionic channels) can be considered to remain constant. The model behaves as expected for short-term dynamic, and some results are given in section 3.6.

Having confirmed that the model is able to simulate short-term dynamics we extended it by adding regulatory mechanisms for the ionic homeostasis of Na^+ and K^+.

3.4.1 Regulation of Na-K-ATPase and Na homeostasis

Experiments show that when mucosal glucose is increased and kept high, the increase in intracellular Na^+ ($[Na_c]$) is followed by a slow decrease back to basal values, indicating a mechanism that increases the number of Na,K-ATPase transporter proteins to maintain Na^+ homeostasis [78]. This increase may stem from increased synthesis, as it has been shown to do in central neurons and cardiocytes [162, 204], or from a cytoplasmic holding area of available Na,K-ATPase proteins [160].

Our hypothesis is that the observed homeostasis can be explained by a production of Na,K-ATPase directly regulated by intracellular Na^+. Intracellular Na^+ has been shown to directly regulate the Na,K-ATPase gene expression in other cell types [162, 204].

Because Na,K-ATPase can be said to work as an outflow controller by transporting Na^+ out of the cell, the activating outflow controller (type 5) is a possible candidate for the mechanism that regulates Na^+ by adjusting the number of Na,K-ATPase proteins. The controller motif is shown in Fig. 3.2.

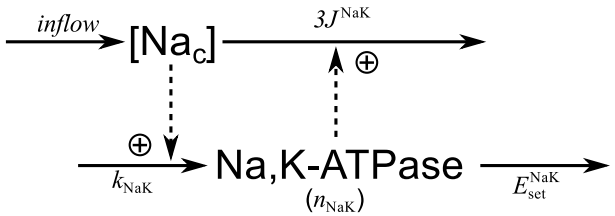

Figure 3.2: Controller motif proposed for the regulation of intracellular Na^+ by production of Na,K-ATPase.

The controller motif treats the concentration of intracellular Na^+ as an activator for the synthesis/insertion of Na,K-ATPase proteins, modeled as a first-order process, where the insertion rate is given as $k_{\mathrm{NaK}} \cdot [\mathrm{Na_c}]$. The degradation (or removal) of Na,K-ATPase is assumed to be similar to an enzymatic process where the degradation enzyme $E_{\mathrm{set}}^{\mathrm{NaK}}$ is saturated. This extends the model with the following differential equation.

$$\dot{n}_{\mathrm{NaK}} = k_{\mathrm{NaK}} \cdot [\mathrm{Na_c}] - \frac{V_{\mathrm{max}}^{E_{\mathrm{set}}^{\mathrm{NaK}}} \cdot n_{\mathrm{NaK}}}{K_{0.5}^{E_{\mathrm{set}}^{\mathrm{NaK}}} + n_{\mathrm{NaK}}} \tag{3.13}$$

where $V_{\mathrm{max}}^{E_{\mathrm{set}}^{\mathrm{NaK}}}$ and $K_{0.5}^{E_{\mathrm{set}}^{\mathrm{NaK}}}$ are the maximum rate and the half saturation constant for the enzyme/process that removes Na,K-ATPase. Saturation of the Na,K-ATPase removing process ensures regulation of intracellular Na^+ to the setpoint $V_{\mathrm{max}}^{E_{\mathrm{set}}^{\mathrm{NaK}}} / k_{\mathrm{NaK}}$, because saturation provides near zero-order kinetics.

The outflow of Na^+ is still given by the J^{NaK} expression (Eq. 3.2), but the amount of Na,K-ATPase (n_{NaK}) will now change dynamically according to Eq. 3.13 to counteract the perturbations in Na^+ inflow. A transient increase in intracellular Na^+ (from increased apical inflow) causes the amount of Na,K-ATPase to increase ($\dot{n}_{\mathrm{NaK}} > 0$); this increase continues until the outflow of Na^+ through Na,K-ATPase is so large that the concentration of intracellular Na^+ is brought back down to its setpoint.

3.4.2 Regulation of basolateral K permeability and K homeostasis

The pump-leak parallelism between K-permeability and the stimulation of basolateral Na,K-ATPase is well studied [22, 74, 160]. An increase in the Na,K-ATPase pump rate, as seen under the uptake of nutrients, is accompanied by an increase in the basolateral K permeability. Whether this increase stems from an increased expression of K channels or from non-transcriptional mechanisms is not yet fully understood as little is known about changes in K-channel expression in enterocytes [74].

Our attention in this work is on the regulation of K permeability by intracellular ATP. Basolateral K_{ATP}-channels have been found in enterocytes [46] and other epithelia [178]. The increased usage of ATP by Na,K-ATPase during absorption lowers the intracellular concentration of ATP; this reduction

in intracellular ATP relieves the inhibition of basolateral K_{ATP}-channels, thus increasing the K permeability.

Structuring this into a regulatory motif we have that intracellular ATP acts as an outflow controller of $[K_c]$, see Fig. 3.3. ATP is used by the Na,K-ATPase at a rate of J^{ATP}=J^{NaK}. We propose that the synthesis of ATP can be modeled by an expression on the form $k_1^{ATP}\left(K_{0.5}^{ATP}/\left(K_{0.5}^{ATP}+[ATP]\right)\right)$, i.e., that the synthesis of ATP increases when the concentration of ATP decreases. The theoretical maximum rate of synthesis is k_1^{ATP} when [ATP] is zero, and $K_{0.5}^{ATP}$ is the concentration of ATP where the rate of synthesis is half of k_1^{ATP}. The synthesis of ATP must increase as the concentration of intracellular ATP is reduced in order to reach a new steady state, otherwise an increase in J^{NaK} would simply deplete the cell of ATP as the synthesis would never catch up with the increased consumption.

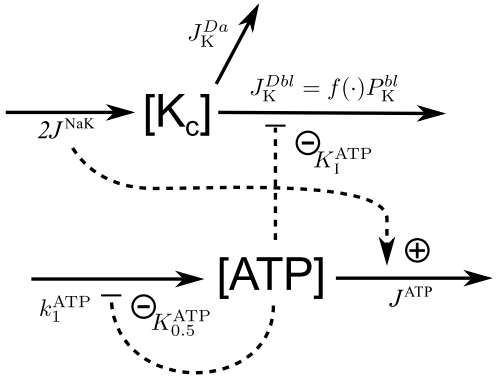

Figure 3.3: Motif proposed for the regulation of intracellular K^+. The degradation of ATP is coupled to the pump rate of the Na,K-ATPase. ATP affects the basolateral permeability to K^+ by inhibiting the K channels. ATP also inhibits its own synthesis.

The inverse relation between the concentration of intracellular ATP and current through K_{ATP}-channels has been quantified in cardiac myocytes [86]. The current through the K channels is inhibited by [ATP] with an inhibition constant K_I^{ATP} of 0.8 mM. From this basis we express the relationship between ATP and basolateral K-permeability on a standard inhibition form as: $P_K^{bl} = P_{Kmax}^{bl}\left(K_I^{ATP}/\left(K_I^{ATP}+[ATP]\right)\right)$.

This motif leads to a differential equation describing the dynamics in

[ATP], and an expression for the basolateral K permeability as[1],

$$[\dot{\mathrm{ATP}}] = \frac{1}{V_c}\left(k_1^{\mathrm{ATP}}\frac{K_{0.5}^{\mathrm{ATP}}}{K_{0.5}^{\mathrm{ATP}}+[\mathrm{ATP}]} - J^{\mathrm{NaK}}\right) \tag{3.14}$$

$$P_{\mathrm{K}}^{\mathrm{bl}} = P_{\mathrm{Kmax}}^{\mathrm{bl}}\left(\frac{K_{\mathrm{I}}^{\mathrm{ATP}}}{K_{\mathrm{I}}^{\mathrm{ATP}}+[\mathrm{ATP}]}\right) \tag{3.15}$$

where V_c is the cell (cytoplasm) volume, and $K_I^{\mathrm{ATP}} = 0.8$ mM. $P_{\mathrm{K}max}^{\mathrm{bl}}$ can be found from $P_{\mathrm{K}}^{\mathrm{bl}}$ and the steady-state level of [ATP], which is around 4.3 mM in enterocytes [41]. We have adjusted k_1^{ATP} so that [ATP] is in steady state (4 mM in our simulations) before the addition of nutrients; $K_{0.5}^{\mathrm{ATP}}$ is set to 0.5 mM.

3.5 Enterocyte simulator built in Matlab/Simulink

We used Matlab/Simulink from MathWorks to implement the enterocyte model. The implementation creates an enterocyte simulator, which numerically solves the model equations for a given set of parameters and initial conditions. Simulink is a graphical block diagram interface where the overall implementation/program is made by connecting blocks that perform different mathematical operations. Each block have inputs and/or outputs and may consist of several subblocks that each performs one or several operations. The overall look and feel is close to that of an ordinary, hand drawn, block schematic diagram in control engineering. Simulink is more or less seamlessly integrated with the rest of the Matlab environment, and one of its strengths is the possibility to create blocks out of ordinary Matlab-code. Once the model is implemented, it can be simulated (solved) through the graphical user interface of Simulink.

Fig. 3.4 shows the main view of our the enterocyte simulator. It consists two blocks (marked in blue) that defines the external concentration of glucose (G), sodium (Na), potassium (K), and chloride (Cl) in the mucosal lumen (m) and on the serosal (s) side of the enterocyte. These external

[1]This motif is strictly speaking not a controller motif as we defined them in chapter 2 (Papers 1 and 3). There is a negative feedback, but the feedback stems from the inflow of K_c and not from the concentration of K_c. Thus there is no way Eq. 3.14 can provide a well-defined setpoint for K_c, as this equation can not be written like the standard integral control law. The negative feedback still performs a regulatory job, although without perfect adaptation. It may be tempting to change the motif, however this cannot be done unless there are experimental evidence to support it.

variables are passed to the *Enterocyte* subblock (marked in white), wherein they are used to calculate the flows and the states (Eqs. 3.1–3.15). The flows and states are then passed, along with the external variables, to two blocks that create various plots of the simulation results, and that also export the results to the Matlab workspace (marked in green).

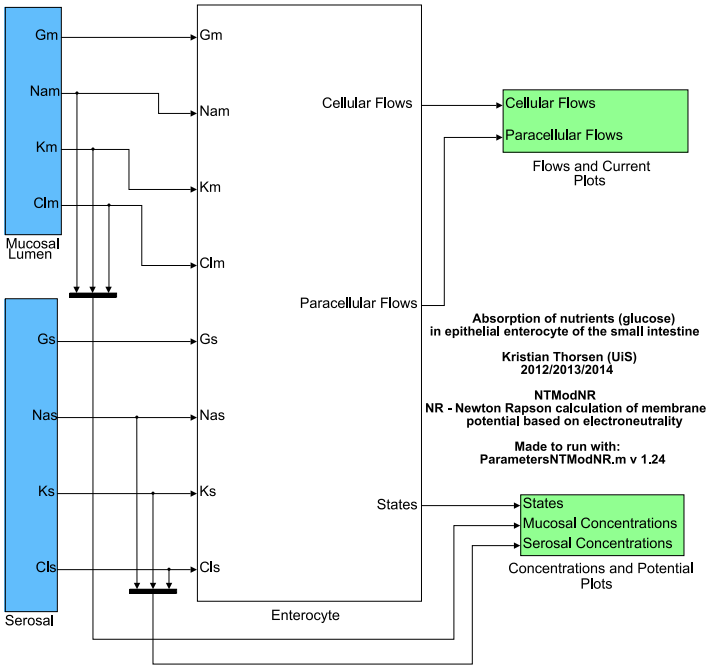

Figure 3.4: Main level of the enterocyte simulator implemented in Simulink. The model consists of several subblocks. The enterocyte model itself is implemented in the big white block in the center, named *Enterocyte*. External concentrations are passed to the *Enterocyte* block from input blocks (blue), and simulation results are treated and visualized inside the output blocks (green). Parameters are set by a separate Matlab script before running the enterocyte simulator. A detailed view of the *Enterocyte* subblock is given in Fig. 3.5.

To facilitate the use of different parameters, a Matlab script (*ParametersNTModNR.m*) is run before running the simulator. This script sets all the different parameters required to simulate a specific experiment. Parameters are listed in Table A2 in Paper 4, and it is clearly noted, in the following results section, if an experiment uses different parameter values.

The detailed contents of the *Enterocyte* block in Fig. 3.4 is shown in Fig. 3.5, and this block is again a collection of different subblocks. The

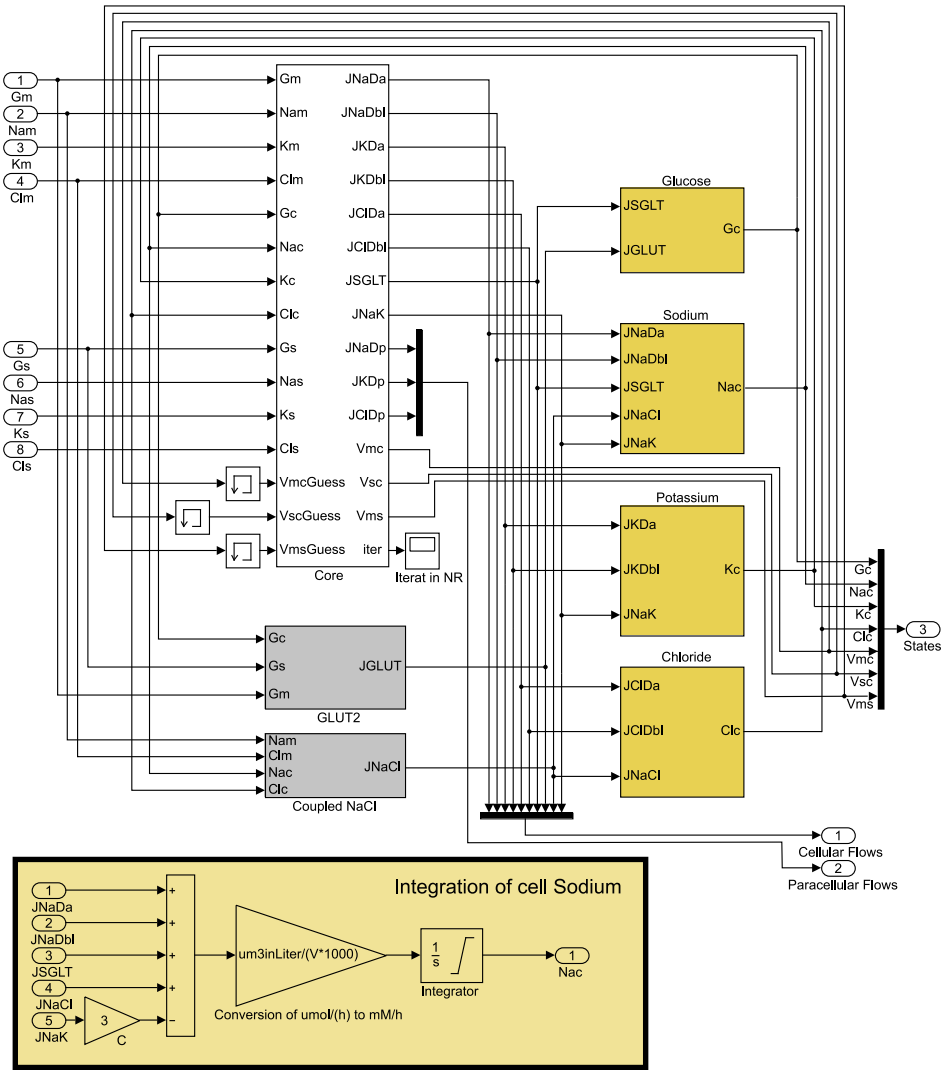

Figure 3.5: Detailed view of the *Enterocyte* subblock from Fig. 3.4. This block does again consist of several subblocks. The *Core* block (white) is responsible for the iterative calculation of flows and membrane potentials. The flow calculation by the *GLUT2* block and the *Coupled NaCl* block is not included in the iterative *Core* block, because these flows are not dependent on membrane potential. The blocks marked in yellow implements numerical integration of the differential equations for the concentration of glucose and ionic species (Eqs. 3.6–3.9). The bottom inset shows the details of the *Sodium* block as an example; the individual flows are summed, converted from mass (umol/h) to concentration (mM/h), and then integrated.

iterative calculation of membrane potentials and membrane-potential dependent flows are collected in a subblock named *Core* (marked in white). The glucose flow through GLUT2 (Eq. 3.4) and the coupled sodium chloride inflow (Eq. 3.3) are calculated in their own subblocks (marked in grey), as they do not depend on the membrane potential. The cellular concentrations of each species: glucose, sodium, potassium, and chloride, are calculated by numerically integrating the flows of each species according to Eqs. 3.6–3.9 (subblocks marked in yellow). The calculated flows and states are passed up to the main level as outputs of the *Enterocyte* block, see Fig. 3.4.

The *Core* subblock is responsible for the calculation of membrane potentials and membrane-potential dependent flows. This is carried out in a subblock of Matlab-code (not shown)[2]. For each time step the *Core* subblock runs an iterative Newton-Raphson procedure; it adjusts and recalculates the flow and membrane potentials until the electroneutrality constraints are met (Eqs. 3.11 and 3.12), i.e., until the net cell current and the net epithelial current are sufficiently close to zero. The following criteria are used:

$$|I^{\mathrm{c}}| = |\sum_i z_i \left(J_i^{\mathrm{a}} + J_i^{\mathrm{bl}}\right)| < 10^{-9} \text{ pmol/h} \tag{3.16}$$

$$|I^{\mathrm{e}}| = |\sum_i z_i \left(J_i^{\mathrm{p}} - J_i^{\mathrm{bl}}\right)| < 10^{-9} \text{ pmol/h} \tag{3.17}$$

For our enterocyte, which has a volume of 450 µm^3 (see Table A2 and appendix of Paper 4), these criteria correspond to a maximum charge difference of 2.22 nM/h (monovalent ions). A charge unbalance in this order will only affect the membrane potential by a few tens of a microvolt.

The iterative calculation of membrane potentials is based on the procedure outlined in [103]. It utilizes two nested Newton-Raphson steps to refine the estimates until the conditions for cell and epithelial electroneutrality are met. The two loops are organized into an inner loop that adjusts ψ_{mc} so that $I^{\mathrm{c}}(\psi_{mc}) = 0$, and an outer loop that adjusts ψ_{ms} so that $I^{\mathrm{e}}(\psi_{ms}) = 0$. The Newton-Raphson adjustments require the computation of the derivatives $dI^{\mathrm{c}}(\psi_{mc})/d\psi_{mc}$ and $dI^{\mathrm{e}}(\psi_{ms})/d\psi_{ms}$. We estimate these by calculating polynomial approximations of $I^{\mathrm{c}}(\psi_{mc})$, treating ψ_{ms} and all the other parameters as constants, and $I^{\mathrm{e}}(\psi_{ms})$, treating ψ_{mc} and all the other parameters as constants.

[2]The two added controller motifs (Eqs. 3.13–3.15) are also subblocks of the *Core* block. They are, however, only calculated once at each time step, and are not a part of the iterative procedure.

The procedure for the iterative method, implemented by Matlab-code in the *Core* block in Fig. 3.5, is as follows for each time step in the simulation:

(i) Use the membrane potentials from the last time step as starting guesses.

(ii) Estimate ψ_{mc} and ψ_{ms} by two nested Newton-Raphson loops.

  (a) Find a polynomial approximation of the net cell current I^{c} as a function of ψ_{mc}. This is done by calculating the individual flows for a range of different ψ_{mc} values.

  (b) Estimate ψ_{mc} by an inner loop.

    i. Calculate the individual flows for the current ψ_{mc} and ψ_{ms}.

    ii. Calculate the apical and the basolateral membrane currents, $I^{\mathrm{a}} = \sum_i z_i J_i^{\mathrm{a}}$ and $I^{\mathrm{bl}} = \sum_i z_i J_i^{\mathrm{bl}}$.

    iii. Calculate the net cell current $I^{\mathrm{c}} = I^{\mathrm{a}} + I^{\mathrm{bl}}$.

    iv. If $|I^{\mathrm{c}}| = |\sum_i z_i \left(J_i^{\mathrm{a}} + J_i^{\mathrm{bl}}\right)| < 10^{-9}$ pmol/h exit the inner loop with the current ψ_{mc} value. Otherwise update ψ_{mc} by a Newton-Raphson step: $\psi_{mc} = \psi_{mc} - I^{\mathrm{c}}/(dI^{\mathrm{c}}(\psi_{mc})/d\psi_{mc})$, where the polynomial approximation of $I^{\mathrm{c}}(\psi_{mc})$ is used to estimate the derivative, then restart the inner loop.

  (c) Find a polynomial approximation of the net epithelial current as a function of ψ_{ms}. This is done by calculating the individual flows for a range of different ψ_{ms} values.

  (d) Calculate the individual flows for the current ψ_{mc} and ψ_{ms}.

  (e) Calculate the current over the basolateral membrane, $I^{\mathrm{bl}} = \sum_i z_i J_i^{\mathrm{bl}}$, and the paracellular current, $I^{\mathrm{p}} = \sum_i z_i J_i^{\mathrm{p}}$.

  (f) Calculate the net epithelial current $I^{\mathrm{e}} = I^{\mathrm{p}} - I^{\mathrm{bl}}$.

  (g) If $|I^{\mathrm{e}}| = |\sum_i z_i \left(J_i^{\mathrm{p}} - J_i^{\mathrm{bl}}\right)| < 10^{-9}$ pmol/h exit the outer loop with the current ψ_{ms}. Otherwise update ψ_{ms} by a Newton-Raphson step: $\psi_{ms} = \psi_{ms} - I^{\mathrm{e}}/(dI^{\mathrm{e}}(\psi_{ms})/d\psi_{ms})$, where the polynomial approximation of $I^{\mathrm{e}}(\psi_{ms})$ is used to estimate the derivative, then restart the outer loop.

(iii) The conditions for electroneutrality are now met. Calculate $\psi_{sc} = \psi_{mc} - \psi_{ms}$. Output the flows so that they can be integrated to the next time step.

The numerical integration of the differential equations (yellow blocks in Fig. 3.5) is done by using the Matlab/Simulink solver *ode23tb*. The solver is set to use an absolute and relative tolerance of 10^{-6} and a variable time step length between 3.6 and 360 ms.

3.6 Simulation results

The model can be simulated either with or without the added regulatory mechanisms provided by Eqs. 3.13 to 3.15. During a short timeframe it is reasonable to assume that the amount of Na-K-ATPase and ATP remains constant. The parameters used in the simulations are listed in Table A2 in Paper 4.

3.6.1 Short-term response to mucosal glucose

Short term response to changes in mucosal glucose is well studied in vitro [22, 78, 151], and thus, provides a sound basis for testing our model. We have simulated its response to a short term increase in mucosal glucose ($[G_m]$) similar to the experimental studies performed on rabbit ileum by Rose and Schultz [151]. Mimicking the conditions of Rose and Schultz, we abruptly increase the mucosal glucose concentration from 100 µM to 20 mM, and then let it fall back to 100 µM in an exponential manner, as to simulate glucose being flushed out, see Fig. 3.6A. The response in state variables from the model is shown in Fig. 3.6 panels B-H, whereas the flows are shown in Fig. 3.7.

The steady-state levels of cell Na^+, K^+ and Cl^- are in the expected range [127, 128]. The short term increase in cell Na^+, see Fig. 3.6C, is supported by experiments [78], but is reported to fall over time if the mucosal concentration is kept high instead of being flushed out, indicating a slower regulatory mechanism that increases the number of Na,K-ATPase transporters.

The reduced concentration of intracellular K^+ (Fig. 3.6D) is a result of an increased outflow of K^+ (Fig. 3.7E) due to membrane depolarization. The change in membrane potential towards more positive values increases the diffusive K^+ outflow, in agreement with Eq. 3.5. K^+ is removed faster than the Na,K-ATPase imports K^+, a property which is anticipated based on experimental results [22, 65].

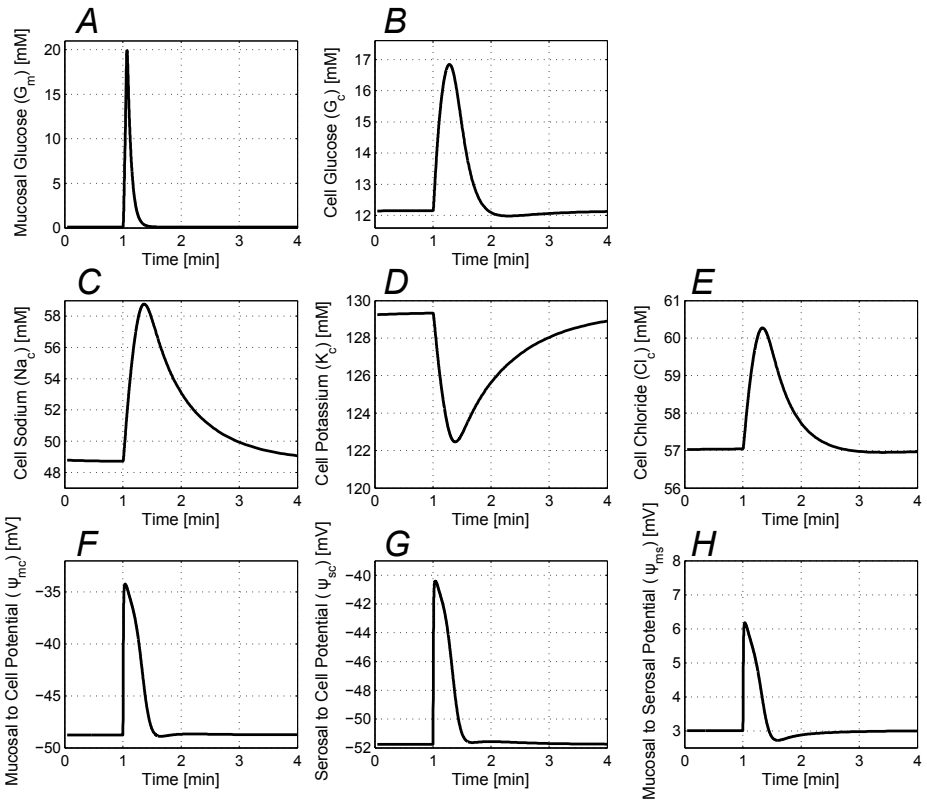

Figure 3.6: Simulated model response to a short term change in mucosal glucose. **A.** At t=1 min mucosal side glucose concentration ($[G_m]$) is increased from 100 µM to 20 mM (step). The mucosal side is then flushed with media without glucose (using a flush time of 20 seconds as in [151]). This gives in an impulse shaped change in $[G_m]$. **B.** Cell glucose concentration ($[G_c]$). **C.** Concentration of cell sodium ($[Na_c]$). **D.** Concentration of cell potassium ($[K_c]$). **E.** Concentration of cell chloride ($[Cl_c]$). **F.** Mucosal to cell membrane potential (ψ_{mc}). **G.** Serosal to cell membrane potential (ψ_{sc}). **H.** Mucosal to serosal membrane potential (ψ_{ms}).

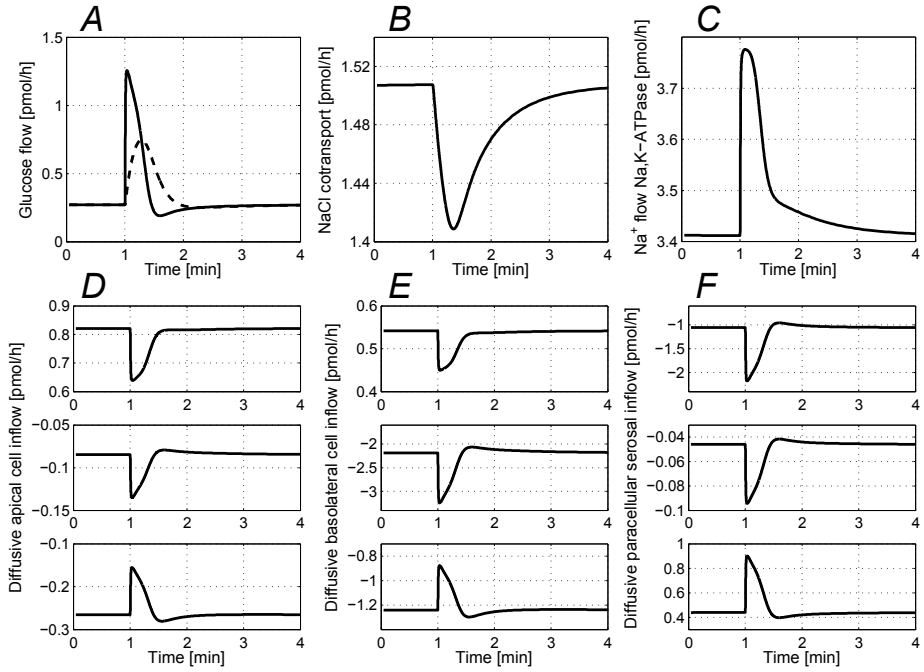

Figure 3.7: Simulated model flows during a short term change in mucosal glucose. **A.** Glucose inflow through SGLT1 (solid) and outflow through GLUT2 (dashed). **B.** Coupled NaCl inflow. **C.** Outflow of Na^+ through Na,K-ATPase. **D.** Diffusive inflow of Na^+ (top), K^+ (middle) and Cl^- (bottom) over the apical membrane. **E.** Diffusive inflow of Na^+ (top), K^+ (middle) and Cl^- (bottom) over the basolateral membrane. **F.** Diffusive inflow to the serosal side of Na^+ (top), K^+ (middle) and Cl^- (bottom) through the paracellular junctions. (The expression for diffusion Eq. 3.5 is positive into the cell, a calculated negative inflow in panels D, E and F is thus an outflow.)

The simulation shows that the addition of mucosal glucose leads to a less negative mucosal to cell membrane potential (ψ_{mc}, Fig. 3.6F) and a more positive mucosal to serosal membrane potential (ψ_{ms}, Fig. 3.6H), in good agreement with the experimental findings of Rose and Schultz [151]. Figure 3.8 shows the membrane potential response from our simulated change in mucosal glucose (from Fig. 3.6) together with the experimental data from the study by Rose and Schultz [151] on rabbit ileum. The match is remarkable considering the fact that most of our parameters (Table A2 in Paper 4) are gathered from the literature of single transporter type studies, done with proteins from different organisms including human type SGLT1 expressed in oocytes [201], guinea pig Na,K-ATPase from ventricular

myocytes [57, 125], and GLUT2 from rat enterocytes [114]. The spikier simulated response in membrane potential (Fig. 3.8) may be related to the effect of unstirred layers around the microvilli. A gradual equilibrating between the mucosal bath and the microvilli area will effectively drag out the response.

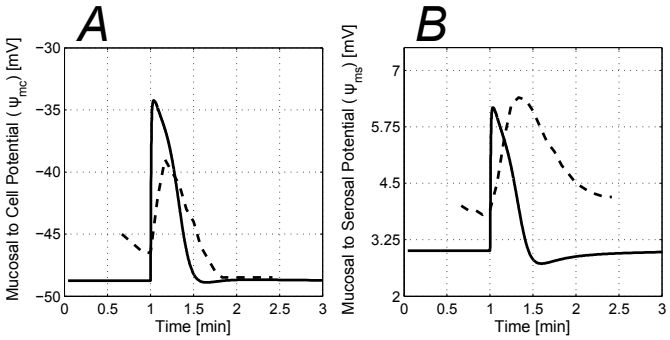

Figure 3.8: Simulated model response in membrane potential (solid) and replotted experimental values from [151] (dashed). At t=1 min the mucosal side glucose concentration ($[G_m]$) is increased from 100 µM to 20 mM (step). The mucosal side is then flushed so that $[G_m]$ falls back to 100 µM (using a flush time of 20 seconds). **A.** Mucosal to cell potential ψ_{mc}. **B.** Mucosal to serosal potential ψ_{ms}.

Because the kinetic flow expressions and physiological parameters are based on single transporter type studies, parameter fitting would probably be needed if we were to evaluate the model's ability to exactly match quantitative results from studies done on whole enterocytes. Cell variance would in that case also have to be considered, e.g. the membrane potential of rabbit enterocytes bathed in a control medium was in the study of Rose and Schultz [151] shown to range from −15 mV to −55 mV indicating considerable variance among cells.

Net epithelial flows of Na^+, K^+, and Cl^- are found by summing the basolateral and paracellular flows. Figure 3.9 shows the net flows during the short term increase in mucosal glucose. Focusing on the steady state before and after the step in mucosal glucose we see that Na^+ and Cl^- are absorbed from the intestine, in keeping with enterocytes being Na^+ absorbing epithelia [160]. There is a small leak of K^+ in the opposite direction which is expected because some of the K^+ pumped into the cell at the basolateral membrane will escape through K-conductance in the apical membrane (Fig. 3.7D). The rate of K^+ secretion is very low (0.14 pmol/h) compared to the inflow of Na^+ and Cl^- (1.82 pmol/h and 1.68 pmol/h),

about 8 % of the Na^+ inflow, and is believed to be of little physiological significance [158]. Although there is an increase in Na^+ pumped by the Na,K-ATPase (Fig. 3.7C) the net epithelial Na^+ inflow decreases during the transient phase (Fig. 3.9A). This is caused by the increase in paracellular back flow of Na^+ into the lumen (Fig. 3.7F); a more positive transepithelial potential ψ_{ms} (Fig. 3.6H) drives this paracellular movement of Na^+.

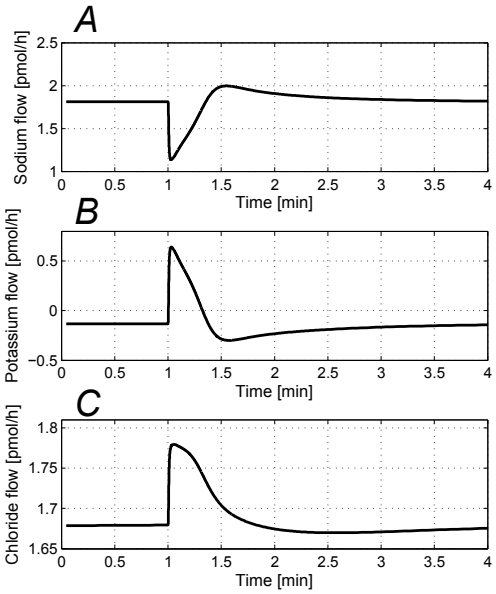

Figure 3.9: Simulated net inflows (positive into serosal area) over the epithelial layer; this is the net sum of transcellular and paracellular flows. **A.** Inflow of Na^+ ($J_{\mathrm{Na}}^{\mathrm{Epi}} = 3J^{\mathrm{NaK}} - J_{\mathrm{Na}}^{Dbl} + J_{\mathrm{Na}}^{Dp}$). **B**. Inflow of K^+ ($J_{\mathrm{K}}^{\mathrm{Epi}} = -2J^{\mathrm{NaK}} - J_{\mathrm{K}}^{Dbl} + J_{\mathrm{K}}^{Dp}$). **C.** Inflow of Cl^- ($J_{\mathrm{Cl}}^{\mathrm{Epi}} = -J_{\mathrm{Cl}}^{Dbl} + J_{\mathrm{Cl}}^{Dp}$).

3.6.2 Short term response to mucosal Na

The enterocyte response to short term changes in mucosal Na^+ is well studied [128, 133, 151]. We simulated short term changes in the concentration of mucosal Na^+ ($[Na_m]$) by changing the mucosal Na^+ from its base value of 140 mM to 100 mM, and back again in a stepwise manner. The concentration of mucosal glucose was kept constant at 0.5 mM. Figure 3.10 shows the simulated model response. When the mucosal sodium concentration is kept at 100 mM the model reaches a new steady state; the reduced availability of mucosal Na^+ leads to a decrease in the intracellular Na^+

concentration ([Na_c]) (see Fig. 3.10A). The decrease in intracellular Na^+ is balanced by decrease in intracellular Cl^- (Fig. 3.10C) and an increase in intracellular K^+ (Fig. 3.10B).

The simulation also shows cell hyperpolarization (see Fig. 3.10 panels D-F) as a result of decreased mucosal Na^+. The reversal of polarity from positive to negative of the transepithelial potential ψ_{ms} is particularly noteworthy. These results are similar to what have been observed in rat duodenum [133]. The change in ψ_{mc} and ψ_{ms} of about -6 mV is in the same range as reported for the same change in mucosal Na^+. Changing the mucosal Na^+ concentration back to 140 mM causes the enterocyte to return to its initial state.

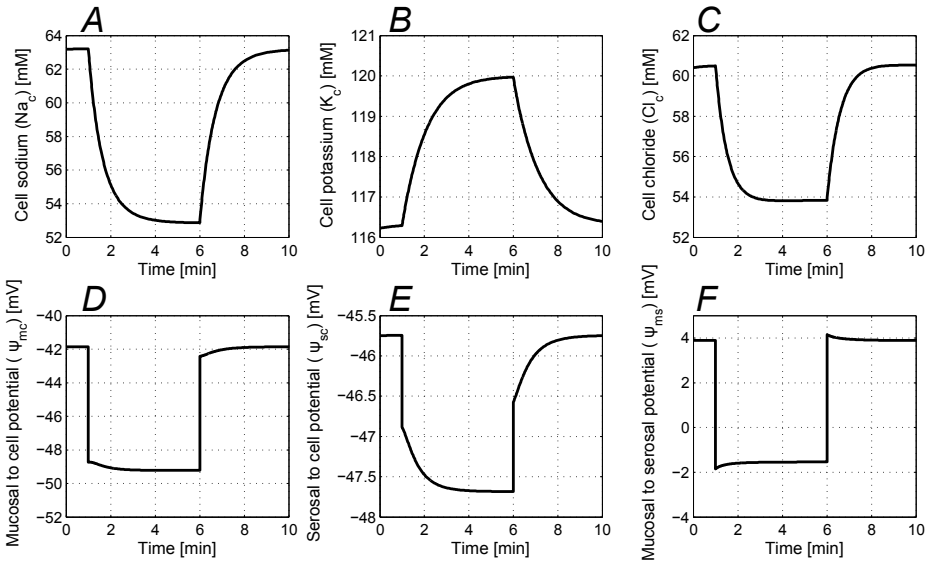

Figure 3.10: Simulated model response to a short term change in mucosal sodium. At t=1 min to t=6 min mucosal side Na^+ concentration ([Na_m]) is decreased from 140 mM to 100 mM (step). **A.** Cell sodium concentration ([Na_c]). **B.** Concentration of cell potassium ([K_c]). **C.** Concentration of cell chloride ([Cl_c]). **D.** Mucosal to cell membrane potential (ψ_{mc}). **E.** Serosal to cell membrane potential (ψ_{sc}). **F.** Mucosal to serosal membrane potential (ψ_{ms}).

There is a continuous net absorbance of Na^+ and Cl^- from the intestine during the whole simulated response to this change in mucosal Na^+. The net inflow of Na^+ goes from 1.86 pmol/h to 0.85 pmol/h when mucosal Na^+ changes from 140 mM to 100 mM (results not shown).

3.6.3 Long term response with controller motifs

Adding the regulatory motifs to the model gives the long term response shown in Figs. 3.11 and 3.12 (solid lines) for a stepwise increase in mucosal glucose (note the time scale). The results show perfect adaptation in the concentration of intracellular Na^+ (Fig. 3.11C), and partly adaptation in K^+ (Fig. 3.11D). The concentrations are regulated towards their setpoints of approximately 49 mM and 130 mM, respectively. Comparing this to the simulation results of an enterocyte without the regulatory mechanisms (dashed lines in Figs. 3.11 and 3.12), which has no adaptation at all, shows how much is gained by these motifs.

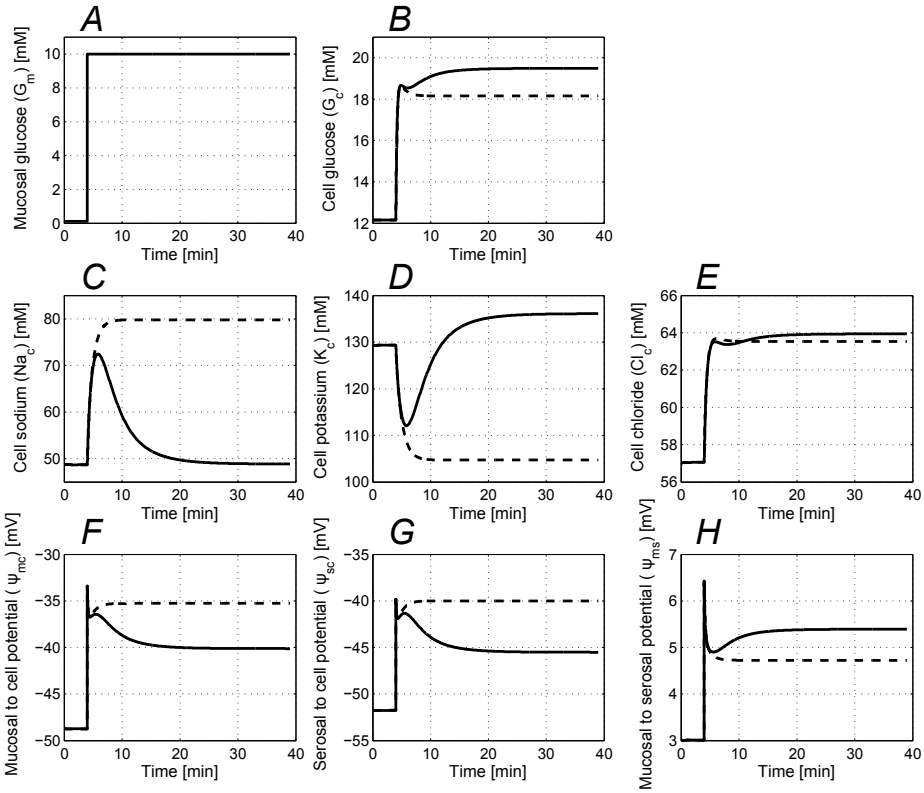

Figure 3.11: Simulated model response to long term change in mucosal glucose with (solid lines) and without (dashed lines) the two regulatory mechanisms. **A.** At time t=4 min mucosal glucose concentration ($[G_m]$) is stepped from 0.1 mM to 10 mM. **B.** Cell glucose ($[G_c]$). **C.** Cell sodium ($[Na_c]$) **D.** Cell potassium ($[K_c]$). **E.** Cell chloride ($[Cl_c]$). **F.** Mucosal to cell membrane potential (ψ_{mc}). **G.** Serosal to cell membrane potential (ψ_{sc}). **H.** Mucosal to serosal membrane potential (ψ_{ms}).

The adaptation in K^+ is not perfect in the sense that exactly the same concentration is achieved before and after the step; the concentration of K^+ is close to 129 mM before the step in mucosal glucose and 136 mM after the step. There is a slight overadaptation [44] (Fig. 3.11D). As expected there is no adaptation in the concentration of Cl^- (Fig. 3.11E) as there is no specific controller motif regulating Cl^-.

The amount of Na,K-ATPase and ATP is shown in Fig. 3.12. The reduction in ATP from 4 mM to 2.8 mM fits well with reported values for absorbing epithelial cells in the renal proximal tubule [178].

In addition to maintaining the ionic concentration at their setpoints the regulation also enables a higher total flow through the enterocyte (data not shown). The net epithelial flow of Na^+ increases by 20% after the step in mucosal glucose with regulation (from 1.8 pmol/h to 2.2 pmol/h) whereas it without regulation only increases by 5% (from 1.8 pmol/h to 1.9 pmol/h). The net flow of glucose is 13% higher with regulation than without.

The results also show a hyperpolarization of the membrane potential compared to the situation with no regulation (Fig. 3.11F-H). The transepithelial potential (ψ_{ms}) increases with the step in mucosal glucose and is higher with regulatory motifs than without. This fits with the higher total ionic flow from mucosal to serosal with regulation.

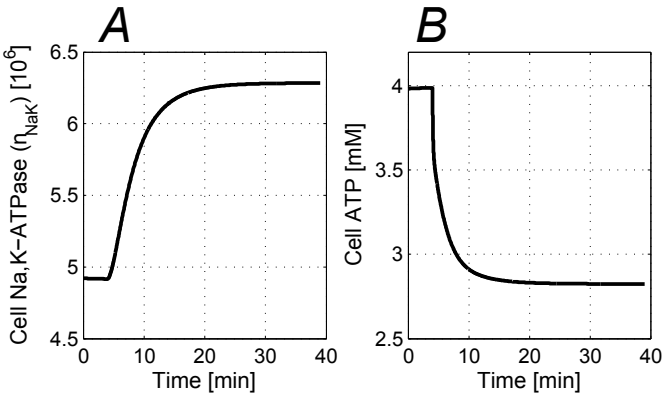

Figure 3.12: Simulated model response to long term change in mucosal glucose. **A.** Amount of Na,K-ATPase (n_{NaK}). **B.** Concentration of ATP ([ATP]).

3.7 Regulatory mechanisms for Na/K homeostasis

When the inflow of Na^+ increases due to absorption of glucose the enterocyte has to adapt the Na,K-ATPase driven compensatory outflow of Na^+. Besides a transient increase, there is no sustained higher concentration of intracellular Na^+ during absorption of nutrients [78, 159]. This means that the Na,K-ATPase driven outflow has to increase by other means than mass action kinetics. The explanation suggested by our controller motif is that the transient increase in intracellular Na^+ brings about an increase in the number of active Na,K-ATPase proteins in the basolateral membrane. This can explain the results of Rokaw et al. [148], which show that the amount of Na,K-ATPase in A6 model cells for kidney collecting ducts epithelium is regulated in correspondence to inflow of Na^+.

The intracellular Na^+ activation of Na,K-ATPase synthesis has been shown for other cell types, where it increases the amount of mRNA coding for both the α and β subunits that combine into Na,K-ATPase [162, 204]. Yamamoto et al. [204] showed that this increase, in cardiocytes, was directly caused by Na^+ due to Na^+ responsive sequences located within the 5'-flanking regions of the α-gene (α_1, α_2, and α_3 isoforms). Parallels can be drawn to the intestinal enterocytes as they express the α_1 isoform [106]. Our simulations confirm that the regulation of Na,K-ATPase by intracellular Na^+ (Fig. 3.2) is a controller motif that is able to achieve homeostasis, thus being a plausible mechanism for how the enterocytes manage to adapt and survive in a changing environment.

In addition to synthesis of Na,K-ATPase, posttranslational regulation by the insertion of pre-existing transporter molecules from cytoplasmic storage pools can also be a contributing factor. Such regulation in response to intracellular Na^+ has been indicated in rabbit cortical collecting tubules [20]. Given the many similarities between kidney and intestine epithelial cells we cannot rule out the possibility that the abundance of membrane bound Na,K-ATPase in enterocytes is regulated by both translational and posttranslational pathways that are dependent on intracellular Na^+. Although we have focused on regulation by synthesis of new Na,K-ATPase in our argument, the ability of the controller to achieve homeostasis is coupled to the action where intracellular Na^+ regulates the number of active transporters, and not whether this happens by de novo synthesis or by insertion/activation of latent transporters.

Earlier work on sodium transporting epithelial cells have speculated whether the relationship between the Na,K-ATPase turnover and intracellular Na^+ can be so steep that small changes in the latter may result in very large changes in the former [78, 159], enabling Na^+ outflow adaptation to occur without an increase in the amount of Na,K-ATPase. This alternative hypothesis is, however, considered unlikely and has also been shown to be incompatible with the experimental measurement of Na,K-ATPase kinetics [57, 125].

Nevertheless, an increase in the amount of Na,K-ATPase can possibly be induced by other means than direct activation by intracellular Na^+. Other mechanisms for the regulation of Na,K-ATPase are known; many studies have focused on the hormonal regulation through protein kinase A and C (PKA and PKC) pathways, see [175] for a review. Although important, hormonal mechanisms (involving sensing or prediction of the Na^+ inflow in enterocytes and secretion of hormones by some organ distant to the enterocyte) may be slower than the direct regulation by intracellular Na^+ and might thus play a secondary role. Effect of hormones on Na,K-ATPase activity have also been shown to be dependent on intracellular Na^+ in proximal tubule cells, suggesting that the level of intracellular Na^+ modulates whether hormones stimulate, inhibit, or have no effect on Na,K-ATPase levels [50].

A coupling between activity of the Na,K-ATPase and the basolateral K permeability have been experimentally shown [22, 65]. While this coupling have been confirmed for decades it is still not clear what mechanism lies behind it [74]. Our proposed regulatory motif (Fig. 3.3) is a mechanism where ATP acts as a regulator. Since intracellular ATP concentration is dependent on the current ATP usage by Na,K-ATPase, i.e. the pump rate, the ATP concentration contains information about the inflow of K^+. ATP regulates the intracellular K^+ concentration by acting as an outflow controller modulating the outflow of K^+ through K_{ATP}-channels which are inhibited by ATP. This mechanism has only one intermediate between Na,K-ATPase pump rate and the basolateral K permeability.

Tsuchiya et al. [178] have reported that ATP is the main coupling modulator between Na,K-ATPase and K-channel activity in epithelial cells in the renal proximal tubule; they showed that an increase in Na,K-ATPase activity due to luminal addition of glucose and alanine leads to a 57% decrease in intracellular ATP, from 3.7 mM to 2.1 mM, followed by an increase in K conductance. Similar experiments [15] report of a reduction

from 4.4 mM to 2.7 mM. These studies show that ATP sensitive K_{ATP}-channels react to a decrease in ATP caused by an increase in Na,K-ATPase activity during transcellular Na^+ transport. The role of ATP as a regulator is supported by the observation that an increase in K permeability is not seen in ATP loaded proximal tubule cells [178]. The kinetics of the inhibition by ATP has a K_I of 0.8 mM (in cardiac myocytes) [86]. ATP sensitive K channels have also been found in enterocytes [46]. Our proposed motif is based on the same type of coupling as is reported for ATP, and our results confirm that this is a mechanism that can provide homeostasis.

For simplicity we did only include consumption of ATP by the Na,K-ATPase. Other usage of ATP can however be included without changing the main results as long as these consumptions are approximately constant or increasing during nutrient transport. The only change is that the k_1^{ATP} parameter must be adjusted so that the synthesis and consumption balance each other at steady state.

The synthesis of ATP, see Eq. 3.14, must increase when the intracellular ATP concentration falls in order for the ATP concentration to reach a new steady state. If not, an increase in J^{NaK} will deplete the cell from ATP; the rate of consumption is in this case always greater than the rate of production. The increase in ATP synthesis with falling ATP concentration is conceivable as this will shift the ATP/ADP balance. The amount of ATP is reduced, and the amount of ADP available for new synthesis into ATP increases. A possible expansion of the current model would be the inclusion of differential equations describing the dynamic relations between ATP and ADP.

The reported [15, 178] and simulated (Fig. 3.12) reduction in intracellular ATP during transport may give reason to speculate whether it also directly affects the pump rate of Na,K-ATPase. Although possible, it is unlikely because studies in red blood cells, done by Marjonovic and Willis [115], have shown that the Na,K-ATPase is ATP saturated already at a concentration of 1.5 mM. The reduction in ATP during transport can thus regulate the K-permeability and the outflow of K^+ without impeding the net transport by lowering the Na,K-ATPase pump rate. We have assumed that Na,K-ATPase is saturated with respect to ATP in our model, i.e. the flow expression, Eq. 3.2, does not include [ATP].

Chapter 4

Implementing a Cu regulating controller in yeast (unpublished)

Copper is essential for cell functioning and survival, but becomes toxic at high concentrations. Copper is an important cofactor for several enzymes such as plastocyanin, an electron transfer protein involved in photosynthesis [154]; superoxide dismutase (SOD), which protects against oxidative stress [144]; and hemocyanins, which act as oxygen transporters (instead of hemoglobin) in some invertebrates [77]. High copper concentrations are toxic because copper can participate in Fenton-like redox reactions with hydrogen peroxide (H_2O_2), a byproduct of oxygen metabolism. These reactions produce highly reactive chemical intermediates, such as hydroxyl ($HO^\bullet$) and superoxide ($O_2^{\bullet -}$) radicals, as well as Cu(III) [141]. Copper can also nonspecifically interact and bind to chains of amino acids, thus causing proteins to fold and bind incorrectly [99]. Excess of misfolded proteins caused by dysfunctional copper homeostasis are in humans connected to neurodegenerative disorders like Alzheimer's, and Parkinson's [58, 150]. Many organisms have developed methods that enable them to obtain the necessary amount of copper, together with methods that prevent the internal concentration from becoming too high.

This chapter explores the mechanisms behind copper homeostasis in the model organism *Saccharomyces cerevisiae* (baker's yeast). This single cell organism is able to live and grow in environments ranging from having trace amounts of copper to concentrations of Cu^{2+} in the millimolar range [198]. We will show how the inflow/outflow controller framework can be used to model and understand homeostatic control of copper in yeast.

Furthermore, by using molecular and synthetic biology tools, we design a homeostasis extending outflow controller, and transform it into *S. cerevisiae*

by genomic integration. The controller is only active when needed and provides the transformed yeast with an improved resistance towards external copper. The outflow controller consists of the gene of a copper transporting Cu-ATPase from another yeast species and a copper dependent promoter controlling this gene. This Cu-ATPase is able to pump copper ions out of the cytoplasm.

This chapter is structured as follows: first a short introduction to yeast as a model system is given in section 4.1. The native copper regulatory system of *S. cerevisiae* is described in section 4.2. Section 4.3 describes the added outflow controller and explains how this controller is built and works. Section 4.4 presents the experimental methods used, and the results are shown in section 4.5. Finally some remarks on the further directions of this project are given at the end of the chapter.

4.1 Yeast as a model organism

S. cerevisiae is a unicellular eukaryotic organism known to most of us simply as the yeast used for baking, brewing, and wine-making. Its popularity as a model system, used to study fundamental cellular mechanisms, has several reasons. It is easy to grow, and can grow on defined synthetic media making it possible to control all environmental parameters. It grows fast with generation times down to around 90 min in nutrient rich media. Yeast grows vegetatively both as a diploid with chromosome pairs, and as a haploid with only a single set of chromosomes. Haploid cells are either of mating type **a** or α, and may mate to form a diploid. Diploids cannot mate, but can undergo miosis and sporulate into four haploids.

The genome of *S. cerevisiae* was the first eukaryotic genome to be fully sequenced (released in April 1996) [61]. The genome and curated information about every gene is available in an online genome database [30, 163]. DNA manipulation is very easy to do in *S. cerevisiae*, partly because of the ease of deleting and disrupting genes in haploids with only single chromosomes, and partly because of the yeast's ability to integrate DNA into its genome by homologous recombination [47]. DNA can be manipulated not only by ordinary shuttle vectors (plasmids), but also directly by PCR products. Selection is easy due to several common selectable markers, most of which complement specific auxotrophies caused by disruptions of particular genes [47, 53]. The *S. cerevisiae* strain we use (YPH500) is for example unable to grow without supplements of

leucine and tryptophan due to deletions in its *LEU2* and *TRP1* genes. Transformants can be selected by using media without leucine, as only cells which have successfully adopted new DNA (conveniently designed to include a functional *LEU2* gene) will be able to survive without leucine.

Apart from being easy to work with, basic functions in yeast cells are almost surprisingly similar to higher eukaryotes such as mammals. Examples include: (i) biosynthetic pathways and their regulation, (ii) cell division and cell cycle , (iii) DNA replication, recombination and repair, (iv) transcriptional regulation and activation, (v) signal transduction pathways, (vi) stress responses, (vii) prion development, and (viii) mitochondrial metabolism [30, 53]. A good representation of the similarities was provided by a *Science* paper published this year, which revealed that nearly half of 414 essential yeast genes could be replaced by their human orthologs [87]. That is, human protein-coding DNA can in many cases replace that of yeast.

4.1.1 A note on yeast genetic nomenclature

We will here use conventional *S. cerevisiae* nomenclature to describe gene names and proteins (gene products). Most noteworthy is:

- Wild-type genes have names with three letters and up to three numbers relevant to gene function[1]. Dominant genes are written with uppercase letters in italics: *CTR1*, *LEU2*, *CUP1*.
- Recessive and nonfunctional genes are written with their respective names in lowercase letters in italics. Mutant alleles are marked by numbers, and/or by a symbol indicating the type of alteration: *leu2-Δ1*, *ura3-52*.
- Gene products, i.e., proteins, are denoted by their corresponding gene name, but written with normal font and only with the first letter in capital. A «p» is added at the end: Ctr1p, Leu2p, Cup1p.

Notice that the notation of proteins names (gene products) is different from the nomenclature used in the previous chapter. Proteins are for most mammals written by their name in uppercase letters. For more detailed conventions we refer to [29, 47].

[1]The letters are somewhat random, but in some way relevant to gene function, localization, or phenotype. It is not always easy for non-geneticists and non-biologists to understand why a gene is given a specific name. The meaning behind the three letters can be found by looking the gene up in the *Saccharomyces* Genome Database [163].

4.2 Regulation of copper in yeast

The dominant form of copper in the cytoplasm of *S. cerevisiae* is cuprous Cu^+ [99, 189]. *S. cerevisiae* maintains internal copper homeostasis in environments with low copper concentrations by using the copper transporter Ctr1p, which is bound to the plasma membrane[2] [39, 53]. The Ctr1p transporters have very high affinity for Cu^+. Environmental copper in the oxidized Cu^{2+} form is reduced to Cu^+ by the reductase Fre1p, which is expressed on the cell outside. Fre1p is both an iron (ferric) and a copper reductase. The transport appears to be passive as Ctr1p lacks motifs for ATP binding [39]. The human analogue, hCr1p, is a trimer with a channel- or pore-like structure [2, 131]. The transport through Ctr1p shows Michaelis–Menten kinetics against external Cu^{2+}, with an apparent K_M estimated around 1-4 µM [40]. Notice, however, that the use of Cu^{2+} implies that the measured kinetics include both reductase and transport[3].

Transcription of *CTR1* is activated at low levels of intracellular copper and inhibited at high levels [101]. The transcription factor Mac1p binds to a promoter element of *CTR1* and activates transcription. Cu^+ binds to Mac1p at high concentrations, causing it to no longer function as an activator [53], see Fig. 4.1. The expression of *CTR1* is thus reduced when sufficient amounts of copper are available. Transcription of the reductase gene *FRE1* is also controlled by Mac1p [101]. In addition to blocking production of Ctr1p, high concentrations of copper are also claimed to activate degradation of already produced and functional Ctr1p [134].

At high external concentrations of copper it is not always enough to stop production of high affinity inflow transporters to maintain intracellular homeostasis. Copper can leak into the cell through low affinity transporters with less ionic specificity. One such transporter is Fet4p, a low affinity transporter of several metal ions including iron, zinc and copper. Transcription of its gene, *FET4*, is regulated by zinc and iron, but not by copper [71, 187].

[2] Another copper transporter Ctr3p is encoded by the *CTR3* gene of *S. cerevisiae*. This gene is however disrupted and nonfunctional in most laboratory strains, including the S288C strain [97]. It is also nonfunctional in the strain used in this work: YPH500, see methods section 4.4.

[3] Most experiments on copper transport use Cu^{2+} in the external medium. Cu^+ is highly insoluble at neutral pH, and will rapidly oxidize to Cu^{2+} under aerobic conditions. The cytoplasm of most eukaryotic cells is on the other hand a reducing environment, and internal copper is thus very often in the Cu^+ form [99]. Cu^+ can be used in experiments if the yeast is grown at anaerobic and acidic conditions (pH $\approx$ 3) [198].

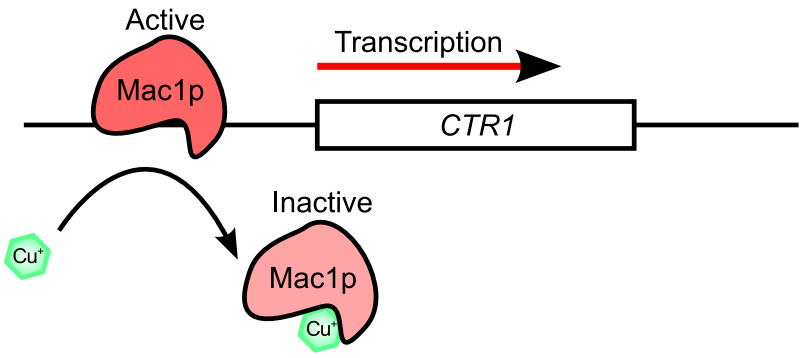

Figure 4.1: Transcription of *CTR1* is inhibited at high internal concentrations of copper. Cu^+ inactivates the transcription factor Mac1p by binding to it.

S. cerevisiae has a copper detoxification system that relies on copper dependent activation of transcription of copper chelators, so called copper *metallothioneins*. Metallothioneins are small proteins that tightly bind heavy metal ions. Copper metallothioneins provide a buffering mechanism for the cytoplasmic concentration of free copper [42, 53 chap. 8]. The Cup1p metallothionein is the primary copper buffer in *S. cerevisiae* [84]; it binds up to eight Cu^+ ions in a tight cysteinyl thiolate cluster [23]. The tight binding of Cu^+ to Cup1p effectively prevents nonspecific copper binding, i.e., it prevents copper mediated protein misfolding.

Transcription of the *CUP1* gene is regulated by the transcription factor Cup2p. Cup2p is activated by copper, in more or less the opposite way of Mac1p. Cu^+ binds to Cup2p causing it to bind to a promoter upstream of the *CUP1* gene, see Fig. 4.2. The *CUP1* promoter contains so-called metal regulatory elements (MREs), specific DNA sequences that Cup2p binds to in the presence of Cu^+ [100].

Fig. 4.3 illustrates the main parts of the system for regulation of internal copper in *S. cerevisiae*. Looking at this system in the light of the controller motif framework, we see that the high affinity inflow transporter Ctr1p acts as an inflow controller. The structure is similar to that of controller motif 3 in Fig. 2.1. Copper (A) inhibits the production of Ctr1p (E), and Ctr1p acts as a controller by adjusting a compensatory inflow of copper. The inflow of copper through Ctr1p depends linearly on the amount of active Ctr1p (E) situated in the membrane. As mentioned, high concentrations of copper may also cause degradation of already produced and functional Ctr1p. A dominating Cu^+ activated removal of Ctr1p makes the structure more like

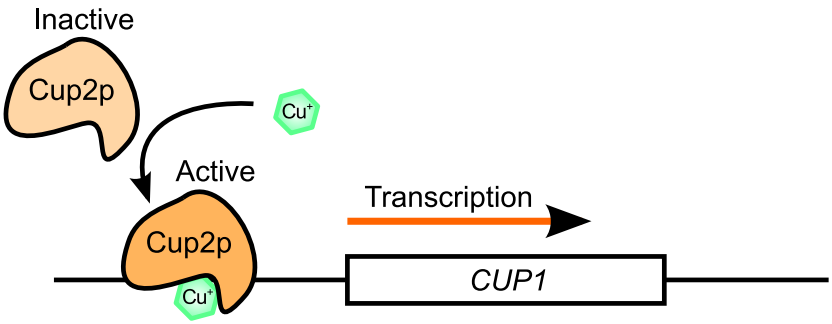

Figure 4.2: Transcription of *CUP1* is activated at high internal concentrations of copper. Cu^{+} activates the transcription factor Cup2p by binding to it.

controller motif 1, Fig. 2.1. Arguably this duality calls for an extension of the controller motifs[4]. Depending on the actual kinetics, controller motif 1 or controller motif 3 may nevertheless be a sufficient description alone.

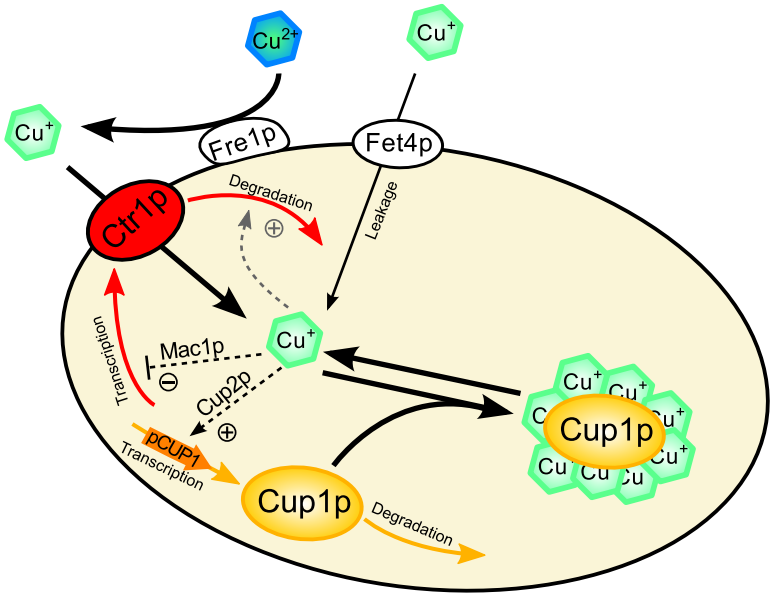

Figure 4.3: Illustration of the copper regulatory system in *S. cerevisiae*. Parts and interactions described in main text.

[4]We did originally only consider motifs where A acts on either the inflow or the outflow for E, not both at the same time, see chapter 2.

An interesting question is whether the inhibition of *CTR1* transcription by Mac1p and Cu^+ can be described as done in the theoretical analysis of the controller motifs, i.e., on the simple form $g_c K_I/(K_I + \mathrm{Cu})$ (Eq. 2.5 assuming $g(\cdot) = 1$). The actual kinetics is to our knowledge not yet known, but experiments have shown that the binding of Cu^+ to Mac1p can be described by a (reversed) *Hill-equation*[5] with n=1 [189]; a form which is equivalent to the simple inhibition expression. The overall inhibition of transcription will in addition also depend the binding characteristics of Mac1p to DNA and the recruitment of RNA polymerase. Still, the above suggests that a simple inhibition term may be an adequate description, at least as long as the amount of Mac1p remains constant.

The regulation of Cup1p appears to work similar to an outflow controller motif of type 5 in Fig. 2.1. The actual kinetics is however, as for the regulation of Ctr1p, not known in detail. Regardless, Cup1p does in essence work as a storage buffer capable of storing excess Cu^+ when availability is high, and supplying necessary Cu^+ when external copper is limiting.

4.3 Extending copper homeostasis by adding an outflow controller

The high affinity Crp1p transporters enable *S. cerevisiae* to survive and grow in environments with very little copper, and the copper binding metallothioneins provides detoxification and supports growth in environments with moderate copper concentrations. There is, however, an obvious limitation in the capacity of the Cup1p system. Copper is never really removed from the cytoplasm, just stored; and the storage capacity is limited both by space and by the metabolic load caused by Cup1p production. A continued production of Cup1p puts a strain of the cell's molecular production machinery, and drains available recourses (amino acids). In our experiments growth is significantly inhibited in synthetic media when Cu^{2+} concentration is around 1 mM. What *S. cerevisiae* lacks is a mechanism

[5]The Hill equation describes a saturable function on the form $Vx^n/(K_{0.5}^n + x^n)$, which is 0 for low x and saturates at V for high x [35]. The exponent n is called the *Hill-coefficient* and may be any positive number; higher n results in a greater steepness in the saturation curve. The opposite function, which is 0 at high x and saturates at V for low x, is often also called a Hill-equation or a reversed Hill-equation: $VK_{0.5}^n/(K_{0.5}^n + x^n)$. The Hill-equation was first proposed by A. V. Hill as an empirical description of oxygen binding to hemoglobin [76].

that can maintain nontoxic levels of cytoplasmic copper in environments with a high copper concentration.

Candida albicans is a pathogenic yeast that shows higher resistance to copper than *S. cerevisiae*. Weissman et al. [198] found that *C. albicans* is able to grow with concentrations of external copper that are much higher than what *S. cerevisiae* is capable of, see Fig. 4.4. The increased resistance is attributed to a P-type ATPase coded by the *C. albicans CRP1* gene. This ATPase functions as a copper pump; it is bound to the cytoplasmic membrane, and cleaves ATP in order to transport Cu^+ ions out of the cytoplasm [147, 198].

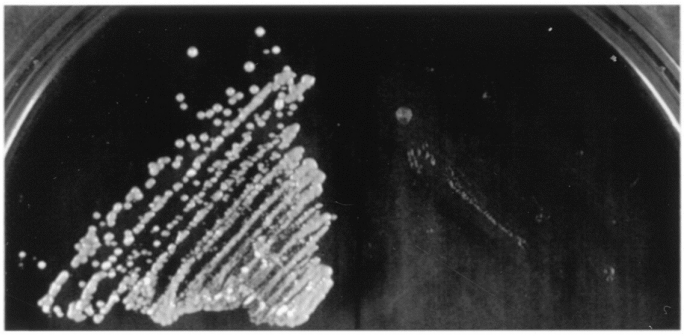

Figure 4.4: Copper resistance of *C. albicans* (left) and *S. cerevisiae* (right). *C. albicans* strain CAF3-1 and *S. cerevisiae* strain W303 were grown for 2 days at 30°C on yeast extract/peptone/dextrose (rich medium) supplemented with 12 mM Cu^{2+} ($CuSO_4$). Reprinted from [198].

The goal of this work is to synthetically add a copper outflow controller to *S. cerevisiae* as to extend the region of homeostatic copper regulation. The idea is to use the copper transporting P-type ATPase from *C. albicans* as a candidate, and fuse it together with a copper dependent promoter. This promoter should be tunable, that is, we should be able to create mutants with different regulatory capabilities and different (tunable) resistances to copper.

The transcription of *CRP1* in *C. albicans* is activated when copper is added to the growth medium [198], indicating that the gene is under control of intracellular copper. It is likely that the upstream regions of *CRP1* contains a copper dependent promoter; this promoter has however not been characterized, and its exact function is therefore unknown.

A more promising candidate for a copper dependent promoter is the *CUP1* promoter native to *S. cerevisiae*, which was described in the previous

section. This promoter is very well characterized, and has been used as a promoter for controlled expression of heterologous proteins in *S. cerevisiae* [100]. It exhibits rapid induction with a maximal level of transcripts detected 30 minutes after addition of external copper [140]. It is also highly tunable; Thiele and Hamer [176] have characterized the induction ratio of nearly 20 different mutations of the promoter.

Fig. 4.5 shows the extended regulatory system of *S. cerevisiae* with the outflow controller added in this study. Crp1p works as an outflow controller motif of type 5, see Fig. 2.1, with its *CRP1* gene under control of a copper activated *CUP1* promoter. We are able to monitor the production of Crp1p by fusing it to a fluorescent protein (enhanced green fluorescent protein: Egfp). The *pCUP1-CRP1-EGFP* fusion is integrated into the genome of *S. cerevisiae* by homologous recombination, explained in the next section.

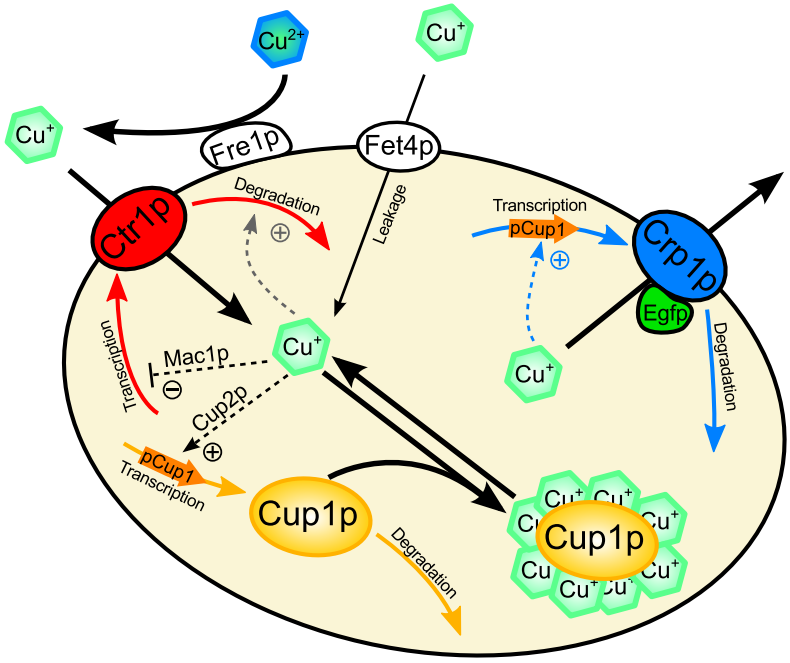

Figure 4.5: Illustration of the copper regulatory system in *S. cerevisiae* extended with an added outflow controller (in blue). The main part of the outflow controller is the Crp1p Cu-ATPase from *C. albicans*, which pumps Cu^+ ions out of the cell. The *CRP1* gene from *C. albicans* is fused to a *EGFP* gene, and is under control of the copper dependent promoter *pCUP1*.

4.4 Experimental methods

4.4.1 Strains, media and reagents

All yeast experiments are done in *S. cerevisiae* haploid strain YPH500, originally created by Sikorski and Hieter[6] [165]. YPH500 has the following genotype: *MATα ura3-52 lys2-801^{amber} ade2-101^{ochre} trp1-Δ63 his3-Δ200 leu2-Δ1* [165]. Chromosomal integrations were targeted to the *leu2-Δ1* locus. Synthetic drop-out medium without leucine (SC-Leu) was prepared according to standard protocols with the following components (Supplier and product numbers in parenthesis): 1.7 g yeast nitrogen base without amino acids and ammonium sulfate (Sigma-Aldrich Y1251), 5 g ammonium sulfate $(NH_4)_2SO_4$ (Sigma-Aldrich A4418), 1.3 g yeast synthetic drop-out medium supplement without leucine (Sigma-Aldrich Y1376), 30 mg adenine hemisulfate (Sigma-Aldrich A9126), 20 g glucose (VWR-BDH BDH0230), and double-distilled water, ddH_2O, to 1 liter. Synthetic complete medium (SC) was made by adding leucine (Sigma-Aldrich L8000) to SC-Leu. Final leucine concentration in SC medium is 380 mg/l. Media for plates were made by the same recipes with the addition of 20 g agar (BioShop Canada AGR001). Copper in the form of Cu^{2+} was added to media from a 0.25 M stock solution of $CuSO_4$ (BioShop Canada CUS803) dissolved in ddH_2O.

All plasmids were grown in, and harvested from, *E. coli* strain DH5α.

4.4.2 Plasmid construction and genomic integration

The *CRP1* gene was kindly donated by D. Kornitzer on plasmid KB806, described in [198]. In our construct *CRP1* is fused to a yeast codon optimized *EGFP* gene [34], followed by a transcription terminator, *CYC*. The *EGFP-CYC* fusion was obtained from plasmid pLAREG, earlier created at the McMillen lab by Mazumder and McMillen [118]. To prepare a plasmid for integration into the yeast genome we used a pRS405 based vector backbone[7], with a *CUP1* promoter already present. The backbone was generated from plasmid pRS5-pCUP1-ClpP (in the McMillen plasmid collection when I joined the lab[8]). The donor plasmids and the parts used in our construct are shown in Fig. 4.6.

[6] YPH500 is based on YNN216, which is congenic with S288C.

[7] pRS405 is structurally similar to pRS305 (see Addendum in [165]), which was developed by Sikorski and Hieter for use in YPH500 [165].

[8] Accurate origin will be tracked down before this work is published in a journal.

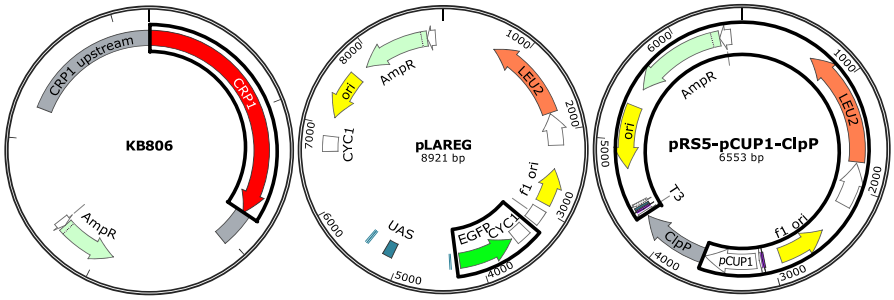

Figure 4.6: Parts used in our constructs, outlined, were copied by PCR from these donor plasmids. KB806 was donated by D. Kornitzer. pLAREG was created at the McMillen lab [118]. pRS5-pCUP1-ClpP is of unknown origin.

Plasmids were harvested from *E.coli* and purified by using a QIAprep Spin Miniprep Kit from QIAGEN. DNA fragments of the different parts, *CRP1* from KB806, *EGFP-CYC* from pLAREG, and the pRS5-pCUP1 backbone from pRS5-pCUP1-ClpP, were amplified from purified plasmids by PCR. NEB Q5 High-Fidelity 2X Master Mix, product number M0492, was used for PCR reactions. We used extended primers with overhang; the overhang creates homology needed for Gibson Assembly [60]. Egfp is fused to Crp1p by removing the stop codon of *CRP1* and inserting a glycine linker (GGTGGTGGT), creating a fused *CRP1-EGFP* gene. The primer design and the target plasmid, named pRS5-pCUP1-CRP1-EGFP, are shown in Fig. 4.7. The primer sequences are listed in Table 4.1.

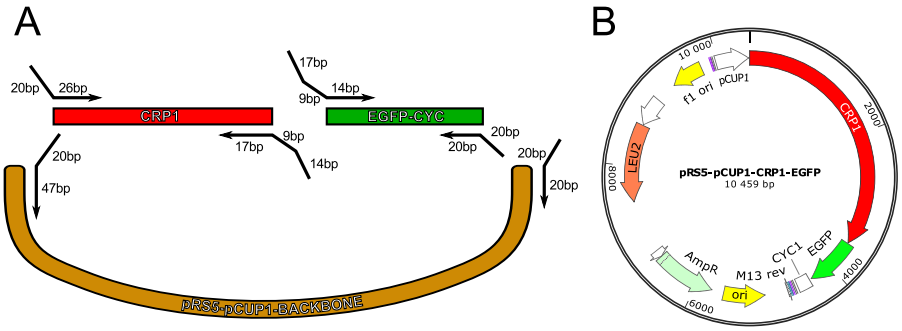

Figure 4.7: **A.** Primer design for PCR of fragments for use in Gibson Assembly. The primers have added tails to create regions of overlapping DNA of about 40 bp. The reverse *CRP1* primer and the forward *EGFP-CYC* primers exclude the *CRP1* stop codon and adds a glycine linker. The primers are listed in Table 4.1. **B.** Target plasmid, pRS5-pCUP1-CRP1-EGFP, created by Gibson Assembly of the fragments in **A**.

Name	Sequence
P_CRP_F	CATAAATCCGGACGACAGAC ATGCAGAAATTTATCATTAATTTTGC
P_CRP_R	TCACCTTTAGACAT ACCACCACC TACTTCGTTTGGTGAAA
P_EGFP_F	TTTCACCAAACGAAGTA GGTGGTGGT ATGTCTAAAGGTGA
P_EGFP_R	GCTCCACCGCGGTGGCGGCC ATCCGCTCTAACCGAAAAGG
P_BB_F	CCTTTTCGGTTAGAGCGGAT GGCCGCCACCGCGGTGGAGC
P_BB_F	TTAATGATAAATTTCTGCAT- GTCTGTCGTCCGGATTTATGTGATGATTGATTGATTGATTGTACAGT

Table 4.1: Primers used to create DNA fragments for use in Gibson Assembly. F and R denotes forward and reverse primers. Sequence overlap is color coded, red is *CRP1*, green is *EGFP-CYC*, and brown is the vector backbone. Spaces are used to improve readability.

All fragments (PCR-products) were confirmed by gel electrophoresis. PCR-products showing only one band of correct size were directly purified using a QIAquick PCR Purification Kit from QIAGEN. PCR-products showing multiple bands were separated by gel electrophoresis, extracted, and purified using a QIAquick Gel Extraction Kit from QIAGEN. The purified fragments were glued together by Gibson Assembly [60] using a Gibson Assembly Master Mix from NEB, product number E2611. Gibson products were treated by DpnI, NEB product number R0176, to destroy any viable background plasmids.

The DpnI treated Gibson product was transformed into *E. coli* by electroporation, and transformed bacteria were plated on LB-AMP plates and incubated at 37°C overnight. Only a single colony was detected on the plate the following day. Colony PCR with primers in backbone and EGFP revealed that a promising construct was present. Plasmids from this colony were then harvested and purified. Restriction digest, PCR, and sequencing were used to confirm that the construct was the correct target plasmid, pRS5-pCUP1-CRP1-EGFP[9].

[9]We experienced some difficulties with getting the Gibson Assembly to work, and when it worked it had a very low yield. We have hypothesized that the relative short regions of overlap compared to the overall size of the construct may have been an issue; this hypothesis is based on experience later gained from other projects using the same Gibson kit. Another issue may have been that the concentration of our fragments was in the lower region of what is suggested in the kit protocol. Nevertheless, we finally ended up with the correct construct.

Transformation into yeast was done using a transformation kit from G-Biosciences (Fast Yeast Transformation, product number GZ-1). Transformation competent yeast cells were prepared according to the protocol provided by the kit. pRS5-pCUP1-CRP1-EGFP is an integrative plasmid in yeast (YIp). We linearized the plasmid with BstEII, NEB product number R0162, prior to transformation; BstEII cuts the plasmid in the *LEU2* gene. Linearization facilitates homologous recombination into the nonfunctional *leu2-Δ1* allele of YPH500 [47, 165]. Recombination results in a functional *LEU2* gene, which is used for selection. Transformation was done by adding a total of 1.8 µg of linearized plasmid (in 5 µl) to 50 µl of component cells prepared according to kit protocol[10] and appropriate amount of reagents from the transformation kit. After having been incubated at 30°C for 90 min the transformed yeast cells were spread on a selective SC-Leu agar plate. The plate was then incubated at 30°C for one week, after which around 100 colonies of transformants had grown to colony sizes approximately equal to this dot: •.

4.4.3 Growth and fluorescence experiments

Measurements of optical density (OD_{600}) were done on a Spectronic 200 spectrophotometer from Thermo Scientific; each sample of cell culture was compared to a blank sample of the medium used in the culture.

Experiments comparing growth in Cu^{2+} of transformed and untransformed yeast cells were done in 24 well plates (Corning Costar 3526). Wells were seeded from cultures grown in appropriate media (SC-Leu and SC) without added copper. The equivalent of 200 µl of a culture with an OD_{600} of 0.9 was seeded to each well, and medium with the appropriate amount of Cu^{2+} was added to a total volume of 1.4 ml. One row of wells containing only media with appropriate amounts of Cu^{2+} was added to each well plate as a reference, and used for blanking. Cells were grown at 30°C with orbital shaking. Growth was measured at different intervals (see results) by taking a 12 µl sample of each well. Samples were added to disposable hemocytometers (InCyto C-Chip), which were digitally photographed by microscopy. This allowed us to sample all wells in short time. Cells were later manually counted from the hemocytometer images.

[10] Equivalent to 0.5 ml of liquid cell culture in log-phase (exponential) growth. Culture used was in log-phase growth with an optical density of 1.4 (OD_{600}), measured on a Spectronic 200 spectrophotometer from Thermo Scientific.

Relative fluorescence was measured directly from each well in a plate reader (Tecan Infinite M1000 Pro, excitation wavelength at 488 nm and emission wavelength at 509 nm). Fluorescence of corresponding wells with only medium was substracted from the measured values. Furthermore, all fluorescence values were normalized by hemocytometer cell counts. We experienced that our yeast cells had a tendency to settle at the bottom of the wells. Therefore, wells were thoroughly mixed by vigorously pipetting up and down before measuring fluorescence.

4.5 Experimental results and discussion

Note that the following results are preliminary and still unpublished. Experiments will be redone with replicates before final publication.

4.5.1 Confirmation of inserted construct

Growth of transformants on SC-Leu show that the *LEU2* gene is functional. To verify genomic integration and function of the whole construct we picked 9 colonies from the selective plate and cultured them in liquid SC-Leu media. Seven of these cultures exhibited green fluorescence after induction with 1 mM Cu^{2+}, confirming the production of the fusion protein Crp1p-Egfp in response to copper. We selected one colony to continue with as our transformed YPH500-pCUP1-CRP1-EGFP. For this colony we confirmed the genomic integration of pCUP1-CRP1-EGFP by genomic PCR and sequencing.

4.5.2 Copper resistance

S. cerevisiae is fairly resistant to copper, and is able to grow in synthetic media with copper concentrations up to 1 mM Cu^{2+}, albeit at a lower than normal growth rate. Fig. 4.8A shows measured growth (cell counts) for untransformed yeast.

Growth is markedly affected in higher copper concentrations with a concentration of 1 mM inhibiting growth by around 65%, Fig. 4.8B. These results fit well with earlier reports of a mean 50% inhibitory concentration of Cu^{2+} at 740 µM for *S. cerevisiae* strain SY1699 in synthetic medium [144].

The transformed YPH500-pCUP1-CRP1-EGFP shows significantly higher resistance to copper. It is able to grow in almost twice the concentration

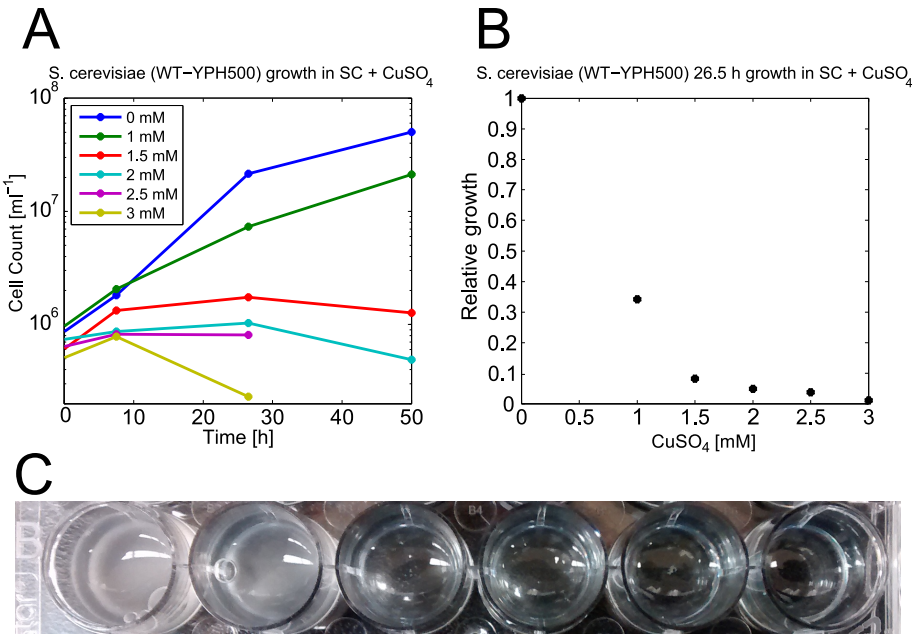

Figure 4.8: **A.** Growth of *S. cerevisiae* YPH500 in synthetic complete media with different concentrations of Cu^{2+} ($CuSO_4$). Amount of cells per ml is estimated from hemocytometer counts, notice the logarithmic y-axis. Counts include all cells; dead cells may have been counted as no staining was used. **B.** Growth inhibition by copper as fraction of normal growth without added copper, based on cell counts after 26.5 hours of growth. **C.** Image of well plate showing the difference in growth after 26.5 hours, concentration of Cu^{2+} from left to right: 0, 1, 1.5, 2, 2.5, 3 mM.

of copper as the untransformed yeast. Fig. 4.9 shows the number of cell doublings over 50 hours for both untransformed and transformed yeast. These results indicate that the added outflow controller works as expected. It is able to maintain nontoxic levels of cytoplasmic copper, and extends the homeostatic range towards external copper.

Looking closer at the results shown in Fig. 4.9, we see that the transformed yeast has normal growth rate in 1 mM Cu^{2+}, with a small, but probably unimportant increase compared to without added Cu^{2+}. The untransformed yeast on the other hand shows a more significant reduction of cell doublings from 5.9 to 4.4, corresponding to a growth reduction to 35% of normal growth. The growth of the transformed yeast is affected and reduced at 1.5 mM Cu^{2+}. This suggests that the range where internal copper is kept within homeostatic limits is extended to somewhere between 1 and 1.5 mM

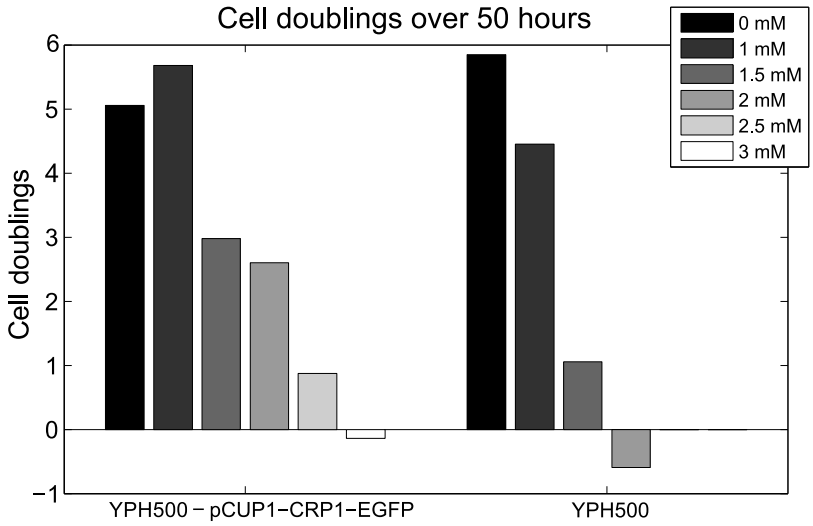

Figure 4.9: Growth after 50 hours shown as number of cell doublings for transformed YPH500-pCUP1-CRP1-EGFP (left) and untransformed YPH500 (right). Gray levels correspond to different concentrations of Cu^{2+}, see legend, black is 0 mM and white is 3 mM. Number of doublings are based on cell counts from hemocytometers. Negative values indicates fewer cells after 50 hours than at the start of the experiment.

in the transformed yeast. The reduced growth at higher concentrations may indicate that the controller at this point is saturated and in its region of breakdown, refer to sections 2.5 and 2.6. It is however not entirely clear that this is the case, because reduced growth may also be caused by the energetic needs of producing and running the pump. After all, the cell uses ATP to pump Cu^{+} out.

We wondered what would happen over a longer time period; would cultures grown with different concentration of Cu^{2+} eventually reach the same saturated growth? Fig. 4.10 shows both yeast-types after 1 week of incubation. We do not have cell counts, but the transformed YPH500-pCUP1-CRP1-EGFP shows visual growth at all copper concentrations, including the highest of 3 mM. Visual growth is only seen up to 1.5 mM for the untransformed yeast.

The clumpy, flocculating-like, behavior of the transformed yeast at higher copper concentrations seen in Fig. 4.10 was typical, and was observed in several experiments. We do not know exactly why this happens, but speculate that it is an environmental response. Although the transformed yeast grows at high copper concentrations, it grows significantly slower

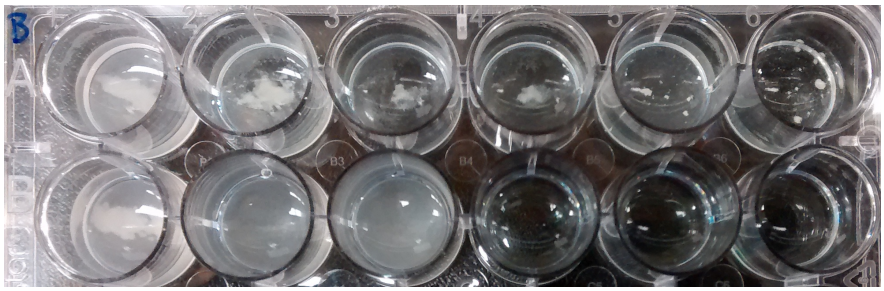

Figure 4.10: Saturated growth after 7 days. YPH500-pCUP1-CRP1-EGFP in top row and untransformed YPH500 in bottom row. Concentration of Cu^{2+} from left to right: 0, 1, 1.5, 2, 2.5, 3 mM.

than normal. Cellular responses may therefore be focused more strongly towards survival than growth.

4.5.3 Controller response

The relative amount of Crp1p can be measured by fluorescence from the Crp1p-Egfp fusion. Fig. 4.11 shows the relative fluorescence (light emission) from cells measured after 7.5 hours and 50 hours. Fluorescence of transformed cells growing without added copper is around the same as the basal level of autofluorescence measured from untransformed cells, showing that very little Crp1p-Egfp is produced. This fits with our expectations, indicating that the outflow controller is only active when needed. The results in Fig. 4.11 also show that the fluorescence of the transformed cells is stronger at higher concentrations of copper, showing that the amount of Crp1p increases with copper concentration.

It is also interesting to see how the fluorescence changes with time after copper is added to the growth medium, which can be used as an estimate of production and insertion of Crp1p into the membrane. Fluorescence microscopy shows that detectable amounts of Crp1-Egfp fusion is produced over a couple of hours, Fig. 4.12. The fusion protein is primarily located in the plasma membrane. For cells grown in copper for longer periods we typically observed an additional spotty glow, indicating some sort of clustering or compartmentalization of the fusion protein.

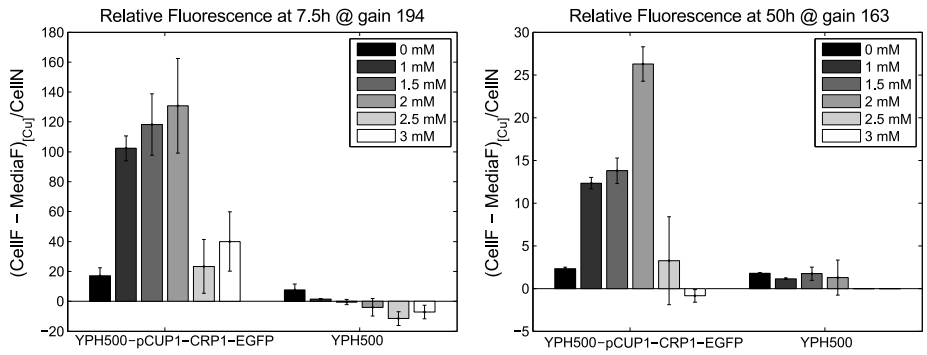

Figure 4.11: Normalized relative fluorescence measured from yeast cells grown at different concentrations of Cu^{2+}. Measurements taken after 7.5 hours (left) and 50 hours (right) of growth. The plate reader is set to take 4 fluorescence measurements of each well, errorbars represent standard deviation of these measurements. Notice that detector gain is set automatically by the plate reader to ensure good dynamic range in the measurements. The fluorescence at 7.5 h and 50 h can because of this not be compared directly, as the relationship between sensitivity and gain in the plate reader is nonlinear.

4.6 Further directions

Our preliminary results clearly show that the outflow controller is working, and that it extends copper homeostasis in *S. cerevisiae*. Nevertheless, we feel that more work is needed before this work is ready for publication in a journal. We want to repeat the experiments done so far with several replicates. This will give us an indication of reproducibility and robustness against cell variance. There is also room to improve our experimental protocols to reduce experimental variability.

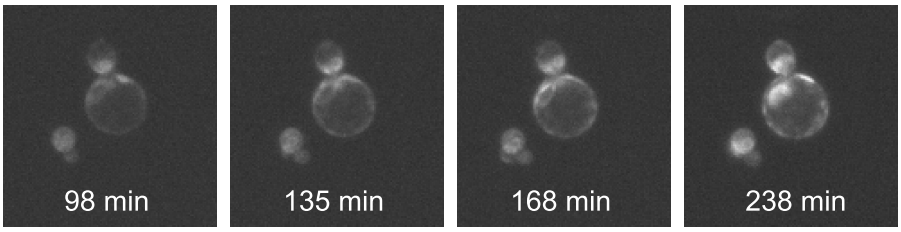

Figure 4.12: Microscope epifluorescence images taken of transformed yeast cells growing in medium with 1.5 mM Cu^{2+}. Time-stamp indicates time after copper was added to medium. All images are taken with the same microscope settings.

We would also like to do further experiments on how the controller responds when copper is added to the medium. One way to do this is to make more detailed series of images from fluorescence microscopy, like the ones shown in Fig. 4.12. In particular, we would like to test how cells already growing in a certain concentration of copper react to further addition of copper, and also how they react to complete removal of copper from the medium. Data from such experiments can tell us whether the controller acts as expected from theory.

Furthermore, there are two remaining major goals in this project that will be discussed in the two following sections.

4.6.1 Concentration of internal copper and integral action

The controlled variable of the added outflow controller is the intracellular concentration of copper. Our experiments have so far only shown extended homeostasis of this variable indirectly, i.e., a regulation of internal copper is implied by the observation that the transformed cells have a higher resistance towards external copper. We have not done or designed experiments that show the actual intracellular level of copper.

One challenge in measuring internal copper is whether to measure total copper content or free cytoplasmic copper. The first is definitely doable; total copper content can be measured in harvested yeast cells by chemical methods, for example by elemental analysis [144]. One issue with measuring total copper is that such measurements cannot be done in vivo.

On the other hand, measuring free intracellular copper is not straightforward. The total copper concentration in *S. cerevisiae* can be as high as 10-100 µM, but virtually all of this is bound to proteins and ligands [189]. It has been estimated that the concentration of free intracellular copper is so low that there in practice is not even a single free (unbound) copper ion in the cytoplasm [144]. Copper is primarily bound to Cup1p metallothioneins, and is only available to be transferred to other high affinity binding sites. A possible in vivo copper sensor must therefore have a very high affinity to compete for copper in the cytoplasm. The picomolar affinity for Cu^+ that can be achieved by some synthetic small molecule sensors [43] is insufficient [188]. More promising is the work on genetically encoded reporters by Wegner et. al [188]; they inserted a high affinity copper binding site from Amt1p of the yeast *Candida glabrata* [188], the homolog of Cup2p from *S. cerevisiae*, between two fluorescent proteins that

are fluorescence resonance energy transfer (FRET) pairs. This causes the emitted fluorescence from the two proteins to differ depending on whether copper ions are bound to the site or not. Since Amt1p is used to activate the promoter of copper defending metallothioneins, its binding site is strong enough to sense free copper. The same group have also used the technique to create a copper sensor with a Cup2p binding site in a YFP[11] protein [107]. The actual change in fluorescence caused by a copper ion binding to the site is however very low, only a 16% change in peak ratios for the FRET [188] and only around 30% for the YFP [107]. It can therefore be difficult to get good measurements. These sensors have also so far only been used in human cells. With these difficulties in mind, we feel that there are more important experiments to consider before we look into in vivo measurements of free intracellular copper.

The primary goal of measuring internal copper, either total or free, is to examine whether or not the internal concentration remains more or less constant for a range of different external concentrations. A near constant level of internal copper would show that the outflow controller provides robust perfect adaptation, and as a consequence also show that the outflow controller has integral action, see section 1.2. Showing that this is the case would provide proof of a successful implementation of an integral controller in synthetic biology.

An alternative way to show that Crp1p has integral action is to examine the kinetics of its synthesis and removal. Future work should therefore also include experiments designed to look into these kinetics.

4.6.2 Controller tuning

This work can also be extended in a different direction by investigating the tunability of the added outflow controller. A relevant question is: Can we tune the controller so that a specified concentration of external copper will cause a certain fractional reduction in cell growth? One way to tune the controller is to adjust the strength of the *CUP1* promoter by mutating it [176]; a change in promoter strength will, in theory, result in a change in the setpoint of the controller. How this affects growth rate in practice remains to be elucidated.

[11] Yellow Fluorescent Protein.

Chapter 5

Linking homeostasis and oscillatory behavior (paper 2 and 5)

Oscillatory systems, so-called *oscillators*, are common in biology [18, 62, 132, 180]. Examples are seen in circadian rhythms [121, 135], metabolism [21, 38, 161], and signaling systems [17, 85, 129]. With oscillation being prevalent one may ask how, if at all, they are related to homeostatic systems. This is in essence what is done in Paper 2 and Paper 5.

The work in this part of the thesis first shows how the controller motifs from Paper 1 and Paper 3 can be modified into oscillatory system. These systems are then shown to have regulatory properties in the sense that they, in spite of external disturbances, maintain the average value in the controlled species. Furthermore this part also shows how controller motifs may be added to achieve robustness in an oscillator's frequency.

The two main types of oscillators that show sustained oscillations are conservative systems, which may be linear or nonlinear, and nonconservative *self-oscillating* systems, which are always nonlinear [5]. This thesis will deal with oscillatory systems that are characterized by that the motions of its variables are periodic, i.e., that they in *phase space* make out a closed path[1]. Phase space is formed by the state variables; a set of values $A(t_1) = A_1$ and $E(t_1) = E_1$ make out a point with coordinates (A_1, E_1). Fig. 5.1 shows the oscillations in both time and phase space for two different oscillatory systems. Panel A shows a conservative system, and panel B shows a self-oscillating system. Both systems have closed paths in phase

[1]Some systems of dimension 3 or higher may have motions in phase space that are bounded, but which never settle at a fixed point or a closed orbit. Such *chaotic* systems may show irregular, aperiodic, oscillations that never repeats exactly [173].

space, but their appearance is different; the distinction will be made clear in the following sections.

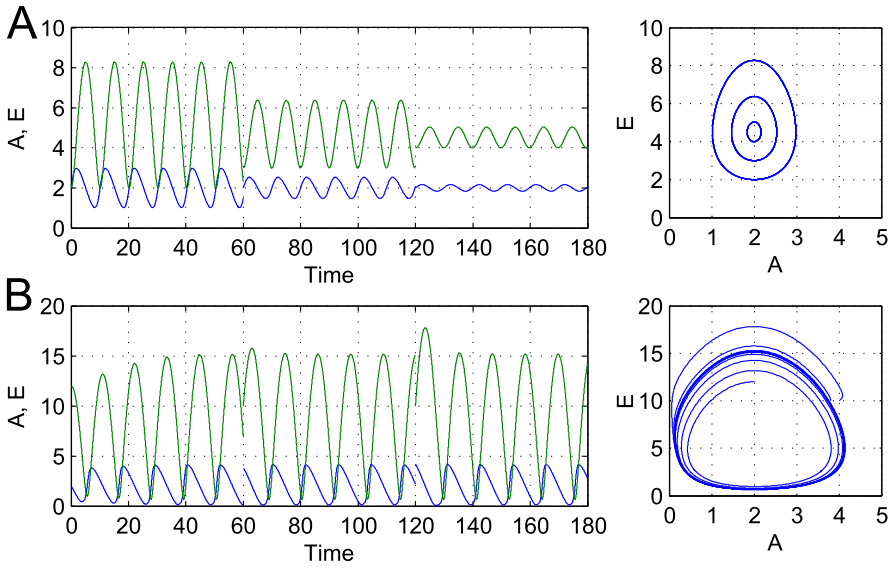

Figure 5.1: Conservative oscillator (**A**) and self-oscillating nonconservative oscillator (**B**). State variables, A (blue) and E (green), are shown in time (left) and phase space (right). The two systems are given new initial conditions at time 0, 60 and 120.

All of the two component controller motifs in Fig. 2.1 can, with some modification, show oscillations.

5.1 Conservative oscillators

The most primitive oscillations that can be generated with the controller motifs are of the conservative type. A necessary attribute of a conservative system is, as defined in [5], the existence of a single valued integral on the form,

$$F(u, v) = C \tag{5.1}$$

where u and v are the state variables, i.e., the coordinates in phase space (u and v are in our case A and E). C is a third coordinate measured along the normal to the phase surface. A closed curve in phase space has the property that the value of C is constant, $C = C_0$, along the curve. Furthermore, conservative systems are characterized by that there cannot exist just one

isolated closed path in phase space, but a continuum of such curves, as seen in Fig. 5.1A. If there is a closed path for $C = C_0$, then there are also neighboring closed curves for neighboring values of C [5].

Furthermore, the oscillations of a conservative system have amplitudes determined by initial conditions, see Fig. 5.1A. This follows from the multiple possible closed paths in phase space.

Many of the conservative systems considered in this thesis can be described by Hamilton-Jacobi type differential equations,

$$\dot{A} = -\frac{\partial H}{\partial E} \qquad \dot{E} = \frac{\partial H}{\partial A} \tag{5.2}$$

where the role of F in Eq. 5.1 is replaced by an H-function, also known as an energy or Hamiltonian function[2].

The following two requirements are needed to get conservative oscillations for any motif from Fig. 2.1: 1, Integral control must be implemented in the rate equation for E, either by perfect zero-order degradation (section 2.3) or by autocatalytic formation and first-order degradation (section 2.10). 2, Integral control of E must likewise be implemented in the rate equation for A, either by zero-order degradation of A, with respect to A, or autocatalytic formation and first-order degradation[3]. When conditions 1 and 2 are fulfilled, we should be able to find a function that satisfies Eq. 5.1. This function may in some cases be H-function that conforms to Eq. 5.2 constructed as:

$$H = -\int \dot{A}\, dE + \int \dot{E}\, dA \tag{5.3}$$

5.1.1 Controller motif 2 and Goodwin's oscillator

I will here use controller motif 2 with zero-order removal of A and E as an example, and illustrate how it can behave as a conservative oscillator. The conservative variant of controller motif 2, shown in Fig. 5.2, is realized when there is zero-order removal[4] of both A and E.

[2]Conservative systems can be further generalized by Pfaff's equations, see [5 p. 131].

[3]I.e., a conservative system is created by having two integrators and no damping.

[4]The zero-order removal is, modeled with very low, but nonzero K_M value, as explained in section 2.9. The oscillators are thus strictly speaking not conservative systems. A conservative system is an idealized type of system. The definition requires that the H-value, often interpreted as the total energy, remains constant for all time. Although oscillations in systems with very low K_M will eventually die out, this happens so slow that the system can be analyzed as a conservative system.

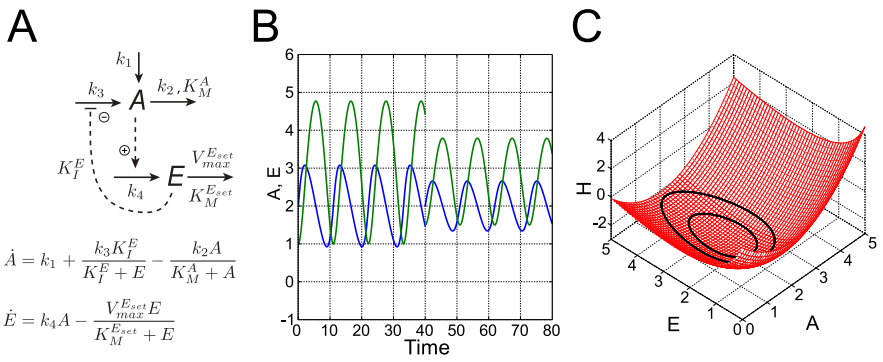

Figure 5.2: A. Inflow controller motif 2. This motif behaves as a conservative oscillator when both species are removed by zero-order kinetics. **B.** Conservative oscillations shown in time. At time $t = 40$ A (blue) and E (green) are abruptly changed to new values (new initial conditions). This gives rise to a different amplitude in the oscillations. **C.** Phase-space paths for the oscillations in panel B plotted together with the H-function from Eq. 5.7. Parameters used: $k_1 = 0$, $k_2 = 1$, $k_3 = 6$, $k_4 = 1$, $K_M^A = 10^{-6}$, $K_M^{E_{set}} = 10^{-6}$, $V_{max}^{E_{set}} = 2$, $K_I^E = 0.5$; initial conditions (2,1) and (2,1.5).

Perfect zero-order means setting $K_M^{E_{set}}$ and K_M^A to zero; the motif equations can then be written as.

$$\dot{A} = k_1 + \frac{k_3 K_I^E}{K_I^E + E} - k_2 \tag{5.4}$$

$$\dot{E} = k_4 A - V_{max}^{E_{set}} \tag{5.5}$$

In the following we assume that $k_1 = 0$ (alternatively that k_1 and k_2 are combined into a new k_2 constant). The H-function is, as in Eq. 5.3, constructed by integrating $\dot{A}$ and $\dot{E}$,

$$H = -\int \left(\frac{k_3 K_I^E}{K_I^E + E} - k_2 \right) dE + \int \left(k_4 A - V_{max}^{E_{set}} \right) dA \tag{5.6}$$

which leads to the final expression for H:

$$H = k_2 E - k_3 K_I^E \ln\left(K_I^E + E\right) + \frac{1}{2} k_4 A^2 - V_{max}^{E_{set}} A \tag{5.7}$$

This function is shown in Fig. 5.2C together with H-values calculated for the oscillations in A and E.

The conservative version of motif 2 bears close resemblance with Goodwin's oscillator. In the literature the Goodwin oscillator comes in two

versions, one conservative version with two components from 1963 [63] and one version with three components from 1965 [64]. Goodwin's two component oscillator is described by the following equations (Eq. 14 in [63]),

$$\frac{dX_i}{dt} = \frac{a_i}{A_i + k_i Y_i} - b_i \tag{5.8}$$

$$\frac{dY_i}{dt} = \alpha_i X_i - \beta_i \tag{5.9}$$

which is structurally similar to Eqs. 5.4 and 5.5. Goodwin later expanded this oscillator to a three component version, with first-order removal of the individual components instead of zero-order[5].

Conservative oscillators can in the same way be constructed for all the eight basic motifs from Fig. 2.1. This can be done both with zero-order removal, or with autocatalytic formation and first-order degradation. Paper 5 shows the construction for controller motif 5 in addition to motif 2. The construction of a H-functions is shown for all four combinations of zero-order removal and first-order removal with autocatalytic synthesis in the supporting material of Paper 5.

5.1.2 Controller motif 5 and the Lotka-Volterra oscillator

The Lotka-Volterra oscillator is arguably one of the best known oscillators in biology. It was formulated independently by Lotka and Volterra [19, 111, 112, 182], and have been the subject of many studies especially within chemical oscillator theory [75, 112] and predator-prey interactions [19, 111]. The Lotka-Volterra oscillator is described by the following equations:

$$\dot{A} = k_1 A - k_3 AE \tag{5.10}$$

$$\dot{E} = k_6 AE - k_8 E \tag{5.11}$$

where A and E are two interacting species, either in the chemical or ecological sense. The Lotka-Volterra oscillator can be viewed as having an outflow controller 5 structure relative to A, Fig. 5.3A, with autocatalysis

[5] A reason for doing so was the fact that only the slightest deviation from perfect zero-order removal breaks the conservativeness of the system. See also section 2.9, and the previous footnote. Goodwin's three component system is an oscillator of the self-oscillating type [64]. Later analysis proved, however, that the three component system is only an oscillator for a very restricted parameter space; it requires cooperativity larger than 8 in the inhibition of the synthesis of A/X_i [66].

and first-order removal in both A and E[6]. This setup has perfect integral control of both A and E. The Lotka-Volterra oscillator is in this way similar to the Goodwin oscillator described in the previous section in that they both consists of two interconnected perfect integrators. Fig. 5.3B shows that different initial conditions gives rise to oscillations with different amplitudes, indicating that the Lotka-Volterra oscillator is conservative.

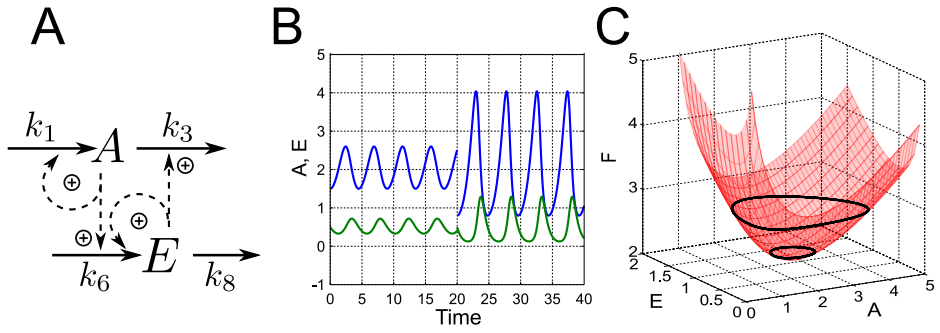

Figure 5.3: A. Inflow controller 5 with autocatalysis and first-order degradation in both A and E. **B.** Conservative oscillations shown in time. At time $t = 20$ A (blue) and E (green) are abruptly changed to new values (new initial conditions). This gives rise to oscillations of different form and amplitude. **C.** Phase-space paths for the oscillations in panel B plotted together with the F-function from Eq. 5.15. Parameters used: $k_1 = 1$, $k_3 = 2$, $k_6 = 1$, and $k_8 = 2$; initial conditions (1.5,0.5) and (0.8,0.5).

We will now show that there exists a function F that satisfies Eq. 5.1. Consider first the transformed system defined by the transformation $\alpha = \ln(A)$, $\varepsilon = \ln(E)$ (valid for all A, $E > 0$).

$$\dot{\alpha} = k_1 - k_3 e^{\varepsilon} \tag{5.12}$$

$$\dot{\varepsilon} = k_6 e^{\alpha} - k_8 \tag{5.13}$$

The H-function of this system, satisfying Eqs. 5.2 and 5.3, is:

$$H(\alpha, \varepsilon) = -k_1\varepsilon + k_3 e^{\varepsilon} + k_6 e^{\alpha} - k_8\alpha \tag{5.14}$$

Replacing α and ε with A and E gives,

$$F(A, E) = -k_1 \ln(E) + k_3 E + k_6 A - k_8 \ln(A) \tag{5.15}$$

which is plotted in Fig. 5.3C, together with the F-values calculated for the oscillations in A and E. The value of F is constant along every closed

[6]It can also be alternatively interpreted as having the structure of inflow controller 1 by interchanging Eqs. 5.10 and 5.11, shown in Fig. 6b in Paper 2.

path created by different initial conditions, Fig. 5.3C. This can be proven analytically by taking the total derivative of F with respect to time.

$$\frac{dF}{dt} = \frac{\partial F}{\partial A}\dot{A} + \frac{\partial F}{\partial A}\dot{E} \tag{5.16}$$

$$= \left(k_6 - \frac{k_8}{A}\right)(k_1 A - k_3 AE) + \left(k_3 - \frac{k_1}{E}\right)(k_6 AE - k_8 E) \tag{5.17}$$

$$= k_1 k_6 A - k_3 k_6 AE - k_1 k_8 + k_3 k_8 E + k_3 k_6 AE - k_3 k_8 E - k_1 k_6 A + k_1 k_8 \tag{5.18}$$

$$= 0 \tag{5.19}$$

Thus the value of F is constant along paths in phase space, as required by Eq. 5.1. Although illustrative for our case this proof is nothing new in itself, as the Lotka-Volterra system is a well known conservative oscillator. Notice that although the F function satisfies the requirement of a conservative system in Eq. 5.1, it is not a H-function as defined in Eqs. 5.2–5.3.

The controller motif interpretation of the Lotka-Volterra oscillator is further examined in Paper 2.

5.2 Limit-cycle oscillators

Self-oscillating systems have *limit-cycles* in phase space. Limit cycles may in general be stable or unstable, but we will limit ourself to stable limit cycles. Stable limit-cycles are closed paths that are *attractive*, that is, nearby motions in the phase space are drawn to, and ends up, at this particular closed-path, see Fig. 5.1B. Because of this, oscillations in self-oscillating systems have amplitudes determined by the properties of the system itself, instead of initial conditions [5].

The controller motifs can be extended into self-oscillating oscillators by including an additional intermediate species in the overall feedback loop. In this work the intermediate may either be on the synthesis of A or the synthesis of E. This makes it possible to create three possible variants of motifs 2 and 3, and one variant of motifs 1, 4, 5, and 8; motif 6 and 7 cannot be extended in this way[7]. The possible extended motifs are shown in Fig. 5.4.

[7]Only extra species upstream of A and E are considered, as this setup preserves the feedback loop. A and E are affected by what happens upstream, but are in most cases not affected by what happens downstream. Further extension with downstream species may be done in cases where the amount of downstream species a_d, or e_d, actually affects the rate of conversion from A to a_d, or E to e_d.

Self-oscillating systems are not only stable in the sense that their limit-cycles are attractive, they are also stable in the sense that their oscillatory behavior is preserved for a large range of system parameters compared to conservative system [5]. The self-oscillating systems in Fig. 5.4 does, for example, not require perfect zero-order degradation of A to show sustained oscillations. However, even self-oscillators may become systems that tend to stationary or diverging solutions for some system parameters. All of the extended systems in Fig. 5.4 can, nevertheless, show self-oscillatory behavior for a certain set or range of system parameters.

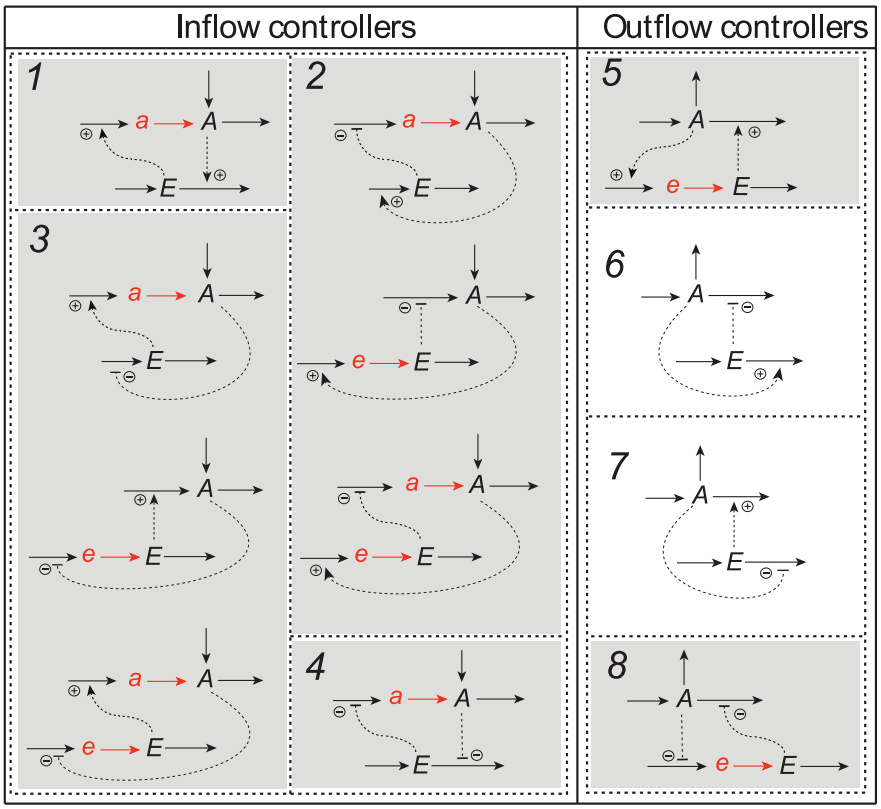

Figure 5.4: Possible realizations of extended controller motifs that may behave as self-oscillators. The motifs are extended by intermediates a and e, but only structures that extend and preserve the feedback loop are considered. For example there is no point in including an intermediate of E in motif 1, as this does not extend the feedback loop.

An underlying condition from the extension scheme is that the outflow of the intermediate species is an inflow of the main species, that is, interme-

diates are converted to the main species. The intermediate species a and e may be considered to be precursors for A and E. Possible interpretations are that a and e may be: protein subunits, unfolded proteins that take some time to fold, or unactive protein that is activated at a certain rate (and cannot, or is not, deactivated back). Another interpretation where the main species don't have to be proteins is that a and e are compartmentalized in a different compartment than A and E. Remark that a and e should not be thought of as mRNA coding for proteins, as more than just one protein can be translated from one individual mRNA.

5.2.1 Extended controller motif 1 with autocatalysis

All the extended motifs in Fig. 5.4 can be implemented with either the ordinary zero-order removal of E or autocatalytic synthesis combined with first-order removal.

Using inflow controller motif 1 with autocatalysis in E as an example the extended system equations are:

$$\dot{a} = k_1 E - k_9 a \tag{5.20}$$

$$\dot{A} = k_9 a + k_p^i - k_p^o A \tag{5.21}$$

$$\dot{E} = k_4 E - k_6 A E \tag{5.22}$$

Fig. 5.5 shows the oscillations in A, E and a and the 3-dimensional limit cycle in phase space. The system ends up at the same limit cycle for different initial conditions. Whether this or any of the extended controller motifs show oscillations or not, depends on the parameter values, explored further in section 5.5.

5.3 Control of concentration during oscillatory conditions

That the controller motifs, with some extensions, can show oscillations is in itself fascinating, nevertheless, it is not the main point of this part of the thesis. More significant is the point that the oscillations, due to the underlying integral action, show homeostatic properties. From the above examples, in Figs. 5.1, 5.2, and 5.5, we notice that oscillations in A oscillates around the same mean value of A. However, that it does so

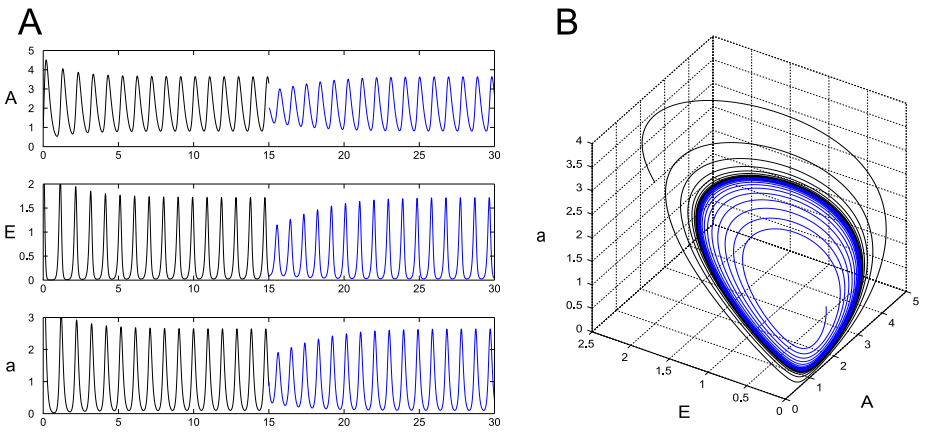

Figure 5.5: Extended controller motif 1 with autocatalysis in E showing self-oscillations. Eqs. 5.20–5.22 with parameter values $k_1 = 20$, $k_4 = 20$, $k_6 = 10$, $k_9 = 10$, $k_p^i = 1$, and $k_p^o = 5$. **A.** Oscillations of A, E, and a plotted against time. Two different sets of initial conditions are used ($A_0 = 1$, $E_0 = 2$, $a_0 = 3$) in black and ($A_0 = 2$, $E_0 = 0.1$, $a_0 = 1$) in blue. **B.** A, E and a plotted in phase space. Both initial conditions approach the same limit cycle.

for different initial conditions may not be surprising, the more important question is what happens when external disturbances are introduced.

Sections 1.2 and 2.3 showed how regulation towards a setpoint is achieved in the controller motifs; the underlying point is that the steady-state condition of $\dot{E}$ provides a unique solution of A. With zero-order removal the equation for $\dot{E}$ has A as its only variable, that is:

$$\dot{E} = h(A) \tag{5.23}$$

The setpoint is then defined by the steady-state condition, i.e., $h(A) = 0$.

This can be extended to oscillatory systems by realizing that all sustained oscillations are periodic motions. For each whole cycle E is back at exactly the same value,

$$E(t + T) = E(t) \tag{5.24}$$

where T is the *period time*, the time of one cycle. We will in the following use the periodic average of a signal defined as:

$$<x> \triangleq \frac{1}{nT} \int_0^{nT} x \, dt \tag{5.25}$$

In this setting the average value is only meaningful for a positive number of whole cycles, nT (n is a positive integer).

Whereas the change in E cannot be assumed to be zero as in the case of nonoscillatory systems, the integrated change in E over one period must be zero.

$$\int_t^{t+T} \dot{E}\, dt = E(t+T) - E(t) = 0 \tag{5.26}$$

From this the periodic average value of $\dot{E}$, denoted $<\dot{E}>$ must also be zero.

$$<\dot{E}> \triangleq \frac{1}{nT} \int_0^{nT} \dot{E}\, dt = 0 \tag{5.27}$$

The rate equation of E for a specific motif can now be inserted into Eq. 5.27. The case of a controller activated by E will be demonstrated by using the expression for $\dot{E}$ from motif 2 and 5. Inserting $\dot{E}$ from Eq. 2.6 into Eq. 5.27 gives:

$$<\dot{E}> = \frac{1}{nT} \int_0^{nT} k_4 A - \frac{V_{max}^{E_{set}} E}{K_M^{E_{set}} + E}\, dt \tag{5.28}$$

$$= k_4 \left(\frac{1}{nT} \int_0^{nT} A\, dt \right) - V_{max}^{E_{set}} \left(\frac{1}{nT} \int_0^{nT} \frac{E}{K_M^{E_{set}} + E}\, dt \right) \tag{5.29}$$

By applying the condition of zero-order, $K_M^{E_{set}} = 0$, this reduces to,

$$<\dot{E}> = k_4 \left(\frac{1}{nT} \int_0^{nT} A\, dt \right) - V_{max}^{E_{set}} \left(\frac{1}{nT} \int_0^{nT} 1\, dt \right) \tag{5.30}$$

$$= k_4 \left(\frac{1}{nT} \int_0^{nT} A\, dt \right) - V_{max}^{E_{set}} \tag{5.31}$$

where the periodic average of A, denoted $<A>$ can be identified. Using this and $<\dot{E}> = 0$ (Eq. 5.27) we find that the controller maintains the periodic average of A at a setpoint.

$$<A> \triangleq \frac{1}{nT} \int_0^{nT} A\, dt = \frac{V_{max}^{E_{set}}}{k_4} = <A>_{set} \tag{5.32}$$

Notice that this derivation of the setpoint also holds for nonoscillatory controller motifs. A system in steady state is a trivial solution of Eq. 5.24.

A similar derivation can be done for controller motifs where A inhibits E, shown in the Supporting Material of Paper 5.

5.3.1 Conservative case with controller motif 2

The reaction kinetic scheme of controller motif 2 is shown in Fig. 5.2A, and given by Eqs. 5.4 and 5.5. In this inflow-type controller, increased outflow disturbances (i.e, increased k_2 values) are compensated by an increase in the compensatory flow.

$$j(E) = k_3 \frac{K_I^E}{K_I^E + E} \tag{5.33}$$

If the average level of $j(E)$ is to increase then the average level of E, $<E>$, has to decrease. In this way the average level of A, $<A>$ is kept at its setpoint at $V_{max}^{E_{set}}/k_4$, see Fig. 5.6.

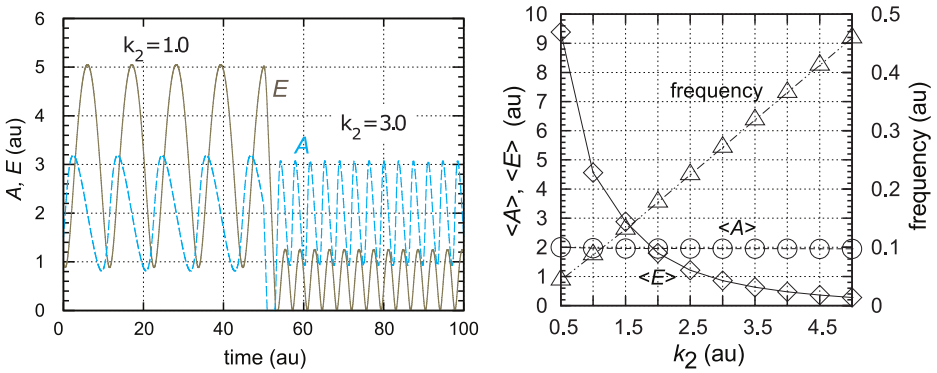

Figure 5.6: Adaptation in periodic average of A, $<A>$, for the conservative version of controller motif 2. Oscillations in A and E when k_2 changes from 1 to 3 is shown in the left panel. $<A>$ is maintained at the same value for a range of different disturbance strengths, right panel. $<E>$ decreases with increasing disturbance strength. The frequency of the oscillations is also calculated, right panel. Motif 2 is given by Eqs.5.4 and 5.5; the parameters used are the same as in Fig. 5.2.

The simulation shows that changing disturbances (when k_2 is changed) affects the controller's frequency as well as the periodic average; the frequency of controller motif 2 seems to increase with increasing disturbance strength in k_2. At high k_2 values, i.e., when the level of $<E>$ becomes lower than K_I^E, the compensatory flow $j(E)$ approaches its maximum value k_3. At this stage the homeostatic capacity of the controller is reached. Any futher increase of k_2 cannot be met by an increased compensatory flow, and will therefore lead to a breakdown of the controller. Controller breakdown and controller accuracies are already discussed in sections 2.5, 2.6, and 2.9. Paper 5 shows a similar example for controller motif 5.

5.3.2 Self-oscillating version of controller motif 5

Maintaining the periodic average of A is also an ability of the self-oscillating controller motifs in Fig. 5.4. The derivation in Eqs. 5.28 to 5.32 holds for the motifs that are extended with only an a intermediate, but becomes somewhat different for motifs extended with an e intermediate. This case will be illustrated here by a self-oscillating version of controller motif 5, see Fig. 5.4. The equations for this motif are:

$$\dot{A} = k_1 - k_2 E \frac{A}{K_M^A + A} - k_3 A \tag{5.34}$$

$$\dot{e} = k_4 A - k_5 e \tag{5.35}$$

$$\dot{E} = k_5 e - \frac{V_{max}^{E_{set}} E}{K_M^{E_{set}} + E} \tag{5.36}$$

As above the equation for $\dot{E}$ is inserted into Eq. 5.27:

$$<\dot{E}> = k_5 \left(\frac{1}{nT} \int_0^{nT} e \, dt \right) - V_{max}^{E_{set}} \left(\frac{1}{nT} \int_0^{nT} \frac{E}{K_M^{E_{set}} + E} \, dt \right) = 0 \tag{5.37}$$

The condition of zero-order and the definition of periodic average, Eq. 5.25 gives,

$$<e> = \frac{V_{max}^{E_{set}}}{k_5} \tag{5.38}$$

where $<e>$ is the periodic average of e. Furthermore, Eq. 5.27 must also hold for $\dot{e}$. Inserting Eq. 5.35,

$$<\dot{e}> = k_4 \left(\frac{1}{nT} \int_0^{nT} A \, dt \right) - k_5 \left(\frac{1}{nT} \int_0^{nT} e, dt \right) = 0 \tag{5.39}$$

and using the definition of periodic average together with the setpoint for $<e>$ found in Eq. 5.38 gives the setpoint for the periodic average of A:

$$<A> = \frac{k_5}{k_4} <e> = \frac{V_{max}^{E_{set}}}{k_4} = <A>_{set} \tag{5.40}$$

Interestingly this periodic average of A is the same as in the case without the e intermediate, as given in Eq. 5.32.

A simulation illustrating how this controller maintains the periodic average of A, $<A>$ in spite changes in the disturbing inflow $d_i(\cdot) = k_1$, is

shown in Fig. 5.7. An increase in k_1 leads to an increase in $<E>$ (Fig. 5.7E), which again leads to an increased outflow of A and homeostasis in $<A>$. The parameter values used in this example are chosen so that they give nice, near sinusoidal, oscillations; this is done to makes it easier to grasp what's going on. The self-oscillating motifs can dependent on rate constants also show more exotic relaxation and pulsative type behavior, and some examples are given in Paper 5.

5.4 Control of frequency by quasi-harmonic kinetics

Looking at the simulation of the self-oscillating version of controller 5 in Fig. 5.7 it seems that the period, T, is conserved in addition to $<A>$. This is obviously not the case for the conservative version of controller motif 2 (Fig. 5.6), and is neither the case for most of the self-oscillatory extended controller motifs in Fig. 5.4.

To understand what occurs in the self-oscillating version of controller 5 (Eqs. 5.34–5.36) consider the case where the dynamics of the intermediate, e, is much faster than the dynamics in A. The differential equation $\dot{e} = f(A, e, k_4, k_5)$ can then be replaced with an algebraic equation relating $e(t)$ to $A(t)$ given by $f = 0$, in this case $e(t) = k_4 A(t)/k_5$. The system behaves very similar to the two component conservative version with the equations:

$$\dot{A} = k_1 - k_2 E \frac{A}{K_M^A + A} \tag{5.41}$$

$$\dot{E} = k_4 A - \frac{V_{max}^{E_{set}} E}{K_M^{E_{set}} + E} \tag{5.42}$$

Replacing the differential equation with an algebraic expression for a component with fast dynamics is called the *quasi-steady-state assumption*[8]. It relies on that the approach to the *nullcline*[9] $f = 0$ in phase space is fast, and that motion along or near the nullcline is slow [55]; i.e., if initial conditions or disturbances move $e(t)$ away from the nullcline, then $\dot{e}$ is large; and once $e(t)$ is near the nullcline, then $\dot{e}$ is small.

[8]The same steady-state assumption that is used in the Briggs-Haldane derivation of the Michaelis–Menten equation.

[9]The nullcline is the set of points that satisfy $f = 0$, for this system (Eqs. 5.34–5.36) the nullcline forms a surface in 3-dimensional phase space.

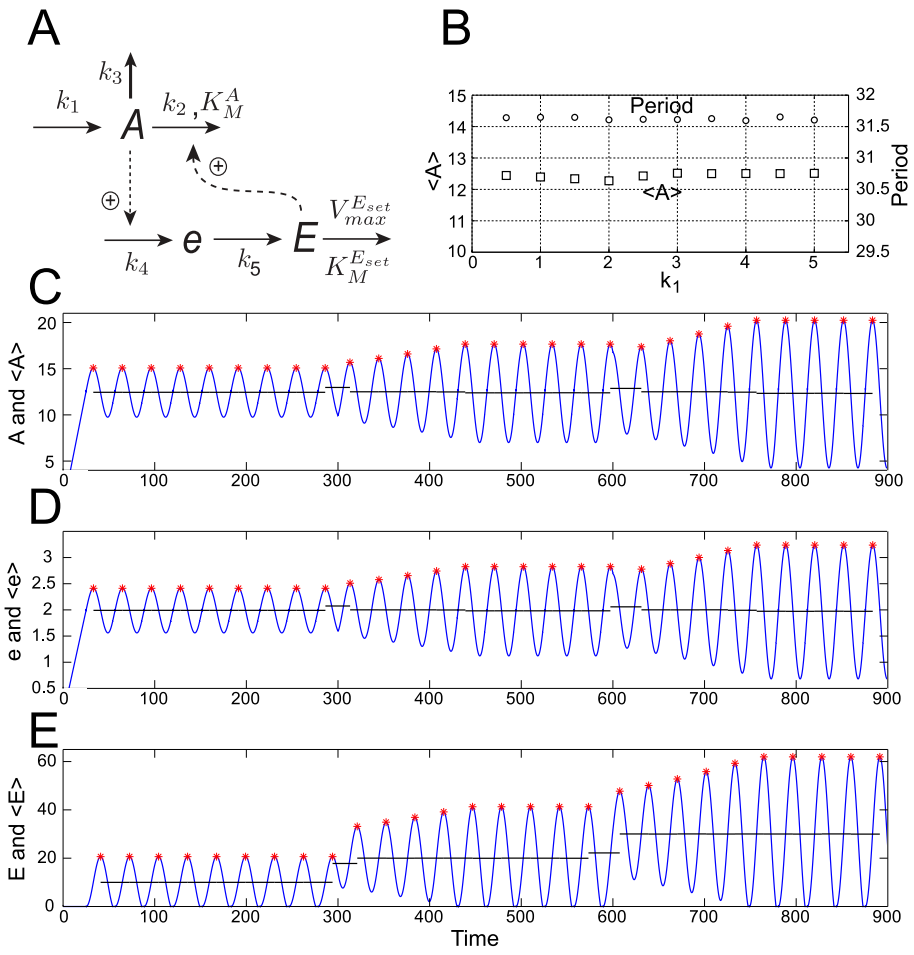

Figure 5.7: A self-oscillating version of controller motif 5 showing adaptation in periodic average of A. System equations in Eqs. 5.34 to 5.36 with parameter values $k_2 = 0.05$, $k_3 = 0$, $k_4 = 0.8$, $k_5 = 5$, $V_{max}^{E_{set}} = 10$, and $K_M^A = K_M^{E_{set}} = 10^{-6}$. **A.** Outflow controller motif 5 extended by an intermediate e. **B.** Homeostatic response in $<A>$ (squares) and period T (circles) with different perturbations in k_1. $<A>$ is kept at the setpoint $<A>_{set} = V_{max}^{E_{set}}/k_4 = 12.5$. **C-E.** Oscillations in A, e, and E shown for three different k_1 values; k_1 starts at 0.5, and is perturbed to 1 at $t = 300$, and to 1.5 at $t = 600$. The period (in panel B) is calculated by taking the time difference between the peaks (in panels C-E) found by the Matlab function *findpeaks*. The periodic average of a system variable (black lines) is calculated for each cycle by integrating the response between two peaks and dividing by the period.

So when does this hold for $\dot{e}$ in the self-oscillating version of controller 5? We will first look at movements on the nullcline. The total time derivative df/dt is zero, i.e.,

$$\frac{df}{dt} = \frac{\partial f}{\partial A}\dot{A} + \frac{\partial f}{\partial e}\dot{e} = 0 \tag{5.43}$$

$$\frac{df}{dt} = k_4\dot{A} - k_5\dot{e} = 0 \tag{5.44}$$

$$\Downarrow$$

$$\dot{e} = \frac{k_4}{k_5}\dot{A} \tag{5.45}$$

if k_4/k_5 is small, then $\dot{e} \approx 0$, and $e(t)$ changes slowly like $A(t)$. Also, once trajectories are near or on the nullcline then changes in $A(t)$ are unlikely to move the trajectory far away from the nullcline, as long as k_4/k_5 is small (Eq. 5.45: $f = \dot{e} \approx 0$).

The next step is to look at movements far from the nullcline, i.e., when $e(t)$ has a value so that $\dot{e}$ is far from 0. This can be done by solving the differential equation for $e(t)$ at some point in time $A(t) = A_0$.

$$\frac{de(t)}{dt} = k_4 A_0 - k_5 e(t) \tag{5.46}$$

A general solution is,

$$e(t) = \frac{k_4 A_0}{k_5}\left[1 - C\mathrm{e}^{-k_5 t}\right] \tag{5.47}$$

where C is a constant, and the time constant $t_e = 1/k_5$ is a measurement of the speed of the movement. For the quasi-steady-state assumption to be valid t_e must be small, i.e., k_5 must be large. Although $A(t)$ may not stay constant at A_0 during the whole movement, Eq. 5.47 is a good estimate of the initial speed of the movement of the trajectory along the e-axis in phase space.

Based on the above, a requirement for the quasi-steady-state assumption for this system is that k_5 is large. The intermediate will in this case, after a transient, always be in a quasi steady state[10].

[10] One could have argued that k_5 must be large from just inspecting the differential equation for e in Eq. 5.35; this was done in Paper 5. I do hope however, that the short analysis above clarified this realization.

In this thesis we term an self-oscillating oscillator's behavior (for a certain set of parameters) *quasi-conservative* if the intermediate compounds (a and e) obeys approximately the quasi-steady-state assumption. These oscillators are still self-oscillating systems, but behave closely to conservative systems.

Moving back to the apparent homeostasis in frequency in the results shown in Fig. 5.7, the conservative version of controller motif 5 is actually the well known linear harmonic oscillator. In the case of zero-order conditions in the removal of A and E, Eqs. 5.41 and 5.42 reduce to:

$$\dot{A} = k_1 - k_2 E \tag{5.48}$$

$$\dot{E} = k_4 A - V_{max}^{E_{set}} \tag{5.49}$$

Taking the second time derivative of Eq. 5.48 and inserting the expression of $\dot{E}$, leads to,

$$\ddot{A} = -k_2 k_4 A + k_2 V_{max}^{E_{set}} \tag{5.50}$$

which can be written as:

$$\frac{\ddot{A}}{k_2 k_4} + A = \frac{v_{max}^{E_{set}}}{k_4} \tag{5.51}$$

This is the equation of a *harmonic oscillator*, which is well known to have a solution on the form [5],

$$A(t) = A_{amp} \sin(\sqrt{k_2 k_4} t + \phi) + \frac{V_{max}^{E_{set}}}{k_4} \tag{5.52}$$

where A_{amp} denotes the amplitude of the oscillations, $\sqrt{k_2 k_4}$ is the angular frequency, and ϕ is a phase angle. The frequency is independent of k_1!

This property is inherited when the self-oscillating version of controller 5 behaves quasi-conservative. The simulation in Fig. 5.7 used $k_2 = 0.05$ and $k_4 = 0.8$ giving a frequency of 0.032, corresponding to a period of 31.4, which is very close to the results in the simulation. Being a self-oscillating system the three component controller motif 5 is a structurally more robust way of achieving frequency homeostasis by near harmonic behavior. The parameter region where the extended controller motif 5 is self-oscillating, and where it shows robust homeostasis in frequency, is examined in the next section.

5.5 Oscillatory regions and quenching of oscillations

Perfect zero-order removal of both A and E, in regard to themself, is a way to obtain conservative oscillations (see section 5.1). A problem with conservative oscillators is that they are structurally unstable; even the tiniest deviation from perfect zero-order removal in A and E will break down the oscillations in a conservative system[11].

The self-oscillating extended controller motifs in Fig. 5.4 are on the other side structurally stable against small deviations away from perfect zero-order removal. Fig. 5.8 shows how deviation from zero-order removal in A affects the oscillatory behavior in the extended controller 5 (see Fig. 5.7A). A smaller K_M^A gives a larger region of oscillatory behavior, but oscillatory behavior exists for some combinations of other parameter values even at higher K_M^A values. A deviation from perfect zero-order removal of A is not the only factor added to the controller in the simulation results shown in Fig. 5.8. The removal of E is not perfect zero-order, with a $K_M^{E_{set}}$ of 0.01, and in addition an uncontrolled first-order removal of A is added by having $k_3 = 0.01$, see Fig. 5.7A.

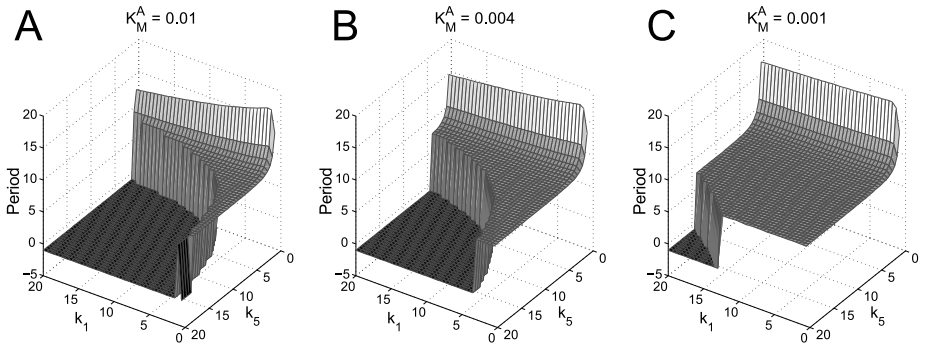

Figure 5.8: Period of oscillations in the extended self-oscillating version of controller 5 (Eqs. 5.34–5.36) for varying k_1 and k_5. The period is set to -1 when there are no oscillations (black area). Panels **A**, **B**, and **C** show the results for different values of K_M^A. The parameter values used are: $k_2 = 0.5$, $k_3 = 0.01$, $k_4 = 0.7$, $V_{max}^{E_{set}} = 0.5$, and $K_M^{E_{set}} = 0.01$.

[11] Note that systems that are very close to being conservative may still be modeled as conservative, at least within a finite timeframe before the oscillations stop.

The results in Fig. 5.8 nicely shows when the motif behaves as an quasi-harmonic oscillator, indicated by when the period surface is flat and above 0. This confirms the analysis in the previous section in that a large k_5 leads to a stable frequency, i.e., a flat surface in Fig. 5.8. Nevertheless, the results also show that an increased k_5 also acts to quench the oscillations. This is the result of moving the behavior of the self-oscillating three component motif too close to the conservative two component variant, which does not oscillate when it is far from perfect zero-order removal of A and E.

As shown above, the self-oscillating motifs can oscillate even when there are uncontrolled first-order type disturbances in the outflow of A. Such disturbances do, however, put a significant restrain on the region of oscillations. First-order removal is equivalent to friction in a mechanic system, which effectively dampens oscillations. Fig. 5.9 shows how an increasing first-order rate constant in uncontrolled removal of A reduces the region of oscillatory behavior.

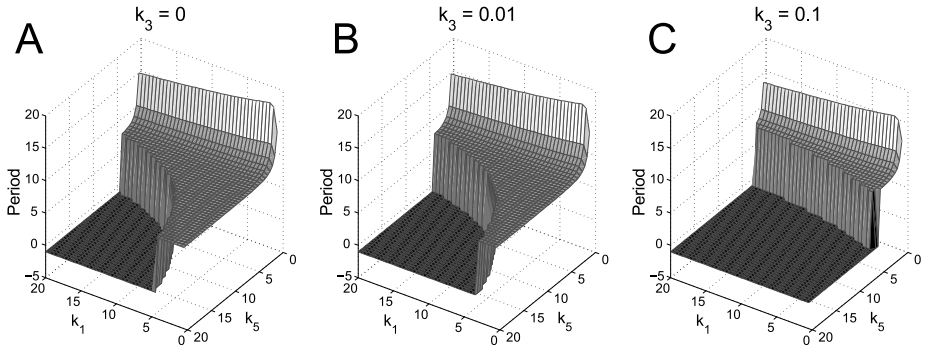

Figure 5.9: Period of oscillations in the extended self-oscillating version of controller 5 (Eqs. 5.34–5.36) for varying k_1 and k_5. The period is set to -1 when there are no oscillations (black area). Panels **A**, **B**, and **C** show the results for different values of k_3 (uncontrolled outflow of A). The parameter values used are: $k_2 = 0.5$, $k_4 = 0.7$, $V_{max}^{E_{set}} = 0.5$, $K_M^A = 0.004$, and $K_M^{E_{set}} = 0.01$.

5.6 Robust control of frequency by control of E

After studying several of the non-quasi-harmonic oscillators we observed that the oscillators in general seem to change frequency when the periodic average of the controller species E changes. (Remember that $<E>$ changes to counter disturbances so that $<A>$ is maintained at its setpoint.). This

realization lead us to hypothesize whether it may be possible to design an oscillator with robust frequency homeostasis by using additional species to control E.

For this purpose, two extra controllers I_1 and I_2 with their own setpoints for $<E>$ are introduced. Fig. 5.10A shows the two extra controllers added to a self-oscillatory version of controller 2. I_1 and I_2 controls the level of E, but do so through A; a necessary arrangement if homeostasis in $<A>$ is to be maintained[12]. The total system is defined by five differential equations:

$$\dot{A} = k_p^i + k_2 a + k_3 I_1 - k_5 I_2 \frac{A}{K_{M2}^A + A} - k_p^o \frac{A}{K_{M1}^A + A} \tag{5.53}$$

$$\dot{a} = k_1 \frac{K_I^E}{K_I^E + E} - k_2 a \tag{5.54}$$

$$\dot{E} = k_6 A - \frac{V_{max}^{E_{set}} E}{K_M^{E_{set}} + E} \tag{5.55}$$

$$\dot{I}_1 = k_8 - k_9 E \frac{I_1}{K_M^{I_1} + I_1} \tag{5.56}$$

$$\dot{I}_2 = k_{10} E - k_{11} \frac{I_2}{K_M^{I_2} + I_2} \tag{5.57}$$

Without the added I-controllers the oscillator changes its frequency when perturbed by disturbances in the uncontrolled inflow and outflow of A, Fig. 5.10C. The frequency is fixed by adding I_1 and I_2, Fig. 5.10D.

The proposed system, see Fig. 5.10A, uses I_1 and I_2 in a combined setup where they function as inflow and outflow controllers, respectively. This type of combination is conceptually the same as discussed in section 2.7, in which several E-controllers where combined. I_1 compensates for increased disturbances in outflow and I_2 compensates for increased disturbances in inflow. The regulatory properties of each controller can be identified by simulating the system with only one controller active. Fig. 5.11 shows the results for the system simulated with I_1 and I_2 disabled; I_2 enabled and I_2 disabled; I_1 disabled and I_2 enabled; and with both controllers enabled. The upper panels (A) shows the response in average level of A and E, and the lower panels (B) shows the response in frequency. The results show robust control of frequency for dominating outflow disturbances (high k_p^o) when only I_1 is active, and contrariwise, robust control of frequency for dominating inflow disturbances (low k_p^i) when only I_2 is active. Robust

[12] I_1 and I_2 may also act on E through both A and a, see Paper 5.

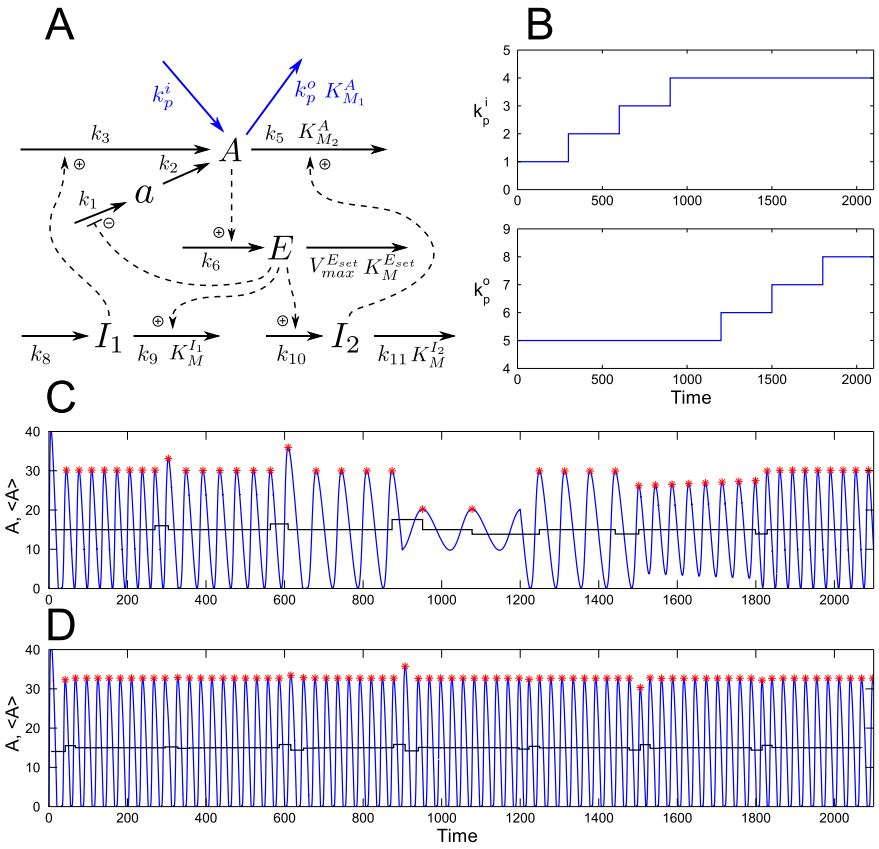

Figure 5.10: Self-oscillating version of controller motif 2 with added I_1 and I_2 controllers for robust control of frequency (Eqs. 5.53–5.57). Parameter values: $k_1 = 20$, $k_2 = 30$, $k_3 = 0.1$, $k_5 = 0.1$, $k_6 = 0.1$, $V_{max}^{E_{set}} = 1.5$, $k_8 = 1$, $k_9 = 0.1$, $k_{10} = 0.1$, $k_{11} = 1$, $K_I^E = 2$, and $K_{M1}^A = K_{M2}^A = K_M^{E_{set}} = K_M^{I_1} = K_M^{I_2} = 0.001$. **A.** Reaction kinetic scheme. **B.** Disturbances are given as changing values of k_p^i and k_p^o. **C.** Simulation of system without I_1 and I_2, by setting $k_3 = k_5 = 0$. Oscillations in A (blue), and periodic average $<A>$ calculated for each cycle (black). **D.** Simulation of system with I_1 and I_2 active.

control of frequency for a wide range of disturbances is achieved when both I-controllers are active.

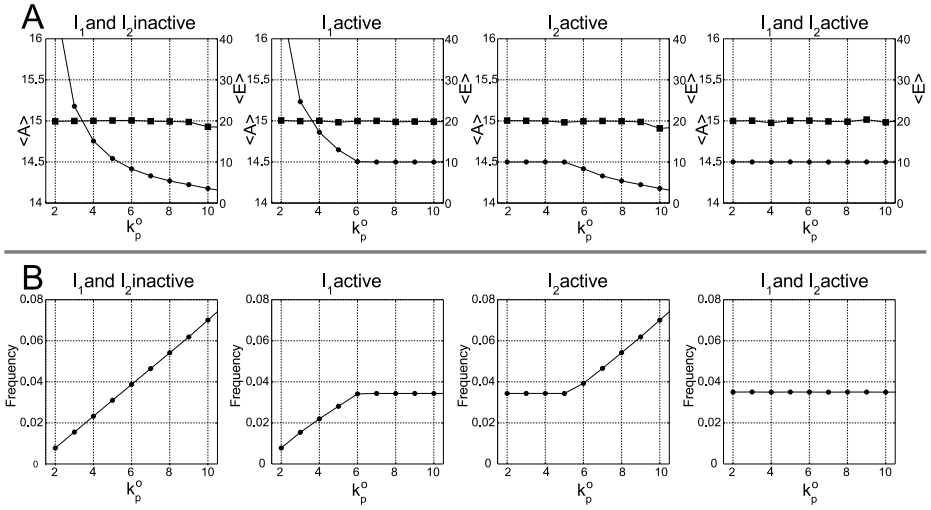

Figure 5.11: Self-oscillating version of controller motif 2 with added I_1 and I_2 controllers for robust control of frequency (Eqs. 5.53–5.57, Fig. 5.10A). Parameter values: $k_1 = 20$, $k_2 = 30$, $k_3 = 0.1$, $k_5 = 0.1$, $k_6 = 0.1$, $V_{max}^{E_{set}} = 1.5$, $k_8 = 1$, $k_9 = 0.1$, $k_{10} = 0.1$, $k_{11} = 1$, $K_I^E = 2$, $K_{M1}^A = K_{M2}^A = K_M^{E_{set}} = K_M^{I_1} = K_M^{I_2} = 0.001$, and $k_p^i = 1$. Results are shown for combinations of active and inactive I_1 and I_2. Leftmost column: I_1 and I_2 inactive ($k_3 = k_5 = 0$). Second column: I_1 active and I_2 inactive ($k_5 = 0$). Third column: I_1 inactive ($k_3 = 0$) and I_2 active. Rightmost column: I_1 and I_2 active. **A.** Periodic average in A and E shown for different levels of disturbance in k_p^o. **B.** Frequency of oscillations shown for different levels of disturbance in k_p^o.

The rationale behind the setup is in effect to control the average level of $<E>$. The setup achieves this, Fig. 5.11A, and the homeostasis in frequency comes as an added bonus. We have so far no analytic explanation to exactly why this setup with control of $<E>$ gives homeostasis in frequency. Nevertheless, the setup is the first, with realistic biochemical kinetics, that can achieve robust frequency control. Furthermore, the strategy can be extended to all the oscillating controllers, some examples are shown in Paper 5. Note that the E controlled level of $<A>$ is kept at its setpoint independently of whether $<E>$ and the frequency is regulated or not, Figs. 5.10C and 5.10D.

5.7 Oscillator with two homeostatic frequency domains

Both I_1 and I_2 define their own setpoints for $<E>$. The requirement of zero-order removal of I_1 in Eq. 5.56 gives a theoretical setpoint of $<E>_{set}^{I_1} = k_8/k_9$, and likewise zero-order removal of I_2 in Eq. 5.57 gives a theoretical setpoint of $<E>_{set}^{I_2} = k_{11}/k_{10}$. The same setpoint was used for both I_1 and I_2 in the simulations above. $<E>_{set}^{I_1} = <E>_{set}^{I_2} = 10$.

It is possible to use different setpoints to create an oscillator with two distinct frequency domains, where both domains are correspondingly robust towards disturbances in either inflow or outflow. This is made possible by the structure of combined controllers, and is completely equivalent to the case with two E-controllers of A as discussed in section 2.7. Fig. 5.12 illustrates this by the same system as above (Eqs. 5.53–5.57), but with the setpoint of the outflow acting I_2-controller changed to $<E>_{set}^{I_2} = 15$. The result is an oscillator that based on whether inflow or outflow disturbances in A are dominating changes between the frequencies of approximately 0.025 (corresponding to $<E>_{set}^{I_2} = 15$) and approximately 0.035 (corresponding to $<E>_{set}^{I_1} = 10$), Fig. 5.12 panels A and B. Note that, although $<E>$ changes between the two different setpoints at different disturbances (k_p^p), $<A>$ is kept at its homeostatic setpoint even during the transition zone when both I_1 and I_2 controllers are inactive.

Fig. 2.8 in section 2.7 shows how an inflow controller and outflow controller with different setpoints for A are active at different levels of disturbances/perturbations. The same type of behavior is observed in the periodic average of the I_1 and I_2 controllers when they have different setpoints for $<E>$, Fig. 5.12 panels C and D.

A different setup for two frequency domains, where I_1 affects the inflow of a and I_2 affects the outflow of A is examined in Paper 5. Yet another setup is given in the Supporting Material of Paper 5; the e-extended version of controller 2 is used as the inner oscillator instead of the a-extended version.

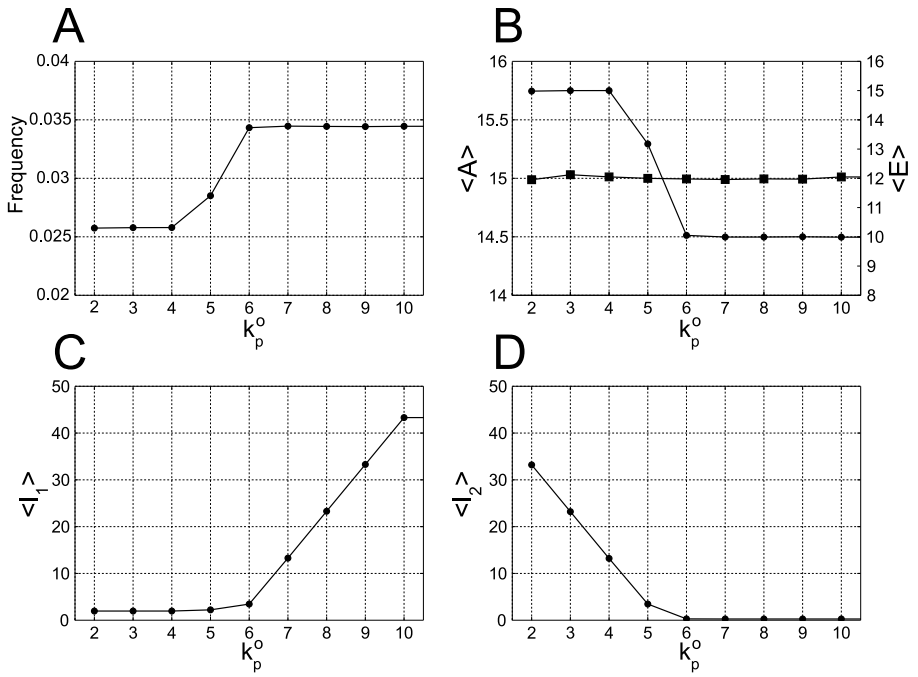

Figure 5.12: Self-oscillating version of controller motif 2 showing two distinct frequency domains, by different $<E>$-setpoints defined by I_1 and I_2 (10 and 15). The system is based on Eqs. 5.53–5.57, Fig. 5.10A. Parameter values: $k_1 = 20$, $k_2 = 30$, $k_3 = 0.1$, $k_5 = 0.1$, $k_6 = 0.1$, $V_{max}^{E_{set}} = 1.5$, $k_8 = 1$, $k_9 = 0.1$, $k_{10} = 0.1$, $k_{11} = 1.5$, $K_I^E = 2$, $K_{M1}^A = K_{M2}^A = K_M^{E_{set}} = K_M^{I_1} = K_M^{I_2} = 0.001$, and $k_p^i = 1$. All panels show values for different levels of outflow disturbances (k_p^o). **A**. Frequency of oscillations. **B.** Periodic average of A and E. **C.** Periodic average of I_1; I_1 is active at relative high levels of outflow disturbances. **D.** Periodic average of I_2; I_2 is active at relative high levels inflow disturbances.

Chapter 6

Discussion and concluding remarks

Altogether, the work in this thesis presents a way of analyzing regulatory systems in biology. This final chapter ties the different facets of the work together, highlighting strength and usefulness. It also discusses the results of the thesis as a whole, with the ambition of connecting it to a broader view of control and communication. It has been a goal to make this chapter something else than a collection of the discussion sections from each individual paper, many of which have instead been combined into their respective chapters where they have a natural place.

This chapter allows for a discussion that includes a more hypothetical and visionary view of biological control systems. In this light we discuss possible interesting extensions and further developments of our work.

6.1 Strength and suitability of the controller motif framework

The controller motifs can be applied to explain, and/or model, control and regulation both on the level of physiology of a whole organism and on the level of cell physiology. The *two species scheme* with a controlled species A and a controller species E can be applied to a range of diverse systems. The controlled species A can on the cellular level be: the concentration of cytosolic copper ions in yeast cells, controlled by a copper inflow (Crt, E_1) and a copper outflow (Crp, E_2) controller, as seen in chapter 4; or A can be the concentration of intracellular sodium ions in enterocytes, as described in chapter 3. On the level of a higher organism, A can be the blood glucose controlled by the effects of insulin E_1 and glucagon E_2; or A can be the concentration of blood calcium controlled by the effects of

calcitonin and parathyroid hormone. An extensive list of hormonal systems that can be related to combinations of controller motifs is given in the supporting material of Paper 1.

The set of controller motifs is strengthened by its generality. The basic structure of the controller motifs (Fig. 2.1) allows for a range of different kinetics in the inflow and outflow of A and E. All motifs have an underlying regulatory function through negative feedback, although the possibilities for perfect adaptation in A is somewhat limited in that it requires zero-order degradation of E or autocatalysis of E combined with first-order degradation. The applicability of the controller motifs in theoretical biology is illustrated by the fact that many of the well known biological model oscillators, such as the Goodwin oscillator (section 5.1.1) and the Lotka Volterra oscillator (section 5.1.2) can be considered to be special cases of oscillators formed by the controller motifs.

6.1.1 Building blocks and submodules

A powerful feature of the controller motif framework is the modularity and the way each motif functions as a building block or submodule. Modularity gives an advantage to both the modeling of existing biological systems within the framework and to the design of new systems, whether those are mostly theoretical as in chapter 5 or practical systems implemented by methods from synthetic biology.

The translation of an existing biological system into the controller motif framework promotes the investigator to separate a complex system into smaller parts that at first can be understood on their own, and then as a part of the whole. An example is how the enterocyte model in chapter 3 was built by combining submodules modeling the inflow and outflow of different species. The enterocyte model was initially built without specific regulatory mechanisms for the control of Na^+ and K^+. These mechanisms were later added by simply including a controller submodule to the model, as described in section 3.4. Although it is a natural feature of the controller motif framework, it should be noted that, the concept of dividing a system into subsystems, or a task into subtasks, is by no means new.

To illustrate how larger systems can be designed in a step-by-step fashion from subsystems, we use the example of robust frequency control from section 5.6. This system, shown in Fig. 6.1, consists of an inner oscillator (marked with red); a subsystem made out of an extended version of controller

motif 2. By itself this subsystem may exhibit self-oscillation, but in general with a frequency that varies with perturbations. This inner oscillator is extended with two additional controllers, I_1 and I_2, each of which may be considered as subsystems (marked with green and yellow). It is relatively easy to distinguish the role of each component, even though the overall system is 5-dimensional. E acts to control the periodic average of A towards a setpoint defined by the kinetics of the inflow and outflow of E. From the perspective of E all inflows and outflows of A, except for the E mediated compensatory flow through a, acts as disturbances. I_1 and I_2 acts to control the periodic average of E, where I_1 primarily compensates for outflows of A (which leads to reduced inflow in E) and I_2 primarily compensates for inflows of A (which leads to increased inflow of E). The setpoints of the periodic average of E, and thus the frequency, are defined by the kinetics of the inflows and outflows of I_1 and I_2.

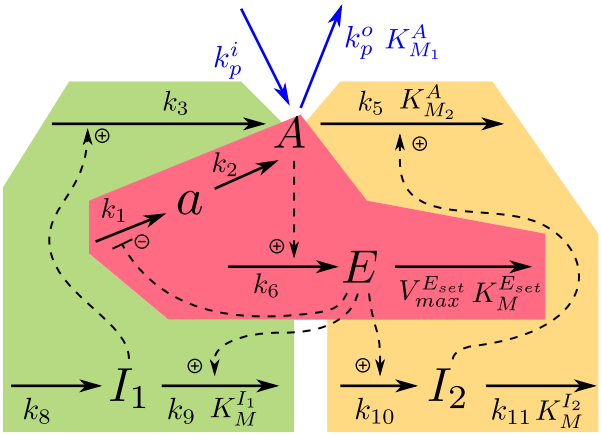

Figure 6.1: 5-dimensional oscillator with robust control of frequency made out of controller motif subsystems. The inner system is a self-oscillating version of controller motif 2, shown in red. The inner system is extended by two controller motifs I_1 (green) and I_2 (yellow), which acts to control the periodic average of E through the inflow and outflow of A, respectively.

We are confident that creating a 5-dimensional oscillatory system with robust control of frequency from scratch, without using the step-by-step process which is inherent in the controller motif framework, would have been very difficult. Especially when one considers the constraint of having a system that is biologically realizable with plausible structure and kinetics.

The controller motif framework fits very well with the essence of synthetic biology, i.e., the idea that complex network behavior can be understood

by well-characterized submodules. We think it can be a useful tool in the design and construction of novel regulatory networks. The extension of the regulatory system for internal copper in yeast by the addition of an extra outflow controller submodule in chapter 4 is a promising example.

Enterocytes: a small part in a large system

Relevant to modularity is the question of how regulation in higher organisms integrates functions on both the cellular and organismal level. We will illustrate some aspects of this by using the enterocyte as an example.

Being vital for cell survival, the regulation of intracellular ionic homeostasis must from the enterocyte's viewpoint, and for any other cell, have high priority. For the whole organism that the enterocyte is a part of, however, other transport related regulatory mechanisms may have just as crucial implications. Regulation of the capacity of nutrient uptake, and the focus of nutrient uptake (sugar, proteins, or lipids), plays a major role in securing organism survivability, but is only of secondary importance for the enterocyte itself. One of the reasons to develop an enterocyte model in the first place was that an enterocyte model could, in the future, be a piece in studying the regulation of nutrient uptake and in particular the glucoregulatory system of the whole animal.

For enterocytes in particular, it has been shown that the capacity of the uptake system can be increased to respond to a high luminal concentration of glucose. This is an important mechanism for securing that as much as possible of the nutrients are absorbed when they are available. Studies have revealed intracellular stores of the glucose transporter SGLT1 [93, 94], which are thought to play a role in the regulation of SGLT1 mediated glucose uptake. SGLT1 has also been shown to be rapidly upregulated by sweet taste receptors [169]. In addition, there is evidence for trafficking of GLUT2, which is normally situated only in the basolateral membrane (Fig. 3.1), to the apical brush border membrane during high luminal glucose concentrations [113, 206]. Due to its properties as a facilitated transporter, GLUT2 can in contrast to SGLT1 only be used when the glucose concentration in the intestinal lumen is higher than inside the enterocyte. This makes GLUT2 a candidate responsible for the observed non-saturable component of glucose uptake from the small intestine [90]. The usage of apical GLUT2 may be of advantage for the enterocyte; it enables the enterocyte to increase the glucose uptake without the ionic and osmotic challenges associated with the Na^+ coupled uptake through SGLT1.

6.1.2 Similarities with industrial controllers

As discussed, there is an abundance of regulatory biological systems where two antagonistic mechanisms cooperate to control one variable, i.e., systems where one mechanism controls supply and one mechanism controls removal. At first this may seem as a somewhat unfamiliar arrangement for most control engineers, who often design systems by the principle of one variable, one controller. As an example, traditional cruise control systems does only use the throttle to maintain a steady speed. Brakes are not even used if the car is going downhill and is overspeeding; the control system just passively waits for the speed to drop down by itself[1].

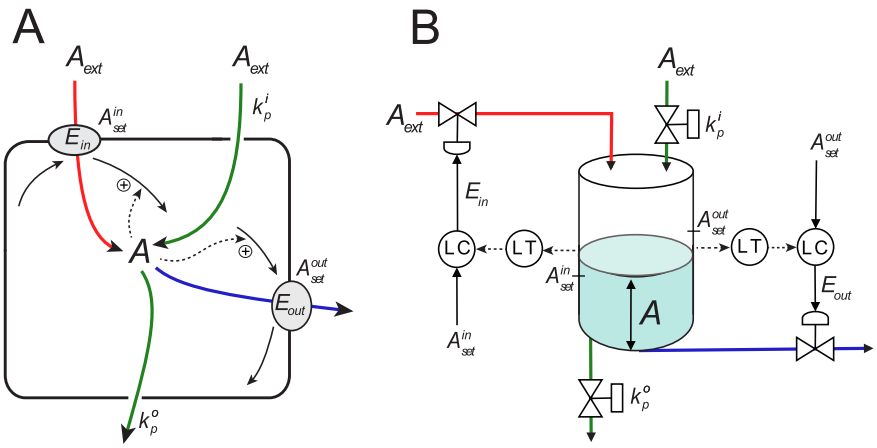

Figure 6.2: A. A typical biological system where A is controlled by a pair of antagonistic controller motifs. **B.** The analogous process and instrumentation diagram using a water tank, control valves, level controllers (LC) and level transmitters (LT).

In the following we will compare the general model of biological antagonistic control of a variable A by inflow and outflow controllers, Fig. 6.2A, to an industrial control system. A corresponding process and instrumentation diagram using a water tank, control valves, level controller (LC) and level transmitters (LT) is shown in Fig. 6.2B. The measurement of the level of A in Fig. 6.2B is indicated as a dotted line into the level transmitter (LT) and further into the level controller (LC). In relation to the biological system in Fig. 6.2A the corresponding measurement is A's activation/inhibition

[1]Some modern, so-called adaptive cruise control, systems will use the brakes, such systems often includes functions to automatically keep a set distance to other vehicles.

on the generation/removal or E (dotted line). Reduced accuracy in the biological controller motifs (section 2.6) is analog to a level transmitter that transfers a measured value of A which is different from the actual value. The controller variables E_{in} and E_{out} adjust the opening of the control valves. If $E = 0$ corresponds to a closed valve, the controller is based on activation from E to A. If $E = 0$ corresponds to a fully open valve, the controller is based on inhibition from E to A. These two cases are equivalent to the use of normally closed (NC) and normally opened (NO) valves. The system will only function properly when the setpoint of the inflow controller A^{in}_{set} is lower or equal to the setpoint of the outflow controller A^{out}_{set}, as discussed in section 2.7.

Antagonistic control design is in fact emerging as a solution to traditional control engineering problems. One example is modern thermostats that combine both heating and cooling (AC) to keep the temperature inside a predefined range, i.e., within two setpoints. Such solutions can be advantageous in climates that require cooling during the day and heating at night.

6.2 Future development of the controller motifs

The work done in this thesis has explored and evolved the theory of controller motifs to an extent where it is matured and ready to be applied to examine and model practical cases. In addition to the practical cases presented herein we are in the process of using the controller motifs to examine and model several biological systems. I am myself involved in two projects. The first is a project on iron regulation in plants, specifically the control of intracellular iron by high affinity IRT1 transporters. We have worked with this project for some time and presented some results at the 26th International Conference on Arabidopsis Research in Paris this summer (ICAR2015). The second project is currently under development and involves the study of biological rhythms in plants and the apparent homeostasis of the circadian period. Some aspects of this second project are discussed in section 6.3.2.

In addition to modeling existing biological systems the controller motif framework is also suitable to be used together with synthetic biology to design novel regulatory systems. The copper regulatory system in yeast is one system that we think have great potential for the future, with several

interesting directions, as discussed in section 4.6. I personally would also like to try to build some of the oscillators from chapter 5.

In parallel to practical applications there are many potentially fruitful directions into which to drive the theoretic development of the controller motifs, discussed in the following sections.

6.2.1 Setpoint tracking

From a control theoretic point of view the performance of a regulatory system can be described in the context of *disturbance rejection* and *setpoint tracking*. The work in this thesis is mostly concerned with disturbance rejection, which is the ability to adapt to environmental disturbances. Setpoint tracking, or simply just tracking, which is the ability to follow a changing setpoint or reference, is a very important design criteria in many man-made systems. A car's cruise control system may for instance experience a stepwise setpoint change from 60 to 90 km/h following a change in the speed limit. It is crucial that engineers are able to design the cruise control systems so that this change happens without overshoot or oscillations; no driver would accept a 20% overshoot and a following ticket for speeding.

Biological setpoint tracking has by Mrosovsky [123] been described under the term *rheostasis*. Rheostasis is presented as an extension of homeostasis, as to allow for an interpretation where the deviation away from the limits set by homeostasis is not seen as a failure of the regulatory system to compensate for environmental disturbances. The trivial example is the case of fever; fever can be interpreted as a change in the setpoint of the thermoregulatory system, where the increase in body temperature is mediated by a still functioning regulatory mechanism. Some physiological examples where setpoint tracking is investigated are incubation weight loss [124, 164], seasonal weight changes [122, 124], lowered body temperature during hibernation [37] and persistent obesity [149]. However, research on setpoint tracking in biology is still relatively rare compared to disturbance rejection.

We have already shown how different setpoints can arise due to the combination of controllers, see section 2.7. While such combinations are useful for defining lower and higher limits of the homeostatic range, as shown by the addition of an Cu-regulating outflow controller in chapter 4, they are different from the concept of rheostatic setpoint shifting. A

rheostatic setpoint shift is the same as moving the whole homeostatic range upwards or downwards. An illustrative example is the regulation of body core temperature. Two important mechanisms for control of the human body temperature are sweating and shivering, which respectively acts to lower and raise the body temperature[2]. These two mechanisms are both primarily controlled by the hypothalamus and have slightly different setpoints [69 chap. 73], i.e., there is a narrow range in temperature for which neither sweating (above basal level) or shivering occurs. Rheostasis describes the combined shifting of both setpoints, which for example occurs during fever. This is illustrated by Fig. 6.3. Rheostasis can also occur in systems with only one controller, where it simply corresponds to shifting of the single setpoint.

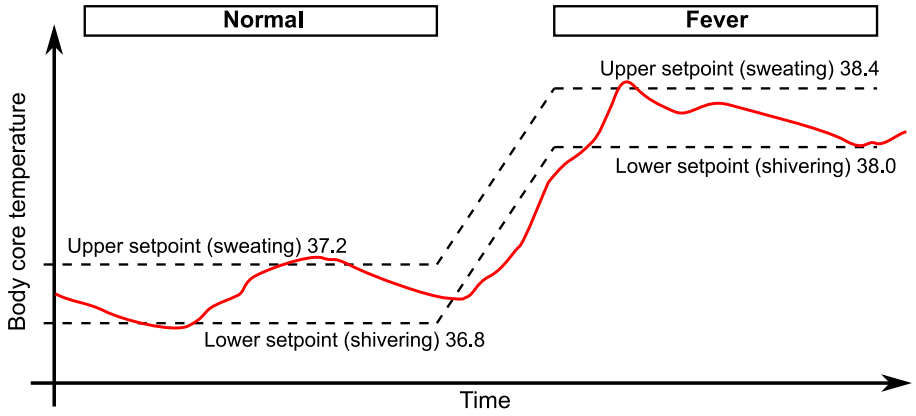

Figure 6.3: Example of a so-called rheostatic shift in setpoints in the control system for core body temperature. Fever causes the whole homeostatic range, the interval between the setpoints where sweating and shivering begins, to shifts upwards. The values for the upper and lower setpoints depends on skin temperature and differs between individuals [69 chap. 73].

It is possible to realize a shifting setpoint within the controller motif framework without much trouble, and we will here demonstrate how. Consider inflow controller 4 shown in Fig. 6.4A. The change in E is described

[2]Although not directly transferable to our two-species controllers, we can think of sweating as the dissipation (outflow) of heat and shivering as the creation (inflow) of heat.

by the following differential equation,

$$\dot{E} = k_s^E - \frac{V_{max}^{E_{set}} E}{K_M^{E_{set}} + E} \frac{K_I^A}{K_I^A + A} \tag{6.1}$$

where the theoretical setpoint is found by assuming perfect zero-order degradation with respect to E ($K_M^{E_{set}} \ll E$) (section 2.4).

$$A_{set} = \frac{V_{max}^{E_{set}} K_I^A}{k_s^E} - K_I^A \tag{6.2}$$

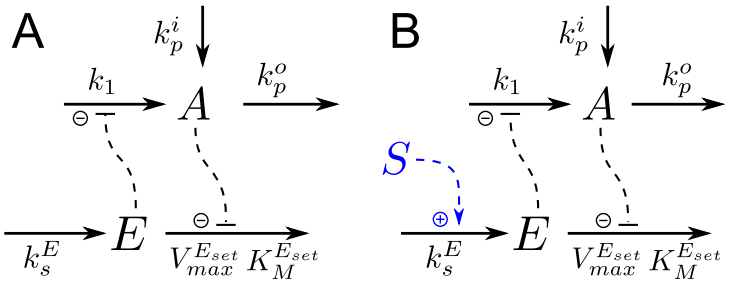

Figure 6.4: A. Inflow controller motif 4. **B.** Realization of a changing setpoint controlled by species S.

One way to allow a changing setpoint is to have one of the parameters in Eq. 6.2 change over time. Consider for example a plant cell where k_s^E depends on light or temperature, where the controlled variable A may then have two different setpoints for day and night.

Another possible mechanism is shown in Fig. 6.4B. The inflow of E is now dependent on a specific species S. The result is an S-dependent setpoint,

$$A_{set} = \frac{V_{max}^{E_{set}} K_I^A}{k_s^E S} - K_I^A \tag{6.3}$$

where S can be thought of as an external signal that controls the setpoint of the controller. We find it highly probable that this or very similar mechanisms are responsible for many of the hormone controlled regulatory networks in cells and organisms, and that examples are sure to be found by careful study of the vast amount of already published research on hormonal control.

A related project would be to implement this sort of setpoint shifting in a synthetic regulatory network. The added outflow controller for copper designed in chapter 4 is a candidate system that may be extended to show this kind of behavior. A promising idea is to develop a dual-mode type modified pCUP1 promoter. A dual mode promoter activated by testosterone through the testosterone-responsive androgen receptor, and repressed (inhibited) by IPTG[3] through the LacI repressor, was recently developed for yeast [118].

6.2.2 Three-component motifs with double integral action

When two controller motifs are combined to model antagonistic regulation, the resulting system does in general not have a single unique setpoint. Each of the two individual controllers have their own setpoint, making the resulting system overspecified. The steady-state level of the regulated species A will, depending on the inflow or outflow disturbances, either end up at one of the setpoints or stay somewhere in-between them, Fig. 2.8.

We have found an alternative way to combine two controller motifs to get a system with only one setpoint. This is achieved by having the two controller motifs act in series rather than parallel, illustrated by Fig. 6.5A. This system consists of an outflow controller (E_1) and an inflow controller (E_2), but only one of the controllers are affected directly by A; the second controller E_2 is now instead affected by the first controller E_1. There is only one setpoint, defined by the differential equation for E_1 as $A_{set} = k_4/k_3$. A series arrangement of controller motifs like this creates an inner loop and an outer loop, highlighted in Fig. 6.5B. There is one feedback path directly from A and back to A via E_1, and a longer feedback path via E_1 and E_2.

An interesting feature of this series arrangement is that it does include both integral action and double integral action in the control of A. This can be realized by inspecting the block schematic representation in Fig. 6.5B. The error between A and the setpoint is first integrated once by E_1 and then integrated once more by E_2, and both the integrated error and the double integrated error is fed back to A through the inner and outer loop, respectively. The block schematic representation can be rearranged to clearly separate the controllers from the system being controlled, see Fig. 6.5C. The two controllers compensate for disturbances, i.e., k_p^i and

[3]IPTG stands for Isopropyl β-D-1-thiogalactopyranoside, a compound which mimic the lactose metabolite allolactose.

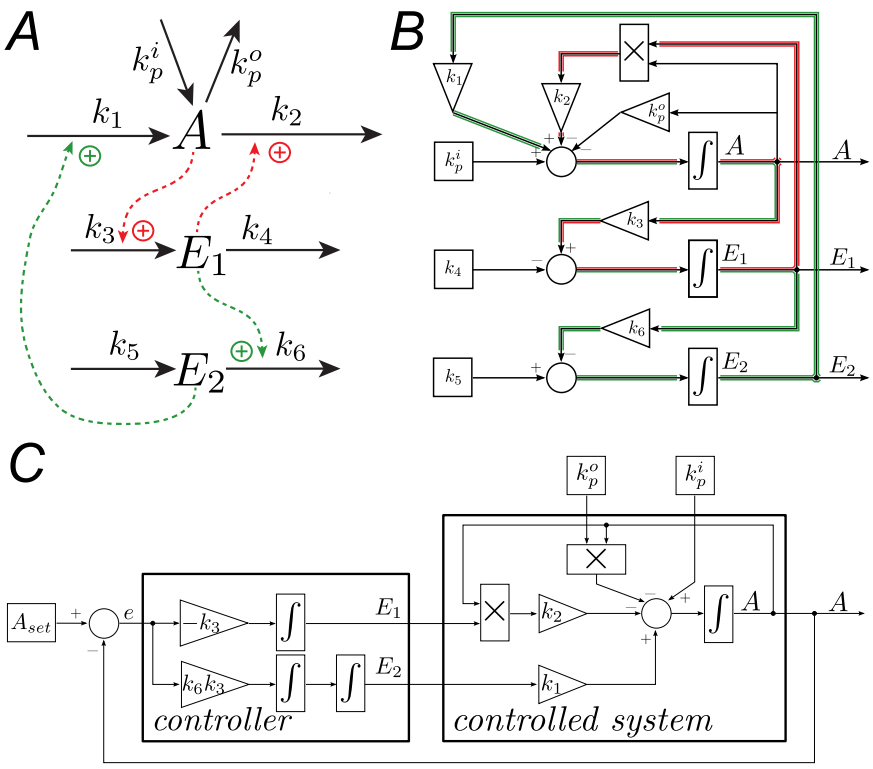

Figure 6.5: **A.** Reaction kinetic representation of a three-component antagonistic system with only a single setpoint of A. **B.** Block schematic representation. The inner integral loop and the outer double integral loop are highlighted in red and green. **C.** Block schematic representation redrawn to show the distinction between the controller and the controlled system. E_1 and E_2 acts as two inputs to the controlled system, and are respectively proportional to the integral and the double integral of the error between the setpoint and the current value of A.

k_p^o, affecting A. A feature added by dual integral action is the ability to perfectly follow a ramping reference, a linearly increasing setpoint. It is well known from control theory that a control system made to perfectly follow, i.e., with no steady-state error, a parabolic reference of order m must, at least, have $m + 1$ integrators in the control loop [51].

Regulation of blood glucose by the antagonistic hormones insulin and glucagon is one system which has been thought to have an parallel arrangement, where glucose directly affects both insulin and glucagon [69 chap. 73]. More recent studies have, however, revealed that insulin directly affects the release of glucagon [67, 89, 202]. Glucagon is produced in α-cells in the pancreas; the α-cells are located downstream of the insulin producing β-cells, making them highly exposed to secreted insulin [202]. The presence of insulin has been shown to be essential for the suppression of glucagon secretion [202], and studies done in insulin receptor knockout mice have provided direct in vivo evidence for how insulin modulates the secretion of glucagon [67, 89].

The three-component structure shown in Fig. 6.5A can be extended to a whole class, or family, of three-component antagonistic regulatory systems. Fig. 6.6 shows the basic reaction kinetic structure for this class of systems. The controlled species A is regulated by two regulatory species E_1 and E_2. The *inner loop* between A and E_1 is constructed by one of the two-component controller motifs, and there is in general 16 different possible combinations (8 with negative feedback and 8 with positive feedback). The *outer loop* is constructed by letting E_1 act on either the inflow or the outflow of E_2 by either activation or inhibition (extending the number of possible configurations to 64), and having E_2 affecting A by either activation or inhibition of the flow *not* affected by E_1. This gives a total of 128 possible configurations, of which only 32 have a negative feedback in both the inner and outer loop. This class of three-component controller motifs is so-far largely unexplored.

6.2.3 Further mathematical analysis and limitations of modeling by ordinary differential equations

One of the goals of this thesis has been to present a control engineer's interpretation of regulation and control in biology through the controller motif framework, and to show how the controller motifs can be applied and used in biology. Having laid out the theoretic foundation we have hence continued to focus much of the work towards establishing biological

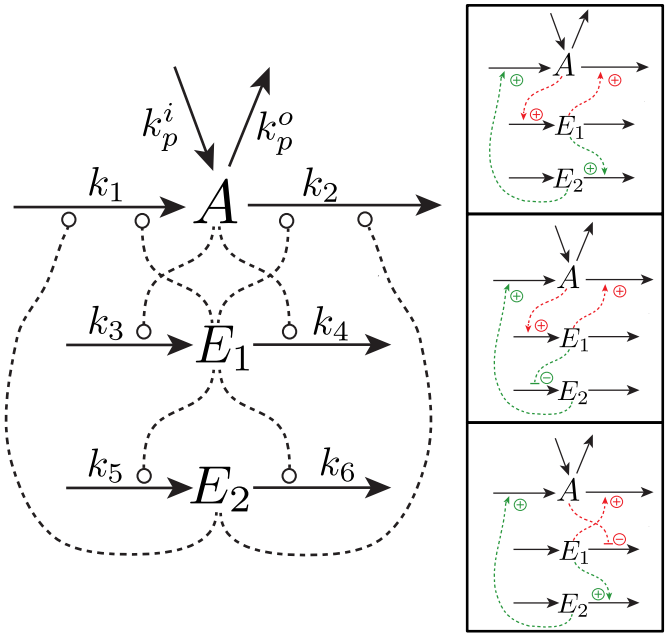

Figure 6.6: Basic structure of a three-component antagonistic controller motif. Dotted lines show possible interactions, which can either be activating or inhibiting (round symbols). Not all interactions are allowed at the same time, see main text. Insets show 3 of the 32 possible configurations with negative inner loop and negative outer loop.

relevance, instead of exploring every nuance of controller motif systems by mathematical analysis. It has still always been the plan to do a further more rigorous mathematical analysis of the controller motifs once we can defend that such work is worthwhile. Some of the areas we plan to look into are stability properties, bifurcation behavior, and tunability.

A possible future direction to extend the description of controller motifs to other types of mathematical models, such as partial differential equation and stochastic systems. The choice of ordinary differential equations has two inherent weaknesses that may be of concern for certain biological systems [32]. The first is the lack of spatial information, i.e., that the concentration of a species is assumed to be evenly distributed in a compartment. The second is the assumption of continuity i.e., that the state variables are continuous (making it possible to have a non-integer amount of molecules).

Both the above assumptions are reasonably true for our model of transport and ionic homeostasis in enterocytes, and the use of ordinary differential

equations is a common approach in studies of epithelial transport [9, 103, 196]. The molecules considered (ionic species and glucose) are small and are easily mixed throughout the cell by molecular diffusion. The modeled concentrations are in the mM range[4], and the flows into and out of the enterocyte are in the range from 10^{-14} to 10^{-12} mol/h. These numbers are well above the range where discreteness plays a role.

Things are a bit less obvious for a future quantitative model of copper regulation in yeast. It is no problem to consider amount of total copper (normally 10–100 µM) as continuous. The amount of free copper is however certainly not continuous, since the binding to proteins such as Cup1p is so strong that there in practice is not even a single unbound copper ion in the cytoplasm [144]. A discrete stochastic model may thus be a more fitting option.

6.3 Homeostasis and oscillatory behavior

Seen from the perspective of control engineering it is no surprise that the presence of negative feedback and integral control can lead to oscillatory behavior, such systems have an innate possibility to exhibit damped and even sustained oscillations [27, 116, 180]. However, that oscillations are so ubiquitously prevalent in biological systems is more of a puzzle. Engineering has taught us that a well designed control system should not oscillate.

It has been argued that oscillations observed in biological systems may, at least in some cases, be without any functional significance [28]. Oscillations are, as discussed above, emergent to occur in adaptive systems, and may be observed simply as a consequence. Experimental procedures have the potential of creating artifactual oscillatory processes by using unnaturally high stimulus, and this is argued by some to be the reason for oscillations seen in NF-κB signaling [13, 27].

Stimulus-dependent oscillations do, however, also occur naturally, and research has shown that such oscillations have functional significance in some biological systems. One system that shows oscillations based on stimulus strength is found in pancreatic β-cells, which are responsible for the production and secretion of insulin in response to elevated levels of glucose. The level of cytosolic Ca^{2+} in these cells oscillates when the cells

[4] In an enterocyte compartment volume of 450 µm, 1 mM correspond to $4.5 \cdot 10^{-16}$ mol or roughly 270 million molecules, a more than sufficient amount to assume continuity.

are exposed to high concentrations of external glucose, and there is indeed an abundance of studies linking insulin release to these Ca^{2+} oscillations [14, 56, 174]. Fig. 6.7 shows experimental measurements of cytosolic Ca^{2+} in β-cells for different concentrations of glucose. Interestingly, the same type of stimulus-dependent behavior is seen in our oscillatory controller motifs; Figs. 5.8 and 5.9 show how the behavior of the extended version of controller motif 5 depends on the level of disturbance in k_1 (stimulus). Oscillations are seen for low k_1's, but they disappear when k_1 is increased above a certain level.

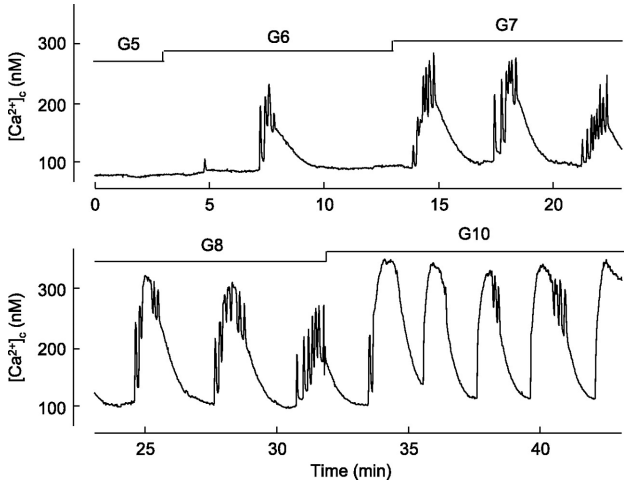

Figure 6.7: Effect of glucose on the behavior of cytosolic Ca^{2+} concentration in β-cells in a pancreatic islet. (The islets of Langerhans are regions in the pancreas with hormone producing cells; β-cells make out 60-70% of the cells in an islet [96].) Glucose concentrations was increased from 5 to 6, 7, 8 and 10 mM as indicated. The response changes from adaptive to oscillatory. Reprinted from [14] with permission.

6.3.1 Control and communication

The key to the prevalence of oscillators in biological systems is likely related to the second part of the subtitle of *Cybernetics*, i.e., communication. Engineers can design systems that are separated, and which carries information and matter over different mediums or channels. The information grid, the power grid, the water grid, and the sewage grid are still mostly separated, even though solutions exist that allows for the combination of them. There is an inherent simplicity in the principle of one system, one media, one job.

Biological systems are on the other hand very different, due to the process of evolution. New systems are most likely to arise from adaptation and/or augmentation of existing systems. Cells and organisms have to maintain homeostasis and at the time same allow signaling, a combination of control and communication. There is no particular reason to assume that protective homeostatic mechanisms should cease to exists once a compound becomes oscillatory and starts to function, as in case of calcium, as a signaling device. In fact, as shown in section 5.5, a regulatory systems based on the controller motifs may behave as an oscillator for some parameter value and as an ordinary damped feedback controller for another value.

Then why do communication systems show oscillatory behavior? A steady-state signal has its level/value as its only characteristic property. An oscillatory signal, on the other hand, has several characteristic properties, such as average level, amplitude, period/frequency, phase, and shape. Oscillatory signals are for this reason better suited to carry information.

Indeed almost all modern electronic communication is based on oscillatory signals; contrary to popular belief, most communication signals are not digital step-type, zero-or-one, signals. Such signals are only used at very close distances, such as inside a device or between devices in close proximity. Most communication signals are *modulated*, that is, the signal is reshaped before it is sent through the medium, or channel. Information is encoded into some characteristic features of a signal. Many modern communication systems uses modulation techniques that encodes information into the phase or the frequency of an oscillating signal. Modern «digital» systems such as DVB-S/T[5], GSM[6], IEEE 802.11[7], Bluetooth, and RFID[8] uses so-called frequency shift keying (FSK) and phase shift keying (PSK). These technologies are again modifications of the old-fashioned frequency modulation (FM) of analog radios. In its simplest form frequency shift keying modulation can be done by an oscillator that changes between two different frequencies (so called binary frequency shift keying), see Fig. 6.8.

The controller motifs presented in this thesis can explain how a biological system may achieve the same. One way to do this is discussed in section 5.7 of chapter 5, which presents an oscillator with two homeostatically defended frequencies. The frequency changes based on whether inflows or

[5]Digital Video Broadcasting Satellite/Terrestrial, broadcasting of audio and video.

[6]Global System for Mobile Communications, used in mobile phones.

[7]Institute of Electrical and Electronics Engineers standard number 802.11, defines the common wireless network known as WiFi.

[8]Radio-frequency identification, ID-tags used in bus-passes, and employee cards.

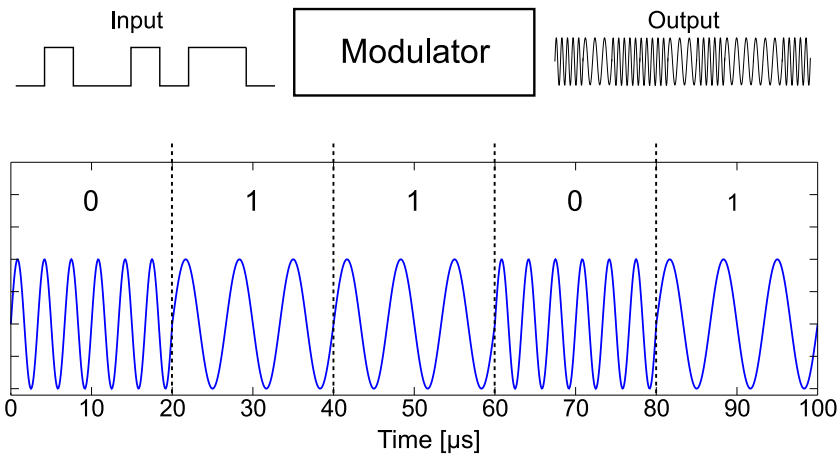

Figure 6.8: Binary frequency shift keying (BFSK). Binary information is encoded into the frequency of an oscillating signal by a modulator. In this example the modulator converts a binary 0 or 1 input into a sinusoidal output with a frequency of either 300 kHz or 150 kHz. In electronics this type of modulation may be realized by a voltage controlled oscillator (VCO).

outflows of A are dominating. Another way for a controller motif based biological system to encode information into frequency is to have a stimulus acting directly on the frequency controller (I).

Fig. 6.9A shows a biological system based on a self-oscillating version of controller motif 2, extended with one frequency controlling motif I_1. A stimulus S acts on the inflow of I_1. The frequency of the oscillator changes when the stimulus changes, because S affects the I_1-controller's setpoint for $<E>$. In the case where S has switch-like behavior this system functions similarly to a binary frequency shift keying (BFSK) modulator, see Fig. 6.9B. If S has a more continuous behavior the system functions as an ordinary frequency modulator (FM), Fig. 6.9C.

Several oscillatory biological systems are claimed to exhibit frequency modulation [105, 137]. We have, however, not yet examined whether such systems have similar structures as proposed above. The structure is in any case interesting in itself and may, even if it does not exist in biology today, be implemented by synthetic biology in the future.

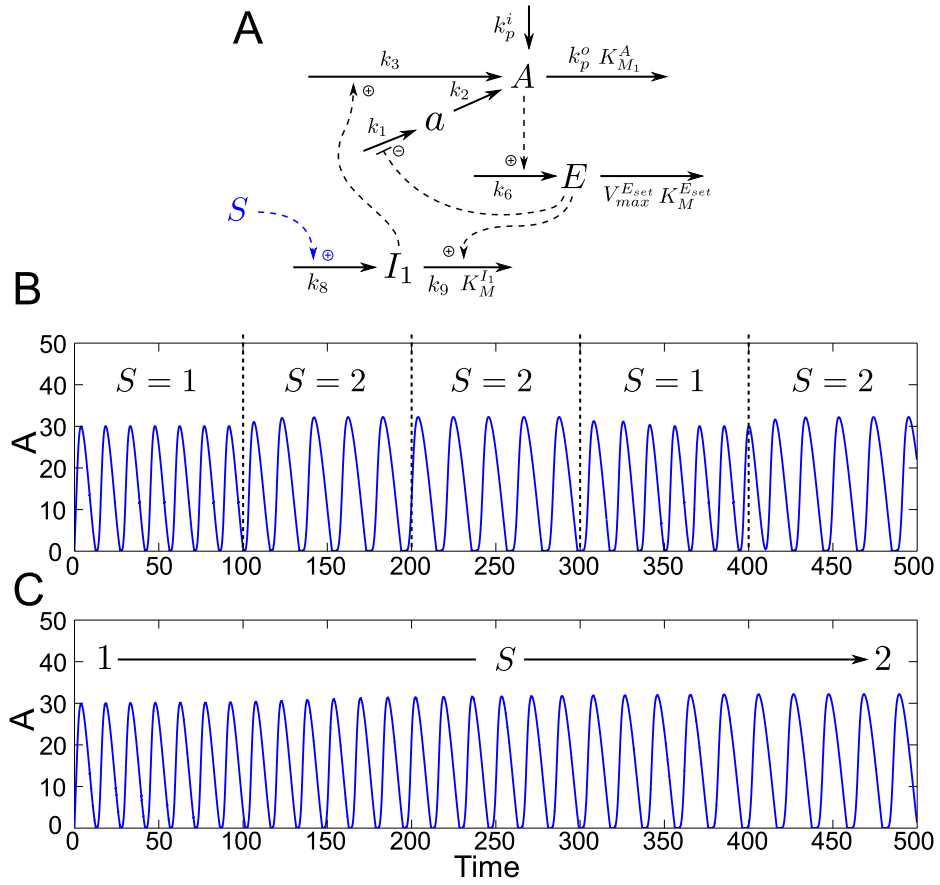

Figure 6.9: Self-oscillating version of controller motif 2 with frequency control by I_1 (Eqs. 5.53–5.56). Parameter values: $k_1 = 20$, $k_2 = 30$, $k_3 = 0.1$, $k_5 = 0$ (I_2 not included) $k_6 = 0.1$, $V_{max}^{E_{set}} = 1.5$, $k_8 = 1$, $k_9 = 0.3$, $K_I^E = 2$, $K_{M1}^A = K_M^{E_{set}} = K_M^{I_1} = 0.001$, $k_p^i = 10$, and $k_p^o = 1$. **A.** Reaction kinetic scheme, a stimulus S affects the inflow of I_1. **B.** The system shows BFSK-like behavior when S changes between distinct values. **C.** Ordinary FM-like modulation of frequency is observed when S changes continuously from 1 to 2.

6.3.2 Homeostasis of the circadian period

Biological oscillators may also serve other purposes than communication. One example is the internal circadian clocks, which have a period close to 24 hours. Circadian rhythms participate in the homeostatic control of a variety of physiological variables, such as body temperature, potassium content, hormone levels as well as sleep [48]. Circadian rhythms can be viewed as the adaptation of organisms to life on a rotating planet. Fig. 6.10 shows how a plant (Mimosa) opens its leafs before the light is turned on in the morning and closes them before the light is turned off at night, anticipating the coming of light/dark. The images are from a recently started project on circadian rhythms by our group.

Figure 6.10: Mimosa grown under a controlled light/dark regime. The top left image shows how the leafs have started to open up at 7.30 am, anticipating the coming of light at 8.00 am, top right. The bottom left image shows how the leafs have started to close at 7.30 pm, half an hour before the set of dark at 8.00 pm, bottom right. Note that the camera sensitivity is enhanced at night to make the plant visible.

Circadian clocks allows organisms to predict changes in the external environment associated with the day/night cycle. Their period is under homeostatic regulation towards a variety of environmental influences, such as temperature (temperature compensation), or food supply (nutritional compensation). Although circadian rhythms may be entrained, they function somewhat independently of the day/night cycle. Circadian rhythms are sustained for a certain time even though the day/night cycle is changed, as is what happens when we experience jet-lag. Fig. 6.11 shows how a Mimosa plant reacts to a change in the day/night cycle.

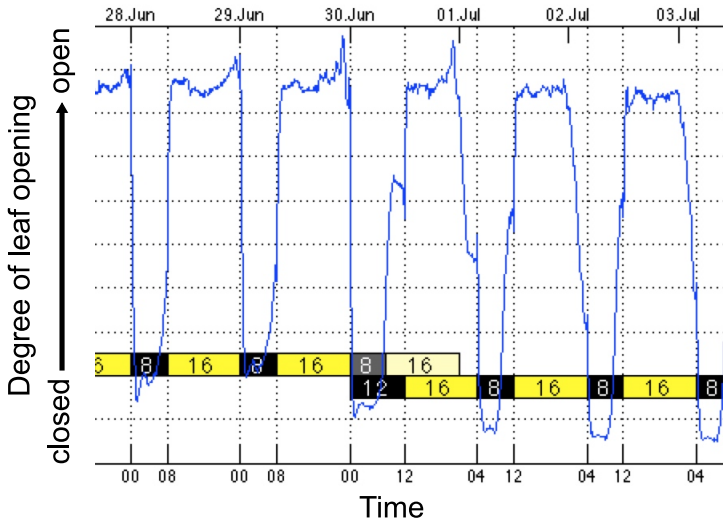

Figure 6.11: Mimosa grown under a controlled light/dark regime. The graph shows how the degree of leaf opening, estimated as amount of green pixels in the image, changes over time. On the 30th of June the day-night cycle is changed from a 16+8 regime (24 hours day) to a 16+12 regime (28 hours day), and then back to a 16+8 regime (24 hours day) on the following day. The change in regime causes the leafs to open too early (after only 8 hours of dark), and to close too early. The internal clock is entrained to the new regime after couple of days.

6.4 The future of cybernetics and biology

Norbert Wiener's concept of cybernetics was at its birth just as much directed towards biology as towards the machine. Maybe not surprising, as Wiener was well aware of the concept of homeostasis and the work of Walter B. Cannon. They both even shared a common co-author in

Arturo Rosenblueth. Coming from today's machine based field of control engineering it is almost surprising to see that so many of the ideas in *Cybernetics* [200] were focused on, and discussed in relation to, regulation in biological systems.

It is also surprising that a lot of these concepts at many times seems to be forgotten in modern molecular biology. The excellent article «Can a biologist fix a radio» from 2002 by Yuri Lazebnik [104] is an illustrative and funny analogy, where the modern methods of biology is tested by whether or not they are applicable to a fix an old broken radio. Lazebnik argues that the lack of an engineering language is a flaw of modern biology.

One should maybe be careful with calling modern biology flawed, but there is an apparent tendency of new discoveries in biology to rapidly evolve with dynamics of a Klondike gold rush, only to crash some years later with failed attempts to develop wonder drugs [104]. Recent reports describe very low success rates for pharmaceutical companies attempting to reproduce seminal biomedical research [16, 120, 142], especially for cancer research. Amgen, a biotechnology company producing drugs for chemotherapy, reported that they were only able to confirm scientific findings in 6 out of 53 published studies [16]. This story has gotten much attention in the research community, and there is now a nonprofit effort trying to replicate 50 high impact cancer papers from 2010 to 2012 [88].

Journal editors and others have called for more rigorously designed experiments, publishing of original data, publishing of negative results, and vigorous peer review [49, 203]. These are all excellent suggestions, but we think, as Lazebnik, that it will help to describe results in a clearer, more formalized, language. Although mathematical models can also be wrong in the sense that they poorly represent empirical data and underlying mechanisms, they are inherently logical, and conveys information with less ambiguity than ordinary language.

The behavior of complex cellular networks can indeed at many times be far from intuitive. Oscillators are good examples of systems that cannot be understood on basis of genetics and molecular biology alone. Their behavior is best described by characteristics such as average level, amplitude, and frequency, and best understood through quantitative mathematical models and system concepts, such as feedback, nonlinearity, phase space, conservative systems, self-oscillations, and attractive limit-cycles.

The rapidly growing fields of systems and synthetic biology are excellent examples of what can be achieved by combining biology with mathematics

and engineering. One of the great achievements of engineering is the creation of new and useful systems and entities that have never before existed. As put by Rosenblueth et al. [152] «no living organism is known that rolls on wheels—imagine what the result would have been if engineers had insisted on copying living organisms and had therefore put legs and feet in their locomotives, instead of wheels». We can only imagine how the powers of synthetic biology will forever change not only biology and medicine, but how it will challenge our society's understanding of what life really is.

My own view, after being exposed to biology, is that a stronger focus on regulatory mechanisms is exactly what is needed to drive research forward. System components should be understood not only by genetic codes and chains of amino-acids (what it is), but by how different molecular species interact in the dynamical sense (how it behaves). The proper way to do this is by mathematical models and the concepts from systems and control theory.

Bibliography

[1] **Adler J, Tso WW**. "Decision"-making in bacteria: chemotactic response of Escherichia coli to conflicting stimuli. *Science* 184: 1292–1294. 1974.

[2] **Aller SG, Unger VM**. Projection structure of the human copper transporter CTR1 at 6-Å resolution reveals a compact trimer with a novel channel-like architecture. *Proc Natl Acad Sci USA* 103: 3627–3632. 2006.

[3] **Alon U, Surette MG, Barkai N, Leibler S**. Robustness in bacterial chemotaxis. *Nature* 397: 168–171. 1999.

[4] **Andrianantoandro E, Basu S, Karig DK, Weiss R**. Synthetic biology: new engineering rules for an emerging discipline. *Mol Syst Biol* 2: 2006.0028. 2006.

[5] **Andronov AA, Vitt AA, Khaikin SE**. *Theory of Oscillators*. Oxford, UK: Pergamon Press. Translated edited and abridged from Russian by F. Immirzi and W. Fishwick. 1966.

[6] **Ang J, Bagh S, Ingalls BP, McMillen DR**. Considerations for using integral feedback control to construct a perfectly adapting synthetic gene network. *J Theor Biol* 266: 723–738. 2010.

[7] **Ang J, McMillen DR**. Physical constraints on biological integral control design for homeostasis and sensory adaptation. *Biophys J* 104: 505–515. 2013.

[8] **Atkinson MR, Savageau MA, Myers JT, Ninfa AJ**. Development of genetic circuitry exhibiting toggle switch or oscillatory behavior in Escherichia coli. *Cell* 113: 597–607. 2003.

[9] **Baerentsen HJ, Christensen O, Thomsen PG, Zeuthen T**. Steady states and the effects of ouabain in the Necturus gallbladder epithelium : a model analysis. *J Membr Biol* 225: 215–225. 1982.

[10] **Bagh S, Mandal M, McMillen DR**. Minimal genetic device with multiple tunable functions. *Phys Rev E* 82: 021911–1 – 021911–8. 2010.

[11] **Baker GF, Widdas WF**. The asymmetry of the facilitated transfer system for hexoses in human red cells and the simple kinetics of a two component model. *J Physiol* 231: 143–165. 1973.

[12] **Barkai N, Leibler S**. Robustness in simple biochemical networks. *Nature* 387: 913–917. 1997.

[13] **Barken D, Wang CJ, Kearns J, Cheong R, Hoffmann A, Levchenko A**. Comment on "Oscillations in NF-κB signaling control the dynamics of gene expression". *Science* 308: 52a. 2005.

[14] **Beauvois MC, Merezak C, Jonas JC, Ravier MA, Henquin JC, Gilon P**. Glucose-induced mixed $[Ca^{2+}]_c$ oscillations in mouse β-cells are controlled by the membrane potential and the SERCA3 Ca^{2+}-ATPase of the endoplasmic reticulum. *Am J Physiol Cell Physiol* 290: C1503–C1511. 2006.

[15] **Beck JS, Breton S, Mairbäurl H, Laprade R, Giebisch G**. Relationship between sodium transport and intracellular ATP in isolated perfused rabbit proximal convoluted tubule. *Am J Physiol Renal Physiol* 261: F634–F639. 1991.

[16] **Begley CG, Ellis LM**. Drug development: raise standards for preclinical cancer research. *Nature* 483: 531–533. 2012.

[17] **Berridge MJ, Bootman MD, Roderick HL**. Calcium signalling: dynamics, homeostasis and remodelling. *Nat Rev Mol Cell Biol* 4: 517–529. 2003.

[18] **Berridge MJ, Rapp PE**. A comparative survey of the function, mechanism and control of cellular oscillators. *J Exp Biol* 81: 217–279. 1979.

[19] **Berryman AA**. The origins and evolution of predator-prey theory. *Ecology* 73: 1530–1535. 1992.

[20] **Blot-Chabaud M, Wanstok F, Bonvalet JP, Farman N**. Cell sodium-induced recruitment of Na^+-K^+-ATPase pumps in rabbit cortical collecting tubules is aldosterone-dependent. *J Biol Chem* 265: 11676–11681. 1990.

[21] **Boiteux A, Goldbeter A, Hess B**. Control of oscillating glycolysis of yeast by stochastic, periodic, and steady source of substrate: A model and experimental study. *Proc Natl Acad Sci USA : Biochemistry* 72: 3829–3833. 1975.

[22] **Brown PD, Sepúlveda FV**. Potassium movements associated with amino acid and sugar transport in enterocytes isolated from rabbit jejunum. *J Physiol* 363: 271–285. 1985.

[23] **Calderone V, Dolderer B, Hartmann HJ, Echner H, Luchinat C, Del Bianco C, Mangani S, Weser U**. The crystal structure of yeast copper thionein: the solution of a long-lasting enigma. *Proc Natl Acad Sci USA* 102: 51–56. 2005.

[24] **Cannon WB**. Organization for physiological homeostasis. *Physiol Rev* 9: 399–431. 1929.

[25] **Cannon WB**. *The Wisdom of the Body*. New York, NY, USA: W. W. Norton & Company Reprint 1967 Norton Library, 2nd edn. 1939.

[26] **Cheng H, Lederer WJ**. Calcium sparks. *Physiol Rev* 88: 1491–1545. 2008.

[27] **Cheong R, Hoffmann A, Levchenko A**. Understanding NF-κB signaling via mathematical modeling. *Mol Syst Biol* 4: (192) 1–11. 2008.

[28] **Cheong R, Levchenko A**. Oscillatory signaling processes: the how, the why and the where. *Curr Opin Genet Dev* 20: 665–669. 2010.

[29] **Cherry JM**. Genetic nomenclature guide: Saccharomyces cerevisiae. *Trends Genet* 14: S.10–S.11. 1998.

[30] **Cherry JM, Hong EL, Amundsen C, Balakrishnan R, Binkley G, Chan ET, Christie KR, Costanzo MC, Dwight SS, Engel SR, Fisk DG, Hirschman JE, Hitz BC, Karra K, Krieger CJ, Miyasato SR, Nash RS, Park J, Skrzypek MS, Simison M, Weng S, Wong ED**. Saccharomyces genome database: the genomics resource of budding yeast. *Nucleic Acids Res* 40: D700–D705. 2012.

[31] **Clynes M**. Cybernetic implications of rein control in perceptual and conceptual organization. *Ann N Y Acad Sci* 156: 629–664. 1969.

[32] **Conrad ED, Tyson JJ**. Modeling molecular interaction networks with nonlinear ordinary differential equations. In: *System Modeling in Cellular Biology: From Concepts to Nuts and Bolts*, edited by Szallasi Z, Stelling J, Periwal V chap. 6, 97–123. Cambridge, MA, USA: MIT Press. 2006.

[33] **Corlan AD**. Medline trend: automated yearly statistics of PubMed results for any query. Available from: `http://dan.corlan.net/medline-trend.html` (Accessed 2015-08-12). 2004.

[34] **Cormack BP, Bertram G, Egerton M, Gow NAR, Falkow S, Brown AJP**. Yeast-enhanced green fluorescent protein (yEGFP): a reporter of gene expression in Candida albicans. *Microbiology* 143: 303–311. 1997.

[35] **Cornish-Bowden A**. *Fundamentals of Enzyme Kinetics*. Weinheim, Germany: Wiley-Blackwell 4 edn. 2012.

[36] **Cosentino C, Bates D**. *Feeback Control In Systems Biology*. Boca Raton, FL, USA: CRC Press. 2012.

[37] **Craig Heller H, Colliver GW, Beard J**. Thermoregulation during entrance into hibernation. *Pflügers Arch* 369: 55–59. 1977.

[38] **Danø S, Hynne F, De Monte S, d'Ovidio F, Sørensen PG, Westerhoff H**. Synchronization of glycolytic oscillations in a yeast cell population. *Faraday Discuss* 120: 261–276. 2001.

[39] **Dancis A, Haile D, Yuan DS, Klausner RD**. The Saccharomyces cerevisiae copper transport protein (Ctr1p). Biochemical characterization, regulation by copper, and physiologic role in copper uptake. *J Biol Chem* 269: 25660–25667. 1994.

[40] **Dancis A, Yuan DS, Haile D, Askwith C, Eide D, Moehle C, Kaplan J, Klausner RD**. Molecular characterization of a copper transport protein in S. cerevisiae: an unexpected role for copper in iron transport. *Cell* 76: 393–402. 1994.

[41] **Davis PK, Wu G**. Compartmentation and kinetics of urea cycle enzymes in porcine enterocytes. *Comp Biochem Physiol B Biochem Mol Biol* 119: 527–537. 1998.

[42] **Dolderer B, Hartmann HJ, Weser U**. Metallothiens in yeast and fungi. In: *Metal Ions in Life Sciences Vol 5: Metallothioneins and Related Chelators*, edited by Sigel A, Sigel H, Sigel RKO chap. 4, 83–105. Cambridge, UK: The Royal Society of Chemistry. 2009.

[43] **Domaille DW, Que EL, Chang CJ**. Synthetic fluorescent sensors for studying the cell biology of metals. *Nat Chem Biol* 4: 168–175. 2008.

[44] **Drengstig T, Ueda HR, Ruoff P**. Predicting perfect adaptation motifs in reaction kinetic networks. *J Phys Chem B* 112: 16752–16758. 2008.

[45] **Drews G**. Contributions of Theodor Wilhelm Engelmann on phototaxis, chemotaxis, and photosynthesis. *Photosynth Res* 83: 25–34. 2005.

[46] **Dubinsky WP, Mayorga-Wark O, Schultz SG**. Potassium channels in basolateral membrane vesicles from Necturus enterocytes: stretch and ATP sensitivity. *Am J Physiol Cell Physiol* 279: C634–C638. 2000.

[47] **Dunham M, Gartenbeg M, Brown GW**. *Methods in Yeast Genetics and Genomics A CSHL Course Manual 2014*. Cold Spring Harbor, NY, USA. 2014.

[48] **Dunlap JC, Loros JJ, DeCoursey PJ**, editors. *Chronobiology Biological Timekeeping*. Sunderland, MA, USA: Sinauer Associates. 2004.

[49] **Editorial**. Must try harder. *Nature* 483: 509. 2012.

[50] **Efendiev R, Bertorello AM, Zandomeni R, Cinelli AR, Pedemonte CH**. Agonist-dependent regulation of renal Na^+,K^+-ATPase activity is modulated by intracellular sodium concentration. *J Biol Chem* 277: 11489–11496. 2002.

[51] **Elgerd OI**. *Control Systems Theory*. Tokyo, Japan: McGraw-Hill Kogakusha. 1967.

[52] **Elowitz MB, Leibler S**. A synthetic oscillatory network of transcriptional regulators. *Nature* 403: 335–338. 2000.

[53] **Feldmann H, Branduardi P, Dujon B, Gaillardin C, Porro D**. *Yeast: Molecular and Cell Biology*. Weinheim, Germany: Wiley-VCH Verlag GmbH & Co. KGaA 2 edn. Editor: Feldmann H. 2012.

[54] **Francis BA, Wonham WM**. The internal model principle for linear multivariable regulators. *Appl Math Optim* 2: 170–194. 1975.

[55] **Fraser SJ**. The steady state and equilibrium approximations: a geometrical picture. *J Chem Phys* 88: 4732–4738. 1988.

[56] **Fridlyand LE, Tamarina N, Philipson LH**. Bursting and calcium oscillations in pancreatic β-cells: specific pacemakers for specific mechanisms. *Am J Physiol Endocrinol Metab* 299: E517–E532. 2010.

[57] **Gadsby DC, Nakao M**. Steady-state current-voltage relationship of the Na/K pump in guinea pig ventricular myocytes. *J Gen Physiol* 94: 511–537. 1989.

[58] **Gaggelli E, Kozlowski H, Valensin D, Valensin G**. Copper homeostasis and neurodegenerative disorders (Alzheimer's, prion, and Parkinson's diseases and amyotrophic lateral sclerosis). *Chem Rev* 106: 1995–2044. 2006.

[59] **Gardner TS, Cantor CR, Collins JJ**. Construction of a genetic toggle switch in Escherichia coli. *Nature* 403: 339–342. 2000.

[60] **Gibson DG, Young L, Chuang RY, Venter JC, Hutchison CA, Smith HO**. Enzymatic assembly of DNA molecules up to several hundred kilobases. *Nat Methods* 6: 343–345. 2009.

[61] **Goffeau A, Barrell BG, Bussey H, Davis RW, Dujon B, Feldmann H, Galibert F, Hoheisel JD, Jacq C, Johnston M, Louis EJ, Mewes HW, Murakami Y, Philippsen P, Tettelin H, Oliver SG**. Life with 6000 genes. *Science* 274: 546, 563–567. 1996.

[62] **Goldbeter A**. Computational approaches to cellular rhythms. *Nature* 420: 238–245. 2002.

[63] **Goodwin BC**. *Temporal Organization in Cells - A Dynamic Theory of Cellular Control Processes*. London, UK: Academic Press. 1963.

[64] **Goodwin BC**. Oscillatory behavior in enzymatic control processes. *Adv Enzyme Regul* 3: 425–438. 1965.

[65] **Grasset E, Gunter-Smith P, Schultz SG**. Effects of Na-coupled alanine transport on intracellular K activities and the K conductance of the basolateral membranes of Necturus small intestine. *J Membr Biol* 71: 89–94. 1983.

[66] **Griffith JS**. Mathematics of cellular control processes I. Negative feedback to one gene. *J Theor Biol* 20: 202–208. 1968.

[67] **Gromada J, Duttaroy A, Rorsman P**. The insulin receptor talks to glucagon? *Cell Metab* 9: 303–305. 2009.

[68] **Guido NJ, Wang X, Adalsteinsson D, McMillen DR, Hasty J, Cantor CR, Elston TC, Collins JJ**. A bottom-up approach to gene regulation. *Nature* 439: 856–860. 2006.

[69] **Guyton AC, Hall JE**. *Textbook of Medical Physiology*. Philadelphia, PA, USA: Elsevier Saunders 11 edn. 2006.

[70] **Hartmann T, Verkman AS**. Model of ion transport regulation in chloride-secreting airway epithelial cells. Integrated description of electrical, chemical, and fluorescence measurements. *Biophys J* 58: 391–401. 1990.

[71] **Hassett R, Dix DR, Eide DJ, Kosman DJ**. The Fe(II) permease Fet4p functions as a low affinity copper transporter and supports normal copper trafficking in Saccharomyces cerevisiae. *Biochem J* 351: 477–484. 2000.

[72] **Hastings JW, Sweeney BM**. On the mechanism of temperature independence in a biological clock. *Proc Natl Acad Sci USA* 43: 804–811. 1957.

[73] **Haupts U, Tittor J, Oesterhelt D**. Closing in on bacteriorhodopsin: progress in understanding the molecule. *Annu Rev Biophys Biomol Struct* 28: 367–399. 1999.

[74] **Heitzmann D, Warth R**. Physiology and pathophysiology of potassium channels in gastrointestinal epithelia. *Physiol Rev* 88: 1119–1182. 2008.

[75] **Higgins J**. The theory of oscillating reactions - kinetics symposium. *Ind Eng Chem* 59: 18–62. 1967.

[76] **Hill AV**. The possible effects of the aggregation of the molecules of hæmoglobin on its dissociation curves. *The Journal of Physiology* 40: iv–vii. Supplement - Proceedings of the physiological society. 1910.

[77] **Holde KEV, Miller KI**. Hemocyanins. In: *Adv Protein Chem*, edited by Anfinsen C, Richards FM, Edsall JT, Eisenberg DS vol. 47 chap. 1, 1–81. San Diego, CA, USA: Academic Press. 1995.

[78] **Hudson RL, Schultz SG**. Sodium-coupled sugar transport: effects on intracellular sodium activities and sodium-pump activity. *Science* 224: 1237–1239. 1984.

[79] **Ideker T, Galitski T, Hood L**. A new approach to decoding life: systems biology. *Annu Rev Genomics Hum Genet* 2: 343–372. 2001.

[80] **Iglesias PA, Ingalls BP**, editors. *Control Theory and Systems Biology*. Cambridge, MA, USA: MIT Press. 2010.

[81] **Ikeda TS, Hwang ES, Coady MJ, Hirayama BA, Hediger MA, Wright EM**. Characterization of a Na^+/glucose cotransporter cloned from rabbit small intestine. *J Membr Biol* 110: 87–95. 1989.

[82] **Ingalls BP**. *Mathematical Modeling in Systems Biology: An Introduction*. Cambridge, MA, USA: MIT Press. 2013.

[83] **Isidori A, Byrnes CI**. Output regulation of nonlinear systems. *IEEE Trans Automat Contr* 35: 131–140. 1990.

[84] **Jensen LT, Howard WR, Strain JJ, Winge DR, Culotta VC**. Enhanced effectiveness of copper ion buffering by CUP1 metallothionein compared with CRS5 metallothionein in Saccharomyces cerevisiae. *J Biol Chem* 271: 18514–18519. 1996.

[85] **Jolma IW, Ni XY, Rensing L, Ruoff P**. Harmonic oscillations in homeostatic controllers: dynamics of the p53 regulatory system. *Biophys J* 98: 743–752. 2010.

[86] **Kabakov AY**. Activation of K_{ATP} channels by Na/K pump in isolated cardiac myocytes and giant membrane patches. *Biophys J* 75: 2858–2867. 1998.

[87] **Kachroo AH, Laurent JM, Yellman CM, Meyer AG, Wilke CO, Marcotte EM**. Systematic humanization of yeast genes reveals conserved functions and genetic modularity. *Science* 348: 921–925. 2015.

[88] **Kaiser J**. The cancer test. *Science* 348: 1411–1413. 2015.

[89] **Kawamori D, Kurpad AJ, Hu J, Liew CW, Shih JL, Ford EL, Herrera PL, Polonsky KS, McGuinness OP, Kulkarni RN**. Insulin signaling in α cells modulates glucagon secretion in vivo. *Cell Metab* 9: 350–361. 2009.

[90] **Kellett GL**. The facilitated component of intestinal glucose absorption. *J Physiol* 531: 585–595. 2001.

[91] **Khalil AS, Collins JJ**. Synthetic biology: applications come of age. *Nat Rev Genet* 11: 367–379. 2010.

[92] **Khalil HK**. *Nonlinear Systems*. Upper Saddle River, NJ, USA: Prentice Hall 3 edn. 2002.

[93] **Khoursandi S, Scharlau D, Herter P, Kuhnen C, Martin D, Kinne RKH, Kipp H**. Different modes of sodium-D-glucose cotransporter-mediated D-glucose uptake regulation in Caco-2 cells. *Am J Physiol Cell Physiol* 287: C1041–C1047. 2004.

[94] **Kipp H, Khoursandi S, Scharlau D, Kinne RKH**. More than apical: distribution of SGLT1 in Caco-2 cells. *Am J Physiol Cell Physiol* 285: C737–C749. 2003.

[95] **Kitano H**. Systems biology: a brief overview. *Science* 295: 1662–1664. 2002.

[96] **Klimstra DS, Hruban RH, Pitman MB**. Pancreas. In: *Histology for Pathologists*, edited by Mills SE chap. 30, 723–760. Philadelphia, PA, USA: Lippincott Williams & Wilkins 3 edn. 2007.

[97] **Knight SAB, Labbé S, Kwon LF, Kosman DJ, Thiele DJ**. A widespread transposable element masks expression of a yeast copper transport gene. *Genes Dev* 10: 1917–1929. 1996.

[98] **Knudsen OS**. *Biological Membranes Theory of Transport, Potentials and Electric Impulses*. Cambridge, UK: Cambridge University Press. 2002.

[99] **Koch KA, Peña MMO, Thiele DJ**. Copper-binding motifs in catalysis, transport, detoxification and signaling. *Chem Biol* 4: 549–560. 1997.

[100] **Labbé S, Thiele DJ**. Copper ion inducible and repressible promoter systems in yeast. *Methods In Enzymology* 306: 145–153. 1999.

[101] **Labbé S, Zhu Z, Thiele DJ**. Copper-specific transcriptional repression of yeast genes encoding critical components in the copper transport pathway. *J Biol Chem* 272: 15951–15958. 1997.

[102] **Langley LL**, editor. *Homeostasis Origins of the Concept, Benchmark Papers in Human Physiology*. Stroudsburg, PA, USA: Dowden, Hutchinson & Ross. 1973.

[103] **Latta R, Clausen C, Moore LC**. General method for the derivation and numerical solution of epithelial transport models. *J Membr Biol* 82: 67–82. 1984.

[104] **Lazebnik Y**. Can a biologist fix a radio?—Or, what I learned while studying apoptosis. *Cancer Cell* 2: 179–182. 2002.

[105] **Levine JH, Lin Y, Elowitz MB**. Functional roles of pulsing in genetic circuits. *Science* 342: 1193–1200. 2013.

[106] **Lingrel JB**. Na,K-ATPase: isoform structure, function, and expression. *J Bioenerg Biomembr* 24: 263–270. 1992.

[107] **Liu J, Karpus J, Wegner SV, Chen PR, He C**. Genetically encoded copper(I) reporters with improved response for use in imaging. *J Am Chem Soc* 135: 3144–3149. 2013.

[108] **Liu W**. *Introduction to Modeling Biological Cellular Control Systems*. Milano, Italy: Springer Verlag Italia S.r.l. 2012.

[109] **Lloyd D, Aon MA, Cortassa S**. Why homeodynamics, not homeostasis? *ScientificWorldJournal* 1: 133–145. 2001.

[110] **Loría A, Panteley E**. Stability, told by its developers. In: *Advanced Topics in Control Systems Theory*, edited by Loriá A, Lamnabhi-Lagarrigue F, Panteley E chap. 6, 199–258. Berlin/Heidelberg, Germany: Springer-Verlag. 2006.

[111] **Lotka AJ**. Analytical note on certain rhythmic relations in organic systems. *Proc Natl Acad Sci USA* 6: 410–415. 1920.

[112] **Lotka AJ**. Undamped oscillations derived from mass action. *J Am Chem Soc* 42: 1595–1599. 1920.

[113] **Mace OJ, Affleck J, Patel N, Kellett GL**. Sweet taste receptors in rat small intestine stimulate glucose absorption through apical GLUT2. *J Physiol* 582: 379–392. 2007.

[114] **Maenz DD, Cheeseman CI**. The Na^+-independent D-glucose transporter in the enterocyte basolateral membrane: orientation and cytochalasin B binding characteristics. *J Membr Biol* 97: 259–266. 1987.

[115] **Marjanovic M, Willis JS**. Is the pump of intact red blood cells saturated for ATP at physiological concentrations? In: *The Sodium Pump: Recent Developments - Society of General Physiologists 44th Annual Symposium*, edited by Kaplan JH, Weer PD 457–459. New York, NY, USA: The Rockefeller University Press. 1990.

[116] **Marshall SA**. *Introduction to Control Theory*. London, UK: Macmillian Press. 1978.

[117] **Marvin ME, Williams PH, Cashmore AM**. The Candida albicans CTR1 gene encodes a functional copper transporter. *Microbiology* 149: 1461–1474. 2003.

[118] **Mazumder M, McMillen DR**. Design and characterization of a dual-mode promoter with activation and repression capability for tuning gene expression in yeast. *Nucleic Acids Res* 42: 9514–9522. 2014.

[119] **Mengel B, Hunziker A, Pedersen L, Trusina A, Jensen MH, Krishna S**. Modeling oscillatory control in NF-κB, p53 and Wnt signaling. *Curr Opin Genet Dev* 20: 656–664. 2010.

[120] **Mobley A, Linder SK, Braeuer R, Ellis LM, Zwelling L**. A survey on data reproducibility in cancer research provides insights into our limited ability to translate findings from the laboratory to the clinic. *PLOS ONE* 8: 1–4. 2013.

[121] **Moore-Ede MC**. Physiology of the circadian timing system: predictive versus reactive homeostasis. *Am J Physiol Regul Integr Comp Physiol* 250: R737–R752. 1986.

[122] **Mortensen A, Blix AS**. Seasonal changes in the effects of starvation on metabolic rate and regulation of body weight in Svalbard Ptarmigan. *Ornis Scandinavica* 16: 20–24. 1985.

[123] **Mrosovsky N**. *Rheostasis The Physiology of Change*. New York, NY, USA: Oxford University Press. 1990.

[124] **Mrosovsky N, Sherry DF**. Animal anorexias. *Science* 207: 837–842. 1980.

[125] **Nakao M, Gadsby DC**. [Na] and [K] dependence of the Na/K pump current-voltage relationship in guinea pig ventricular myocytes. *J Gen Physiol* 94: 539–565. 1989.

[126] **National Center for Biotechnology Information US National Library of Medicine**. PubMed Search [Internet]. Available from: `http://www.ncbi.nlm.nih.gov/pubmed` (Accessed 2015-08-12).

[127] **Nellans HN, Frizzell RA, Schultz SG**. Coupled sodium-chloride influx across the brush border of rabbit ileum. *Am J Physiol* 225: 467–475. 1973.

[128] **Nellans HN, Schultz SG**. Relations among transepithelial sodium transport, potassium exchange, and cell volume in rabbit ileum. *J Gen Physiol* 68: 441–463. 1976.

[129] **Nelson DE, Ihekwaba AEC, Elliott M, Johnson JR, Gibney CA, Foreman BE, Nelson G, See V, Horton CA, Spiller DG, Edwards SW, McDowell HP, Unitt JF, Sullivan E, Grimley R, Benson N, Broomhead D, Kell DB, White MRH**. Oscillations in NF-κB signaling control the dynamics of gene expression. *Science* 306: 704–708. 2004.

[130] **Ni XY, Drengstig T, Ruoff P**. The control of the controller: molecular mechanisms for robust perfect adaptation and temperature compensation. *Biophys J* 97: 1244–1253. 2009.

[131] **Nose Y, Rees EM, Thiele DJ**. Structure of the Ctr1 copper trans'PORE'ter reveals novel architecture. *Trends Biochem Sci* 31: 604–607. 2006.

[132] **Novák B, Tyson JJ**. Design principles of biochemical oscillators. *Nat Rev Mol Cell Biol* 9: 981–991. 2008.

[133] **Okada Y, Sato T, Inouye A**. Effects of potassium ions and sodium ions on membrane potential of epithelial cells in rat duodenum. *Biochim Biophys Acta* 413: 104–115. 1975.

[134] **Ooi CE, Rabinovich E, Dancis A, Bonifacino JS, Klausner RD**. Copper-dependent degradation of the Saccharomyces cerevisiae plasma membrane copper transporter Ctr1p in the apparent absence of endocytosis. *EMBO J* 15: 3515–3523. 1996.

[135] **Panda S, Hogenesch JB, Kay SA**. Circadian rhythms from flies to human. *Nature* 417: 329–335. 2002.

[136] **Pappenheimer JR**. Intestinal absorption of hexoses and amino acids: from apical cytosol to villus capillaries. *J Membr Biol* 184: 233–239. 2001.

[137] **Parekh AB**. Decoding cytosolic Ca^{2+} oscillations. *Trends Biochem Sci* 36: 78–87. 2011.

[138] **Parent L, Supplisson S, Loo DDF, Wright EM**. Electrogenic properties of the cloned Na^+/glucose cotransporter: I. Voltage-clamp studies. *J Membr Biol* 125: 49–62. 1992.

[139] **Parent L, Supplisson S, Loo DDF, Wright EM**. Electrogenic properties of the cloned Na^+/glucose cotransporter: II. A transport model under nonrapid equilibrium conditions. *J Membr Biol* 125: 63–79. 1992.

[140] **Peña MMO, Koch KA, Thiele DJ**. Dynamic regulation of copper uptake and detoxification genes in Saccharomyces cerevisiae. *Mol Cell Biol* 18: 2514–2523. 1998.

[141] **Pham AN, Xing G, Miller CJ, Waite TD**. Fenton-like copper redox chemistry revisited: hydrogen peroxide and superoxide mediation of copper-catalyzed oxidant production. *J Catal* 301: 54–64. 2013.

[142] **Prinz F, Schlange T, Asadullah K**. Believe it or not: how much can we rely on published data on potential drug targets? *Nat Rev Drug Discov* 10: 712. 2011.

[143] **Radhakrishnan K, Hindmarsh AC**. *Description and Use of LSODE, the Livermore Solver for Ordinary Differential Equations*. Tech. rep. Lawrence Livermore National Laboratory, Report UCRL-ID-113855 Livermore, CA, USA. NASA Reference Publication 1327. 1993.

[144] **Rae TD, Schmidt PJ, Pufahl RA, Culotta VC, Halloran TVO**. Undetectable intracellular free copper: the requirement of a copper chaperone for superoxide dismutase. *Science* 284: 805–808. 1999.

[145] **Rakowski RF, Gadsby DC, De Weer P**. Stoichiometry and voltage dependence of the sodium pump in voltage-clamped, internally dialyzed squid giant axon. *J Gen Physiol* 93: 903–941. 1989.

[146] **Reuss L**. Epithelial transport. In: *Handbook of Physiology Section 14 - Cell Physiology*, edited by Hoffman JF, Jamieson JD chap. 8, 309–388. New York, NY, USA: Oxford University Press for Am. Physiol. Soc. 1997.

[147] **Riggle PJ, Kumamoto CA**. Role of a Candida albicans P1-type ATPase in resistance to copper and silver ion toxicity. *J Bacteriol* 182: 4899–4905. 2000.

[148] **Rokaw MD, Sarac E, Lechman E, West M, Angeski J, Johnson JP, Zeidel ML**. Chronic regulation of transepithelial Na^+ transport by the rate of apical Na^+ entry. *Am J Physiol Cell Physiol* 270: C600–C607. 1996.

[149] **Rolls BJ, Rowe EA, Turner RC**. Persistent obesity in rats following a period of consumption of a mixed, high energy diet. *J Physiol* 298: 415–427. 1980.

[150] **Rose F, Hodak M, Bernholc J**. Mechanism of copper(II)-induced misfolding of Parkinson's disease protein. *Sci Rep* 1: 1–5. 2011.

[151] **Rose RC, Schultz SG**. Studies on the electrical potential profile across rabbit ileum effects of sugars and amino acids on transmural and transmucosal electrical potential difference. *J Gen Physiol* 57: 639–663. 1971.

[152] **Rosenblueth A, Wiener N, Bigelow J**. Behavior purpose and teleology. *Philos Sci* 10: 18–24. 1943.

[153] **Ruoff P, Zakhartsev M, Westerhoff HV**. Temperature compensation through systems biology. *FEBS J* 274: 940–950. 2007.

[154] **Sato K, Kohzuma T, Dennison C**. Active-site structure and electron-transfer reactivity of plastocyanins. *J Am Chem Soc* 125: 2101–2112. 2003.

[155] **Saunders PT, Koeslag JH, Wessels JA**. Integral rein control in physiology. *J Theor Biol* 194: 163–173. 1998.

[156] **Saunders PT, Koeslag JH, Wessels JA**. Integral rein control in physiology II: a general model. *J Theor Biol* 206: 211–20. 2000.

[157] **Schultz SG**. *Basic Principles of Membrane Transport*. Cambridge, UK: Cambridge University Press. 1980.

[158] **Schultz SG**. Cellular models of epithelial ion transport. In: *Membrane Transport Processes in Organized Systems*, edited by Andreoli TE, Hoffman JF, Fanestil DD, Schultz SG 135–150. New York, NY, USA: Plenum Publishing. 1987.

[159] **Schultz SG, Hudson RL**. How do sodium-absorbing cells do their job and survive? *Physiol* 1: 185–189. 1986.

[160] **Schultz SG, Hudson RL**. Biology of sodium-absorbing epithelial cells: dawning of a new era. In: *Supplement 19: Handbook of Physiology. The Gastrointestinal System, Intestinal Absorption and Secretion* chap. 2, 45–81. Bethesda, MD, USA: Am. Physiol. Soc. 1991.

[161] **Sel'kov EE**. Self-oscillations in glycolysis. *Eur J Biochem* 4: 79–86. 1968.

[162] **Senatorov VV, Stys PK, Hu B**. Regulation of Na^+,K^+-ATPase by persistent sodium accumulation in adult rat thalamic neurones. *J Physiol* 525: 343–353. 2000.

[163] **SGD**. The Saccharomyces Genome Database (SGD Project). Available online: `http://www.yeastgenome.org/`.

[164] **Sherry DF, Mrosovsky N, Hogan JA**. Weight loss and anorexia during incubation in birds. *J Comp Physiol Psychol* 94: 89–98. 1980.

[165] **Sikorski RS, Hieter P**. A system of shuttle vectors and yeast host strains designed for efficient manipulation of DNA in Saccharomyces cerevisiae. *Genetics* 122: 19–27. 1989.

[166] **Sontag ED**. Adaptation and regulation with signal detection implies internal model. *Syst Control Lett* 50: 119–126. 2003.

[167] **Spiro PA, Parkinson JS, Othmer HG**. A model of excitation and adaptation in bacterial chemotaxis. *Proc Natl Acad Sci USA* 94: 7263–7268. 1997.

[168] **Stauffer EA, Holt JR**. Sensory transduction and adaptation in inner and outer hair cells of the mouse auditory system. *J Neurophysiol* 98: 3360–3369. 2007.

[169] **Stearns AT, Balakrishnan A, Rhoads DB, Tavakkolizadeh A**. Rapid upregulation of sodium-glucose transporter SGLT1 in response to intestinal sweet taste stimulation. *Ann Surg* 251: 865–871. 2010.

[170] **Steele R**. Influences of glucose loading and of injected insulin on hepatic glucose output. *Ann N Y Acad Sci* 82: 420–430. 1959.

[171] **Stelling J, Sauer U, Szallasi Z, Doyle III FJ, Doyle J**. Robustness of cellular functions. *Cell* 118: 675–685. 2004.

[172] **Stephenson JL, Tewarson RP, Mejia R**. Quantitative analysis of mass and energy balance in non-ideal models of the renal counterflow system. *Proc Natl Acad Sci USA* 71: 1618–1622. 1974.

[173] **Strogatz SH**. *Nonlinear Dynamics and Chaos*. Cambridge, MA, USA: Westview Press. 1994.

[174] **Tengholm A, Gylfe E**. Oscillatory control of insulin secretion. *Mol Cell Endocrinol* 297: 58–72. 2009.

[175] **Therien AG, Blostein R**. Mechanisms of sodium pump regulation. *Am J Physiol Cell Physiol* 279: C541–C566. 2000.

[176] **Thiele DJ, Hamer DH**. Tandemly duplicated upstream control sequences mediate copper-induced transcription of the Saccharomyces cerevisiae copper-metallothionein gene. *Mol Cell Biol* 6: 1158–1163. 1986.

[177] **Thorens B, Cheng ZQ, Brown D, Lodish HF**. Liver glucose transporter: a basolateral protein in hepatocytes and intestine and kidney cells. *Am J Physiol Cell Physiol* 259: C279–C285. 1990.

[178] **Tsuchiya K, Wang W, Giebisch G, Welling PA**. ATP is a coupling modulator of parallel Na,K-ATPase-K-channel activity in the renal proximal tubule. *Proc Natl Acad Sci USA* 89: 6418–6422. 1992.

[179] **Turchin P, Taylor AD**. Complex dynamics in ecological time series. *Ecology* 73: 289–305. 1992.

[180] **Tyson JJ**. Biochemical oscillations. In: *Computational Cell Biology* chap. 9, 230–260. New York, NY: Springer New York. 2002.

[181] **Verkman AS, Alpern RJ**. Kinetic transport model for cellular regulation of pH and solute concentration in the renal proximal tubule. *Biophys J* 51: 533–546. 1987.

[182] **Volterra V**. Variations and fluctuations of the number of individuals in animal species living together. *J Cons Int Explor Mer* 3: 3–51. 1928.

[183] **Wall JS, Steele R, de Bodo RC, Altszuler N**. Effect of insulin on utilization and production of circulating glucose. *Am J Physiol* 189: 43–50. 1957.

[184] **Wang B, Kitney RI, Joly N, Buck M**. Engineering modular and orthogonal genetic logic gates for robust digital-like synthetic biology. *Nat Commun* 2: 508:1–9. 2011.

[185] **Warth R, Barhanin J**. Function of K^+ channels in the intestinal epithelium. *J Membr Biol* 193: 67–78. 2003.

[186] **Waterhouse JM, DeCoursey PJ**. Human circadian organization. In: *Chronobiology Biological Timekeeping*, edited by Dunlap JC, Loros JJ, DeCoursey PJ chap. 9, 291–324. Sunderland, MA, USA: Sinauer Associates. 2004.

[187] **Waters BM, Eide DJ**. Combinatorial control of yeast FET4 gene expression by iron, zinc, and oxygen. *J Biol Chem* 277: 33749–33757. 2002.

[188] **Wegner SV, Arslan H, Sunbul M, Yin J, He C**. Dynamic copper(I) imaging in mammalian cells with a genetically encoded fluorescent copper(I) sensor. *J Am Chem Soc* 132: 2567–2569. 2010.

[189] **Wegner SV, Sun F, Hernandez N, He C**. The tightly regulated copper window in yeast. *Chem Commun* 47: 2571–2573. 2011.

[190] **Weinstein AM**. Nonequilibrium thermodynamic model of the rat proximal tubule epithelium. *Biophys J* 44: 153–170. 1983.

[191] **Weinstein AM**. Glucose transport in a model of the rat proximal tubule epithelium. *Math Biosci* 76: 87–115. 1985.

[192] **Weinstein AM**. A mathematical model of the rat proximal tubule. *Am J Physiol Renal Physiol* 250: F860–F873. 1986.

[193] **Weinstein AM**. Chloride transport in a mathematical model of the rat proximal tubule. *Am J Physiol Renal Physiol* 263: F784–F798. 1992.

[194] **Weinstein AM**. Ammonia transport in a mathematical model of rat proximal tubule. *Am J Physiol Renal Physiol* 267: F237–F248. 1994.

[195] **Weinstein AM**. Modeling epithelial cell homeostasis: steady-state analysis. *Bull Math Biol* 61: 1065–1091. 1999.

[196] **Weinstein AM**. Modeling epithelial cell homeostasis: assessing recovery and control mechanisms. *Bull Math Biol* 66: 1201–1240. 2004.

[197] **Weinstein AM, Stephenson JL**. Electrolyte transport across a simple epithelium steady-state and transient analysis. *Biophys J* 27: 165–186. 1979.

[198] **Weissman Z, Berdicevsky I, Cavari BZ, Kornitzer D**. The high copper tolerance of Candida albicans is mediated by a P-type ATPase. *Proc Natl Acad Sci USA* 97: 3520–3525. 2000.

[199] **Wiener N**. *The Human Use of Human Beings, Cybernetics and Society*. Boston, MA, USA: Hougthon Mifflin 2nd edn. 1954.

[200] **Wiener N**. *Cybernetics: or Control and Communication in the Animal and the Machine*. Cambridge, MA, USA: MIT Press 2nd edn. 1965.

[201] **Wright EM, Loo DDF, Hirayama BA**. Biology of human sodium glucose transporters. *Physiol Rev* 91: 733–794. 2011.

[202] **Xu E, Kumar M, Zhang Y, Ju W, Obata T, Zhang N, Liu S, Wendt A, Deng S, Ebina Y, Wheeler MB, Braun M, Wang Q**. Intra-islet insulin suppresses glucagon release via GABA-$GABA_A$ receptor system. *Cell Metab* 3: 47–58. 2006.

[203] **Yamada KM, Hall A**. Reproducibility and cell biology. *J Cell Biol* 209: 191–193. 2015.

[204] **Yamamoto K, Ikeda U, Seino Y, Tsuruya Y, Oguchi A, Okada K, Ishikawa S, Saito T, Kawakami K, Hara Y, Shimada K**. Regulation of Na,K-adenosine triphosphatase gene expression by sodium ions in cultured neonatal rat cardiocytes. *J Clin Invest* 92: 1889–1895. 1993.

[205] **Yi TM, Huang Y, Simon MI, Doyle J**. Robust perfect adaptation in bacterial chemotaxis through integral feedback control. *Proc Natl Acad Sci USA* 97: 4649–4653. 2000.

[206] **Zheng Y, Scow JS, Duenes JA, Sarr MG**. Mechanisms of glucose uptake in intestinal cell lines: role of GLUT2. *Surgery* 151: 13–25. 2012.

Paper 1:
A Basic Set of Homeostatic Controller Motifs

Not available in UiS Brage due to copyright.

Paper 2: Robust Adaptation and Homeostasis by Autocatalysis

Not available in UiS Brage due to copyright.

Paper 3: Control Theoretic Properties of Physiological Controller Motifs

Not available in UiS Brage due to copyright.

Paper 4: Transepithelial glucose transport and Na/K homeostasis in enterocytes: an integrative model

Not available in UiS Brage due to copyright.

Paper 5:
Robust Concentration and Frequency Control in Oscillatory Homeostats

OPEN ACCESS Freely available online

PLOS ONE

Robust Concentration and Frequency Control in Oscillatory Homeostats

Kristian Thorsen[1], Oleg Agafonov[2], Christina H. Selstø[2], Ingunn W. Jolma[2], Xiao Y. Ni[2], Tormod Drengstig[1], Peter Ruoff[2]*

1 Department of Electrical Engineering and Computer Science, University of Stavanger, Stavanger, Norway, **2** Centre for Organelle Research, University of Stavanger, Stavanger, Norway

Abstract

Homeostatic and adaptive control mechanisms are essential for keeping organisms structurally and functionally stable. Integral feedback is a control theoretic concept which has long been known to keep a controlled variable A robustly (i.e. perturbation-independent) at a given set-point A_{set} by feeding the integrated error back into the process that generates A. The classical concept of homeostasis as robust regulation within narrow limits is often considered as unsatisfactory and even incompatible with many biological systems which show sustained oscillations, such as circadian rhythms and oscillatory calcium signaling. Nevertheless, there are many similarities between the biological processes which participate in oscillatory mechanisms and classical homeostatic (non-oscillatory) mechanisms. We have investigated whether biological oscillators can show robust homeostatic and adaptive behaviors, and this paper is an attempt to extend the homeostatic concept to include oscillatory conditions. Based on our previously published kinetic conditions on how to generate biochemical models with robust homeostasis we found two properties, which appear to be of general interest concerning oscillatory and homeostatic controlled biological systems. The first one is the ability of these oscillators ("oscillatory homeostats") to keep the average level of a controlled variable at a defined set-point by involving compensatory changes in frequency and/or amplitude. The second property is the ability to keep the period/frequency of the oscillator tuned within a certain well-defined range. In this paper we highlight mechanisms that lead to these two properties. The biological applications of these findings are discussed using three examples, the homeostatic aspects during oscillatory calcium and p53 signaling, and the involvement of circadian rhythms in homeostatic regulation.

Citation: Thorsen K, Agafonov O, Selstø CH, Jolma IW, Ni XY, et al. (2014) Robust Concentration and Frequency Control in Oscillatory Homeostats. PLoS ONE 9(9): e107766. doi:10.1371/journal.pone.0107766

Editor: Gianluca Tosini, Morehouse School of Medicine, United States of America

Received July 31, 2014; **Accepted** August 11, 2014; **Published** September 19, 2014

Data Availability: The authors confirm that all data underlying the findings are fully available without restriction. All relevant data are within the paper and its Supporting Information files.

Funding: Funding provided by Grant no. 167087/V40 by Norwegian Research Council (http://www.forskningsradet.no) for IWJ and Grant no. 183085/S10 by Norwegian Research Council (http://www.forskningsradet.no) for XYN. This research was also funded by Program Area Fund "Organelle Biology" and the Program Area Fund "Biomedical data analysis group" from the Faculty of Science and Technology, University of Stavanger (https://www.uis.no/fakulteter-institutter-og-sentre/). The funders had no role in study design, data collection and analysis, decision to publish, or preparation of the manuscript.

Competing Interests: The authors have declared that no competing interests exist.

* Email: peter.ruoff@uis.no

Introduction

The biological motivation of this work can be summarized as follows: How can homeostatic mechanisms possibly work when many or even most of the regulatory processes within a cell are based on oscillations? Versions of this question and how oscillatory processes participate in homeostatic and adaptive mechanisms have been repeatedly asked and discussed [1–5]. Our aim is to identify and build homeostatic/adaptive motifs on a rational basis with possible applications within physiology and synthetic biology. In this paper we apply control-engineering and kinetic methods and show how the classical concept of homeostasis [6,7] is linked to oscillatory behavior. We demonstrate how biological oscillators can have robust (perturbation-independent) homeostatic/adaptive behaviors both with respect to average concentration of a regulated variable and with respect to a robust control of the oscillator's frequency. By taking three examples, we argue that such properties appear closely linked to the controlled period lengths of the p53-Mdm2 oscillatory system and circadian rhythms [1,8] or to the homeostatic regulation of cytosolic calcium during signaling [9].

Organisms have developed defending homeostatic mechanisms in order to survive changing or stressful conditions by maintaining their internal physiologies at an approximately constant level [7,10,11]. In this respect, many compounds are tightly regulated within certain concentration ranges, because they are essential for cellular function, but may lead to dysfunction and diseases when their concentrations are outside of their regulated regimes. The term "homeostasis" was introduced by Cannon [6,7] to indicate that the internal milieu of an organism is regulated within narrow limits. The examples Cannon addresses in 1929 [6] are still actual research topics, such as the regulations of body temperature, blood sugar, blood calcium and blood pH levels [12–15]. Today many more homeostatic controlled compounds have been identified, including hormones [16], transcription factors and transcription factor related compounds [17], cellular ions such as plant nitrate

levels [18,19], iron [20], and calcium [21]. The Supplementary Material of Ref. [22] contains further examples.

Because many biochemical processes are oscillatory [1,8,23–27], Cannon's definition of homeostasis has been perceived as unsatisfactory and various alternative homeostasis concepts have been suggested. The term *predictive homeostasis* [1] has been introduced in order to stress the anticipatory homeostatic behavior of circadian regulation. Other concepts include *allostasis* [2,5] to focus on the concerted and interwoven nature of the defending mechanisms, *rheostasis* [3] to put emphasis on set-point changes, and *homeodynamics* [4] to stress the nonlinear kinetic behaviors of the defending mechanisms as part of an open system.

The appearance of cybernetics together with system theory [28–31] caused an interest to understand homeostasis and biological control from the angle of system analysis and control theory [32–39] by introducing control-engineering concepts such as *integral control* [22,40–45]. Integral control allows to keep a controlled variable (say A) precisely and robustly at a given set-point A_{set} by feeding the integrated error back into the process by which A is generated [46]. To gain insights how integral control and homeostasis may appear in biochemical and physiological processes, we started [43] to study two-component negative feedback controllers, where one component is the (homeostatic) controlled variable A, while the other is the manipulated or controller variable E. Each controller consists of the two species A and E and three fluxes, the inflow and outflow to and from E and an E -controlled compensatory flux (either inflow or outflow) of A, denoted j_{comp}. The compensatory flux compensates for disturbances in the level of A caused by perturbations in other uncontrolled inflows/outflows of A. By considering activating or inhibitory signaling events from A to E and vice versa, eight basic negative feedback configurations (controller motifs, Fig. 1a) can be created [22,47]. Two kinetic requirements leading to integral control have so far been identified, one based on a zero-order kinetic removal of the manipulated variable E [22,43,48], the other on an autocatalytic formation of E in association with a first-order degradation [45]. Fig. 1b gives a brief summary of these two kinetic approaches by using motif 5 as an example. For details, the reader is referred to [22,45]. We feel that this approach provides a rational basis to build networks which allow to view the behaviors of the individual controllers and to understand emergent properties of the overall network. By combining individual controller motifs with integral control we previously showed that an integrative and dynamic approach to cellular homeostasis is possible, which includes storage, excretion and remobilization of the controlled variables [19,22,49].

In the present study we extend the concept of homeostasis to include sustained oscillatory or pulsatile conditions. We show that oscillatory homeostats based on the controller motifs in Fig. 1a can maintain robust homeostasis in A. For controllers where E is inhibiting the compensatory flux (motifs 2, 4, 6, and 8, Fig. 1a), the frequency can be shown to depend on the level of E and therefore on the applied perturbation strength. In this class of controllers the frequency generally increases upon increased perturbation strengths; here we use motif 2 as a representative example. For the remaining controller motifs the frequency has been found to be less dependent upon perturbations. As a representative example for this behavior we use motif 5. We further show that robust frequency control can be achieved by either using additional controllers, which keep the average levels of A and E homeostatic regulated, or by using the intrinsic harmonic/quasi-harmonic properties of motifs 1 or 5. The biological significance of these findings is discussed with respect to the oscillatory signaling of cytosolic calcium and p53, as well as the regulating properties of circadian rhythms with respect to homeostasis and temperature compensation.

Results

Kinetic Approach to Implement Integral Control

We consider the negative feedback motifs in Fig. 1. A general condition for integral control can be formulated if the rate equation of the manipulated variable E allows for a rearrangement in form of two functions $g(E)$ and $h(A)$, and where the integral of $1/g(E)$ with respect to E exists and can be written as $G(E)$. Then, the set-point in A is determined by the solution of $h(A)=0$, i.e.

$$\dot{E} = h(A)\cdot g(E) \tag{1}$$

Rearranging Eq. 1 and requiring steady state conditions gives:

$$\frac{\dot{E}}{g(E)} = \dot{G}(E) = h(A) = 0 \tag{2}$$

Eq. 2 has been applied for nonoscillatory steady states with $g(E)=1$ by using zero-order kinetic degradation/inhibition of E [22,43] or with $g(E)=E$ by using first-order autocatalytic formation and degradation in E [45]. Other functions of $g(E)$ may be possible but plausible reaction kinetic mechanisms need to be identified. For the sake of simplicity, we consider here that integral control is achieved by a zero-order removal of E using $g(E)=1$.

To extend the condition of Eq. 2 to sustained stable and marginally stable oscillations, we observe that the integral of the periodic reaction rates $\dot{A}$ and $\dot{E}$ along a closed orbit c in the system's phase space is zero. For $\dot{E}$ this can be written as:

$$<\dot{E}>_c = \oint_c \dot{E}\,dt = \oint_c h(A)\,dt = 0 \tag{3}$$

Dependent on whether A is activating or inhibiting the production or removal of E, two expressions for the set-point of the oscillatory controller can be derived from Eq. 3. In case A is activating (motifs 1, 2, 5, 6) and by assuming first-order kinetics with respect to A in the rate equation for E, the set-point of A is given by (see Eq. S1 in (File S1))

$$<A>_c = \oint_c A(t)\,dt = <A>_{set} \tag{4}$$

where the integral is taken along one (or multiple) closed and stable orbit(s) in the system's phase space. With increasing time t, the average concentration of A, $<A>_t$, will approach its set-point $<A>_{set}$, i.e.,

$$<A>_t = \frac{1}{t}\cdot\int_0^t A(\tau)\,d\tau \rightarrow <A>_{set} \qquad \text{when} \qquad t\rightarrow\infty \tag{5}$$

When A is inhibiting the production or removal of E (motifs 3, 4, 7, 8) and assuming (for the sake of simplicity) that the inhibiting term has a first-order cooperativity with respect to A with an inhibition constant K_I^A, the following expression is conserved and perturbation-independent (see derivation in File S1, Eq. S8):

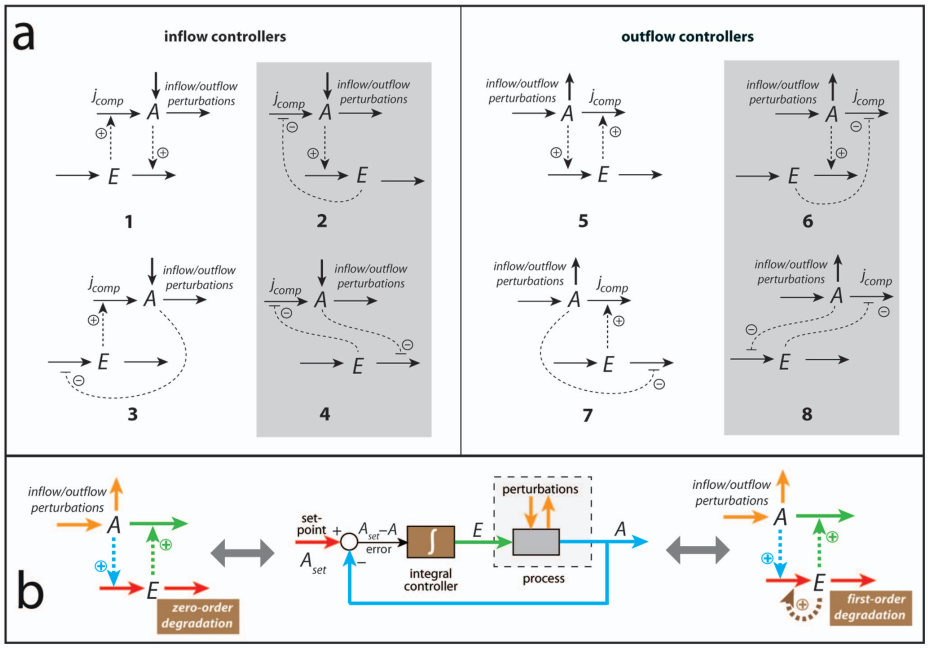

Figure 1. A basic set of two-component homeostatic controller motifs with two implementations of integral control. (a) Compound A is the homeostatic controlled variable and E is the controller or manipulated variable [22]. The motifs fall into two classes termed as inflow and outflow controllers, dependent whether their compensatory fluxes j_{comp} add or remove A from the system. In motifs outlined in gray the controller compound E inhibits the compensatory flux, while in the other motifs E activates the compensatory flux. (b) middle figure shows a standard control engineering flow chart of a negative feedback loop, where the negative feedback results in the subtraction of the concentration of A (blue line) from A's set-point (red line) leading to the error ($A_{set}-A$). The error feeds into the integral controller (brown box). The controller output (the integrated error) is the concentration of E (green line) which regulates the process that creates A. The perturbations which affect the level of A are indicated in orange color. (b) left panel shows the structure of negative feedback (outflow) controller 5. The colors correspond to those of the control engineering flow chart. For example, the set-point (red) is given by the ratio between removing and synthesis rates of E, while the integral controller (brown) is related to the processing kinetics of E, in this case E is removed by zero-order [22,43]. (b) right panel shows the same outflow controller (motif 5). The only difference is that the integral controller is now represented by a first-order autocatalytic formation (indicated by brown dashed arrow) and a first-order removal with respect to E [45].
doi:10.1371/journal.pone.0107766.g001

$$< \frac{1}{K_I^A + A} >_c = \oint_c \frac{dt}{K_I^A + A(t)} = \text{constant} \qquad (6)$$

Homeostasis by Oscillatory Controllers

To illustrate the homeostatic response of the oscillatory controllers, we use, as mentioned above, conservative and limit-cycle versions of inflow controller motif 2 and outflow controller motif 5 as representative examples. These motifs have been chosen, because they represent different ways to achieve negative feedback and homeostasis of the controlled variable A. In motif 2 (as in motifs 4, 6, and 8) E inhibits the compensatory flux, while in motif 5 (as in motifs 1, 3, and 7) the compensatory flux is activated by E. A limit-cycle version of motif 6 will be used to discuss cytosolic Ca^{2+} oscillations in terms of a homeostatic mechanism.

Conservative Oscillatory Controllers. A conservative system is a system for which an energy or Hamiltonian function (H-function) can be found and for which the values of H remain constant in time. Conservative oscillators show periodic motions characterized by that they in phase space do not occur in isolation (i.e. they are not limit cycles). For a given H-level h a periodic motion (a closed path in phase space) is surrounded by a continuum of near-by paths, obtained for neighboring values of h [50]. The dynamics of a two-component conservative oscillator can be derived from the H-function using the following equations:

$$\frac{\partial H}{\partial E} = -\dot{A}\,; \quad \frac{\partial H}{\partial A} = \dot{E} \qquad (7)$$

which are analogous to the Hamilton-Jacobi equations from classical mechanics. In general, solutions of these equations are not necessarily oscillatory, but here we focus only on the conservative

oscillators, which can be derived from the eight controller motifs (Fig. 1a). Dependent on how integral control is implemented, some of the conservative oscillators are well-known; they are: the *harmonic oscillator* [51] based on either motifs 1 or 5 (using zero-order implementation of integral control; see left panel in Fig. 1b), the *Lotka-Volterra oscillator* [45,52,53] also here based on motifs 1 or 5 (but using the autocatalytic implementation of integral control; see right panel in Fig. 1b), and Goodwin's oscillator from 1963 [54] based on motif 2. In the literature the Goodwin oscillator comes in two versions, which are both based on motif 2. There is a conservative oscillator version from 1963 [54] with two components. There is also another version from 1965 with three components [55]. The difference between the two versions lies in the kinetics of the degradation rates of the oscillators' components. In the 1965 three-component version the degradation rates are first-order with respect to the degrading species, while in the conservative case (1963 version) the degradation rates have zero-order kinetics. These kinetic differences change the oscillatory behavior of the two systems significantly. To get limit-cycle oscillations, it is well-known from the literature [56] that the three-dimensional system where the components are degraded by first-order kinetics requires a cooperativity of the inhibiting species of about 9 or higher. Our results presented here using motif 2 confirms Goodwin's 1963 results that when components are degraded by zero-order kinetics the system can oscillate with a cooperativity of 1 with respect to the inhibiting species E. Here we also extend Goodwin's results by showing that *limit-cycle oscillations* can be created based on motif 2, but still using a cooperativity of 1 with respect to the inhibiting species E (see below).

The following two requirements are needed to get conservative oscillations for any motif from Fig. 1a: (i) integral control has to be implemented in the rate equation for E, and (ii) all removal of A should either occur by zero-order kinetics with respect to A, or, when the removal of A is first (or nth)-order with respect to A, the formation of A needs to be a first (or nth)-order autocatalytic reaction [45]. When conditions (i) and (ii) are fulfilled, a function $H(A,E)$ can be constructed, which describes the dynamics of the system analogous to the Hamilton-Jacobi equations from classical mechanics, where the form of H depends on the system's kinetics. Details on how H is constructed for the various situations is given in File S1.

Fig. 2a shows a reaction kinetic representation of motif 2, which is closely related to Goodwin's 1963 oscillator [54]. It was Goodwin who first drew attention to the analogy between the dynamics of a set of two-component cellular negative feedback oscillators and classical mechanics [54]. In this inflow-type of controller, increased outflow perturbations (i.e., increased k_2 values) are compensated by a decreased average amount of E (i.e., $<E>$, Fig. 2b), thereby neutralizing the increased removal of A by use of an increased compensating flux

$$j_{comp} = k_3 \cdot K_I^E / (K_I^E + E) \tag{8}$$

In this way the average level of A, $<A>$, is kept at its set-point $V_{max}^{E_{set}}/k_4$ (see Eq. S5 in the File S1). During the adaptation in $<A>$ (when k_2 is changed) the controller's frequency as well as the $<E>$-level are affected. The frequency ω for each of the eight conservative oscillators can roughly be estimated by a harmonic approximation (see File S1), which in case of motif 2 (Fig. 2a) is given by (assuming $k_1 = 0$)

$$\omega = \frac{\sqrt{k_3 \cdot k_4 \cdot K_I^E}}{K_I^E + E_{ss}} \tag{9}$$

E_{ss} $(= k_3 K_I^E / k_2 - K_I^E)$ is the steady state of E, which is obtained when $\dot{A} = 0$ (Fig. 2a). Because the level of $<E>$ is decreasing with increasing k_2 values, Eq. 9 indicates, and as shown by the computations in Figs. 2b and 2c, that the frequency of the oscillator increases with increasing perturbation strengths (k_2 values) while keeping $<A>$ at its set-point. In fact, the increase in frequency upon increased perturbation strengths appears to be a general property of oscillatory homeostats, where the manipulated variable E inhibits the compensatory flux (for limit-cycle examples, see below).

At high k_2 values, i.e., when the E level becomes lower than K_I^E, the compensatory flux j_{comp} approaches its maximum value k_3. At this stage the homeostatic capacity of the controller is reached. Any further increase of k_2 cannot be met by an increased compensatory flux and will therefore lead to a breakdown of the controller. For discussions about controller breakdowns and controller accuracies, see Refs. [22,48].

The scheme in Fig. 2d shows outflow controller motif 5, which will compensate any inflow perturbations of A (due to changes in k_1) by increasing the compensatory flux

$$j_{comp} = k_3 \cdot E \tag{10}$$

When $K_M^A \ll A$ and $K_M^{E_{set}} \ll E$ the oscillator is harmonic and is described by a single sine function which oscillates around the set-point $<A>_{set} = V_{max}^{E_{set}}/k_4$ with frequency $\omega = \sqrt{k_3 \cdot k_4}$ and a period of $2\pi/\sqrt{k_3 \cdot k_4}$. Increased levels in k_1 (Figs. 2e and 2f) are compensated by increased $<E>$ levels which keep $<A>$ at its set-point. Harmonic oscillations can also be obtained for the counterpart inflow motif 1 (see Fig. S9 and Eqs. S44–S50 in File S1).

For the harmonic oscillators (motifs 1 or 5) $<A>$-homeostasis is kept by an increase in $<E>$, which matches precisely the increase in the (average) compensatory flux without any need to change the frequency. For the other motifs either an increase or a decrease in frequency is observed with increasing perturbation strengths dependent whether E inhibits or activates the compensatory flux, respectively.

Limit-Cycle Controllers. The conservative oscillatory controllers described above can be transformed into limit-cycle oscillators by including an additional intermediate, and, as long as integral control is present, homeostasis in A is maintained by means of Eq. 4 or 6. Fig. 3a gives an example of a limit-cycle homeostat using motif 2. Dependent on the rate constants the oscillations can show pulsatile/excitable behavior (Fig. 3b). In these pulsatile and highly nonlinear oscillations $<A>$ homeostasis is maintained at the set-point $<A>_{set} = V_{max}^{E_{set}}/k_4$, although the peak value in A exceeds the set-point by over one order of magnitude (Fig. 3b). As already observed for the conservative case, an increase in the perturbation strength (i.e., by increasing k_2) leads to an increase in frequency while homeostasis in $<A>$ is preserved (Fig. 3c).

Similarly, a limit-cycle homeostat of motif 5 can be created (Fig. 4a) by including intermediate e and maintaining integral control with respect to A. With increasing perturbation strengths (k_1 values, Fig. 4b), homeostasis in $<A>$ is maintained by increasing $<E>$. Compared to the conservative situation

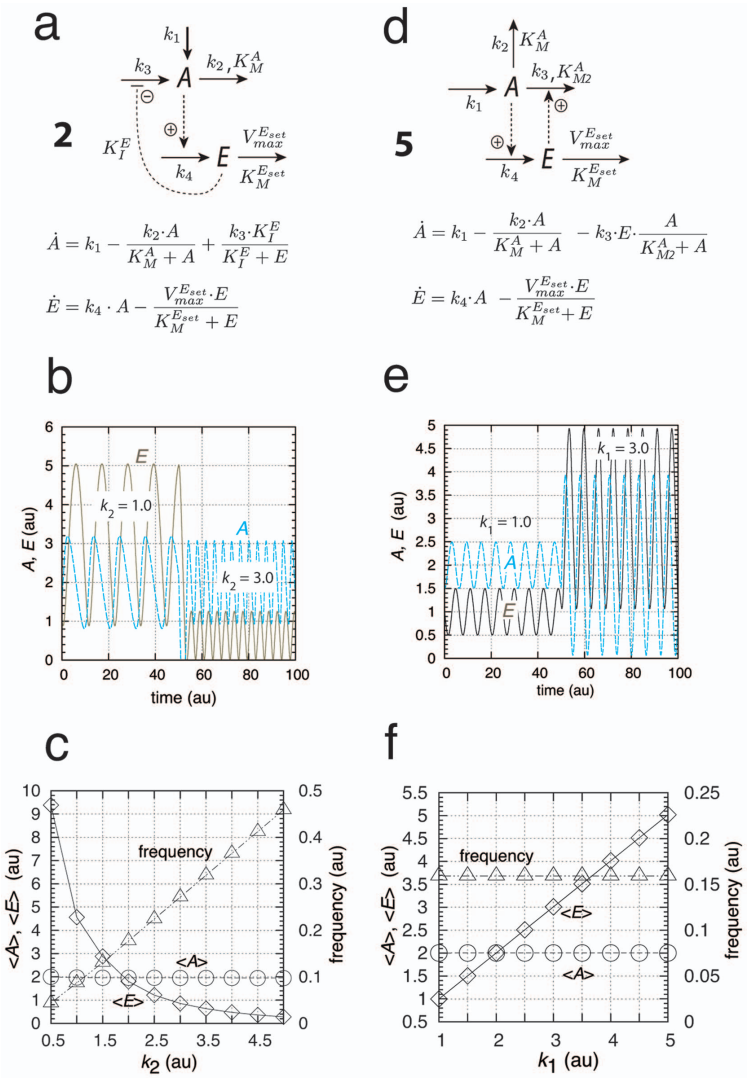

Figure 2. Representation and kinetics of conservative oscillators based on motif 2 and motif 5. (a)–(c) "Goodwin's oscillator" (motif 2). Conservative oscillations occur when $K_M^A \ll A$ and $E \ll K_M^{E_{set}}$; the latter condition introduces integral feedback and thereby robust homeostasis [22,43]. (b) Conservative oscillations in A and E, with $k_1 = 0.0$, $k_2 = 1.0$, $K_M^A = 1 \times 10^{-6}$, $k_3 = 6.0$, $K_I^E = 0.5$, $k_4 = 1.0$, $V_{max}^{E_{set}} = 2.0$, $K_M^{E_{set}} = 1 \times 10^{-6}$. Initial concentrations: $A_0 = 1.5$, $E_0 = 1.0$. At time t = 50.0 k_2 is changed from 1.0 to 3.0. (c) $<A>$, $<E>$, and frequency as a function of the perturbation k_2. While the frequency increases and $<E>$ decreases with increasing k_2, $<A>$ is kept at its set-point $V_{max}^{E_{set}}/k_4 = 2.0$. (d)–(f) Harmonic oscillator representation of motif 5. Conservative (harmonic) oscillations occur when $K_M^A \ll A$ (or $k_2 = 0$) and $E \ll K_M^{E_{set}}$. (e) Harmonic oscillations in A and E, with $k_1 = 1.0$ (the perturbation), $k_2 = 0.0$, $k_3 = 1.0$, $K_{M2}^A = 1 \times 10^{-6}$, $k_4 = 1.0$, $V_{max}^{E_{set}} = 2.0$, and $K_M^{E_{set}} = 1 \times 10^{-6}$. At time t = 50.0 k_1 is changed from 1.0 to 3.0. Initial concentrations: $A_0 = 1.5$, $E_0 = 1.0$. (f) $<A>$, $<E>$, and frequency as a function of the perturbation k_1. Typical for the harmonic oscillator is the constancy of the frequency upon changing k_1 values. $<E>$ increases with increasing k_1, while $<A>$ is kept at its set-point $V_{max}^{E_{set}}/k_4 = 2.0$.
doi:10.1371/journal.pone.0107766.g002

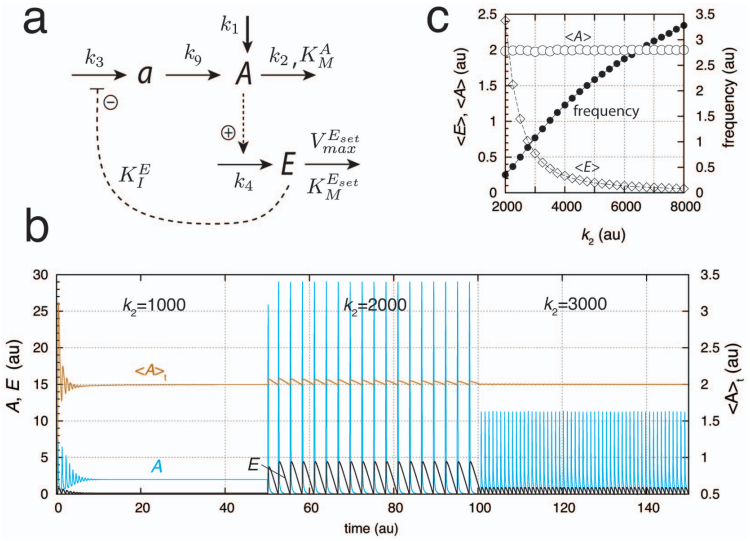

Figure 3. A limit-cycle model of controller motif 2. (a) Reaction scheme. Rate equations: $\dot{A}=k_1 - k_2 \cdot A/(K_M^A+A)+k_9 \cdot a$; $\dot{E}=k_4 \cdot A - V_{max}^{E_{set}} \cdot E/(K_M^{E_{set}}+E)$; $\dot{a}=k_3 \cdot K_I^E/(K_I^E+E) - k_9 \cdot a$. (b) Homeostatic response of the model for three different perturbations (k_2 values). For time t between 0 and 50 units, $k_2=1.0\times10^3$, for t between 50 and 100 units, $k_2=2.0\times10^3$, and for t between 100 and 150 units, $k_2=3.0\times10^3$. In the oscillatory case $<A>$ at time t is given as $<A>_t=(1/t)\times\int_0^t A(t')dt'$ (ordinate to the right) showing that $<A>$ is under homeostatic control despite the fact that A peak values may be over one order of magnitude larger than the set-point. (c) $<A>$, $<E>$, and frequency values as a function of k_2. Simulation time for each data point is 100.0 time units. Note that $<A>$ is kept at $<A>_{set}$ independent of k_2. Rate constant values (in au): $k_1=1.0$, $k_3=1.0\times10^5$, $k_4=1.0$, $K_I^E=1.0\times10^{-3}$, $K_M^A=1.0$, $V_{max}^{E_{set}}=2.0$, $K_M^{E_{set}}=1.0\times10^{-6}$, and $k_9=2.0$. It may further be noted that the degradation kinetics with respect to A are no longer zero-order as required in the conservative case (Figs. 2a–c). Initial concentrations in (b): $A_0=1.5$, $E_0=0.3$, and $a_0=166.17$. Initial concentrations in (c) for each data point: $A_0=1.725\times10^{-6}$, $E_0=1.585$, and $a_0=0.861$.
doi:10.1371/journal.pone.0107766.g003

(Fig. 2f), the frequency now shows both slight decreasing and increasing values. However, the overall frequency changes are not as large as for motif 2, indicating that similar to the harmonic case, the frequency of the motif 5 based oscillator has a certain intrinsic frequency compensation on k_1-induced perturbations (Fig. 4c).

Robust Frequency Control and Quenching of Oscillations

In this section we present for the first time biochemical models that can show robust (perturbation-independent) frequency control. There are several biological oscillators where the frequency/period is under homeostatic regulation. Probably the best known example is the temperature compensation of the circadian period, i.e. these rhythms show an approximately constant period length of about 24 h at different but constant temperatures [57]. Temperature compensation is also observed in certain ultradian rhythms [58,59]. Another biological oscillator with a fairly constant period is the p53-Mdm2 system [60], where the number of oscillations may indicate the strength of the DNA damage in the cell [61].

We show two ways how robust frequency control can be achieved. One is due to the presence of quasi-harmonic kinetics, i.e. the system, although still being a limit-cycle oscillator, behaves more like a harmonic oscillator. On basis of experimental results, we believe that the p53-Mdm2 system falls into this category (see discussion below). In the other approach, frequency homeostasis is obtained by regulating E itself by additional inflow/outflow controllers I_1,I_2. This approach leads to many possible ways how I_1,I_2 can interact with the central negative feedback A-E loop/oscillator and several ways are illustrated using motif 2 and motif 5. Such an approach may apply to the period homeostasis of circadian rhythms (see discussion below).

Robust Frequency Control by Quasi-Harmonic Kinetics. We consider now the case when the intermediate that has been implemented to obtain limit-cycle behavior (compounds a or e in Figs. 3a or 4a) obeys *approximately* the steady-state assumption, i.e., $\dot{a}\approx0$ or $\dot{e}\approx0$. We term the oscillators' resulting behavior as *quasi-conservative*, because these systems still have a limit-cycle, but behave also as a conservative system. An interesting case occurs when the system is quasi-harmonic, i.e. when motifs 1 or 5 are used. In this case the limit-cycle oscillations and the frequency can approximately be described by a harmonic oscillator, i.e., a single sine function. This is illustrated in Fig. 5 where an increased k_5 value is applied to the scheme of Fig. 4a (which leads to $\dot{e}\approx0$). Fig. 5a shows the oscillations for three different perturbations (k_1 values). The oscillations in A show a practically perfect overlay with a single sine function, outlined in black for $k_1=1.0$. When k_1 is increased the oscillations (outlined in blue) undergo a phase shift and an increase in amplitude, but the frequency stays constant at the value of the (quasi) harmonic oscillator. For high k_1 values the

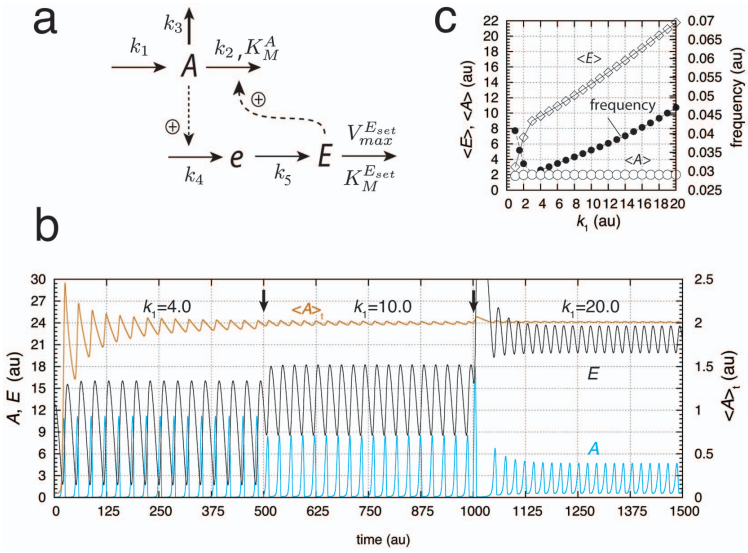

Figure 4. A limit-cycle model of controller motif 5. (a). Rate equations: $\dot{A}=k_1-k_2\cdot E\cdot A/(K_M^A+A)-k_3\cdot A$; $\dot{e}=k_4\cdot A-k_5\cdot e$; $\dot{E}=k_5\cdot e-V_{max}^{E_{set}}\cdot E/(K_M^{E_{set}}+E)$. (b) Homeostatic behavior in $<A>$ illustrated by three different perturbations (k_1 values). At time $t=500.0$ k_1 is changed from 4.0 to 10.0, and at $t=1000.0$ k_1 is changed from 10.0 to 20.0 (indicated by solid arrows). The set-point of $<A>$ is given as $V_{max}^{E_{set}}/k_4=2.0$. Rate constant values: k_1 is variable, $k_2=1.0$, $K_M^A=0.1$, $k_3=0.0$, $k_4=0.5$, $k_5=0.2$, $V_{max}^{E_{set}}=1.0$, and $K_M^{E_{set}}=1.0\times10^{-6}$. Initial concentrations: $A_0=1.9964\times10^{-2}$, $e_0=8.0983$, and $E_0=12.0258$. (c) $<A>$, $<E>$, and frequency values as a function of k_1 showing that $<A>$ is kept at the set-point independent of k_1. Rate constants as in (b). Initial concentrations for each data point: $A_0=7.6383\times10^{-1}$, $e_0=1.6887$, and $E_0=18.8155$. Simulation time for each data point is 10000.0 time units.
doi:10.1371/journal.pone.0107766.g004

A-amplitude of the oscillator becomes saturated, which is a secondary effect of the oscillator's homeostatic property. Due to symmetry reasons and because the oscillator is locked on to the harmonic frequency, the value of A cannot exceed beyond twice the level of its set-point, which in this case has been set to 12.5 (Figs. 5a and 5b). As in the harmonic case (Fig. 2f), $<E>$ increases with increasing k_1 (Fig. 5b). Fig. 5c shows the approach to the limit-cycle (outlined in black). When k_5 increases further and the steady state approximation for e becomes better and better, the limit-cycle disappears and the system becomes purely harmonic.

Quenching of Oscillations in Quasi-Conservative Systems. A requirement to obtain conservative oscillations and an oscillatory promoting condition for limit cycle oscillations is the presence of zero-order degradation in A. Changing the zero-order degradation in A may lead to the loss of oscillations. For example, in quasi-conservative systems the oscillations can be effectively quenched by either adding a first-order removal term with respect to A (with rate constant k_3, Fig. 4a) or by replacing the zero-order kinetics degradation in A (using k_2, K_M^A) by first-order kinetics with respect to A, or by increasing K_M^A. Fig. 5d illustrates the suppression of the quasi-harmonic oscillations by adding a first-order removal with respect to A. In contrast, when an oscillatory system does not show quasi-conservative kinetics, addition of a first-order removal with respect to A does not necessarily abolish the oscillations. A detailed parameter analysis showing how the value of k_5 affects the period of the oscillations and how first-order degradation in A affects the size of the parameter space in which sustained oscillations are found is given in (Figs. S10 and S11 in File S1).

Robust Frequency Homeostasis by Control of $<E>$. When considering the relationship between $<E>$ and the frequency, as for example shown in Fig. 3c, we wondered whether it would be possible to design an oscillator with a robust frequency homeostasis by using an additional control of $<E>$. For this purpose, two extra controllers I_1 and I_2 with their own set-points for $<E>$ are introduced. Note, that the integral control for $<A>$ by E is still operative and has its own defined set-point. In the following we show three examples of robust frequency control using motifs 2 and 5. Two of the examples illustrate different feedback arrangements of I_1 and I_2 using motif 2. An example using still another arrangement using motif 2 is described in File S1 (Figs. S12–S14).

In Fig. 6a a set-up for robust frequency homeostasis is shown by using a limit-cycle oscillator based on controller motif 5. The set-points for $<E>$, given by the rate equations for I_1 and I_2, are $<E>_{set}^{I_1}=k_6/V_{max}^{I_1}$ and $<E>_{set}^{I_2}=V_{max}^{I_2}/k_7$. Fig. 6b shows the results for a set of calculations when k_1 varies from 1 to 20 au. In these calculations it was assumed that the I_1 and I_2 controllers have the same set-point of 20.0 au. In the absence of controllers I_1 and I_2, the frequency varies as indicated in Fig. 4c, which in Fig. 6b is shown as gray dots. When I_1 and I_2 controllers are both

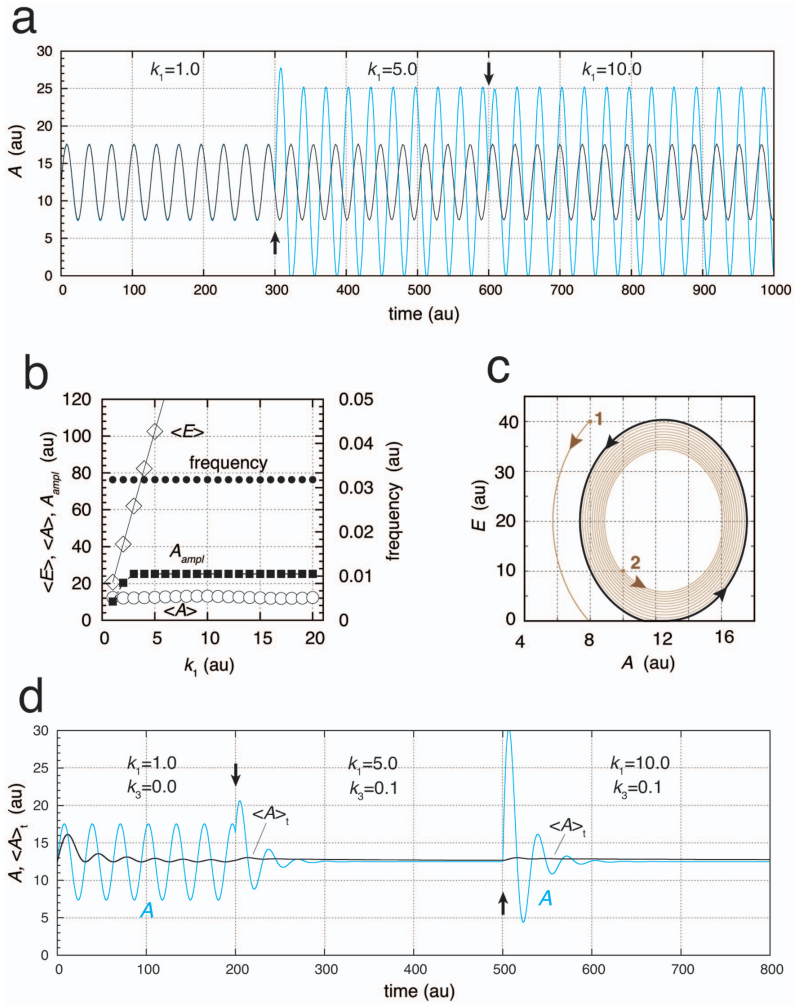

Figure 5. Quasi-harmonic behavior of motif 5 oscillator (Fig. 4a). For time $t<300$, a perfect overlay between the numerical calculation of $A(t)$ (blue color) and the single harmonic $A(t)=A_{ampl}\cdot\sin(2\pi/P+\phi)\ +<A>_{set}$ (black color) is found, where $k_1=1.0$, $A_{ampl}=5.0791$, $P=31.44$, $\phi=-0.05$, and $<A>_{set}=V_{max}^{E_{set}}/k_4\ =12.5$. A_{ampl} and P represent the numerically calculated amplitude and period length, respectively. ϕ was adjusted to give a closely matching overlay. Other rate constant values (numerical calculations): $k_2=5.0\times10^{-2}$, $k_3=0.0$, $K_M^A=1.0\times10^{-6}$, $k_4=0.8$, $k_5=20.0$, $V_{max}^{E_{set}}=10.0$, and $K_M^{E_{set}}=1.0\times10^{-6}$. Initial concentrations: $A_0=12.4290$, $e_0=0.4952$, and $E_0=1.0139\times10^{-4}$. At times $t=300$ and $t=600$ (solid arrows) k_1 is changed to respectively 5.0 and 10.0. For these k_1 values the amplitude of A has reached its maximum, which is twice the value of the set-point. (b) $<A>$, A_{ampl}, $<E>$, and frequency as a function of k_1. Simulation time for each data point is 1000.0 time units. (c) Demonstration of limit-cycle behavior of the quasi-harmonic oscillations. Same initial conditions as in (a) with $k_1=1.0$, and $e_0=0.4952$. (d) Same system as in (a), but at times $t=200$ and $t=500$ (solid arrows) k_3 is changed and kept to 0.1. The oscillations are efficiently quenched, but A remains under homeostatic control.

doi:10.1371/journal.pone.0107766.g005

active, $<E>$ shows robust homeostasis at 20.0 (Fig. 6b) and the frequency is practically constant (black dots). Fig. 6c shows the response when controller I_1 has been "knocked out". While in this case the $<A>$ values are still under homeostatic control, $<E>$ approaches its set-point (defined by $<E>^{I_2}_{set}$) only at high k_1 values, but without a control of the frequency. When controller I_2 is knocked-out (Fig. 6d), control of $<E>$ and frequency homeostasis is observed. Due to the absence of controller I_2, homeostasis in $<E>$ and in the frequency is lost for higher k_1 values. The role of I_2 in this type of regulator is to diminish/suppress the inflow to A by k_1, such that controller I_1 can supply the necessary amount of A in order to keep $<E>$ and the frequency under homeostatic control. This mechanism is illustrated in Fig. 6e by a "static" work mode of I_2, where the concentration of I_2 is kept constant. In this case the k_1-region of frequency homeostasis increases with increasing but constant concentrations of I_2 (Fig. 6f).

A corresponding approach to achieve robust frequency homeostasis by using motif 2 is shown in Fig. 7a. The set-up differs from that used for motif 5 (Fig. 6a) by allowing that I_1 and I_2 act upon a and upstreams of A. For the sake of simplicity, both controllers are assumed to have set-points at 20.0 au. Note that in this version of the motif 2 oscillator, the removal of A is now purely first-order with respect to A (using only k_2). Because motif 2 has been the core for many circadian rhythm models, we will below discuss implications of robust frequency control with respect to properties of circadian rhythms. In this context we note that the region outlined in gray in Fig. 7a shows the part of the oscillator where rate constants have no influence on the frequency, i.e. the sensitivity coefficients $\partial(frequency)/\partial k_i$ are zero.

Fig. 7b shows the homeostatic behavior in frequency (black dots) in comparison with the uncontrolled oscillator (gray dots). In the controlled case, both $<A>$ and $<E>$ are under homeostatic regulation with set-points of 2.0 au and 20.0 au, respectively. To elucidate the effect of the added controllers I_1 and I_2, we removed them one by one (knocking them out). In Figs. 7c and 7d controllers I_1 and I_2 have been removed, respectively. When outflow controller I_1 is not operative, the system is not able to remove sufficient a at low k_2 values. In this case $<E>$ levels are high and unregulated at low k_2's and showing an increase in frequency. Only at sufficiently high k_2 values controller I_2 is able to compensate for the decreased levels in $<E>$. The situation is reversed in Fig. 7d, when controller I_2 is not operative. At low k_2 values controller I_1 can remove excess of E by diminishing the level of a and keeping $<E>$ at its set-point. However, the $<E>$ regulation breaks down at high values of k_2, because no additional supply for E via a can now be provided. In this way controllers I_1/I_2 act as an antagonistic pair of outflow/inflow controllers, respectively. Note that the by E controlled level of $<A>$ (with set-point of 2.0 au) is kept at its set-point independently whether $<E>$ is regulated by I_1/I_2 or not. Fig. 7e shows the oscillations when both I_1 and I_2 are operative (Fig. 7b, black dots) and k_2 being changed from 3.0 to 8.0 at t = 250.0 units (indicated by arrow). The level of $<E>$ is controlled to its set-point (20.0), while the amplitude of A has increased with the increase of k_2. For each spike (after steady state has been established) the average amount of A is the same and independent of the value of k_2, leading to the same frequency and homeostasis in $<A>$.

Oscillator with Two Homeostatic Frequency Domains

In the I_1 and I_2-controlled oscillators described above the set-point of $<E>$ will determine the frequency. Fig. 8a shows an example of a motif-2-based homeostat, where I_1 and I_2 feed back to A and a, respectively. For an example where I_1 and I_2 feed back to A only, see Fig. S12 in File S1. In the calculations of Fig. 8, different set-points for $<E>$ by controllers I_1 and I_2 have been chosen. As a result, dependent whether the perturbation strength (value of k_2) is high or low, the oscillator shifts between two different homeostatic controlled frequency regimes separated by a transition zone (Fig. 8b). Fig. 8c shows the oscillations, $<A>$ and $<E>$ values and the frequency switch when k_2 is changed from 3.0 to 8.0.

Discussion

Classifications of Biochemical Oscillators and Influence of Positive Feedback

There has been several approaches how chemical and biochemical oscillators can be understood and classified [62–66]. The controller motifs shown in Fig. 1a can be considered as a basic set of negative feedback oscillators. For example, the Lotka-Volterra oscillator can be viewed as a negative feedback oscillator based on motifs 1 or 5, but where integral control is implemented in terms of autocatalysis [45] and where the controlled variable A is formed by autocatalysis and degraded by a first-order process with respect to A. The same motif can show harmonic oscillations, when integral control and removal of the controlled variable is incorporated by means of zero-order kinetics. Two additional oscillator types based on the same motif can be created by implementing mixed autocatalytic/zero-order kinetics for integral control and for the generation/degradation of the controlled variable ('Text S1'). The other motifs can be extended in a similar way, giving rise to 32 basic (mostly unexplored) oscillator types. This type of classification supplements the one given earlier by Franck, where the eight negative feedback loops where combined with their positive counterparts to create what Franck termed *antagonistic feedback* [63] An often discussed question is the role positive feedback, or autocatalysis, may play in biological oscillators. Using a Monte-Carlo approach Tsai et al. [26] studied the robustness and frequency responses of oscillators with only negative feedback loops and oscillators with a combined positive-plus-negative feedback design. The authors concluded that the combination of a negative and a positive feedback is the best option for having robust and tunable oscillations. In particular, the positive loop appears necessary to make the oscillator tunable at a constant amplitude. We here have shown how homeostasis and tunable oscillators may be achieved without any positive feedback (but generally associated with a changing amplitude). To put our results in relation to those from Tsai et al. [26], we wondered, triggered by the comments from a reviewer, how an oscillator with an autocatalytic-based integral controller might behave in comparison. For this purpose we used controller motif 2 (Fig. 9a), analogous to the scheme shown in Fig. 3a. Interestingly, and in agreement with the findings by Tsai et al. [26], the autocatalytic step resulted now in relaxation-type of oscillations. As expected, the frequency of the oscillator increases with increasing perturbation strengths k_2, and $<A>$ is under homeostatic control (Fig. 9b). However, as indicated by the results of Tsai et al. the oscillator's amplitude has now become independent of k_2! These results show that Franck's original concept of antagonistic feedback, i.e. combining positive and negative feedback loops in various ways [63] appear to be of relevance for many biological oscillators [26].

Homeostatic Regulation under Oscillatory Conditions

In his definition of homeostasis Cannon introduced the term *homeo* instead of *homo* to indicate that certain variations in the concentrations of the homeostatic controlled species are still

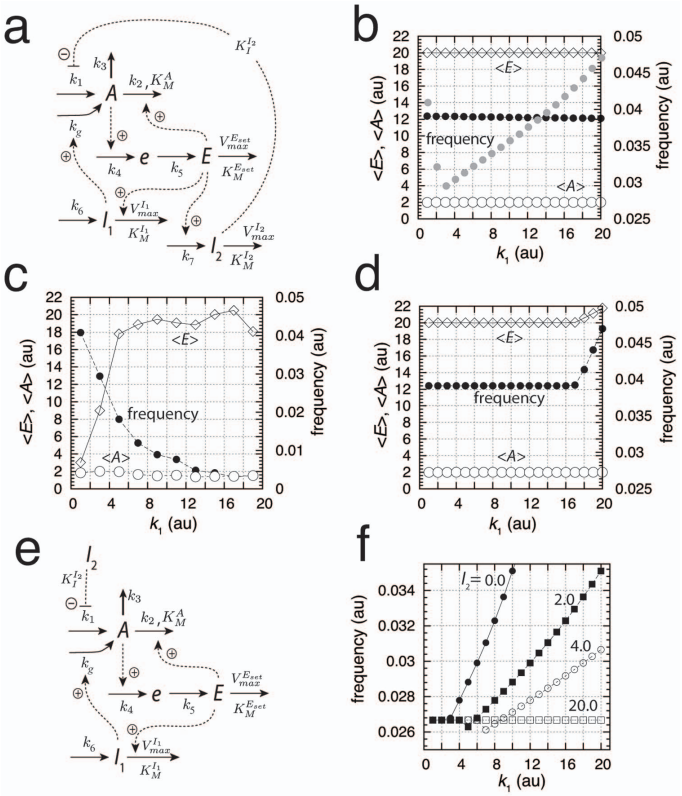

Figure 6. Oscillator based on motif 5 with robust frequency control. (a) Reaction scheme. Rate equations: $\dot{A}=k_1\cdot K_I^{I_2}/(K_I^{I_2}+I_2)+k_g\cdot I_1-k_2\cdot E\cdot A/(K_M^A+A)-k_3\cdot A$; $\dot{e}=k_4\cdot A-k_5\cdot e$; $\dot{E}=k_5\cdot e-V_{max}^{E_{set}}\cdot E/(K_M^{E_{set}}+E)$; $\dot{I}_1=k_6-E\cdot V_{max}^{I_1}\cdot I_1/(K_M^{I_1}+I_1)$; $\dot{I}_2=k_7\cdot E-V_{max}^{I_2}\cdot I_2/(K_M^{I_2}+I_2)$. (b) Demonstration of robust frequency control. $<A>$, $<E>$, and frequency are shown as functions of k_1. Rate constants: $k_1=1.0$, $k_2=1.0$, $K_M^A=0.1$, $k_3=0.0$, $k_4=0.5$, $k_5=0.2$, $V_{max}^{E_{set}}=1.0$, $K_M^{E_{set}}=1.0\times10^{-6}$, $k_6=20.0$, $V_{max}^{I_1}=1.0$, $K_M^{I_1}=1.0\times10^{-6}$, $k_7=1.0$, $V_{max}^{I_2}=20.0$, and $K_M^{I_2}=1.0\times10^{-6}$. Set-points for E by controllers I_1 and I_2 are given as $<E>_{set}^{I_1}=k_6/V_{max}^{I_1}=20.0$ and $<E>_{set}^{I_2}=V_{max}^{I_2}/k_7=20.0$, respectively. Initial concentrations for each data point (black dots): $A_0=0.7638$, $E_0=18.8155$, $e_0=1.6887$, $I_{1,0}=1.6695\times10^3$, and $I_{2,0}=2.7657\times10^2$. Gray dots show the frequency as a function of k_1 without control by I_1 and I_2. (c) System as in (b), but controller I_1 not present. (d) System as in (b), but controller I_2 not present. (e) Reaction scheme of oscillator, but with a constant I_2 concentration. Rate constants otherwise as in (b). (f) Frequency as a function of k_1 for the system described in (e) using different constant I_2 concentrations (indicated within the graph). The homeostatic region of the frequency increases with increasing I_2 concentrations.
doi:10.1371/journal.pone.0107766.g006

allowed, but within certain limits [6]. As typical examples, Cannon mentions the variations of body temperature, variations in blood sugar, blood calcium, and blood pH levels [6]. We have shown that the concept of homeostasis can be extended to oscillatory conditions and that the term *set-point* still can be given a precise meaning, even when peak values of the controlled variable may exceed the set-point by over one order of magnitude (Figs. 3 and 7). In these cases the set-point relates to the mean value of the oscillatory species, $<A>$. Many compounds are known to be under a tight homeostatic regulation to avoid cellular dysfunction, such as is the case for cytosolic calcium. There is no particular reason to assume that protective homeostatic mechanisms should cease to exist once a compound becomes oscillatory and functions, as in case of calcium, as a signaling device. Allowing a species (such as cytosolic calcium) to oscillate while defending the mean value of these oscillations makes it possible to relay signaling without exposing the cell to long term overload. In the following we discuss three examples where oscillatory homeostats appear to be involved: in the homeostatic regulation of calcium and p53 during oscillations/signaling, and in the homeostatic function and period regulation of circadian rhythms.

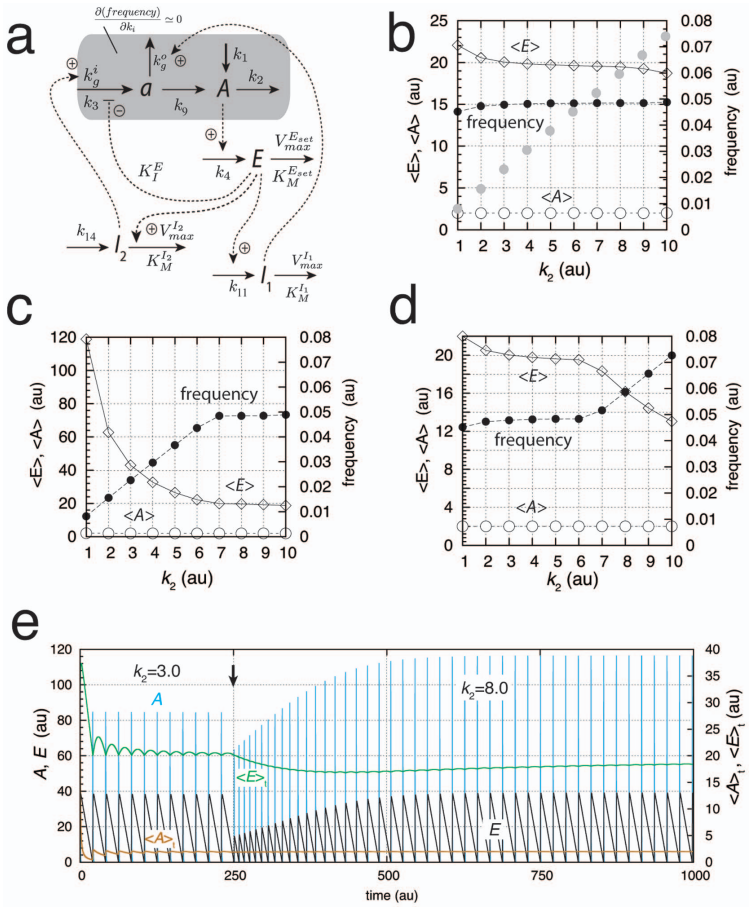

Figure 7. Oscillator based on motif 2 with robust frequency control. (a) Reaction scheme. Rate equations: $\dot{A}=k_1-k_2\cdot A+k_9\cdot a$; $\dot{E}=k_4\cdot A-V^{E_{set}}_{max}\cdot E/(K^{E_{set}}_M+E)$; $\dot{a}=(k_3+k^i_g\cdot I_2)\cdot K^E_I/(K^E_I+E)-(k_9+k^o_g\cdot I_1)\cdot a$; $\dot{I}_1=k_{11}\cdot E-V^{I_1}_{max}\cdot I_1/(K^{I_1}_M+I_1)$; $\dot{I}_2=k_{14}-E\cdot V^{I_2}_{max}\cdot I_2/(K^{I_2}_M+I_2)$. Shaded area indicates part of the model for which the control coefficents of the frequency/period with respect to the parameters within this area become zero when frequency homeostasis is enforced by controllers I_1 and I_2. (b) Demonstration of frequency homeostasis by varying k_2. Black dots show the frequency when controllers I_1 and I_2 are active. Rate constants: $k_1=0.0$, $k_2=1.0$, $k_3=1.0\times10^6$, $k_4=1.0$, $K^E_I=1.0\times10^{-6}$, $V^{E_{set}}_{max}=2.0$, $K^{E_{set}}_M=1.0\times10^{-6}$, $k_9=2.0$, $k^i_g=1.0\times10^2$, $k^o_g=1.0\times10^{-3}$, $k_{11}=5.0$, $V^{I_1}_{max}=1.0\times10^2$, $K^{I_1}_M=1.0\times10^{-6}$, $k_{14}=99.99$, $V^{I_2}_{max}=5.0$, and $K^{I_2}_M=1.0\times10^{-6}$. Set-points for E by controllers I_1 and I_2 are given as $<E>^{I_1}_{set}=V^{I_1}_{max}/k_{11}=20.0$ and $<E>^{I_2}_{set}=k_{14}/V^{I_2}_{max}=19.998$, respectively. The set-point $<E>^{I_1}_{set}$ of the *outflow* controller I_1 has been set slightly higher than $<E>^{I_2}_{set}$ for the *inflow* controller I_2 to avoid integral windup and that the controllers work "against" each other [22]. Initial concentrations for each data point (black dots): $A_0=50.4903$, $E_0=23.9425$, $a_0=3.2629$, $I_{1,0}=8.2955\times10^3$, and $I_{2,0}=57.8533$. Gray dots show the frequency as a function of k_2 for the uncontrolled case, i.e., in the absence of controllers I_1 and I_2. (c) System as in (b), but controller I_1 is "knocked out" by setting k_{11} and $I_{1,0}$ to zero. Homeostasis occurs only at high k_2 values when controller I_2 is active. (d) System as in (b), but inflow controller I_2 is inactivated by setting k_{14} and $I_{2,0}$ to zero. Frequency homeostasis is observed for low k_2 when controller I_1 is active. At high k_2 values the frequency homeostasis breaks down, because controller I_2 is not present to compensate the increased outflow of A, which leads to low $<E>$ values. (e) Oscillations of system in (b) illustrating frequency homeostasis. At time $t=250$ (solid arrow) k_2 is changed from 3.0 to 8.0. Initial concentrations: $A_0=27.3167$, $E_0=31.7283$, $a_0=0.1237$, $I_{1,0}=1.3473\times10^4$, and $I_{2,0}=5.0919\times10^2$.
doi:10.1371/journal.pone.0107766.g007

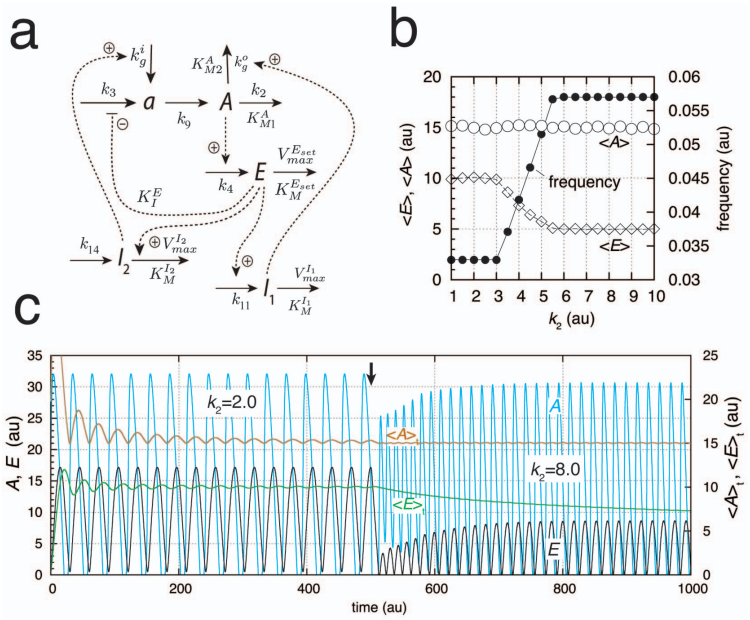

Figure 8. Oscillator based on motif 2 with robust frequency control but alternative feedback regulation by I_1 and I_2. (a) Reaction scheme. Rate equations: $\dot{A}=k_9\cdot a-k_2\cdot A/(K_{M1}^A+A)-k_g^o\cdot A\cdot I_1/(K_{M2}^A+A)$, $\dot{E}=k_4\cdot A-V_{max}^{E_{set}}\cdot E/(K_M^{E_{set}}+E)$; $\dot{a}=k_3\cdot K_I^E/(K_I^E+E)-k_9\cdot a+k_g^i\cdot I_2$; $\dot{I}_1=k_{11}\cdot E-V_{max}^{I_1}\cdot I_1/(K_M^{I_1}+I_1)$; $\dot{I}_2=k_{14}-E\cdot V_{max}^{I_2}\cdot I_2/(K_M^{I_2}+I_2)$. (b) Using different set-points $<E>_{set}^{I_1}=V_{max}^{I_1}/k_{11}=10.0$ and $<E>_{set}^{I_2}=k_{14}/V_{max}^{I_2}=5.0$, the frequency (solid dots) can switch between two homeostatic frequency regimes, dependent whether k_2 is low or high. The two regimes are separated by a transition zone. Rate constants: $k_2=1.0$, $k_3=20.0$, $k_4=0.1$, $V_{max}^{E_{set}}=1.5$, $K_M^{E_{set}}=1.0\times10^{-6}$, $k_{11}=1.0$, $V_{max}^{I_1}=10.0$, $K_M^{I_1}=1.0\times10^{-6}$, $k_{14}=5.0$, $V_{max}^{I_2}=1.0$, $K_M^{I_2}=1.0\times10^{-6}$, $K_I^E=1.0$, $k_g^i=k_g^o=1.0\times10^{-2}$, $K_{M1}^A=K_{M2}^A=1.0\times10^{-6}$. Initial concentrations: $A_0=0.6677$, $E_0=1.0536$, $a_0=2.5828\times10^{-2}$, $I_{1,0}=1.1614\times10^3$, and $I_{2,0}=7.5008\times10^2$. (c) Oscillations of system in (b) illustrating frequency switch. At time $t=500$ (solid arrow) k_2 is changed from 2.0 to 8.0. Initial concentrations: $A_0=19.7178$, $E_0=0.6272$, $a_0=0.4178$, $I_{1,0}=1.3696\times10^2$, and $I_{2,0}=12.9828$.
doi:10.1371/journal.pone.0107766.g008

Calcium Signaling. Cytosolic calcium (Ca^{2+}) levels are under homeostatic control to concentrations at about 100 nM while extracellular levels are in the order of 1 mM. High Ca^{2+} concentrations are also found in the endoplasmatic reticulum (ER) and in mitochondria (between 0.1–10 mM), which act as calcium stores. To keep cytosolic Ca^{2+} concentrations at such a low level Ca^{2+} is actively pumped out from the cytoplasm into the extracellular space and into organelles by means of various Ca^{2+} ATPases located in the plasma membrane (PMCA pumps) and in organelle membranes [21,67]. Dysfunction of these pumps leads to a variety of diseases including cancer, hypertension, cardiac problems, and neurodegeneration [68–70]. During Ca^{2+} signaling [71,72] cytosolic Ca^{2+} levels show oscillations [73–75] but signaling can also occur as individual sparks or spikes [76]. Ca^{2+} oscillations have been found to occur in many cell types and differ considerably in their shapes and time scales with peak levels up to one order of magnitude higher than resting levels. Similar to the behavior of stimulated (perturbed) oscillatory homeostats as for example shown in Fig. 3b, Ca^{2+} oscillations have been found to increase their frequency upon increased stimulation of cells [73–75]. The frequency modulation of Ca^{2+} oscillations [77] is considered to be an important property for controlling biological processes [75]. The tight homeostatic regulation of cytosolic calcium combined with its oscillatory signaling suggests that oscillatory homeostats appear to be operative also under signaling conditions.

Although a variety of mathematical models have been suggested to describe Ca^{2+} oscillations [78–84], none of them have so far included an explicit homeostatic regulation of cytosolic Ca^{2+}. Fig. 10a shows how Ca^{2+} oscillations can be obtained based on an outflow homeostatic controller, which removes excess and toxic amounts of cytosolic Ca^{2+}. The model considers a stationary situation of an activated cell, where a Ca^{2+} channel is activated by an external signal leading to the inflow of Ca^{2+} into the cytosol. The increased Ca^{2+} levels in the cytosol induce an additional inflow of Ca^{2+} from the internal Ca^{2+} store, a mechanism termed "Calcium-Induced Calcium Release" (CICR) [85]. Both inflows are lumped together and described by rate constant k_1. The CICR flux is maintained by pumping cytosolic Ca^{2+} into the ER and keeping the Ca^{2+} load in the ER high. It should be mentioned that

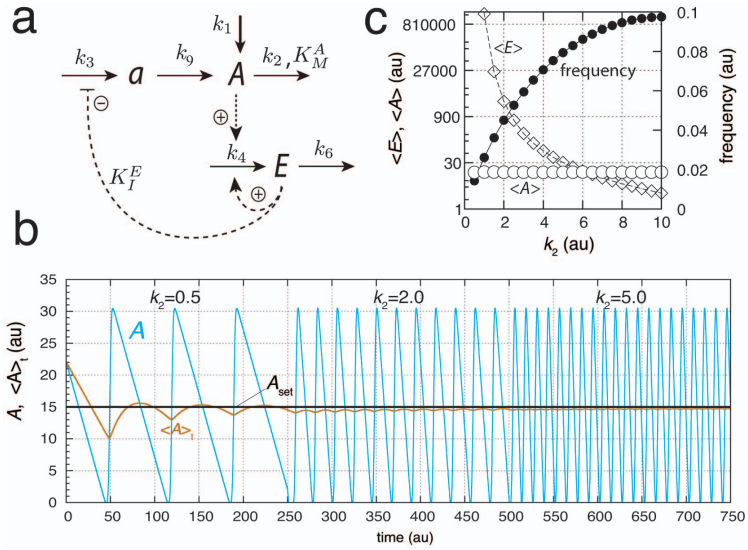

Figure 9. A limit-cycle model of controller motif 2 using autocatalysis as an integral controller. (a) Reaction scheme. Rate equations: $\dot{A}=k_1-k_2\cdot A/(K_M^A+A)+k_9\cdot a$; $\dot{E}=k_4\cdot A\cdot E-k_6\cdot E$; $\dot{a}=k_3\cdot K_I^E/(K_I^E+E)-k_9\cdot a$. (b) Homeostatic response of the model for three different perturbations (k_2 values). For time t between 0 and 250 units, $k_2=0.5$, for t between 250 and 500 units, $k_2=2.0$, and for t between 500 and 750 units, $k_2=5.0$. $<A>$ at time t is defined as in Fig. 3. (c) $<A>$, $<E>$, and frequency values as a function of k_2. Simulation time for each data point is 2000.0 time units. Note that $<A>$ is kept at $A_{set}=15.0$ (solid black line) independent of k_2. Rate constant values (in au): $k_1=0.0$, $k_3=20.0$, $k_4=0.1$, $K_I^E=1.0$, $K_M^A=1.0\times10^{-3}$, $k_6=1.5$, and $k_9=30.0$. Initial concentrations in (b): $A_0=22.09$, $E_0=1.71\times10^{10}$, and $a_0=4.0\times10^{-11}$. Initial concentrations in (c) for each data point are the same as in (b).
doi:10.1371/journal.pone.0107766.g009

the cause of the Ca^{2+} entry across the plasma membrane into the cytosol is not fully understood and different views have been expressed how this can occur [86,87].

For the sake of simplicity, the Ca^{2+} concentration in the ER is considered to be constant and only the pumping of Ca^{2+} from the cytosol into the extracellular space is taken into account without an increased cooperativity (Hill-function) with respect to the Ca^{2+} concentration. Fig. 10b shows the oscillations of cytosolic Ca^{2+} and the homeostat's performance at different inflow rates $k_1\cdot Ca_{ext}^{2+}$ into the cytosol, which can reflect different external Ca^{2+} concentrations and/or different activation levels of the cell. As observed experimentally [74] the period of the oscillations decreases with increased external Ca^{2+} concentration or with an increased stimulation of the cell. As shown by $<Ca_{cyt}^{2+}>_t$ in Fig. 10b and by total $<Ca_{cyt}^{2+}>$ in Fig. 10c, on average, robust Ca^{2+} homeostasis is preserved at varying Ca^{2+} inflow rates. In the absence of oscillations the Ca^{2+} concentration is still kept at its homeostatic set-point (Fig. 10b).

Why Ca^{2+} oscillations? A non-oscillatory signaling mechanism by cytosolic Ca^{2+} would clearly be limited, because a homeostatic regulation of cytosolic Ca^{2+} would not allow varying Ca^{2+} levels as a function of external stimulation strengths. On the other hand, a frequency-based signaling due to an oscillatory Ca^{2+}-homeostat would overcome these limitations, because homeostasis is still maintained. This has been a brief outline on how Ca^{2+} oscillations may be understood on basis of oscillatory homeostasis. More detailed studies will be needed, for example by including the homeostatic aspect in existing models in order to investigate in more detail the implications oscillatory homeostats have on the regulatory role of Ca^{2+}.

p53 Signaling. p53 is a transcription factor with tumor suppressor properties. In more than half of all human tumors p53 is mutated and in almost all tumors p53 regulation is not functional [88]. In the presence of DNA damage and other abnormalities p53 initiates the removal of damaged cells by apoptosis. A central negative feedback component in p53 regulation is Mdm2, an ubiquitin E3 ligase, which leads to the proteasomal degradation of p53 and other tumor suppressors [89]. In the presence of DNA damage, p53 is upregulated by several mechanisms [90–92], and both p53 and Mdm2 have been found to oscillate [60]. An interesting feature of these oscillations is that their amplitude is highly variable, while their frequency is fairly constant [60]. The mean height of the oscillations was found to be constant [61]. It was also found that with an increased strength of DNA damaging radiation the number of cells with increased p53 cycles increased statistically [61]. Jolma *et al*. [51] used the basic negative feedback motif 5 (where A is p53 and E is Mdm2) and found that the influence of noise on the harmonic properties of the oscillations was able to describe the variable amplitudes and the approximately constancy of the period. Fourier analysis of the experimental data indeed showed that the p53-Mdm2 oscillations have a major harmonic component [93] supporting a quasi-harmonic character of the p53-Mdm2 oscillations. For such

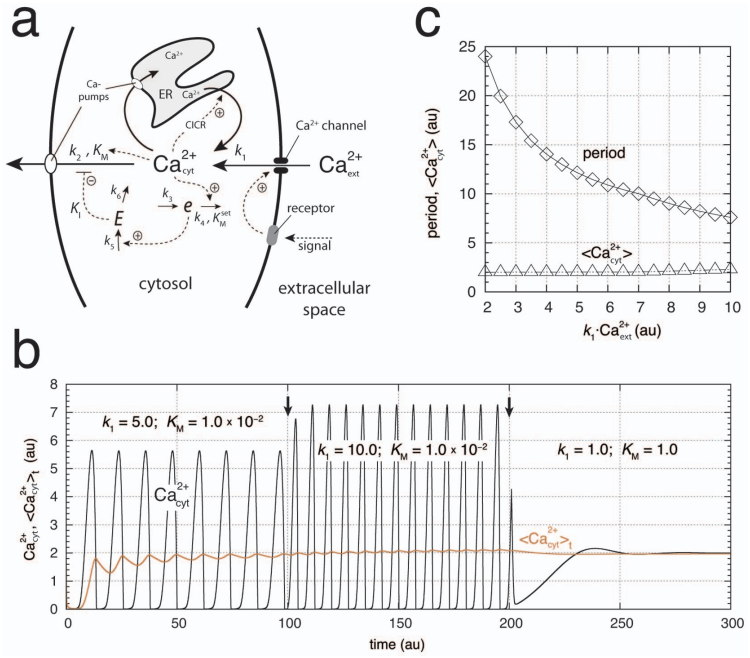

Figure 10. A homeostatic model of cytosolic Ca^{2+} oscillations. The model considers a stimulated non-excitable cell under stationary conditions using an extended version of outflow controller motif 6, where E is the controller molecule. Intermediate e has been included to get limit-cycle oscillations. Rate constant k_1 describes the total inflow of Ca^{2+} from the ER and from the extracellular space into the cytosol and reflects the strength of the stimulation. For the sake of simplicity the external Ca^{2+} concentration (Ca^{2+}_{ext}) is considered to be constant ($Ca^{2+}_{ext}=1.0$). Ca^{2+}_{cyt} denotes cytosolic Ca^{2+} and its concentration. (a) Reaction scheme. Rate equations: $Ca^{2+}_{cyt}=k_1-k_2\cdot K_I\cdot Ca^{2+}_{cyt}/((K_M+Ca^{2+}_{cyt})\cdot(K_I+E))$; $\dot{e}=k_3-k_4\cdot e\cdot Ca^{2+}_{cyt}/(K^{set}_M+e)$; $\dot{E}=k_5\cdot e-k_6\cdot E$. Rate constants: k_1, variable; $k_2=500$; $k_3=2.0$; $k_4=1.0$; $K^{set}_M=1.0\times10^{-6}$; $k_5=k_5=1.0$; $K_I=0.1$. The homeostat's set-point for Ca^{2+}_{cyt} is given by $k_3/k_4=2.0$. (b) Ca^{2+}_{cyt} oscillations and average cytosolic Ca^{2+} concentration, $<Ca^{2+}_{cyt}>_t$, at different stimulations and as a function of time t. Initial concentrations: $Ca^{2+}_{cyt,0}=1.772$, $e_0=2.908\times10^{-3}$; $E_0=1.643$. The quenching of oscillations at low k_1 is due to an increased K_M value. (c) Period length and average cytosolic Ca^{2+} concentration ($<Ca^{2+}_{cyt}>$) calculated after 2000 time units for different stimulation strengths (k_1 values). Same rate constants as in (b) with $K_M=0.01$. Initial concentrations for each calculated data point: $Ca^{2+}_{cyt,0}=6.126\times10^{-2}$, $e_0=30.693$; $E_0=28.806$.

doi:10.1371/journal.pone.0107766.g010

harmonic or quasi-harmonic oscillations our results (Figs. 2f and 5b) indicate that p53 is homeostatic regulated both in average concentration and in period length to allow to expose the system probably to an optimum amount of p53 during each cycle. Because the number of p53 cycles appear positively correlated with an increased exposure of damaging radiation, the total amount of released p53 may be related to a repair mechanism. A support along these lines comes from a recent study, which indicates that p53 oscillations lead to the recovery of DNA-damaged cells, while p53 levels kept at their peak value lead to senescence and to a permanent cell cycle arrest [94]. Thus, like for cytosolic Ca^{2+}, elevated and oscillatory p53 levels seem to remain under homeostatic control in order to mediate signaling events and information which appear to be encoded in the oscillations.

Homeostasis of the Circadian Period. Circadian rhythms play an important role in the daily and seasonal adaptation of organisms to their environment and act as physiological clocks [8,95,96]. Functioning as clocks, their period is under homeostatic regulation towards a variety of environmental influences, such as changing temperature (''temperature compensation'') or food supply (''nutritional compensation''). Circadian rhythms participate in the homeostatic control of a variety of physiological variables, such as body temperature, potassium content, hormone levels, as well as sleep [1,8,95,96]. As an example, potassium homeostasis in our bodies is under a circadian control, where potassium ion is daily excreted with peak values at the middle of the day [1].

One of the questions still under discussion is how the circadian period P is kept under homeostatic control as for example seen in temperature compensation. In the antagonistic balance approach [97] the variation of the period P with respect to temperature T, expressed as $\mathrm{d}\ln P/\mathrm{d}\ln T$, is given as the sum of the control

coefficients [36] $C_{k_i}^P = \partial \ln P / \partial \ln k_1$ multiplied with the RT-scaled activation energies E_i (R is the gas constant):

$$C_T^P = \frac{\mathrm{d}\ln P}{\mathrm{d}\ln T} = \sum_i \left(\frac{\partial \ln P}{\partial \ln k_i}\right) \cdot \left(\frac{\partial \ln k_i}{\partial \ln T}\right) = \sum_i C_{k_i}^P \cdot \left(\frac{E_i}{RT}\right) \qquad (11)$$

The sum runs over all temperature-dependent processes i with rate constants k_i, where the temperature dependence of the rate constants is expressed in terms of the Arrhenius equation $k_i = A_i \cdot \exp(-E_i/RT)$ [98]. A_i is the so-called pre-exponential factor and can, to a first approximation, be treated as temperature-independent. Eq. 11 applies to any kinetic model as long as the temperature dependence of the individual reactions are formulated in terms of the Arrhenius law.

The condition for temperature compensation is obtained by setting Eq. 11 to zero. Because in oscillatory systems the $C_{k_i}^P$'s have generally positive and negative values, there is a large set of balancing E_i combinations which can lead to temperature compensation. The various combinations can be considered to arise by evolutionary selective processes acting on the activation energies [99]. Because the temperature homeostasis of circadian rhythms involves a compensatory mechanism [100], which needs to be distinguished from temperature-independence where all $C_{k_i}^P$'s are zero, temperature compensation implies that there is a certain set of non-zero control coefficients with associated activation energies which (under ideal conditions) will satisfy the balancing condition $C_T^P = 0$ within a certain temperature range.

The argument has been made that the balancing condition $C_T^P = 0$ should be non-robust and should therefore not match the many examples where mutations have no influence on the circadian period [101]. However, it should be noted that Eq. 11 is *model-independent* and provides a general description how the period of an oscillator will depend on temperature in terms of the individual reactions defined by the k_i's. Robustness, on the other hand, is a property of the actual oscillator model, where the number of zero $C_{k_i}^P$'s can be taken as a measure for robustness. For the frequency controlled oscillators described earlier, there are certain regions in parameter space such as the shaded region in Fig. 7a, for which the oscillator's period is independent towards variations of those k_i's which lie within this region. As a result, frequency controlled oscillators will show an increased robustness against environmental factors that affect rate constants, such as pH, salinity, or temperature [43,98] and therefore appear to be candidates for modeling temperature compensation.

We feel that the here shown possibilities how robust concentration and period homeostasis can be achieved provide a new handle how the negative (and positive) feedback regulations in circadian pacemakers [102] can be approached. The incorporation of these principles into models of circadian rhythms may provide further insights how temperature compensation is achieved and how circadian rhythms participate in the homeostatic regulation of organisms [1,103].

Materials and Methods

Computations were performed by using Matlab/Simulink (mathwork.com) and the Fortran subroutine LSODE [104]. Plots were generated with gnuplot (www.gnuplot.info)/Matlab. To make notations simpler, concentrations of compounds are denoted by compound names without square brackets. All concentrations, time units, and rate constants are given in arbitrary units (au).

Supporting Information

File S1 (with Figs. S1–S14 and Eqs. S1–S57), contains derivation of the set-point under oscillatory conditions, construction of the *H*-function in conservative systems, the harmonic approximation of the frequency in conservative controllers, quenching of quasi-harmonic oscillations, and an alternative example of I_1/I_2 feedback leading to robust frequency control in a motif 2 based limit-cycle oscillator.
(PDF)

Author Contributions

Conceived and designed the experiments: KT TD PR. Performed the experiments: KT OA CHS IWJ XYN TD PR. Analyzed the data: KT OA CHS TD PR. Contributed reagents/materials/analysis tools: KT OA CHS IWJ XYN TD PR. Wrote the paper: KT TD PR.

References

1. Moore-Ede M (1986) Physiology of the circadian timing system: Predictive versus reactive homeostasis. Am J Physiol 250: R737–52.
2. Sterling P, Eyer J (1988) Allostasis: A new paradigm to explain arousal pathology. In: Fisher, S and Reason, J, editor, Handbook of Life Stress, Cognition and Health, New York: John Wiley & Sons. pp. 629–49.
3. Mrosovsky N (1990) Rheostasis. The Physiology of Change. New York: Oxford University Press.
4. Lloyd D, Aon M, Cortassa S (2001) Why Homeodynamics, Not Homeostasis? The Scientific World 1: 133–145.
5. Schulkin J (2004) Allostasis, Homeostasis and the Costs of Physiological Adaptation. Cambridge, Massachusetts: Cambridge University Press.
6. Cannon W (1929) Organization for Physiological Homeostatics. Physiol Rev 9: 399–431.
7. Cannon W (1939) The Wisdom of the Body. Revised and Enlarged Edition. New York: Norton.
8. Dunlap J, Loros J, DeCoursey P (2004) Chronobiology. Biological Timekeeping. Sunderland, MA: Sinauer.
9. Berridge M, Bootman M, Roderick H (2003) Calcium signalling: dynamics, homeostasis and remodelling. Nat Rev Mol Cell Biol 4: 517–529.
10. Bernard C (1957) An Introduction to the Study of Experimental Medicine. English translation of the 1865 French edition by Henry Copley Greene. Dover: Macmillan & Co., Ltd.
11. Langley LL, editor (1973) Homeostasis. Origins of the Concept. Stroudsbourg, Pennsylvania: Dowden, Hutchinson & Ross, Inc.
12. Hers H (1990) Mechanisms of blood glucose homeostasis. J Inherit Metab Dis 13: 395–410.
13. Osundiji M, Evans M (2013) Brain control of insulin and glucagon secretion. Endocrinol Metab Clin North Am 42: 1–14.
14. Powell T, Valentinuzzi M (1974) Calcium homeostasis: responses of a possible mathematical model. Med Biol Eng 12: 287–294.
15. El-Samad H, Goff J, Khammash M (2002) Calcium homeostasis and parturient hypocalcemia: an integral feedback perspective. J Theor Biol 214: 17–29.
16. Galton V, Wood E, St Germain E, Withrow C, Aldrich G, et al. (2007) Thyroid Hormone Homeostasis and Action in the Type 2 Deiodinase-Deficient Rodent Brain during Development. Endocrinology 148: 3080–3088.
17. O'Dea E, Barken D, Peralta R, Tran K, Werner S, et al. (2007) A homeostatic model of IκB metabolism to control constitutive NF-κB activity. Mol Syst Biol 3: 111.
18. Miller A, Smith S (2008) Cytosolic nitrate ion homeostasis: Could it have a role in sensing nitrogen status? Annals of Botany 101: 485–489.
19. Huang Y, Drengstig T, Ruoff P (2011) Integrating fluctuating nitrate uptake and assimilation to robust homeostasis. Plant, Cell and Environment 35: 917–928.
20. Jeong J, Guerinot M (2009) Homing in on iron homeostasis in plants. Trends in Plant Science 14: 280–285.
21. Hancock J (2010) Cell Signalling. New York: Oxford University Press.
22. Drengstig T, Jolma I, Ni X, Thorsen K, Xu X, et al. (2012) A Basic Set of Homeostatic Controller Motifs. Biophys J 103: 2000–2010.
23. Goldbeter A (1996) Biochemical Oscillations and Cellular Rhythms. Cambridge: Cambridge University Press.
24. Goldbeter A (2002) Computational approaches to cellular rhythms. Nature 420: 238–245.

25. Tyson J, Chen K, Novak B (2003) Sniffers, buzzers, toggles and blinkers: dynamics of regulatory and signaling pathways in the cell. Curr Opin Cell Biol 15: 221–231.
26. Tsai T, Choi Y, Ma W, Pomerening J, Tang C, et al. (2008) Robust, tunable biological oscillations from interlinked positive and negative feedback loops. Science 321: 126–9.
27. Maroto M, Monk N (2008) Cellular oscillatory mechanisms. New York: Springer.
28. Wiener N (1961) Cybernetics: or Control and Communication in the Animal and the Machine. Second Edition. Cambridge, Massachusetts: The MIT Press.
29. von Bertalanffy L (1975) Perspectives on General System Theory. New York: George Braziller.
30. Savageau M (1976) Biochemical Systems Analysis. A Study of Function and Design in Molecular Biology. Reading: Addison-Wesley.
31. Voit E (2013) Biochemical Systems Theory: A Review. ISRN Biomathematics 2013: 1–53.
32. Wiener N (1954) The Human Use of Human Beings. Boston: Houghton Mifflin and Da Capo Press.
33. Curtis H, Koshland M, Nims L, Quastler H (1957) Homeostatic Mechanisms. Brookhaven Symposia in Biology, Number 10. Upton, New York: Brookhaven National Laboratory.
34. Hughes G (1964) Homeostasis and Feedback Mechanisms. New York: Academic Press.
35. Milsum J (1966) Biological Control Systems Analysis. New York: McGraw-Hill.
36. Heinrich R, Schuster S (1996) The Regulation of Cellular Systems. New York: Chapman and Hall.
37. Sontag E (2004) Some new directions in control theory inspired by systems biology. Syst Biol 1: 9–18.
38. Alon U (2006) An Introduction to Systems Biology: Design Principles of Biological Circuits. New York: Chapman & Hall.
39. Ingalls B, Yi TM, Iglesias P (2006) Using Control Theory to Study Biology. In: Szallasi, Z and Stelling, J and Periwal, V, editor, System Modeling in Cellular Biology, Cambridge, Massachusetts: MIT Press. pp. 243–267.
40. Yi T, Huang Y, Simon M, Doyle J (2000) Robust perfect adaptation in bacterial chemotaxis through integral feedback control. PNAS 97: 4649–53.
41. El-Samad H, Goff J, Khammash M (2002) Calcium homeostasis and parturient hypocalcemia: an integral feedback perspective. J Theor Biol 214: 17–29.
42. Drengstig T, Ueda H, Ruoff P (2008) Predicting Perfect Adaptation Motifs in Reaction Kinetic Networks. J Phys Chem B 112: 16752–16758.
43. Ni X, Drengstig T, Ruoff P (2009) The control of the controller: Molecular mechanisms for robust perfect adaptation and temperature compensation. Biophys J 97: 1244–53.
44. Ang J, Bagh S, Ingalls B, McMillen D (2010) Considerations for using integral feedback control to construct a perfectly adapting synthetic gene network. J Theor Biol 266: 723–738.
45. Drengstig T, Ni X, Thorsen K, Jolma I, Ruoff P (2012) Robust Adaptation and Homeostasis by Autocatalysis. J Phys Chem B 116: 5355–5363.
46. Wilkie J, Johnson M, Reza K (2002) Control Engineering. An Introductory Course. New York: Palgrave.
47. Thorsen K, Drengstig T, Ruoff P (2013) Control Theoretic Properties of Physiological Controller Motifs. In: ICSSE 2013, IEEE International Conference on System Science and Engineering. Budapest, pp. 165–170.
48. Ang J, McMillen D (2013) Physical constraints on biological integral control design for homeostasis and sensory adaptation. Biophys J 104: 505–15.
49. Thorsen K, Drengstig T, Ruoff P (2014) Transepithelial glucose transport and Na^+/K^+ homeostasis in enterocytes: an integrative model. Am J Physiol - Cell Physiol: in press.
50. Andronov A, Vitt A, Khaikin S (1966) Theory of Oscillators. New York: Dover.
51. Jolma I, Ni X, Rensing L, Ruoff P (2010) Harmonic oscillations in homeostatic controllers: Dynamics of the p53 regulatory system. Biophys J 98: 743–52.
52. Lotka A (1910) Contribution to the Theory of Periodic Reaction. J Phys Chem 14: 271–74.
53. Lotka A (1920) Undamped Oscillations Derived from the Law of Mass Action. J Am Chem Soc 42: 1595–99.
54. Goodwin B (1963) Temporal Organization in Cells. London: Academic Press.
55. Goodwin B (1965) Oscillatory behavior in enzymatic control processes. In: Weber, G, editor, Advances in Enzyme Regulation, Vol. 3, Oxford, UK: Pergamon Press. pp. 425–438.
56. Griffith J (1968) Mathematics of cellular control processes I. Negative feedback to one gene. J Theor Biol 20: 202–208.
57. Rensing L, Ruoff P (2002) Temperature effect on entrainment, phase shifting, and amplitude of circadian clocks and its molecular bases. Chronobiology International 19: 807–864.
58. Iwasaki K, Liu D, Thomas J (1995) Genes that control a temperature-compensated ultradian clock in *Caenorhabditis elegans*. PNAS 92: 10317–10321.
59. Dowse H, Ringo J (1987) Further evidence that the circadian clock in Drosophila is a population of coupled ultradian oscillators. J Biol Rhythms 2: 65–76.
60. Geva-Zatorsky N, Rosenfeld N, Itzkovitz S, Milo R, Sigal A, et al. (2006) Oscillations and variability in the p53 system. Mol Syst Biol 2: 2006 0033.
61. Lahav G (2008) Oscillations by the p53-Mdm2 Feedback Loop. In: Maroto, M and Monk, NAM, editor, Cellular Oscillatory Mechanisms, New York: Landes Bioscience and Springer Science+Business Media. pp. 28–38.
62. Higgins J (1967) Oscillating reactions. Industrial & Engineering Chemistry 59: 18–62.
63. Franck U (1980) Feedback Kinetics in Physicochemical Oscillators. Berichte der Bunsengesellschaft für Physikalische Chemie 84: 334–41.
64. Eiswirth M, Freund A, Ross J (1991) Mechanistic classification of chemical oscillators and the role of species. Adv Chem Phys 80: 127–199.
65. Goldbeter A (2002) Computational approaches to cellular rhythms. Nature 420: 238–245.
66. Novák B, Tyson J (2008) Design principles of biochemical oscillators. Nat Rev Mol Cell Biol 9: 981–991.
67. Marks F, Klingmüller U, Müller-Decker K (2009) Cellular Signal Processing. An Introduction to the Molecular Mechanisms of Signal Transduction. New York: Garland Science.
68. Bodalia A, Li H, Jackson M (2013) Loss of endoplasmic reticulum Ca^{2+} homeostasis: contribution to neuronal cell death during cerebral ischemia. Acta Pharm Sinica 34: 49–59.
69. Giacomello M, De Mario A, Scarlatti C, Primerano S, Carafoli E (2013) Plasma membrane calcium ATPases and related disorders. Int J Biochem & Cell Biol 45: 753–762.
70. Schapira A (2013) Calcium dysregulation in Parkinson's disease. Brain 136: 2015–2016.
71. Carafoli E (2002) Calcium signaling: A tale for all seasons. PNAS 99: 1115–1122.
72. Berridge M, Bootman M, Roderick H (2003) Calcium signalling: dynamics, homeostasis and remodelling. Nat Rev Mol Cell Biol 4: 517–529.
73. Woods H, Cuthbertson K, Cobbold P (1986) Repetitive transient rises in cytoplasmic free calcium in hormone-stimulated hepatocytes. Nature 319: 600–602.
74. Berridge M, Galione A (1988) Cytosolic calcium oscillators. The FASEB Journal 2: 3074–3082.
75. Parekh A (2011) Decoding cytosolic Ca^{2+} oscillations. Trends Biochemical Sciences 36: 78–87.
76. Cheng H, Lederer W (2008) Calcium Sparks. Physiol Rev 88: 1491–1545.
77. De Koninck P, Schulman H (1998) Sensitivity of CaM Kinase II to the Frequency of Ca^{2+} oscillations. Science 279: 227–230.
78. Goldbeter A, Dupont G, Berridge M (1990) Minimal model for signal-induced Ca2+ oscillations and for their frequency encoding through protein phosphorylation. PNAS 87: 1461–1465.
79. Dupont G, Berridge M, Goldbeter A (1991) Signal-induced Ca^{2+} oscillations: Properties of a model based on Ca^{2+}-induced Ca^{2+} release. Cell Calcium 12: 73–85.
80. Schuster S, Marhl M, Höfer T (2002) Modelling of simple and complex calcium oscillations. From single-cell responses to intercellular signalling. Eur J Biochem 269: 1333–1355.
81. Sneyd J, Tsaneva-Atanasova K, Yule D, Thompson J, Shuttleworth T (2004) Control of calcium oscillations by membrane fluxes. PNAS 101: 1392–6.
82. Politi A, Gaspers L, Thomas A, Höfer T (2006) Models of IP3 and Ca2+ oscillations: frequency encoding and identification of underlying feedbacks. Biophys J 90: 3120–33.
83. Putney J, Bird G (2008) Cytoplasmic calcium oscillations and store-operated calcium influx. J Physiol 586: 3055–9.
84. Knoke B, Bodenstein C, Marhl M, Perc M, Schuster S (2010) Jensen's inequality as a tool for explaining the effect of oscillations on the average cytosolic calcium concentration. Theory Biosci 129: 25–38.
85. Berridge M (2005) Unlocking the secrets of cell signaling. Annu Rev Physiol 67: 1–21.
86. Shuttleworth T (1999) What drives calcium entry during Ca_i^{2+} oscillations?–challenging the capacitative model. Cell calcium 25: 237–246.
87. Bird G, Putney J (2005) Capacitative calcium entry supports calcium oscillations in human embryonic kidney cells. J Physiol 562: 697–706.
88. Levine A (1997) p53, the cellular gatekeeper for growth and division. Cell 88: 323–31.
89. Fu W, Ma Q, Chen L, Li P, Zhang M, et al. (2009) MDM2 acts downstream of p53 as an E3 ligase to promote FOXO ubiquitination and degradation. J Biol Chem 284: 13987–4000.
90. Michael D, Oren M (2003) The p53-Mdm2 module and the ubiquitin system. Semin Cancer Biol 13: 49–58.
91. Stommel J, Wahl G (2004) Accelerated MDM2 auto-degradation induced by DNA-damage kinases is required for p53 activation. EMBO J 23: 1547–56.
92. Asher G, Lotem J, Kama R, Sachs L, Shaul Y (2002) NQO1 stabilizes p53 through a distinct pathway. PNAS 99: 3099–104.
93. Geva-Zatorsky N, Dekel E, Batchelor E, Lahav G, Alon U (2010) Fourier analysis and systems identification of the p53 feedback loop. PNAS 107: 13550–13555.
94. Purvis J, Karhohs K, Mock C, Batchelor E, Loewer A, et al. (2012) p53 dynamics control cell fate. Science 336: 1440–1444.
95. Bünning E (1963) The Physiological Clock. Berlin: Springer-Verlag.
96. Edmunds L (1988) Cellular and Molecular Bases of Biological Clocks. New York: Springer-Verlag.
97. Ruoff P (1992) Introducing temperature-compensation in any reaction kinetic oscillator model. J Interdiscipl Cycle Res 23: 92–99.
98. Noggle J (1996) Physical Chemistry. Third Edition. New York: Harper Collins.

99. Ruoff P (1994) General homeostasis in period-and temperature-compensated chemical clock mutants formed by random selection conditions. Naturwissenschaften 81: 456–459.
100. Zimmerman W, Pittendrigh C, Pavlidis T (1968) Temperature compensation of the circadian oscillation in *Drosophila pseudoobscura* and its entrainment by temperature cycles. J Insect Physiol 14: 669–684.
101. Hong C, Conrad E, Tyson J (2007) A proposal for robust temperature compensation of circadian rhythms. PNAS 104: 1195–1200.
102. Dunlap J (1999) Molecular bases for circadian clocks. Cell 96: 271–290.
103. Bonny O, Firsov D (2009) Circadian clock and the concept of homeostasis. Cell Cycle 8: 4015–14.
104. Radhakrishnan K, Hindmarsh A (1993) Description and Use of LSODE, the Livermore Solver for Ordinary Differential Equations. NASA Reference Publication 1327, Lawrence Livermore National Laboratory Report UCRL-ID-113855. Cleveland, OH 44135-3191: National Aeronautics and Space Administration, Lewis Research Center.

Supporting Material, File S1

Robust Concentration and Frequency Control in Oscillatory Homeostats

K. Thorsen[1], O. Agafonov[2], C. H. Selstø[2], I. W. Jolma[2], X. Y. Ni[2], T. Drengstig[1], and P. Ruoff[2*]

[1]Department of Electrical Engineering and Computer Science,
[2]Centre for Organelle Research
University of Stavanger, Stavanger, Norway

[*]Corresponding author. Address: Centre for Organelle Research, University of Stavanger, N-4036 Stavanger, Norway, Tel.: (47) 5183-1887, Fax: (47) 5183-1750, E-mail: peter.ruoff@uis.no

Set-point of Controlled Variable A under Oscillatory Conditions

A-Activating Controller Motifs

The A-activating motifs are 1, 2, 5, and 6 (Fig. 1, main paper). As an example we use the harmonic oscillator described in Fig. 2d. The rate equation for E is given as:

$$\dot{E} = k_4 \cdot A - \frac{V_{max}^{E_{set}} \cdot E}{K_M^{E_{set}} + E} \tag{S1}$$

Integral control is introduced by zero-order kinetics when $K_M^{E_{set}}$ becomes negligible in comparison to E (1, 2). Under oscillatory conditions the set-point in the average concentration of A, $<A>_c$, is obtained by using the following condition

$$<\dot{E}>_c = \oint_c \dot{E}\, dt = \frac{1}{P}\int_0^P \dot{E}\, dt = 0 \tag{S2}$$

where integration occurs along one orbit/cycle of stable oscillations with period P. By inserting the expression of $\dot{E}$ (Eq. S1) into Eq. S2 we get

$$<\dot{E}>_c = k_4 \cdot <A>_c - V_{max}^{E_{set}} \left\langle \frac{E}{K_M^{E_{set}} + E} \right\rangle_c = 0 \tag{S3}$$

Using ideal zero-order condition, $K_M^{E_{set}} \to 0$, we have $<E/(K_M^{E_{set}}+E)>_c \to 1$, i.e.,

$$\left\langle \frac{E}{K_M^{E_{set}}+E} \right\rangle_c = \lim_{K_M \to 0} \left\{ \frac{1}{P}\int_o^P \left(\frac{E}{K_M+E} \right) dt \right\} = \frac{1}{P}\int_o^P \lim_{K_M \to 0} \left\{ \frac{E}{K_M+E} \right\} dt$$

$$= \frac{1}{P}\int_o^P 1\, dt = 1 \tag{S4}$$

Inserting this result into Eq. S3, we get

$$<A>_c = \frac{V_{max}^{E_{set}}}{k_4} = <A>_{set} \tag{S5}$$

Note that $<A>_c$ is identical with the set-point of A when the system is non-oscillatory. This is shown in Fig. 3b and Fig. 5d for limit-cycle oscillators based on motif 2 and 5, respectively.

A-Inhibiting Controller Motifs

The A-inhibiting controller motifs are 3, 4, 7 and 8. As an example we use controller motif 3.

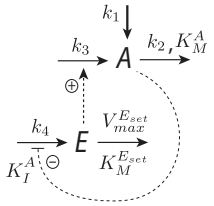

Figure S1. Motif 3.

The rate equation for E is given as:

$$\dot{E} = \frac{k_4 \cdot K_I^A}{K_I^A + A} - \frac{V_{max}^{E_{set}} \cdot E}{K_M^{E_{set}} + E} \tag{S6}$$

Considering zero-order conditions in the Michaelis-Menten removal of E, the condition $<\dot{E}>_c$=0 gives:

$$<\dot{E}>_c = k_4 \cdot K_I^A \left\langle \frac{1}{K_I^A + A} \right\rangle_c - V_{max}^{E_{set}} = 0 \tag{S7}$$

$$\Rightarrow \quad \left\langle \frac{1}{K_I^A + A} \right\rangle_c \stackrel{\text{def}}{=} \frac{1}{P} \int_o^P \frac{1}{K_I^A + A}\, dt = \frac{V_{max}^{E_{set}}}{k_4 \cdot K_I^A} \tag{S8}$$

where P is the period of the oscillator and $V_{max}^{E_{set}}/k_4 \cdot K_I^A$ is the homeostatic conserved property. In case the system becomes non-oscillatory the homeostatic set-point of A, A_{set}, is given as (2):

$$\frac{1}{K_I^A + A_{set}} = \frac{V_{max}^{E_{set}}}{k_4 \cdot K_I^A} \quad \Rightarrow \quad A_{set} = \frac{k_4 \cdot K_I^A}{V_{max}^{E_{set}}} - K_I^A \tag{S9}$$

Conservative Oscillator Types and Construction of their H-functions

We illustrate here the construction of the H-functions of the four different conservative oscillator types that can be constructed by using motif 2.

Oscillator with both A and E Removals Being Zero-Order

Fig. 2a in the main paper shows the reaction scheme and rate equations for this case. For the sake of simplicity we assume that k_1=0. The H-function obeys the following equations, which are analogous to the Hamilton-Jacobi equations (3)

$$\frac{\partial H}{\partial E} = -\dot{A}\,; \quad \frac{\partial H}{\partial A} = \dot{E} \tag{S10}$$

The H-function is constructed by integrating $\dot{A}$ and $\dot{E}$, i.e.,

$$H = -\int \dot{A}\,\mathrm{d}E + \int \dot{E}\,\mathrm{d}A \tag{S11}$$

Applying the zero-order conditions with respect to the removal kinetics of A and E, we get

$$H = -\int \left(-k_2 + \frac{k_3{\cdot}K_I^E}{K_I^E + E}\right)\,\mathrm{d}E + \int \left(k_4{\cdot}A - V_{max}^{E_{set}}\right)\,\mathrm{d}A \tag{S12}$$

which leads to the final expression of H (see also Fig. S2)

$$H = k_2{\cdot}E - k_3{\cdot}K_I^E{\cdot}\ln(K_I^E + E) + \tfrac{1}{2}k_4{\cdot}A^2 - V_{max}^{E_{set}}{\cdot}A \tag{S13}$$

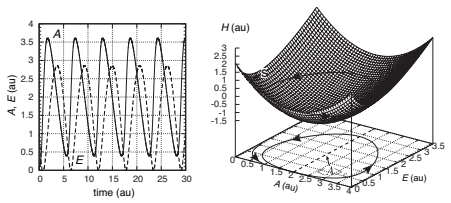

Figure S2. Left panel: conservative oscillations in A and E using motif 2 with rate constant as given in Fig. 2b (t<50, k_2=1). Initial concentrations A_0=0.1 and E_0=1.0. Right panel: H-function (Eq. S13) showing the oscillations of the left panel as curves in A-E phase space and on the surface of H. Dashed line indicates the oscillator's set-point $<A>_c$=2.0.

Oscillator with Autocatalysis in A and E and First-Order Removals

In the case the degradation of E is first order, integral control in A can be implemented by first-order autocatalysis in E (3). To keep the system conservative with first-order degradation in A, the formation in A needs to be first-order autocatalytic as indicated in Fig. S3 and shown by the rate equations.

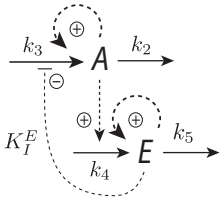

Figure S3. Motif 2 with autocatalysis and first-order degradations in A and E.

The rate equations are:

$$\dot{A} = \frac{k_3 \cdot K_I^E}{K_I^E + E} \cdot A - k_2 \cdot A \tag{S14}$$

$$\dot{E} = k_4 \cdot A \cdot E - k_5 \cdot E \tag{S15}$$

Introducing the variables $\xi = \ln A$ and $\eta = \ln E$, the rate equations can be transformed to:

$$\dot{\xi} = \frac{\dot{A}}{A} = \frac{k_3 \cdot K_I^E}{K_I^E + E} - k_2 = \frac{k_3 \cdot K_I^E}{K_I^E + e^{\eta}} - k_2 \tag{S16}$$

$$\dot{\eta} = \frac{\dot{E}}{E} = k_4 \cdot A - k_5 = k_4 \cdot e^{\xi} - k_5 \tag{S17}$$

By expressing E and A in Eqs. S16 and S17 in term of ξ and η, the function

$$H(\xi, \eta) = \int \dot{\xi} \, \mathrm{d}\eta - \int \dot{\eta} \, \mathrm{d}\xi \tag{S18}$$

describes the kinetics of this conservative system and, after integration, is given by

$$H(\xi,\eta) = (k_3 - k_2)\cdot\eta - k_3\cdot\ln(K_i^E + e^{\eta}) - k_4\cdot e^{\xi} + k_5\cdot\xi \tag{S19}$$

By using $\xi = \ln A$ and $\eta = \ln E$, H can be expressed in terms of A and E, i.e,

$$H(A,E) = (k_3 - k_2)\cdot\ln E - k_3\cdot\ln(K_i^E + E) - k_4\cdot A + k_5\cdot\ln A \tag{S20}$$

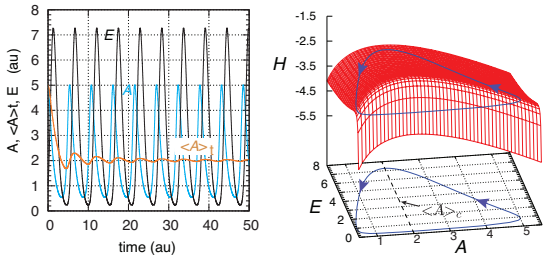

Figure S4. Left panel: conservative oscillations in A, E, and $<A>_t$ as a function of time using motif 2 when both A and E are formed autocatalytically and degraded by first-order reactions (eqs. S14 and S15). Rate constants: K_I^E=0.1, k_2=1.0, k_3=10.0, k_4=1.0, k_5=2.0 Initial concentrations A_0=5.0 and E_0=1.0. Right panel: H-function (Eq. S20) showing the oscillations of the left panel as curves in A-E phase space and on the surface of H. Dashed line indicates the oscillator's set-point $<A>_c$=2.0.

Oscillator with Autocatalysis in A and Zero-order Removal of E

The scheme of this conservative oscillator is given in Fig. S5. The rate equations are:

$$\dot{A} = \frac{k_3\cdot K_I^E}{K_I^E + E}\cdot A - k_2\cdot A \tag{S21}$$

$$\dot{E} = k_4\cdot A - \frac{V_{max}^{E_{set}}\cdot E}{K_M^{E_{set}} + E} \tag{S22}$$

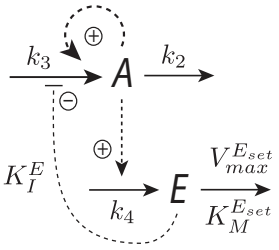

Figure S5. Motif 2 with autocatalysis and first-order degradation in A and and zero-order removal of E.

The H-function is given by the following integral:

$$H(\xi, E) = -\int \dot{\xi}\,\mathrm{d}E + \int \dot{E}\,\mathrm{d}\xi \tag{S23}$$

$$= -k_3 k_6 \ln(k_6{+}E) + k_2 E + k_4 e^{\xi} - k_5 \xi \tag{S24}$$

where

$$\dot{\xi} = \frac{\dot{A}}{A} = \frac{k_3{\cdot}K_I^E}{K_I^E + E} - k_2 \tag{S25}$$

Inserting the expression $\xi{=}\ln(A)$ into Eq. S24 gives the final form of $H(A, E)$:

$$H(A, E) = -k_3{\cdot}k_6{\cdot}\ln(k_6{+}E) + k_2{\cdot}E + k_4{\cdot}A - k_5{\cdot}\ln(A) \tag{S26}$$

Fig. S6 shows the numerically calculated oscillations and the constructed H-function describing these oscillations in phase-space.

Oscillator with Zero-order Removal of A and Autocatalysis in E

The reaction scheme of this conservative oscillator is given in Fig. S7.

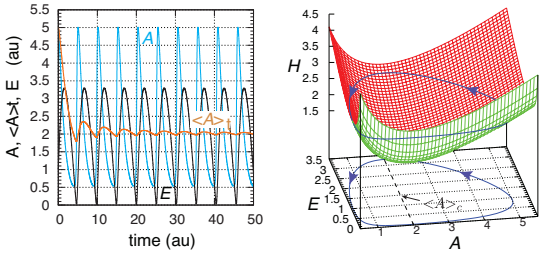

Figure S6. Left panel: conservative oscillations in A, E, and $<A>_t$ as a function of time using motif 2 (Fig. S5) and rate eqns. S21 and S22. Rate constants: K_I^E=0.1, k_2=1.0, k_3=10.0, k_4=1.0, $V_{max}^{E_{set}}$=2.0, and $k_M^{E_{set}}$=1×10^{-6}. Initial concentrations A_0=5.0 and E_0=1.0. Right panel: H-function (Eq. S26) showing the oscillations of the left panel as curves in A-E phase space and on the surface of H. Dashed line indicates the oscillator's set-point $<A>_c$=2.0.

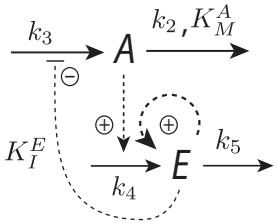

Figure S7. Motif 2 with autocatalysis and first-order degradation in A and zero-order removal in E.

The rate equations are:

$$\dot{A} = \frac{k_3 \cdot K_I^E}{K_I^E + E} - \frac{k_2 \cdot A}{K_M^A + A} \tag{S27}$$

$$\dot{E} = k_4 \cdot A \cdot E - k_5 \cdot E \tag{S28}$$

The H-function is given by the integral:

$$H(A,\eta) = -\int \dot{A}\,\mathrm{d}\eta + \int \dot{\eta}\,\mathrm{d}A \tag{S29}$$

where

$$\eta = \ln E \quad \text{and} \quad \dot{\eta} = \frac{\dot{E}}{E} = k_4{\cdot}A - k_5 \tag{S30}$$

$$\Rightarrow \quad H(A,\eta) = -\int \left(\frac{k_3 K_I^E}{K_I^E + e^{\eta}} - k_2\right)\mathrm{d}\eta + \int (k_4 A - k_5)\,\mathrm{d}A \tag{S31}$$

$$= -k_3 K_I^E \int \frac{\mathrm{d}\eta}{K_I^E + e^{\eta}} + k_2\eta + \tfrac{1}{2}k_4{\cdot}A^2 - k_5 A \tag{S32}$$

$$= -k_3\eta + k_3 \ln(K_I^E + e^{\eta}) + k_2\eta + \tfrac{1}{2}k_4{\cdot}A^2 - k_5 A \tag{S33}$$

where

$$\int \frac{\mathrm{d}\eta}{K_I^E + e^{\eta}} = \frac{1}{K_I^E}\left(\eta - \ln(K_I^E + e^{\eta})\right) \tag{S34}$$

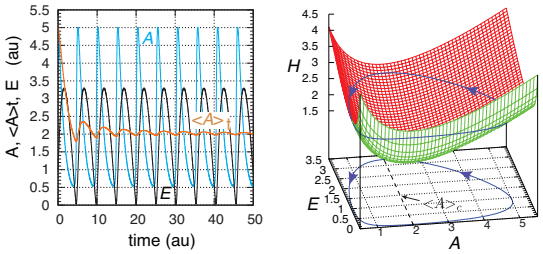

Figure S8. Left panel: conservative oscillations in A, E, and $<A>_t$ as a function of time using motif 2 (Fig. S7) and rate eqns. S27 and S28). Rate constants: K_I^E=0.1, k_2=1.0, k_3=10.0, k_4=1.0, k_5=2.0, and K_M^A=1×10^{-6}. Initial concentrations A_0=3.0232 and E_0=10.2342. Right panel: H-function (Eq. S35) showing the oscillations of the left panel as curve in A-E phase space and on the surface of H. The curve on the H-surface is located at H=0.9464 (calculated from the initial concentration A_0 and E_0). Dashed line indicates the homeostats's set-point $<A>_c$=2.0.

Inserting η= ln(E) into Eq.S33 leads to

$$H(A,E) = -k_3 \ln(E) + k_3 \ln(K_I^E + E) + k_2 \ln(E) + \tfrac{1}{2} k_4 \cdot A^2 - k_5 A \qquad \text{(S35)}$$

Fig. S8 shows the numerically calculated oscillations and the constructed H-function.

Harmonic Approximation of Frequency in Conservative Oscillatory Controllers

The harmonic approximation of the frequency in conservative controllers provides insights why oscillatory controllers based on even-numbered motifs (Fig. 1) increase their frequency upon increased perturbation strengths. As an example we show how the harmonic approximation of the frequency can be obtained for the conservative oscillatory controller based on motif 2 (Fig. 2a). We assume zero-order removal in A and E and $k_1 = 0$. The rate equations read then:

$$\dot{A} = \frac{k_3 \cdot K_I^E}{K_I^E + E} - k_2 \qquad \text{(S36)}$$

$$\dot{E} = k_4 \cdot A - V_{max}^{E_{set}} \qquad \text{(S37)}$$

Taking the second time derivative of Eq. S36 gives:

$$\ddot{A} = -\frac{k_3 \cdot K_I^E}{(K_I^E + E)^2} \cdot \dot{E} = -\frac{k_3 \cdot K_I^E}{(K_I^E + E)^2} (k_4 A - V_{max}^{E_{set}}) \qquad \text{(S38)}$$

Eq. S38 can be rearranged into the following form:

$$\frac{\ddot{A}}{\frac{k_3 \cdot k_4 \cdot K_I^E}{(K_I^E + E)^2}} + A = \frac{V_{max}^{E_{set}}}{k_4} = A_{ss} = <A>_{set} \qquad \text{(S39)}$$

When E in Eq. S39 is replaced by E_{ss} we get the equation of a harmonic oscillator, i.e., $\ddot{A}/\omega^2 + A$=constant, with frequency ω given as

$$\omega = \sqrt{\frac{k_3 \cdot k_4 \cdot K_I^E}{(K_I^E + E_{ss})^2}} \qquad \text{(S40)}$$

and which approximately describes the frequency of the conservative oscillator (Eq. S39). A corresponding second-order differential equation can be derived for E:

$$\frac{\ddot{E}}{\frac{k_3 \cdot k_4 \cdot K_I^E}{(K_I^E+E)(K_I^E+E_{ss})}} + E = \frac{k_3 \cdot K_I^E}{k_2} - K_I^E = E_{ss} \tag{S41}$$

A_{ss} and E_{ss} denote the steady state concentrations when $\dot{A}$=0 and $\dot{E}$=0. When replacing E by E_{ss} in Eq. S41 the same harmonic frequency approximation as described by Eq. S40 is obtained. Similar expressions are found for the other E-inhibiting oscillatory controllers. Because the level of E decreases with increasing perturbation strength, Eq. S40 indicates that the E-inhibiting controllers will increase their frequency when perturbations are increased as shown in Fig. 3 for the motif-2-based controller.

For the conservative oscillators based on motifs 4 and 8, i.e., when both A and E are inhibiting, the harmonic oscillator approximations are:

$$\frac{\ddot{A}}{\frac{k_i \cdot k_j \cdot K_I^E \cdot K_I^A}{(K_I^E+E_{ss})^2(K_I^A+A_{ss})^2}} + A = A_{ss} \tag{S42}$$

$$\frac{\ddot{E}}{\frac{k_i \cdot k_j \cdot K_I^E \cdot K_I^A}{(K_I^E+E_{ss})^2(K_I^A+A_{ss})^2}} + E = E_{ss} \tag{S43}$$

where k_i and k_j denote rate constants of the reactions which are inhibited by A and E.

For conservative oscillators based on motifs 1 and 5, the frequency is not dependent on either A or E giving harmonic oscillators (see next section).

Harmonic Oscillations (Inflow Controller Motif 1)

Fig. S9 shows a two-component representation of motif 1. When $K_M^A \ll A$ and $K_M^{E_{set}} \ll E$ the system becomes an harmonic oscillator with set point $<A>_c = k_4/V_{max}^{E_{set}}$.

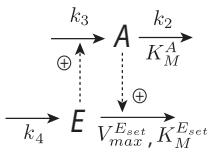

Figure S9. Motif 1. The two-component system shows harmonic oscillations when $K_M^A \ll A$ and $K_M^{E_{set}} \ll E$, i.e. removal of A and E follow zero-order kinetics.

We consider the rate equations:

$$\dot{A} = k_3 \cdot E - \frac{k_2 \cdot A}{K_M^A + A} \tag{S44}$$

$$\dot{E} = k_4 - \frac{V_{max}^{E_{set}} \cdot E}{K_M^{E_{set}} + E} \cdot A \tag{S45}$$

In case of zero-order conditions in the removal of A and E they reduce to:

$$\dot{A} = k_3 \cdot E - k_2 \tag{S46}$$

$$\dot{E} = k_4 - V_{max}^{E_{set}} \cdot A \tag{S47}$$

Taking the second time derivative of Eq. S46 and inserting the expression of $\dot{E}$ into it, leads to:

$$\ddot{A} = k_3 \cdot \dot{E} = k_3 \cdot k_4 - k_3 \cdot V_{max}^{E_{set}} \cdot A \tag{S48}$$

Dividing Eq. S48 by $k_3 \cdot V_{max}^{E_{set}}$ gives the equation of a harmonic oscillator around the set-point $<A>_c$:

$$\frac{\ddot{A}}{\omega^2} + A = \frac{k_4}{V_{max}^{E_{set}}} = <A>_c \tag{S49}$$

where $A(t)$ is given as:

$$A(t) = A_{amp} \sin(\omega \cdot t + \phi) + <A>_c \tag{S50}$$

A_{amp} denotes the A-amplitude of the oscillations, ω is the frequency, and ϕ is a phase angle.

Quenching of Oscillations in Quasi-Conservative Systems

First-Order Degradation Restrains Oscillations

The amount of uncontrolled first-order degradation of A has a major influence on the size of the parameter space for the extended motif 5 (Figs. 4a and 5d in main paper) in which sustained oscillations are observed.Our results show that first-order degradation has the ability to quench the oscillations and does so for a large range of parameters. Fig. S10 shows how an increasing first-order rate constant in the removal of A reduces the oscillatory behavior in the k_1 (uncontrolled inflow of A)-k_5 (conversion of precursor e into E) parameter space. The parameter space in which sustained oscillations are observed shrinks markedly when when the first-order degradation rate constant k_3 is increased by one order of magnitude, i.e. from 0.01 to 0.1 (Fig. S10, panel c)

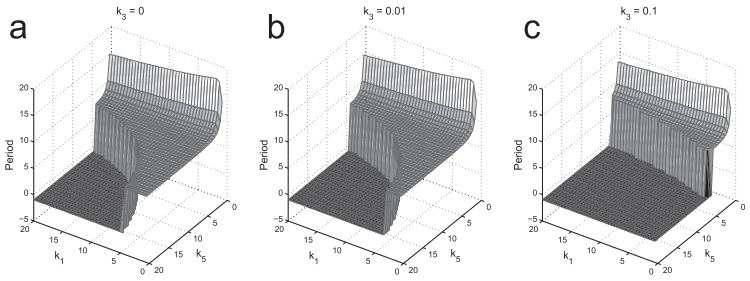

Figure S10. Period of oscillations for varying k_1 and k_5 values using the limit-cycle verion of motif 5 described in the main paper (Fig. 4a). The period is set to -1 when there are no oscillations (black area). Panels (a), (b), and (c) show the results for three different values for the first-order A-removing rate constant k_3. The parameter values used are: k_2=0.5, k_4=0.7, $V_{max}^{E_{set}}$=0.5, $K_M^A = 4 \times 10^{-3}$, and $K_M^{E_{set}} = 1 \times 10^{-2}$.

Fig. S10 also shows the propagation towards quasi-harmonic kinetics. With increasing k_5 values the periods approaches the harmonic values of $2\pi/\sqrt{k_2 k_4}$. When the conversion from e to E is fast (high k_5), the motif gives quasi-

harmonic oscillatory period homeostasis as discussed in the main paper. A very fast conversion from e to E does however lead to a non-oscillatory homeostasis in A, i.e., the range of k_1 values that give oscillations shrinks with increasing k_5.

Zero-Order Degradation Facilitates Oscillations

How close the controlled degradation of A is to a perfect zero-order degradation is another factor that influences the size of the oscillatory regime. With a controlled degradation of A by the compensatory flux j_{comp}

$$j_{comp} = \frac{k_2 \cdot A \cdot E}{K_M^A + A} \tag{S51}$$

K_M^A becomes an indicator of how close the degradation is to perfect zero-order, i.e. when $K_M^A \to 0$. Fig. S11 shows the size of the parameter space in which one observes oscillatory behavior in the extended motif 5 (Fig 4a in the main paper) for three different values of K_M^A. The uncontrolled first-order degradation rate constant k_3 is 1×10^{-2} in all cases.

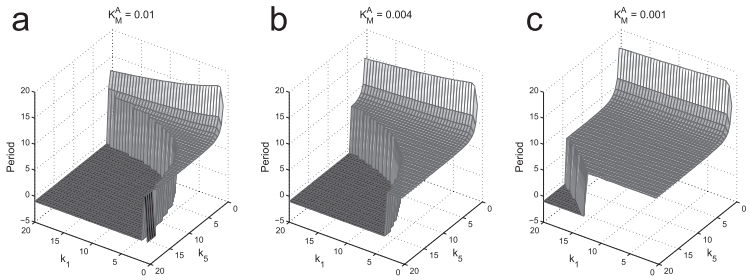

Figure S11. Period of oscillations for varying k_1 and k_5 values using the limit-cycle verion of motif 5 described in the main paper (Fig. 4a). The period is set to -1 when there are no oscillations (black area). Panels (a), (b), and (c) show the results for three different values of K_M^A. The parameter values used are: k_2=0.5, k_3=1×10^{-2}, k_4=0.7, $V_{max}^{E_{set}}$=0.5, and $K_M^{E_{set}}$=1×10^{-2}.

Robust Frequency Control With Inflow Controller Motif 2 and Alternative I_1/I_2 Feedback

In the main manuscript the feedbacks from I_1 and I_2 were applied on intermediate a (Fig. 7) or were "mixed", i.e. were applied to both "a" and "A" (Fig. 8). In the following we show a model where the feedbacks from I_1/I_2 are returned to A only. The scheme is given in Fig. S12.

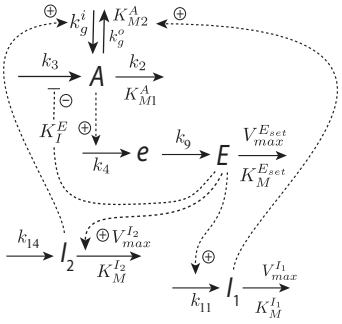

Figure S12. Alternative I_1/I_2 feedback arrangement in a motif-2-based oscillator. The feedbacks from I_1 and I_2 act on A only.

The rate equations are:

$$\dot{A} = \frac{k_3 \cdot K_I^E}{K_I^E + E} + k_g^i \cdot I_2 - \left(\frac{k_g^o \cdot A}{K_{M2}^A + A}\right) \cdot I_1 - \frac{k_2 \cdot A}{K_{M1}^A + A} \tag{S52}$$

$$\dot{e} = k_4 \cdot A - k_9 \cdot e \tag{S53}$$

$$\dot{E} = k_9 \cdot e - \frac{V_{max}^{E_{set}} \cdot E}{K_M^{E_{set}} + E} \tag{S54}$$

$$\dot{I}_1 = k_{11} \cdot E - \frac{V_{max}^{I_1} \cdot I_1}{K_M^{I_1} + I_1} \tag{S55}$$

$$\dot{I}_2 = k_{14} - \left(\frac{V_{max}^{I_2} \cdot I_2}{K_M^{I_2} + I_2}\right) \cdot E \tag{S56}$$

The controller molecules (manipulated variables) E, I_1, and I_2 define the set-points $<A>_{set}$, $<E>^{I_1}_{set}$, and $<E>^{I_2}_{set}$, respectively, which are given by

$$<A>_{set} = \frac{V^{E_{set}}_{max}}{k_4}; \quad <E>^{I_1}_{set} = \frac{V^{I_1}_{max}}{k_{11}}; \quad <E>^{I_2}_{set} = \frac{k_{14}}{V^{I_2}_{max}} \tag{S57}$$

Fig. S13 shows the oscillator's behavior, i.e., $<A>$, $<E>$, and the frequency as a function of the perturbation k_2 when $<A>_{set}$=2.0, $<E>^{I_1}_{set} = 5.0$, and $<E>^{I_2}_{set} = 2.0$. Due to the two set-points $<E>^{I_1}_{set}$ and $<E>^{I_2}_{set}$ the frequency has a corresponding homeostatic regulation at two frequencies. Note that, although $<E>$ changes between different set-points when k_2 is changed, $<A>$ is kept at its homeostatic set-point $<A>_{set}$=2.0.

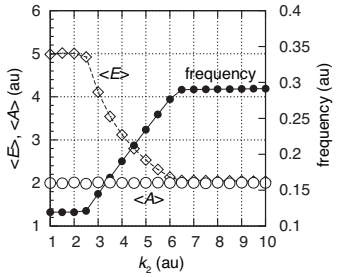

Figure S13. $<A>$, $<E>$, and the frequency as a function of the perturbation strength k_2. Rate constant values: k_3=100.0, k_4=1.0, K^E_I=0.1, $V^{E_{set}}_{max}$=2.0, $K^{E_{set}}_M$=1×10^{-6}, K^A_{M1}=1×10^{-6}, k_9=20.0, k_{11}=1.0, $V^{I_1}_{max}$=5.0, $K^{I_1}_M$=1×10^{-6}, k_{14}=2.0, $V^{I_2}_{max}$=1.0, $K^{I_2}_M$=1×10^{-6}, k^o_g=1×10^{-2}, K^A_{M2}=1×10^{-6}, k^i_g=1×10^{-2}. Initial concentrations (the same for each k_2 value): A_0=0.6677, E_0=1.0536, e_0=2.5827×10^{-2}, I_{1_0}=1.1614×10^{-3}, I_{2_0}=7.5008×10^2. The values of $<A>$, $<E>$, and the frequency were determined after 1500 time units.

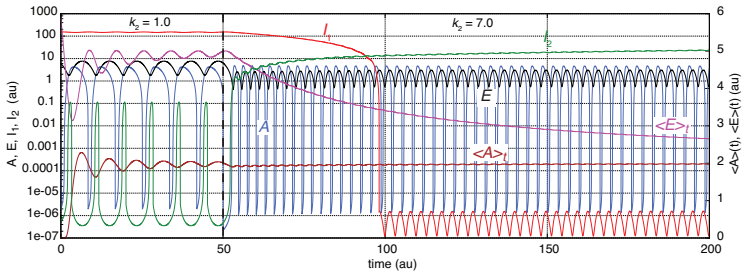

Figure S14. Time plot of the system from Fig. S13 at low and high k_2 values. At k_2=1.0 controller I_1 dominates and removes A to achieve the set-point $<E>^{I_1}_{set}$=5.0. When k_2 is high (7.0) controller I_2 is up-regulated and adds A such that $<E>$ homeostasis at $<E>^{I_2}_{set}$=2.0 is obtained. A_0=6.1923×10^{-3}, E_0=5.9023, e_0=2.5385×10^{-3}, I_{1_0}=153.26, I_{2_0}=5.1252×10^{-7}.

Fig. S14 shows the oscillations and the I_1/I_2 regulation of the system when k_2 is changed from a relative low value (k_2=1.0) to a relative high value (k_2=7.0) at time t=50.0 (dashed line). At low k_2 values controller I_1 is dominant and removes A such that this controller's set-point in $<E>$ is maintained. At high k_2 values I_2 is up-regulated and I_1 downregulated. I_2 now adds A to the system in order to keep the $<E>$ level at the set-point determined by controller I_2.

References

[1] Ni, X. Y.; Drengstig, T.; Ruoff, P. *Biophys J* **2009**, *97*, 1244–53.

[2] Drengstig, T.; Jolma, I. W.; Ni, X. Y.; Thorsen, K. G.; Xu, X. M.; Ruoff, P. *Biophys J* **2012**, *103*, 2000–10.

[3] Drengstig, T.; Ni, X. Y.; Thorsen, K.; Jolma, I. W.; Ruoff, P. *J Phys Chem B* **2012**, *116*, 5355–5363.